AMERICAN SOCIETY FOR MICROBIOLOGY Microbiology and Molecular Biology Reviews®

REVIEW

Bacterial Vivisection: How Fluorescence-Based Imaging Techniques Shed a Light on the Inner Workings of Bacteria

Alexander Cambré,[a] Abram Aertsen[a]

[a]KU Leuven, Department of Microbial and Molecular Systems, Faculty of Bioscience Engineering, Leuven, Belgium

(continued)

Citation Cambré A, Aertsen A. 2020. Bacterial vivisection: how fluorescence-based imaging techniques shed a light on the inner workings of bacteria. Microbiol Mol Biol Rev 84:e00008-20. https://doi.org/10.1128/MMBR.00008-20.

Address correspondence to Abram Aertsen, abram.aertsen@kuleuven.be.

SUMMARY The rise in fluorescence-based imaging techniques over the past 3 decades has improved the ability of researchers to scrutinize live cell biology at increased spatial and temporal resolution. In microbiology, these real-time vivisections structurally changed the view on the bacterial cell away from the "watery bag of enzymes" paradigm toward the perspective that these organisms are as complex as their eukaryotic counterparts. Capitalizing on the enormous potential of (time-lapse) fluorescence microscopy and the ever-extending pallet of corresponding probes, initial breakthroughs were made in unraveling the localization of proteins and monitoring real-time gene expression. However, later it became clear that the potential of this technique extends much further, paving the way for a focus-shift from observing single events within bacterial cells or populations to obtaining a more global picture at the intra- and intercellular level. In this review, we outline the current state of the art in fluorescence-based vivisection of bacteria and provide an overview of important case studies to exemplify how to use or combine different strategies to gain detailed information on the cell's physiology. The manuscript therefore consists of two separate (but interconnected) parts that can be read and consulted individually. The first part focuses on the fluorescent probe pallet and provides a perspective on modern methodologies for microscopy using these tools. The second section of the review takes the reader on a tour through the bacterial cell from cytoplasm to outer shell, describing strategies and methods to highlight architectural features and overall dynamics within cells.

KEYWORDS fluorescence microscopy, GFP, advanced microscopy, bacterial physiology, dyes, fluorescence

INTRODUCTION

When Antoni Van Leeuwenhoek (1632 to 1723) took a first glance through a new home-made instrument combining the power of lenses and light, he discovered a novel universe filled with small single-celled organisms or "animalcules" hidden away in plain sight. At that time, this groundbreaking discovery that allowed visualization of an invisible world was met with skepticism and critique, but it later paved the way for microbiology as a new scientific field that focuses on life at and below the micrometer level (1).

The limited resolving power of bright-field light microscopy and the absence of any obvious internal compartmentalization in bacteria long supported the view that these tiny organisms were no more than watery bags of randomly distributed molecules and enzymes that constantly collided into each other, thereby making unstructured, prokaryotic life possible. This long-standing paradigm quickly changed with the introduction of fluorescent techniques into the field of bacteriology that allowed vivisection of the bacterial "black matter" to find a complex and highly structured subcellular organization (2–7). In particular, the arrival of (auto)fluorescent proteins such as green fluorescent protein (GFP) initiated a new era in microscopy and microbiology by providing a highly specific output with high signal-to-noise ratios while at the same time being minimally invasive due to their endogenous implementation in the host's genetic blueprint. These first studies mainly focused on protein localization patterns and expression profiles of target genes (2, 4, 8–13), while over the years the focus shifted to capturing the intra- and intercellular dynamics in a more quantitative manner (14–16). This transformation was supported by the expansion of the fluorescent probe pallet combined with an increased sophistication of the microscopy hardware and software. The high-paced maturation of fluorescence microscopy and its toolbox enabled spatiotemporally tracking of various characteristics at the (sub)cellular level, eventually leading to the discovery of new concepts such as intercellular heterogeneity within isogenic populations (17–19).

In this review, we attempt to give an extensive overview of fluorescence-based imaging methodologies and strategies that can be used to uncover architectural and dynamic features at the bacterial intra- and intercellular level. In the first main section of the text ("A Fluorescent Toolbox for Bacterial Vivisection"), we focus primarily on the technical aspect of fluorescence imaging, describing the different fluorescent probe types and imaging techniques that are commonplace in the field. The second main section of the text ("A Fluorescent Journey through the Cell Body") focuses on different case studies to exemplify the use of state-of-the-art strategies and probes to address outstanding questions in bacterial physiology.

A FLUORESCENT TOOLBOX FOR BACTERIAL VIVISECTION

Fluorescent Probe Pallet

Closely following the initial description of fluorescence as a phenomenon in 1845 (20), the first synthetic fluorophores were developed (21). However, it was not until the arrival of microscopes compatible with these earliest fluorescent probes (22, 23) that applications in different research fields of biology emerged (24–27). These early fluorescent labeling strategies contributed to the initial understanding of the subcellular order in bacteria (2, 28), but it was the advent of green fluorescent protein (GFP) as a live-cell molecular beacon that transformed live cell biology and provided an avant-garde approach to convert standing theories into visual experiments. It soon became apparent that this novel fluorescent protein (FP) had several limitations, leading different research groups into attempts to find the ideal fluorescent (protein- or dye-based) probe that is bright, photostable, and highly specific in its tagging and does not perturb the target's function or other aspects of cellular physiology (29–36). Initial studies mainly focused on directed evolution and targeted synthetic rearrangements of the GFP scaffold (37–39), but the field gradually shifted toward discovering and rationally developing completely new probes (40–49). This led to an enormous probe pallet with a variety of spectral and photochemical properties that is still rapidly expanding to date.

The experimental quality and outcome of fluorescence-based experiments is always highly dependent on the fluorophore used in a particular setup. Selecting the right probe for a specific experimental setup has thus become an integral part of the cell biologist's task and requires thorough knowledge of the numerous tagging possibilities and their characteristics. Despite its widespread application, there is unfortunately no standard "one size fits all" protocol for using fluorescent probes in microscopy or cell cytometry.

Here, we will first discuss the different classes of fluorophores that are currently available and commonly used in bacteriology. Since the potential of these fluorophores as probes to peek inside the cell was recognized, a vast collection of probes was created, every single one of them having specific advantages and disadvantages. Three main classes of probes can meanwhile be distinguished: (auto)fluorescent proteins (FPs), chemical or small molecule dyes, and hybrid probes. The choice for a specific fluorophore belonging to one of these classes depends on numerous factors, such as the stability and optical properties of the probe, the cellular environment of the target, and the nature and duration of the experiment. Furthermore, the surge in new probe development has paved the way for multiplexing different tag types and colors, leading to an unprecedented advancement in capturing the global cellular workings.

(Auto)fluorescent proteins. The most widespread probe type used in live-cell biology is based on (auto)fluorescent proteins (FPs) that are defined by a cofactor-independent chromophore that is inherent to the protein sequence itself (3, 50). This protein family constitutes bulky probes (~27 kDa) with high tagging specificity and a need for molecular oxygen to mature the intramolecular chromophore (51). Over the years, directed evolution and rational design approaches have led to a collection of spectral variants with improved photochemical properties, such as shorter maturation times, lower oligomerization probability, and better photostability. Several reviews (50, 52–54) and websites (http://www.fpvis.org; https://www.fpbase.org [55]) provide a thorough overview of the existing fluorescent protein probes and their characteristics.

More than 2 decades ago, Chalfie et al. (3) were the first to successfully clone GFP as an expression and localization tag in both prokaryotic and eukaryotic organisms. Their experiments followed almost 30 years after the serendipitous discovery of the autofluorescent GFP by Osamu Shimomura in "squeezates" of luminescent organs from the jellyfish *Aequorea victoria* and clearly showed that no exogenous substrates or cofactors were necessary for its fluorescence (3, 56, 57). The attractive characteristics of this new probe type caused a rush on fluorescent protein evolution aiming to find new and more spectrally desirable variants (29, 30, 32, 39, 50, 53). However, these evolutionary attempts also uncovered the limitations of directed evolution in improving the spectral abilities of GFP, pushing scientists to look for new autofluorescent proteins in the marine ecosystem (41, 43, 58).

All the intrinsic fluorescent proteins known to date share a similar tertiary structure and have similar mechanisms of fluorophore formation but can differ in their tendency to oligomerize (38, 50, 58–60). The GFP chromophore is encoded by its primary amino acid sequence and forms spontaneously under aerobic conditions through a self-catalyzed protein folding mechanism and intramolecular rearrangements (61). The light-absorbing properties of GFP depend on the cyclization of residues within a single hexapeptide sequence starting at amino acid 64. It is assumed that this self-catalyzed reaction is initiated by two other residues (Arg^{96} and Glu^{222}) invariantly present in every FP discovered to date (61). The typical 11-stranded cylindrical β-barrel geometry protects the structural integrity of the chromophore, while leaving the N and C termini exposed at the surface and accessible as protein fusion linkers (Fig. 1A).

It is this rigid protein topology that allows for an exploitation of the fluorescent protein's structural characteristics and paves the way for new functionalities. FPs have proven to be extremely robust to circular permutations whereby the original spatially adjacent N- and C- termini are joined and new termini are created (Fig. 1Bv), retaining the overall structure and ability to fluoresce but changing characteristics such as pKa value and orientation of the chromophore to the fusion partner (62–65). Furthermore, the barrel can be split into two separate fragments which are each nonfluorescent but can reconstitute into a native-like fluorescent complex when brought into close proximity via the interaction of a fusion partner (Fig. 1Bvi). This technique (called Bimolecular Fluorescence Complementation [BiFC] or split FP) has over the years improved the detection of protein-protein interactions and is finding its way to other *in vivo* applications (66–72). It is important to note here that the maturation of the split FP, a process that starts when the complementary fragments associate, is equivalent to that of the intact fluorescent protein (73).

New mutations and characteristics were gradually added to the GFP toolbox over the course of the past 20 years, leading to a dispersion of different GFP alleles in labs and institutes all over the world. Even though specific mutations can have a severe impact on the probe's photochemical properties, proper information on the genealogy of the used GFP allele is often lacking. Wild-type *Aequorea* GFP (wtGFP) exhibits a dual-excitation phenotype with a maximal excitation peak occurring at 397 nm and a minor secondary peak residing at 476 nm as a consequence of the protonated-deprotonated equilibrium at Tyr^{66} (74–76). The first mutation that was thoroughly characterized replaced Ser^{65} with a threonine, leading to a permanent deprotonation of Tyr^{66} and thus a single excitation peak at 489 nm. In addition, this amino acid change also increased the brightness and maturation speed of the FP without changing the emission characteristics (29, 77, 78). This $\mathrm{GFP}^{\mathrm{S65T}}$ was further modified (F64L) to yield enhanced GFP (EGFP or GFPmut1), which showed increased protein maturation efficiency at 37°C (79) but is slightly more sensitive to pH and still has a weak tendency to form homodimers. Another significant contribution to the field was made through the development of "superfolder" GFP (sfGFP), a highly mutated GFP allele that has

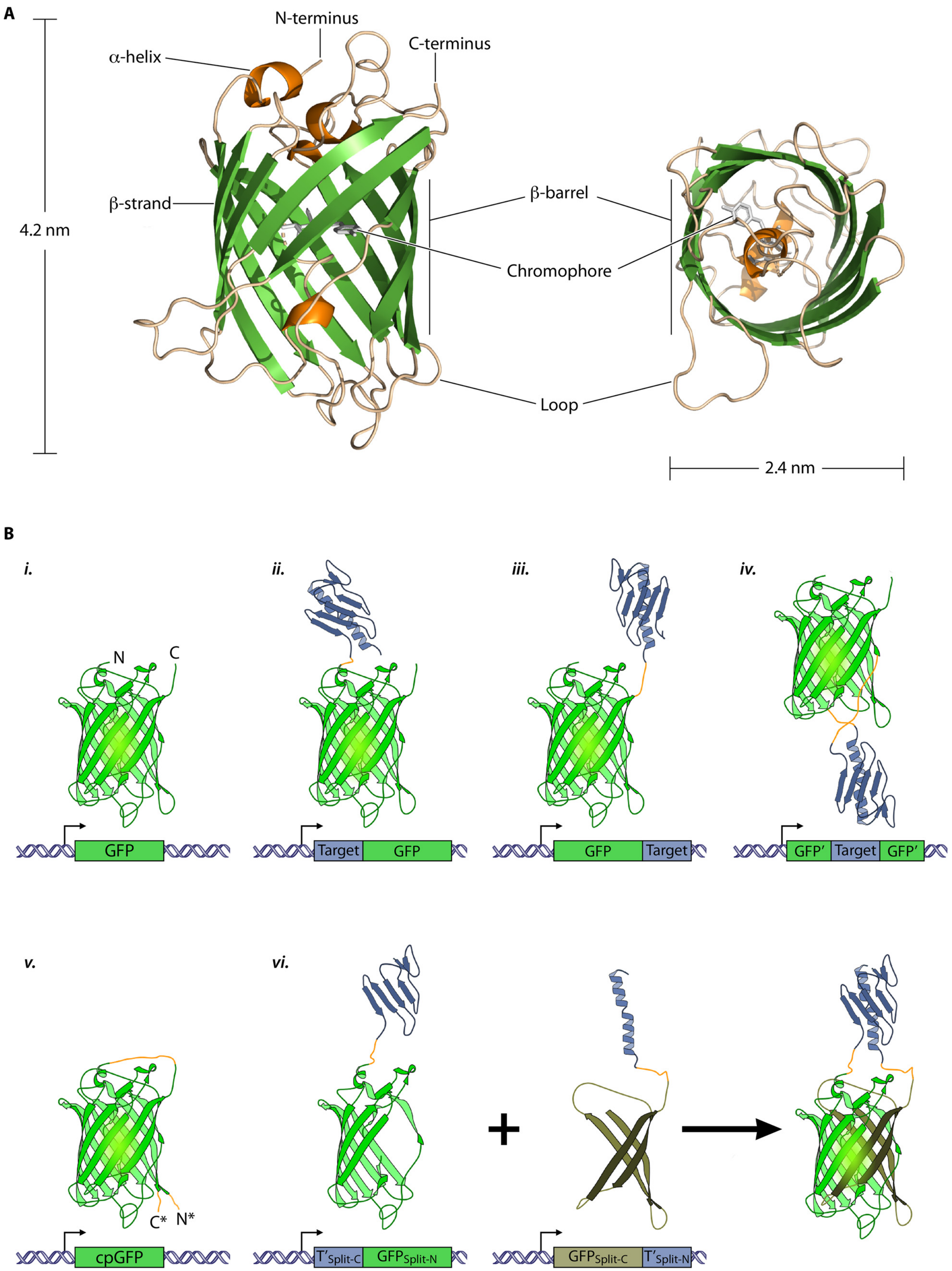

FIG 1 Tertiary structure and tagging possibilities of (auto)fluorescent proteins. (A) Typical structure of an (auto)fluorescent protein exemplified by GFP^{S65T} (38; PDB ID 1EMA). This probe family is characterized by the typical 11-stranded, β-barrel geometry that is found in all FPs known to date and

(Continued on next page)

improved folding kinetics, is more resistant to chemical denaturants, and displays an improved tolerance to circular permutation (80).

Besides enhancing functionality and robustness through the use of rational design, structure-based mutagenesis and directed evolution, several groups focused on widening the spectral range of GFP-derived probes looking for orthogonal combinations (50, 81). The availability of spectrally independent variants supports the imaging of multiple fluorophores in the same sample (i.e., multiplex or multicolor imaging) and enhances the dynamic range of fluorescence microscopy (82). However, to ensure a reliable separation of each fluorophore signal, it is essential to have a (large) separation between the spectral distributions of the multiplexing probes (83). As the ranges in which fluorophores accept and reemit photons (i.e., excitation and emission spectra, respectively) are generally known to be broad, finding valuable spectral GFP variants that are neither excited by the same wavelength (i.e., cross-excitation) nor emit an overlapping signal (i.e., cross talk or bleed-through) presented a long-standing challenge (50, 82, 84). Eventually, this search for compatibly colored GFP derivates led to a wealth of new synthetic FPs of which a few are highlighted in the section below. It is noteworthy that for multicolor imaging, GFP is often difficult to combine with its derived FPs, whereas the blue- and yellow-shifted variants (see further in this section) themselves effortlessly support dual-color experiments. For setting up multiplex experiments, the online FPbase Fluorescence Spectra Viewer provides a valuable tool that enables inspecting the spectral distribution overlaps of different probes (55).

Blue FP (BFP) was one of the first spectral variants that was derived from wild-type GFP and contains a substitution of Tyr^{66} with a histidine shifting the excitation band close to 380 nm, while emission peaked at 488 nm (37, 39, 85). Quickly, an alternative arose for this poorly photostable color variant of GFP by changing the same Tyr^{66} to a tryptophan (Y66W), building cyan FP (CFP), which was further enhanced in other versions by adding additional substitutions in the chromophore and the β-barrel structure (29, 37, 81, 85). This Y66W mutation yielded a fluorophore with a complex, bimodal excitation (433 and 445 nm) and emission (475 and 503 nm) spectrum. Efforts to simplify the CFP excited state led to Cerulean, a high-performance variant that carries additional mutations, leading to a higher extinction coefficient (i.e., stronger light absorption) and increased quantum yield (86). Other important variants in this spectral region are the mTurquoise series (87, 88) and CyPet (89).

The quest for longer-wavelength emitting variants of *Aequorea* GFP halted in the yellow spectrum. A substitution of Thr^{203} leads to a shift toward longer wavelengths and generates yellow FP (YFP), a yellowish-green emission protein (38, 50, 90, 91). Its enhanced version (EYFP) has become one of the brightest and most utilized FPs, despite its increased acid and chloride sensitivity (81, 92). Continuous efforts in improving this spectral variant led to the development of Citrine, in which a Q69M substitution drastically increases both acid and chloride resistance (93). Later, Nagai et al. (94) further improved this FP to Venus (named after the brightest object in the nighttime sky) by switching a phenylalanine with leucine (F64L) and thereby dramat-

FIG 1 Legend (Continued)
that forms a protective structure around the endogenous, hexapeptide chromophore. Both the N and C termini of the protein remain surface exposed in the tertiary structure and are accessible as protein fusion linkers. The dimensions given are specific to GFP. (B) Overview of the different tagging possibilities of FPs and their structural variants. It is important to note that the chromophore of these fluorescent probes forms spontaneously under aerobic conditions through a self-catalyzed folding mechanism and intramolecular rearrangements and has no need for exogeneous cofactors. (i) FPs can be used to report on promoter activity by putting the FP gene under the control of the promoter of interest (i.e., transcriptional fusion). (ii to iv) The rigid protein topology and surface-exposed termini of FPs support the formation of protein chimera between the fluorescent probe and a target protein. The protein of interest can be translationally fused to one of the termini of the FP or can be inserted internally in the probe sequence to function as a sandwich fusion. (v) FPs have proven to be extremely robust to circular permutations. In circular permutation, the original N and C termini are joined, and new termini are created. This modification changes the characteristics of the fluorescent probe without changing the overall structure, nor its ability to fluoresce. (vi) In Bimolecular Fluorescence Complementation (BiFC or split FP) FPs are split into two separate, nonfluorescent fragments. When these two fragments are brought into close proximity of each other via the interaction of their corresponding fusion partners, a native-like fluorescent complex can be reconstituted. Native N and C termini are indicated in panel i, the target protein (exemplified by PDB ID 1DZO) (863) and its gene are indicated in purple, an apostrophe indicates a split-up gene structure, cp indicates circular permutation, N* and C* indicate nonnative termini, Split-N or Split-C indicate split fragments corresponding to the original N- or C-terminal domain of the cognate protein, and orange lines represent (additional) linker amino acids or peptides.

ically improving maturation efficiency and halide resistance. However, the photostability of this protein still remains only 25% that of EYFP.

These yellow spectral variants of *Aequorea*-based FPs remain the most red-shifted GFP derivatives to date, despite years of mutagenesis and evolutionary attempts (50, 90, 95). The interest in more red-emitting proteins was further driven by the fact that cellular autofluorescence (mainly emitted at the blue-green wavelengths) is significantly lower in that specific spectral region and that these wavelengths allow greater penetration depths and longer excitation times due to the lower energy of the incident light (96–98). Among others, these properties make red-shifted fluorescent proteins (RFPs) superior probes for approaches requiring low background noise and for visualization of bacteria in tissue samples and eukaryotic hosts (97). To find these RFPs, several groups of researchers searched the marine ecosystem for GFP-like proteins and found these in the color diversity of the Anthozoa family covering the coral reefs (99, 100). One of the first FPs that was isolated and characterized from this new family of autofluorescent proteins came from the sea anemone *Discosoma striata* and was originally called drFP583 but is nowadays better known as DsRed (41). This protein provided the long-sought characteristics of a high wavelength excitation (558 nm) and emission (583 nm) but proved more difficult to work with than *Aequorea*-based proteins. Two major limitations to this protein for its use in *in vivo* experiments are its obligate tetrameric form and the maturation "green state." In contrast to *Aequorea*-derived FPs, which only have a weak tendency to oligomerize at low concentrations, DsRed tends to tetramerize even at very low concentrations, limiting its potential as a fusion protein due to the possible aggregation and mislocalization of the target fusion (101, 102). Another acute problem associated with this second FP-family is the slow maturation of the chromophore that proceeds via an intermediate "green state," where most of the emission from the chromophore is in the green spectral region (101, 103). This maturation state introduces signal cross talk in multicolor experiments and would thus limit its use. Both of these limitations were overcome for the first time by mRFP1, a variant that carries more than 30 amino acid substitutions (58). It succeeded in dealing with many of the critical problems associated with this class of proteins but had a significantly reduced emission and was extremely sensitive to photobleaching. Nevertheless, this protein provided the starting point for one of the most productive attempts to create RFPs using directed evolution (43). The result of these experiments was a group of six new monomeric FPs in the red spectral region called the mFruit series. The most promising members in this series are mOrange, mStrawberry, and mCherry, with the latter having the highest photostability and intrinsic brightness, making it the preferred partner for *in vivo* experiments. In that same study, Shaner et al. (43) also constructed tdTomato, an artificial derivative of DsRed that consists of a genetic fusion of two copies of the obligate dimer dTomato gene connected by a 12-residue linker. This tandem dimer strategy fused the protein in such a way that the critical dimer interactions can now be met through intramolecular contacts with the tandem partner encoded within the same polypeptide, creating a nonaggregating (though bulky) tag with extreme brightness (58). Another important branch of RFPs is derived from the sea anemone *Entacmaea quadricolor*, providing valuable probes such as TagRFP, mRuby, and mKate derivatives (104–106). Recently, mScarlet was brought to the attention as the new, high-value red FP (49). This new synthetic RFP outperforms all existing red fluorescent proteins as a fusion tag and presents a truly monomeric red protein with excellent brightness and faster maturation. More information on the evolutionary track of red fluorescent proteins and all the different mutations can be found in other reviews (50, 97). In recent years, many variants of these coral-derived fluorescent proteins in the blue to yellow spectrum have surfaced as good alternatives and additions to the existing toolbox (100, 107, 108). One such example is mNeonGreen, a very bright monomeric FP derived from *Branchiostoma lanceolatum* that covers a similar spectral region as GFP (109).

Almost all known FPs tend to form quaternary structures to some degree, often inhibiting the fluorophore to operate as an inert part of the formed chimera. This propensity to oligomerize is known as "stickiness" and can possibly lead to interference with the tagged protein's native localization and functionality. Although *Aequorea* GFP derivatives only have a weak tendency to dimerize, this can vary significantly depending on the target of choice (110, 111). In many *Aequorea*-based variants, dimerization can be either significantly reduced or even eliminated by replacing key hydrophobic amino acids at the dimer interface with positively charged residues (112, 113). The three most successful mutations, in increasing order of effectiveness, are F223R, L221K, and A206K, in which the nonpolar phenylalanine, leucine, and alanine are replaced by hydrophilic alternatives (arginine or lysine). This creates a repulsive effect between the residues of different FP molecules and leads to the so-called monomeric fluorescent proteins (mFP). Creating monomeric forms of the obligate tetrameric reef coral and sea anemone proteins has proven to be much more challenging but eventually was equally successful (43, 49, 106, 114). This FP stickiness or oligomerization propensity can be measured in several ways, both in *in vitro* and in *in vivo* setups. The current golden standard is the Organized Smooth Endoplasmic Reticulum (OSER) assay (115) that measures oligomer interactions of FPs targeted to the endoplasmic reticulum in eukaryotic cells. The higher the FP's tendency to oligomerize, the more OSER whorls will appear in the sample. A second method exploits protease substrate breakdown rates in *Escherichia coli* as a metric for the oligomerization tendency of FPs translationally coupled to the protease subunit (110). Other important characteristics of FPs, such as brightness, maturation time, photostability, and acid sensitivity, have also been tested in a variety of setups but can be best reevaluated in the system of choice (52, 55, 60, 116–118).

The extent of artifacts induced by FP tagging was not completely clear until the fairly recent key paper by Landgraf et al. (110). This study from the Paulsson lab used a newly designed function-based validation assay to link the single-focal localization pattern of Clp proteases (119–124) to a stickiness artifact induced by the specific FP used. These researchers were able to confirm these results with a variety of independent tests such as immunofluorescence microscopy and an alternative tagging probe (i.e., SNAP, see "Hybrid tags"), showing that the natural tendency of Clp proteins to self-assemble was reinforced by a similar but weak multimerization tendency in (m)FPs (110). It should be pointed out that the clustering of FP-labeled ClpP was not merely an aggregation phenomenon but rather a wrongful localization of a functional target protein in larger unnatural clusters. Around the same time, similar findings were published for the extensively studied localization pattern of the bacterial actin homolog, MreB (125–131). Using electron cryotomography, Swulius and Jensen (132) refuted the reported formation of helical MreB filaments in the inner cell body and showed that the perceived cables only occur when the protein was tagged with YFP at its N terminus. However, it is believed that this artifact is the consequence of a functional disruption of MreB rather than a FP-induced oligomerization, since no bundles were formed with an internal ("sandwich") fusion with the red fluorescent mCherry (111, 132). More recently, other artifact issues such as the influence of photoswitchable FPs on the localization of DNA-binding proteins (117) and the single-molecule specific mislocalization of *Entacmaea quadricolor* RFPs were highlighted (133). The examples presented above clearly underscore the potential of fluorescent (protein) tags to cause label-induced oligomerization and trivial localization patterns, highlighting the importance of solid control experiments. Throughout this review, but mainly in the second text section ("A Fluorescent Journey through the Cell Body"), many such control strategies will be touched upon. However, for practical reasons, we will list some commonly used verification methods that can help in detecting artifactual localization patterns (e.g., focus formation, polar localization or helical filament formation): (i) changing the position and (the nature of) the fluorescent tag (110, 132, 134), (ii) using a direct binding partner or orthogonal reporter system to visualize the protein (structure) of interest (134–139), (iii) applying different (super-resolution) fluorescence microscopy techniques, (iv) verifying the localization with immunofluorescence microscopy in fixed cells, (v) using a label-free visualization technique (132), and (vi) verifying the functionality of the fluorescently labeled target and its influence on general cell physiology.

A final, special class of FPs are the smart fluorescent proteins, also known as optical highlighter or phototransformable FPs, that are capable of changing their spectral properties in response to light of a specific wavelength and intensity or as a factor of time (140, 141). These FPs either can be activated (photoactivation), converted (photoconversion), or switched (photoswitchable) by the incident light (142) or can spontaneously change their spectral properties over time (143).

In the process of photoactivation, the spectral properties of a specific FP are changed from a very low emission level to bright fluorescence. The prototypical example of this group is photoactivatable GFP (PA-GFP) (144), mainly differing from wtGFP by a single amino acid substitution (T203H). This specific amino acid alteration changes the protonation equilibrium of the chromophore toward the protonated state. The incident UV-light can then irreversibly activate PA-GFP by converting the chromophore from the neutral (protonated) to anionic (deprotonated) state, thereby causing a 100-fold increase in fluorescence (142, 144). Over the years, similar new and improved photoactivatable proteins have been developed in both the *Aequorea* and Anthozoa protein families (145–148). The PA-FP color palette is still very limited, and these probes are difficult to track in their nonactivated form. Furthermore, the brightness of the photoactivated form in all reported variants is less than 50% of that of EGFP, and their photostability is diminished compared to the parental FPs. These proteins play a key role in super-resolution microscopy (see "Super-resolution microscopy" below) since they allow the activation of specific subsets of FP molecules, thereby providing true single-molecule resolution.

Photoconvertible proteins represent a second class of smart proteins and bear the capacity to change from green to red emission after blue light excitation. This transition occurs by a light-dependent, irreversible chemical conversion that changes the chromophore of the protein from a two-ring GFP-like chromophore to a three-ring structure (149). The nature of this chemical conversion limits the process to members of the Anthozoa (i.e., coral) family and is reminiscent of the chromophore maturation in these proteins. All these photoconvertible proteins contain a chromophore that contains His^{62}-Tyr^{63}-Gly^{64}, initially emitting green fluorescence until a light-catalyzed cleavage of the polypeptide backbone drives the chromophore into the red state (95, 150). The first photoconvertible highlighter discovered was a tetrameric FP isolated from the stony Open Brain Coral, *Trachyphyllia geoffroi*, and was named Kaede after the leaves of the Japanese maple tree, which also turn from green to red in the fall (151). Other forms were meanwhile developed that have slightly different properties and can circumvent the obligate tetrameric structure of Kaede (152–156). One of the major advantages of these photoconvertible proteins is that they can be tracked even before their conversion, something which is not possible for photoactivatable FPs.

The third group of optical highlighters, photoswitchable proteins, can combine either photoactivation or photoconversion with a reversible switching between two states. This group of proteins spontaneously relaxes back into the original ground state were the protein started or can be induced to do this reversion by illumination with a specific wavelength. The most prominent and well-studied example of these proteins is Dronpa, a monomeric green spectral variant that can switch between the ON and OFF states (157). Dronpa is driven to the dark state by illumination at 488 nm, whereas 405 nm can subsequently switch the protein's fluorescence back on, toggling the protein between its two absorption peaks (390 and 503 nm). This type of cycle can be repeated several hundred times without any significant photobleaching (158, 159). Other members of this category adopt more complex switching schemes with IrisFP forming a unique representative as it combines reversible photoactivation and photoconversion in one protein (160). In this specific protein, illumination with 488 nm drives the highlighter into the dark state, which can be reverted with low-intensity 405-nm laser light. Increasing the intensity of this 405 nm wavelength drives the chromophore toward the red spectral region. Finally, the protein can further be switched ON and OFF in this red state by using 532- and 440-nm light (160). In the same category, we can find NijiFP (161) and Dreiklang (162), a YFP protein which switches at 405 and 365 nm but is excited at 515 nm. A unique feature of the latter protein is that its fluorescence excitation spectrum is completely decoupled from its optical switching, while in most other photoswitchable FPs, excitation also leads to photoswitching.

A final class of optical highlighters are Fluorescent Timer (FT) proteins which form a unique but limited collection of FPs that spontaneously change their spectral properties as a function of time. These proteins can function as a visual molecular clock that slowly changes its emission spectrum over a specific period of time and is able to provide spatiotemporal resolution on both gene expression and protein localization in one single snapshot. DsRed-Timer, also known as DsRed-E5, was the first FT protein, but its obligate tetrameric form prevented its application as a protein tag, though not as a gene expression readout tool (143, 163, 164). This E5 timer indicates recent activity with a green color, but over time it changes its emission toward the red side of the spectrum, indicating full maturation. The bulk change in color of these proteins is gradual and moves over a continuous spectrum between both colors determined by the different ratios of nonmaturated (green) and maturated (red) proteins in the cell. In addition to the DsRed-Timer, an array of mCherry-based timers was also developed that can be divided into three classes based on their conversion time, ranging from as fast as 15 min to approximately 10 h (165). These latter monomeric FTs can be used as genetically encoded tools to track intracellular movement of target proteins and are able to provide accurate insight into the timing of intracellular processes without any harsh conditions (e.g., FRAP; see section below on “Fluorescence recovery after photobleaching”).

Chemical dyes. Before the discovery and first application of GFP as an intracellular molecular beacon (3) to uncover the whereabouts and/or concentrations of biomolecules *in vivo*, chemical dye fluorophores were the preferred tool to peek into the intracellular environment (166). The aspecific labeling and cellular toxicity associated with these dyes shifted the main focus of bacterial fluorescent imaging to the use of FPs, pushing small dye molecules and their favorable optical properties (e.g., higher photostability, higher brightness, narrower bandwidth) more to the sideline. Currently, the crossroads between these organic dyes and novel chemical techniques have paved the way for a renaissance leading to the development of novel, sophisticated probes with tailored characteristics and a broad color spectrum (31, 33–36, 166). As a consequence, these small molecules are being rediscovered, expanding the fluorescent toolbox with new bright, photostable probes that can readily penetrate the cell envelope. However, as the older generation of dyes had difficulties crossing the bacterial outer layer barrier, the majority of studies to date have focused on visualization of the extracellular components (167).

All of these chemical fluorescent probes are based on a small collection of modular scaffolds functionalized with different chemical moieties. These side groups give this probe type its highly versatile and custom-made character necessary for the precise interrogation of biological systems (166, 168). Here, we will limit ourselves to describing the different situations in which these small organic molecules are used, and we refer to other reviews for more (structural) information (166–170). Throughout the biological section of this review, we will give several examples of recent studies using a dye-based approach to decipher specific questions in bacterial physiology.

Aspecific binding is an inseparable characteristic of this oxygen-independent fluorophore type and has created different utilization strategies, either exploiting this intrinsic feature or providing strategies to bypass it. Dye fluorophores are mainly used in four types of situations: (i) direct visualization of larger macromolecular structures, (ii) to light up dye-conjugated molecules, (iii) to readout enzymatic reactions, and (iv) in combination with hybrid tags (for the latter, see “Hybrid tags”).

Fluorescently labeling the boundary of the bacterial cytoplasm with membrane-specific probes such as FM4-64 (171, 172) might be the best-known example of using small dye molecules to visualize larger macromolecular structures. This styryl dye is believed to insert into the outer leaflet of membranes, where it shifts from the low fluorescent state in watery environment to an intensive bright form as it interacts with the phospholipid lipid bilayer. In this type of situation, the dye can be used to label a specific cellular structure because other similar chemical structures are absent within the cell. Another well-known example is the use of DAPI (4′,6′-diamidino-2-phenylindole) for the visualization of the bacterial nucleoid (173–175). Rational design and screening can further expand the collection of dyes that can specifically bind certain cellular structures in their native state (33, 34, 166).

Dye conjugate molecules can be formed *in vitro* or *in vivo* and consist of a covalent coupling between a dye molecule on the one hand and a macromolecule (8, 176), oligonucleotide (177), antibiotic (178), or even a small molecule (46, 179) on the other. The eventual probe can therefore be divided into two domains, each with its own function. The first domain will consist of the tagged molecule (e.g., antibody, amino acid, nucleotide, etc.) and will convey specificity to the probe, while the second part solely functions as a molecular "torch" enabling the fluorescent visualization. This type of strategy can be used in bacteria to visualize important cellular components such as peptidoglycan, lipopolysaccharide (LPS), and FtsZ rings without the need for fusion proteins or genetic disturbances (46, 167, 180, 181).

Furthermore, functionalized dye molecules can also be used as substrates to check for certain enzymatic reactions in the cells. In these reactions, the properties of the dye molecule are changed, leading to a fluorescent readout. Viability assays in bacterial populations can be based on this type of assay. For example, membrane-permeant fluorescein diacetate (FDA) is nonfluorescent until it is converted by intracellular esterase activity and thus can give a readout of single-cells' enzymatic activity and viability (182).

Finally, dye molecules can also be used in hybrid tagging systems where specific endogenous proteins are labeled with a nonfluorescent protein or peptide moiety that can uniquely interact with specific dye molecules to form a covalent or noncovalent interaction. This type is further discussed in the following section since it is on the border between the other two probe types discussed here and is becoming a trending topic especially in applications such as super-resolution microscopy.

Hybrid tags. Hybrid tags consist of a peptide or protein unit that cannot fluoresce by itself but needs an artificial or natural cofactor (or ligand) to enable visualization of its cellular fusion partner. The use of this tag type combines the advantages of both other probe categories, namely, the specificity of an endogenous tag with the superior spectroscopic properties (and oxygen independence) of the wide variety of dye molecules currently available. Well-known examples such as the tetracysteine tag and self-labeling protein tags, such as Halo, SNAP, and CLIP, have already been used in multiple studies (183–186), but newer systems such as FAST (48, 187) are on the rise. The rationale behind all these systems is that a small peptide/protein domain is translationally fused to the intracellular target and forms covalent or noncovalent linkages to exogenously added fluorophores or endogenously produced natural cofactors, thereby allowing microscopic investigation of the labeled chimeric proteins. To ensure high imaging contrast, most of these ligands are fluorogenic chromophores or fluorogens, only lighting up when bound to the cognate tag while being in a low-fluorescent state when unbound (188–190). Furthermore, the inherent need of these hybrid tags to react with nonself fluorophores allows for consecutive labeling of the target molecules within one cell by different color variants, facilitating the examination of cellular processes over time. For these systems to be usable in living organisms, several premises have to be fulfilled: the genetic tag must (i) fold and (ii) function in the cellular space of choice, while the fluorescent probes must be (iii) nontoxic and (iv) membrane permeant, (v) must have low fluorescence when not bound, and (vi) must not show unspecific interactions/reactions with other cellular components. Besides the advantages of reduced probe size and oxygen independence, there are also some downsides to using organic dyes for labeling intracellular structures. These methods can suffer from cytotoxicity, poor cell permeability, and a high level of background fluorescence, leading to a need for the removal of the excess of unassociated dye. More elaborate reviews of these systems can be found elsewhere (190).

The oldest system in this category is based on a tetracysteine tag (Cys-Cys-X-X-Cys-Cys) that can be fluorescently labeled via a chemical reaction with the biarsenical compounds FlAsH-EDT_2 (fluorescein arsenical hairpin binder-ethanedithiol; green) or ReAsH-EDT_2 (resorufin arsenical hairpin binder- ethanedithiol; red) (40, 191–193). These small, synthetic ligands ($<$700 Da) are basically nonfluorescent in their free-floating state bound to EDT_2 but light up upon binding the tetracysteine-labeled target (40). This technique uses the easy, reversible formation of covalent bonds between organo-arsenicals and the thiols of the tetracysteine to label *in vivo* targets. The specificity of the reaction between the label and the basically nonfluorescent free-floating dye reduces the need for extensive washing steps, while the sparse natural presence of the cysteine motive minimizes aspecific binding events. Another considerable advantage is the small size of the tag (6 to 12 amino acids), placing it among the smallest genetic tags, thus limiting steric hindrance. However, tetracysteine labeling is limited to reducing environments and can display low signal-to-noise ratios when imaging diffusing or low-abundance proteins (190). A number of studies have successfully used this technique to study living bacteria (183, 194–196).

Labeling selectivity vastly increased with the development of new hybrid tags based on self-labeling reporter systems, albeit this came at the expense of larger tag sizes. A first example of such a self-labeling system is HaloTag, a modified dehalogenase from *Rhodococcus rhodochrous* that genetically adds a 34-kDa tag to the target protein. This enzyme tag catalyzes the formation of a high affinity, covalent linkage between the chimeric protein fusion and the synthetic chloroalkane ligand (e.g., tetramethylrhodamine [TMR]) (44, 197, 198). In contrast to the tetracysteine system, HaloTag enables the visualization of proteins in both the bacterial cytoplasm and periplasm (185, 186, 199). However, caution is advised since the HaloTag does not seem to be truly monomeric (185) and can thus cause localization artifacts. Nevertheless, this tag has proven its worth in different super-resolution approaches, allowing specific tagging with very bright and stable fluorophores (14, 184, 200, 201). Another self-labeling reporter system is based on a modified O^6-alkylguanine-DNA alkyltransferase, a human DNA repair enzyme, that can transfer the functionalized alkyl group of its substrate fluorophore to one of its active-site cysteine residues (42, 202). The two orthogonal variants of this alkyltransferase tag, SNAP and CLIP (both ca. 20 kDa), each react with a unique type of functionalized fluorophore (O^6-benzylguanine and O^6-benzylcytosine conjugates, respectively) to form an irreversible covalent bond and support dual labeling in the same cell if required (42, 202). SNAP in particular has already been used in different super-resolution microscopy and anaerobic experiments (184, 200, 203, 204). All of these self-labeling systems are very promising but still face challenges, such as the need for additional washing steps to further lower off-target fluorescence and relatively large fusion tags. However, the development of new fluorescent compounds with increased specificity (205) and new self-labeling tags (206, 207) is paving the way for a more widespread use in bacteria.

All the systems discussed above use enzymatic or chemical reaction to create a covalent binding between the tag and the corresponding small molecule dye. Some hybrid systems, however, rely on a noncovalent binding equilibrium between both components for the visualization. The advantages of this type of approach include lower photobleaching rates because of the exchange with new fluorogens and spectral flexibility within the same experiment. Furthermore, the noncovalent binding leads to more versatility in microfluidics setups via an easy switching between labeling and delabeling. A recent system based on such noncovalent interactions was developed by Plamont et al. (48) and consists of a small (14 kDa) tag that supports reversible binding to a cognate fluorogen, a synthetic analogue of hydroxybenzylidene rhodamine (e.g., 4-hydroxybenzylidene-rhodanine [HBR]). This protein tag is an engineered monomeric variant of the Photoactive Yellow Protein (PYP), a blue light receptor found in *Halorhodospira halophila* (208–210), and can form a nonnatural fluorescent complex upon binding with the cell-permeant fluorogens. The unique activation mechanism of the FAST (Fluorescence-activating and Absorption-Shifting Tag) fluorogens is based on both a red-shift in the absorption spectrum and an increase in fluorescence quantum yield when the tag-dye complex is formed (48). Since there is only fluorescence when the HBR analogs are immobilized within the FAST tag (because of conformational locking), the labeling is highly selective and the absence of nonspecific fluorescence in the cells makes washing steps redundant. Its noncovalent complex formation allows for rapid ON/OFF switching of the fluorescence by washing away the fluorogen and, furthermore, easily supports pulse-chase experiments because of these characteristics. A first application of this system in a bacterial biofilm clearly demonstrated its advantages compared to autofluorescent proteins for visualization in a heterogeneous microaerobic environment (187). Since no covalent reaction or maturation is required, the fluorescent signal can be observed soon after fluorogen addition. The main disadvantage of the system, however, is that the dye molecules need to be present throughout the experiment which thus requires careful inspection of possible toxicity. Currently, of all the hybrid techniques described above, this might be the most promising for further implementation in live cell imaging of bacteria.

Interestingly, hybrid systems that utilize natural cofactors to produce a fluorescent signal are receiving more and more attention as a novel type of hybrid FPs (47, 53, 211–220). The most popular sort, flavin-based fluorescent proteins (FbFPs) (6, 221), are characterized by a LOV (light, oxygen, or voltage sensing) domain that interacts with a flavin mononucleotide (FMN) cofactor. This interplay then turns the protein into a blue-light absorbing FP that can undergo a complex photocycle (222–226). The small size (12 to 19 kDa), oxygen independence, fast maturation times (in the order of minutes), and high pH and thermostability, combined with the abundance of the required cofactor in bacterial, plant, and human cells (45, 227), provides this new class with several competitive advantages compared to autofluorescent proteins. The protein iLove represents one of the more advanced proteins in this category and was engineered from a mutant version of the *Arabidopsis thaliana* phototropin 2 LOV domain (45). This tag has already been used to visualize protein diffusion in the periplasmic space and FtsZ formation in bacteria under anaerobic conditions (221, 227). Furthermore, it was also shown that EcFbFP, an *E. coli* codon optimized LOV protein derived from *Bacillus subtilis* (228), can outperform YFP when monitoring gene expression dynamics in high-density *E. coli* cultures (229). In addition, a near-infrared fluorescent (iRFP) protein relying on the eukaryotic natural compound biliverdin as a chromophore (213) was recently tested by two groups for use in *Borrelia burgdorferi* (230) and *Neisseria meningitidis* (226). The latter protein accepts excitation in the far-red wavelengths, which are less toxic to the cells, and is thus less hindered by autofluorescence than more blue-shifted spectral proteins (53, 116).

When comparing the characteristics of these different hybrid systems to autofluorescent proteins and organic dye molecules, several advantages become apparent (Fig. 2). Their often-smaller tag sizes, lower response times, and oxygen independence addresses three of the most prominent issues encountered with the modern autofluorescent proteins, creating a more robust and faster readout system. Furthermore, the freedom of using nonnatural cofactors allows for synthetic modulation of the photostability and spectral properties, although it can sometimes require extensive washing steps to achieve a high signal-to-noise ratio. Through their characteristics, these systems can thus combine high specificity of endogenous tagging with the photochemical excellence of organic dyes. On the other hand, hybrid tags supported by natural cofactors provide a new approach free of exogenous addition of chemical compounds, thereby decreasing the risk of potential toxic effects.

Fluorescence Microscopy as Powerful Analytical Tool

Light microscopes are indispensable instruments in modern cell biology, using visible light and magnifying lenses to look beyond what the naked eye can see. As a picture often says more than a thousand words, the ability to visualize the invisible and

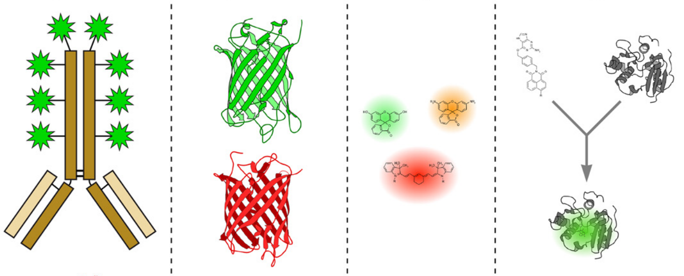

	Antibody probe	(Auto)fluorescent protein	Chemical dye	Hybrid tag
Live cell imaging	✗	✓	✓	✓
Probe size*	~15 nm	~3 nm	~1 nm	~1-3 nm
Oxygen independent	NA	✗	✓	✓
Oligomerization tendency	NA	±	−	±
Cytotoxicity	NA	±	+	±
Genetic engineering	✓/✗	✓	✗	✓
Exogenous cofactor	NA	✗	✓	✓/✗
Labeling specificity	++	++	±	+
Signal-to-noise	++	++	±	+
Signal response time	++	±	++	+
Photostability	++	±	++	++
Brightness	++	+	++	++
Spectral range	++	±	++	++
Tailor fitting	✓	✗	✓	✓
Cytoplasmic labeling	✓	✓	✓/✗	✓
Periplasmic labeling	✓	✓/✗	✓	✓/✗
Pulse chase	NA	✓/✗	✓	✓

FIG 2 Comparison of antibody probes, (auto)fluorescent proteins, chemical dyes, and hybrid tags for use in fluorescence microscopy. A red cross ("X") indicates the probe type is not compatible with this feature or application; a green check mark indicates the probe type is compatible with this feature or application; a green check mark/red cross combination indicates that some specific probes within this category are compatible with this feature or application. Other symbols: ++, excellent performance; +, very good performance; ±, good performance; –, poor performance. NA, the label is not relevant to this probe type. *Probe size values are based on a study by Turkowyd et al. (864).

perform real-time vivisection with high-precision fluorescent tools has pushed our insights into the inner workings of the cell to new depths. The microscope itself has undergone a tremendous evolution since Anthony Van Leeuwenhoek's self-made instrument, resulting in today's multimodal imaging units capable of high-resolution and high-throughput (fluorescence) imaging. The relatively nonperturbing nature of light allows for long-term live-cell imaging with high spatiotemporal resolution and has forwarded light microscopy as the tool of choice to visually unravel inter- and intracellular dynamics of bacteria. The latter being highly supported by the wide variety of fluorescent probes and imaging techniques that have been developed over the past decades, further matching the resolution of fluorescence microscopy to the bacterial scale.

As already underscored in the previous section, different types of fluorescent probes possess distinct characteristics, making the selection of a proper tag for each experi-

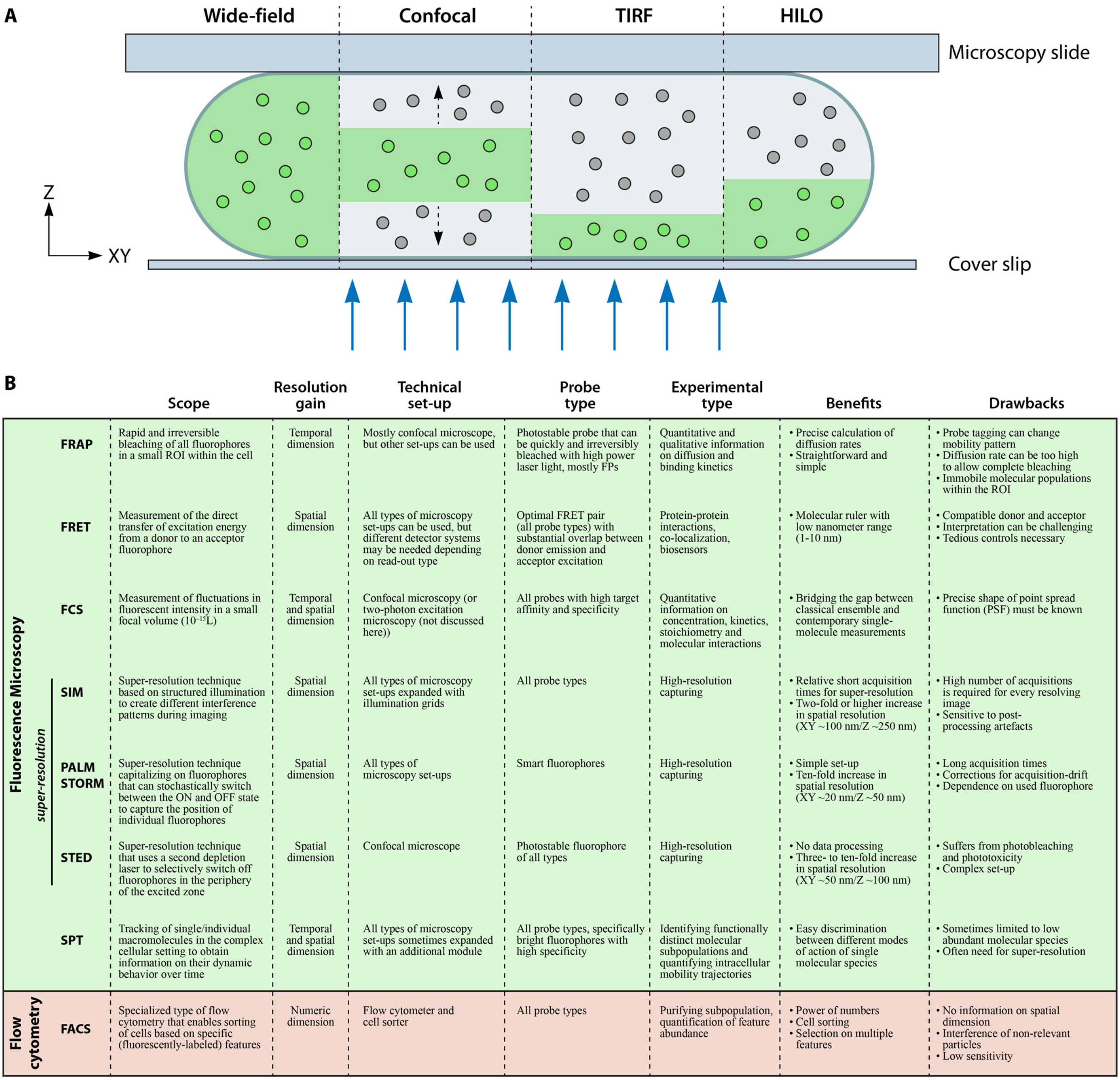

			Scope	Resolution gain	Technical set-up	Probe type	Experimental type	Benefits	Drawbacks
Fluorescence Microscopy		FRAP	Rapid and irreversible bleaching of all fluorophores in a small ROI within the cell	Temporal dimension	Mostly confocal microscope, but other set-ups can be used	Photostable probe that can be quickly and irreversibly bleached with high power laser light, mostly FPs	Quantitative and qualitative information on diffusion and binding kinetics	• Precise calculation of diffusion rates • Straightforward and simple	• Probe tagging can change mobility pattern • Diffusion rate can be too high to allow complete bleaching • Immobile molecular populations within the ROI
		FRET	Measurement of the direct transfer of excitation energy from a donor to an acceptor fluorophore	Spatial dimension	All types of microscopy set-ups can be used, but different detector systems may be needed depending on read-out type	Optimal FRET pair (all probe types) with substantial overlap between donor emission and acceptor excitation	Protein-protein interactions, co-localization, biosensors	• Molecular ruler with low nanometer range (1-10 nm)	• Compatible donor and acceptor • Interpretation can be challenging • Tedious controls necessary
		FCS	Measurement of fluctuations in fluorescent intensity in a small focal volume (10^{-15}L)	Temporal and spatial dimension	Confocal microscopy (or two-photon excitation microscopy (not discussed here))	All probes with high target affinity and specificity	Quantitative information on concentration, kinetics, stoichiometry and molecular interactions	• Bridging the gap between classical ensemble and contemporary single-molecule measurements	• Precise shape of point spread function (PSF) must be known
	super-resolution	SIM	Super-resolution technique based on structured illumination to create different interference patterns during imaging	Spatial dimension	All types of microscopy set-ups expanded with illumination grids	All probe types	High-resolution capturing	• Relative short acquisition times for super-resolution • Two-fold or higher increase in spatial resolution (XY ~100 nm/Z ~250 nm)	• High number of acquisitions is required for every resolving image • Sensitive to post-processing artefacts
		PALM STORM	Super-resolution technique capitalizing on fluorophores that can stochastically switch between the ON and OFF state to capture the position of individual fluorophores	Spatial dimension	All types of microscopy set-ups	Smart fluorophores	High-resolution capturing	• Simple set-up • Ten-fold increase in spatial resolution (XY ~20 nm/Z ~50 nm)	• Long acquisition times • Corrections for acquisition-drift • Dependence on used fluorophore
		STED	Super-resolution technique that uses a second depletion laser to selectively switch off fluorophores in the periphery of the excited zone	Spatial dimension	Confocal microscope	Photostable fluorophore of all types	High-resolution capturing	• No data processing • Three- to ten-fold increase in spatial resolution (XY ~50 nm/Z ~100 nm)	• Suffers from photobleaching and phototoxicity • Complex set-up
		SPT	Tracking of single/individual macromolecules in the complex cellular setting to obtain information on their dynamic behavior over time	Temporal and spatial dimension	All types of microscopy set-ups sometimes expanded with an additional module	All probe types, specifically bright fluorophores with high specificity	Identifying functionally distinct molecular subpopulations and quantifying intracellular mobility trajectories	• Easy discrimination between different modes of action of single molecular species	• Sometimes limited to low abundant molecular species • Often need for super-resolution
Flow cytometry		FACS	Specialized type of flow cytometry that enables sorting of cells based on specific (fluorescently-labeled) features	Numeric dimension	Flow cytometer and cell sorter	All probe types	Purifying subpopulation, quantification of feature abundance	• Power of numbers • Cell sorting • Selection on multiple features	• No information on spatial dimension • Interference of non-relevant particles • Low sensitivity

FIG 3 Microscopy setups and strategies. (A) Overview of the different microscopy setups routinely used for fluorescence microscopy in bacteria and their excitation zones. (Left to right) During sample excitation in wide-field epifluorescence microscopy, a wide cone of light with a specific wavelength evenly and simultaneously activates all the fluorophores in a large 3D volume. Fluorophores in the different *z* planes throughout the sample will contribute to the eventual signal. Confocal microscopy, on the other hand, uses point illumination to scan across the sample and enables optical sectioning throughout the sample. In TIRF, only fluorophores close to the surface will be excited by an evanescent excitation wave created by illumination at or above the critical angle. Similarly, in HILO, the sample is illuminated at a subcritical angle, leading to an increased penetration depth of the signal. This supports the excitation of structures in both the bacterial outer shell, as well as in the cytoplasm, while keeping background fluorescence at a low level. Blue arrows indicate the direction of the illumination light. (B) The different imaging strategies discussed in this review are compared in terms of scope, resolution gain, technical setup, suited probe types, types of experiments in which they are routinely used, and their specific benefits and drawbacks.

mental setup desirable. Concomitantly, selecting a well-suited imaging method to address specific scientific questions also plays an important role in determining the quality of the experimental results (Fig. 3). It must be pointed out that imaging techniques developed for eukaryotic systems are largely applicable in bacteriology as well. The small sizes of these organisms can pose some specific restrictions on the experiment, but in practice, the limits are set by fluorescence intensities and fluorophore concentration.

In the following section, we will briefly discuss different imaging modalities and imaging approaches that are routinely used in fluorescence (time-lapse) microscopy of bacteria. Furthermore, we will briefly touch on the subject of flow cytometry, since the majority of fluorescent probes can be used for in this technique as well.

Microscopy setup determines experimental focus. The field of fluorescence microscopy continues to evolve rapidly, offering new and improved commercialized imaging methods to every cell biologist. For scientist with a limited background in fluorescence microscopy, it can be difficult to match the best microscopy setup (i.e., imaging method) to a specific biological question. In most cases, imaging modalities are based on an epifluorescence setup in which the fluorescence excitation light illuminates the sample through the same objective that is used to detect the emission from the sample, limiting contamination of the output signal by the exciting light (231). For all of the microscopy setups described below, multiplexing with at least three different fluorescent colors (blue, yellow, and red) is routinely possible. Some setups allow for more thorough spectral unmixing, limiting the restrictions posed by the overlap of the multiplexing probes and possibly supporting a more elaborate color line-up (84).

(i) Wide-field epifluorescence microscopy. Wide-field epifluorescence microscopy is the most straightforward and most commonly used technical setup in the field of bacterial fluorescence microscopy. Despite its relative simplicity, this type of microscopy can be used to attain high resolution in both temporal and spatial (two-dimensional [2D] or *xy*) dimensions. During the image capturing, a wide cone of light with a specific wavelength evenly and simultaneously activates all the fluorophores in a large 3D volume (Fig. 3A), thereby creating an image of the sample on the camera without additional optical manipulations. Fluorophores in different *z* planes (i.e., imaging planes) throughout the sample will contribute to the eventual signal, leading to large amounts of out-of-focus emission light that can obscure valuable intracellular information. Because this out-of-focus light comes from above and below the focal plane, wide-field epifluorescence microscopy can suffer from a low signal-to-noise ratio. However, this does not present a major issue in samples not too densely labeled with fluorophores and limited in thickness such as a single layer of bacteria. For samples that require optical sectioning in the *z* direction, other techniques such as confocal microscopy (see "Confocal microscopy") might be preferred, although *z* sectioning can also be done with wide-field epifluorescence microscopy. Here, multiple *xy* sections are imaged through the sample in the *z*-dimension, creating a stack where discrimination in this dimension is still lacking. Using a deconvolution algorithm on this type of data to remove blurring out-of-focus signals then yields a 3D or volumetric representation of the sample and constitutes a simple approach to probe the 3D localization of subcellular targets (232, 233).

(ii) Confocal microscopy. In contrast to the even illumination of samples described above, confocal microscopy uses point illumination to scan across the sample and only excites a limited number of fluorophores in a very small intracellular volume (Fig. 3A). The emitted light is detected after passing through a pinhole such that only light from the desired focal plane reaches the detector, which further decreases the amount of out-of-focus light and increases the signal-to-noise ratio. Since the image is recorded point by point in laser scanning confocal microscopy, the temporal resolution is lower compared to the wide-field approach. This issue has been partially addressed with the development of spinning-disk confocal microscopes that use a disk of pinholes to scan the sample, making it possible to cover more sample area in a smaller time frame.

This optical sectioning in the 3D space does not *per se* present a particular advantage over wide-field microscopy when it comes to studying structures at the subcellular level in bacteria. Individual bacterial cells are only slightly thicker than the focal plane (defined by the wavelength of the emitting light (λ) and the numerical aperture (NA); $\sim$0.5 μm) and the pinhole blocks much of the emitted light, thus lowering the fluorescence intensity and requiring higher excitation energies (6, 234). However, this setup does provide substantial benefits when 3D sectioning of thicker samples is required, such as in imaging bacterial interactions with eukaryotic cells (235, 236) or biofilm structures (237, 238). Similar to wide-field fluorescence microscopy, deconvolution algorithms can provide considerable improvement of the signal-to-noise ratio.

(iii) Total internal reflection microscopy. A large number of dynamic, molecular events take place close to the cell surface. In conventional fluorescence microscopy, the emission of fluorophores close to the surface is often overwhelmed by the fluorescent signal stemming from the cytoplasm. Total internal reflection microscopy (TIRF) allows selective excitation of fluorophores close to the surface by creating an exponentially decaying evanescent wave through illumination of the sample using incident light at or above the critical angle. At this angle, total internal reflection occurs and the accompanying evanescent wave excites fluorophores only within a couple of hundred nanometers from the coverslip (i.e., near field) enabling high signal-to-noise without loss of temporal resolution as seen in confocal microscopy (233, 234). Furthermore, this technique provides improved *z*-axis resolution compared to a confocal section of the same focal plane.

TIRF microscopy has the necessary spatial and temporal resolution to take a closer look at the highly dynamic processes that occur at the bacterial cell surface (239). Several studies focusing on bacterial cytoskeletal factors and peptidoglycan synthases have used TIRF to visualize these processes (14, 240–243).

(iv) Highly inclined laminated optical sheet microscopy. Highly inclined laminated optical sheet (HILO) microscopy is another near-field technique that combines advantageous characteristics from TIRF and epifluorescence microscopy to enable the visualization of organized structures in the cytoplasm (and not just at the surface) (244, 245). The incident light in a HILO setup reaches the sample at a subcritical angle away from total internal reflection, increasing the penetration depth of the exciting signal while keeping background fluorescence at a lower level than in epi-illumination. An important advantage of both near-field techniques (i.e., TIRF and HILO) described here is that they are readily compatible with epifluorescence setups, limiting additional costs for groups with such a setup.

The first application of HILO in bacteria explored the dynamics of a *Bacillus subtilis* DNA pump at the sporulating septum (246). This study exploited both the high temporal resolution and low signal-to-noise ratio of HILO to show that this component consists of highly dynamic foci rather than a static ring structures (246, 247). Later, other studies underscored the potential of this imaging technique to delve deeper into organized cytoplasmic structures such as the forespore surface in *Bacillus* (110, 201, 248).

Imaging strategies increase image resolution. Snapshot and time-lapse capturing of fluorescently labeled processes and structures can provide key information on *in vivo* expression and localization profiles in bacteria. Already in the 1990s, this way of image capturing introduced the concept of strict spatiotemporal regulation in the bacterial cell, with key studies looking at how protein localization changed during the cell cycle (12, 249). However, this simple imaging strategy has limitations in both the spatial (~200-nm resolution limit) and temporal dimension (approximate acquisition time of fluorescent signal), restricting the amount of valuable information that can be extracted. To circumvent these limitations and increase the resolving power of fluorescence microscopy, several strategies were developed that enable a deeper insight into spatial and/or temporal dynamics on a scale fit for bacteria (i.e., approximately nm resolution; protein diffusion timescale). A comparison overview between the different imaging strategies can be found in Fig. 3B.

(i) Fluorescence recovery after photobleaching. The rapid diffusion of proteins in the limited cytoplasmic space (1 to 10 $\mu m^2/s$) (250, 251) and the surrounding membrane (0.1 to 1 $\mu m^2/s$) (252) results in a seemingly random distribution of these molecules in their corresponding subcellular compartment. However, different proteins display different kinetics depending on their size and interaction with other cellular targets. Since the temporal resolution of the described imaging techniques is insufficient to monitor these motions, different strategies were developed that do allow quantification of these fast kinetics. A widely used method to study protein diffusion is Fluorescence Recovery After Photobleaching (FRAP) in which a high-intensity laser pulse is used to rapidly and irreversibly photobleach all the fluorophores in a small region within a single cell (253, 254). By monitoring the return of fluorescence intensity in this region of interest (ROI), models can be fitted to precisely calculate diffusion rates for specific targets (250, 252, 255) or obtain qualitative information on protein mobility toward/within (sub)cellular structures (256–260). This type of strategy often exploits the ability of laser scanning confocal microscopes for targeted, high-power illumination, but other setups can also be used.

Although FRAP is straightforward and simple, interpretation of the data can be challenging. For example, incomplete recovery of fluorescence can indicate the presence of one or more immobile populations bound to structures within the ROI. In addition, a protein mobility rate that is too high might not allow for complete photobleaching of the region. Furthermore, additional photobleaching during image capturing and the presence of cellular photodamage always have to be taken into account. FRAP studies are inevitably limited by ensemble averaging and cannot reliably describe the complex diffusion processes that are sometimes going on, whereas single-molecule tracking (see “Single-molecule tracking” below) can give more detailed information on the behavior of individual proteins.

Fluorescence Loss In Photobleaching (FLIP) or inverse FRAP (iFRAP) are modifications of the original experimental setup that measure the loss of fluorescence from a ROI after photobleaching of an adjacent region. Similar approaches to FRAP can use smart fluorescent proteins and activate them in a small region of the cell to monitor their diffusion out of the ROI. Such techniques reduce some of the concerns of FRAP by providing a more gentle alternative to the relatively harsh photobleaching that generally requires high power and repeated laser illumination (261).

(ii) Förster resonance energy transfer. The nature of *in vivo* interactions between different proteins in living cells is often difficult to determine since diffraction-limited traditional imaging methods do not have the necessary resolving power. Therefore, considerable distance may actually separate proteins that appear to be colocalized by multicolor fluorescence microscopy (262). Förster resonance energy transfer (FRET) is an imaging strategy that can provide the necessary nanometer resolution to visualize protein-protein interactions and measures the direct transfer of excitation energy from a donor fluorophore attached to one protein to an acceptor fluorophore attached to the putative interacting partner (263). The mechanism behind this energy transfer involves the excitation of a donor fluorophore to a higher electronic state, followed by a nonradiative, distance-dependent transfer of that energy to a nearby compatible chromophore via dipole-dipole interactions. This interaction can only occur when two chromophores that share a substantial overlap in donor emission and acceptor absorption spectra are in close proximity of each other (~80 to 100 Å), with the FRET signal increasing at decreasing donor-acceptor distances. One of the first bacterial studies using this technique to investigate protein-protein interactions combined the traditional CFP donor and YFP acceptor to grasp the dynamic interactions in the bacterial chemotaxis apparatus (264). Next to using FRET as a molecular ruler for interprotein distance, the underlying principle can also be exploited to study intramolecular conformational changes and be used as a basis for *in vivo* ligand concentration measurements (265–270).

Reading out the FRET signal can be done in different ways, typically by monitoring changes in the fluorescence of the donor and/or acceptor. Again, data acquisition can be straightforward and simple, but data interpretation can be challenging and requires careful corrections via tedious controls (271). *In vivo* ratio imaging (266, 269, 270) is one of the most commonly used methods to read-out FRET signals, but other methods, such as acceptor photobleaching and fluorescence life-time imaging (FLIM), can also be used (271–275).

A similar but less widely used approach is BRET (Bioluminescence Resonance Energy Transfer) in which the donor energy is produced by a chemical reaction rather than stemming from an external light source. A particular advantage of these BRET approaches, where a luciferase provides the donor energy (RLuc/YFP compared to CFP/YFP), is the absence of autofluorescence and phototoxicity due to excitation. However, a problem with this system can be that the acquisition times become quite lengthy due to the dim RLuc signal (276).

(iii) Fluorescence correlation spectroscopy. In fluorescence correlation spectroscopy (FCS), fluctuations in fluorescence intensity are measured within a small focal volume usually not larger than 1 femtoliter (10^{-15} liter). The basis for these fluorescence fluctuations lies in the diffusion of fluorophores in and out of this tiny sample volume, leading to an intensity readout that can be decoded with autocorrelation models to yield data on the concentration, kinetics, molecular interactions, stoichiometry, and dynamics of fluorescently tagged targets in both the cytoplasm and membrane of living bacterial cells (277–285). In essence, FCS is able to grasp the temporal and spatial correlation of individual molecules and can bridge the gap between classical ensemble and contemporary single-molecule measurements (286).

Most commonly, FCS is performed in a confocal or two-photon microscopy setup where a focused laser beam is used to create a very small sample volume favoring the detection and recording of fluorescence specifically coming from the detection volume itself. To enable the extraction of valuable information from the fluctuation profile of the detected signal, two premises have to be fulfilled: (i) the number of particles diffusing through a small open volume in an infinitely large reservoir obeys Poisson statistics, and (ii) the precise shape of the detection volume, also known as the point spread function (PSF), must be known. More insight into the principles of this technique can be found in several other reviews (286–291).

Numerous modalities and strategies have been developed for FCS over the years, supporting the measurement of various molecular parameters (286, 287, 289). Fluorescence cross-correlation spectroscopy (FCCS) and scanning number and brightness analysis (sN&B) are two examples of FCS-based methods that allow the determination of molecular stoichiometry *in vivo*. In the former technique, the intensity fluctuation patterns of two compatible fluorophores (and thus two different biological targets) are measured to provide detailed information on their interactions and stoichiometry (283, 292), while the sN&B technique uses FCS in a way that produces more quantitative data for *in vivo* stoichiometric analyses (282, 285), as well as expression level measurements (280, 293). sN&B is based on an image scanning fluctuation approach where the moments of fluctuations at each pixel in a series of raster-scanned images (ca. 50 to 100) are used, as in moment analysis (294), to calculate the number and molecular brightness of diffusing fluorescent molecules (295). Ferguson et al. (280) fitted the technique to prokaryotic use and were able to virtually eliminate all photobleaching of the fluorophore inside the small, confined volume of the bacterial cell by going away from single point FCS and performing a series of raster scans (between 50 and 100 images) using pixel dwell times that are faster than the diffusion time (280). It is worth noting that the timescale of fluctuations in sN&B corresponds to the time it takes to return to a given pixel (frame-time; ca. several seconds) in contrast to traditional point FCS where acquisitions happen on the millisecond timescale. This provides the sN&B technique with the additional benefit of also being able to study slow-moving particles. The quantitative nature of this technique was already exploited to gain information on the subunit and oligomerization state of the SpoIIIE DNA pump *B. subtilis* (282) and the Mrr restriction endonuclease in *E. coli* (285).

(iv) Super-resolution microscopy. All forms of conventional fluorescence microscopy are restricted in their resolving power by the wavelength of the used light, limiting the lateral (*xy* dimension; ~250 nm) and axial (*z* dimension; ~600 nm) resolution to various extents depending on the imaging technique used. This implies that all fluorescently labeled proteins and protein complexes show up as blurred focal spots of ~250 nm in diameter (and ~600 nm in the *z*-axis) while in reality only spanning lengths in the low nanometer ranges. Super-resolution nanoscopy provides a resolution that surpasses this diffraction limit and has over the past decade delivered the extra resolving power necessary in bacteria, which themselves only marginally exceed the diffraction limit (296). Live-cell super-resolution imaging can be challenging, mainly due to the long acquisition times and high phototoxicity inherent to most of these techniques, and thus requiring a well-planned experimental setup (297). In-depth reviews on super-resolution techniques and their applications can be found elsewhere (234, 298–300).

One of the most popular approaches for live-cell, super-resolution imaging is Structured Illumination Microscopy (SIM). SIM owes this status to its relative short acquisition times and the ability for common fluorophores to be employed. This type of microscopy applies wide-field fluorescence illumination (including TIRF and HILO) in combination with a high-tech grid to generate predetermined illumination patterns that interfere with the sample structure and allow the extraction of fine structural details (resolution in *xy* [~100 nm] and *z* [~250 nm]). Eventually, multiple images with different interference patterns will be combined to reconstruct a higher-resolution 2D SIM or 3D SIM image (234, 282, 301–304). For SIM to give good results, a large number of acquisitions is required for every resolving image, putting a technical limit on the temporal resolution. It should be pointed out that this technique is particularly sensitive to artifacts during the image reconstruction process.

Stochastic Optical Reconstruction Microscopy (STORM) (305) and Photoactivation Localization Microscopy (PALM) (306) also use wide-field illumination but require smart dyes or smart fluorescent proteins, respectively, to switch individual fluorophores on and off in a stochastic manner. By using low activation light to turn on single fluorophores within diffraction limited areas at certain time points, the captured position of individual, activated fluorophores is separated in time leading to resolutions in the 20-nm range after image processing and reconstruction (resolution in *xy* [~20 nm] and *z* [~50 nm]) (305–307). This attained resolution almost exclusively depends on the properties of the specific fluorophore and the labeling density in the sample. Data acquisition is a time-consuming process that strongly affects the temporal resolution but still allows live-cell imaging. Furthermore, the image reconstruction requires powerful computers to process the enormous amounts of acquired data. Bacterial application of PALM and STORM are getting more popular and have yielded breakthroughs with respect to chemotaxis protein localization, division septum nanostructure, and peptidoglycan architecture (282, 308–314).

A third type of nanoscopy technique utilizes laser scanning confocal microscopy to selectively switch off fluorophores in the periphery of the excitation zone, making it possible to collect only a limited number of photons from the central part of that region. To achieve this, a second depletion laser in the confocal setup stimulates excited molecules back to their ground state in a doughnut-shaped region around the central confocal spot. Through this method, stimulated emission depletion microscopy (STED) only detects molecules within 30 to 80 nm of the center of the excitation spot and can reach up to a 3- to 10-fold improvement in lateral resolution albeit severely suffering from photobleaching and phototoxicity (resolution in *xy* [~50 nm] and *z* [~100 nm]). Furthermore, this depletion concept was also extended to smart photoswitchable fluorophores, turning the peripheral fluorophores into an off state instead of stimulating emission depletion (315). New approaches using extremely stable fluorophores and other technical setups are being developed making STED more and more suitable for live-cell imaging (304, 316–318).

(v) Single-molecule tracking. Single-molecule tracking/single-particle tracking (SMT/SPT) exploits the power of modern microscopy hardware and the sensitivity of the newest tagging probes to study the dynamics of individual molecules in living cells. By tracking single/individual macromolecules with millisecond time resolution and nanometer spatial precision, this technique allows answering many enduring questions in molecular biology and provides insights on the properties of different molecular subpopulations *in vivo* (319–321). SMT has the ability to discriminate between different modes of action of a single molecular species under native conditions, stepping away from the use of bulk measurements to probe characteristics such as protein binding affinity or dwell times. This technique furthermore enables *in vivo* quantitative biology by counting molecules and their stoichiometry, characterizing their intracellular location and mobility, and identifying functionally distinct molecular distributions (319, 320, 322–325).

Most fluorescence SMT techniques employ common fluorescence microscopy setups (as described above in "Microscopy setup determines experimental focus") to achieve single-molecule tracking in multiple cells at once, albeit sometimes using equipment with higher sensitivity or alternate illumination patterns. Essential to the approach is the ability to pinpoint the location of a single molecule in an image captured with the microscope, after which the dynamics of the molecule can be tracked by analyzing the subsequent frames with algorithms to monitor the probe's motion (326). Most commonly, fluorescent dyes or fluorescent proteins are used to tag the macromolecule, with a preference for the latter since they provide higher precision. Where the initial single-molecule approaches *in vivo* were limited to low-abundance molecules, advances such as super-resolution microscopy now allow for essentially any type of cellular protein, as well as other cellular structures, to be tracked (321, 327).

A more extensive description of SMT can be found in numerous reviews on the topic (299, 327–331) and recent studies that use the technique to advance the understanding of bacterial cell functions (251, 326, 332–339).

(vi) Flow cytometry and fluorescence-activated cell sorting. The high spatiotemporal resolution of fluorescence microscopy puts a constraint on the number of cells that can be analyzed. While improvements in software-based automation and development of high-throughput platforms for microscopy have over the years increased the ability to use the power of numbers (340–352), investigating hundreds of thousands of cells still remains a tedious task. Flow cytometry on the other hand takes advantage of the power of numbers with single-cell resolution and can interrogate large numbers of cells on their physiological characteristics in very short time intervals using a laser-based detection system.

In essence, flow cytometry is very similar to microscopy but instead of producing an image as output it quantifies cellular parameters as voltage signals. Once aggregation-free liquid samples are presented to the machine, the cellular content will be mixed with a saline solution (sheat fluid) in the fluidics chamber, and cells will be hydrodynamically steered through a narrowing channel, giving rise to a single file of cells that is analyzed with laser light at the interrogation point. As individual cells pass the laser beam, their content will scatter the light in multiple directions allowing for photomultiplier tubes (PMTs) to capture the signal under specific angles. Forward scatter (FSC) can be detected by a PMT diametrically placed to the illumination light and is indicative of the particle size, while the side scatter (SSC) is captured perpendicularly to the laser beam and provides information on the inner complexity (e.g., granularity) of the cell. These detected photons will then be turned into voltage signals proportional to the specific characteristics that are measured. Furthermore, flow cytometry supports the use of fluorophores, thereby enhancing the repertoire of cellular properties that can be quantified. The emitted fluorescent light is guided through emission filters perpendicular to the excitation beam and allows multiplexing of different fluorophores at the same time. It is worth noting that many fluorophores can serve in both flow cytometry and fluorescence microscopy, explaining why this related technique is briefly touched upon in this review.

For a long time, flow cytometric applications solely focused on eukaryotic applications since the small bacterial sizes made it difficult to correctly distinguish between the small cells and other contaminating particles (353–355). However, advances in the technological setup and the widespread use of fluorescent probes have helped to overcome these issues, making this technique very suitable to investigate heterogeneity within bacterial populations (356, 357). This is further endorsed by the extension of the flow cytometry setup with a fluorescence-activated cell sorting (FACS) module that can physically separate and retrieve subpopulations with measurable characteristics. For example, Rego et al. (358) recently used a FACS-based transposon screen in the identification of factors influencing the high variability of antibiotic tolerance profiles seen in isogenic *Mycobacterium* populations.

Altogether, flow cytometry can be seen as an extremely quantitative and high-throughput technique that allows studying bacterial populations at the single-cell level in order to obtain answers to physiological questions. However, this technique fails to address the intracellular localization of fluorescent markers, as well as the genealogical relationship among cells, which are features easily discriminated in fluorescence time-lapse microscopy.

A FLUORESCENT JOURNEY THROUGH THE BACTERIAL CELL BODY

In this second part of the manuscript, we will illustrate how the bacterial cellular organization and physiology can be visualized and vivisected using the instruments of the fluorescence microscopy toolbox described in the previous section. The bacterial anatomical outline will serve as a practical guide to classify mechanistically relevant case studies, leading the reader throughout the cell while exemplifying and explaining the different fluorescent dissection strategies that have enabled gaining insight into the overall architecture and inner workings of the bacterial cell. Starting from the inside, we will dissect the bacterial cell into three categories (nucleic acids, cytoplasm, and cell periphery) and use each category to zoom in on different reasonings and strategies that can be used to solve biological questions by means of (live) fluorescent visualization.

Nucleic Acids

Visualizing the genetic code. The bacterial genetic blueprint differs from those of eukaryotes by the fact that a single, uncompartmentalized, and often circular DNA molecule (frequently supported by smaller, circular plasmids) carries all the information necessary to define the bacterial cell. The lack of confinement by an intracellular membrane contrasts the spatial separation seen in eukaryotes, leaving room for a coupling between transcription and translation. Stretching out a typical bacterial chromosome would give a lengthy string-like structure a few hundred times longer than the bacterial cell length itself, underscoring the tremendous compaction that occurs intracellularly. Hence, organizational mechanisms must be in place to make this compaction compatible with the range of cellular processes, including DNA repair, replication and segregation, that are essential to life. Figuring out how these processes can proceed in a reproducible, precise, and timely manner without internal compartmentalization might be one of the most challenging tasks in bacteriology to date.

The first clues indicating that the bacterial chromosome had a particular spatial organization came from light microscopy studies using specific staining dyes that revealed intracellular bodies of DNA (reviewed in reference 359). This nucleoid, formed by the chromosomal molecule and its ensemble of bound proteins, attains its highly compacted shape via a number of mechanisms and ingenuities to fit the small cytoplasmic space of the bacterium (360–362). Further insights into these intracellular nucleoid regions have rapidly advanced with new microscopy technologies and improved fluorescent probes. These new features sparked interest in how this nucleoid is shaped, how it behaves in the three-dimensional space of the cell cylinder, and how it eventually influences bacterial physiology. These advanced insights pointed out that certain fundamental cellular processes depend on the dynamic and spatial organization of this chromosome and that its 3D structure is central to bacterial cellular organization and physiology (363).

(i) Three-dimensional architecture of the nucleoid. Lacking a distinct compartmentalization of the chromosome, it was long assumed that the genetic material of bacteria was freely floating around the cytoplasm without any higher-order structuring or intentional organization. The ability to capture three-dimensionality in the bacterial cell cylinder provided a basis for in-depth research on the nucleoid's spatial structure and dynamics, proving that prokaryotes can compete with eukaryotes in organizational complexity.

Multiple mechanisms underlie the compaction of the chromosomal DNA into the three-dimensional shape and size of the nucleoid (360, 364). Major factors that contribute to the structural organization of the bacterial chromatin are architectural proteins associated with the nucleoid, DNA supercoiling, and macromolecular crowding. Carrying a variety of functionalities beyond structural scaffolding, most of the nucleoid-associated proteins (NAPs) are bound to the chromosomal DNA roughly every 100 bp via nonspecific DNA-binding interactions (365), making them outstanding beacons to visualize the entire nucleoid when fluorescently labeled (309, 361, 366) (Fig. 4A, diagram 1). Wang et al. (309) mapped the distribution of some of the most important NAPs in live *Escherichia coli* cells using super-resolution microscopy and demonstrated a variety of distribution patterns. While NAPs such as HU, FIS, and IHF are found to be scattered throughout the nucleoid, other members of this protein family, such as H-NS, display a more localized motif. Similar mapping experiments have been done for a variety of NAPs in other bacterial species (367–369).

Exploiting the high-density coverage of fluorescent HU, combined with the high spatiotemporal resolution of deconvoluted *z*-stack epifluorescence microscopy, Fisher et al. (232) were recently able to model the 3D architecture and organizational dynamics of the *E. coli* nucleoid. Using a translational fusion of the mCherry FP to the alpha subunit of HU (i.e., HupA), it was shown that the chromosomal DNA does not just fill up the interior of the cell, but rather is a discrete, delimited object. In fact, the bacterial chromatin presents itself as a dynamic helical ellipsoid of which the helicity is determined (and maintained) by the cell radius, rather than being internally regulated by the nucleoid itself. Furthermore, it was also seen that there are temporal dynamics in the chromosome where nucleoid density fluxes occur along the cellular axis, leading to a net nucleoid length increase (232). In a similar approach, using a GFP-FIS fusion to nonspecifically decorate the entire chromosome of *E. coli*, Hadizadeh Yazdi et al. (370) found supporting evidence for the coiled organization of the nucleoid with a helical pattern depending on the growth conditions and thus the cell size. This three-dimensional shape of the nucleoid visualized by fluorescent protein fusions agreed with earlier results from Berlatzky et al. (179), who used exogenously added fluorescently labeled deoxynucleoside triphosphate (dNTP) derivatives to visualize newly synthesized DNA in living *Bacillus subtilis* cells. Capitalizing on the increased resolution provided by the effective incorporation of these fluorescent nucleotides solely in the newly synthesized strand, these researchers were able to infer 3D geometrical patterns during replication. Another benefit of this technique compared to the NAP approach is the ability to switch to a pulse-chase experimental setup to further increase temporal resolution.

NAPs and other fluorescently labeled DNA-binding proteins are very useful tools to grasp the nucleoid shape in the two- and three-dimensional space (175, 232, 370–372). However, possible problems with these whole-genome labeling proteins in time-resolved studies can come from their growth-phase-dependent behavior. For example, in *E. coli* a large part of the "histone-like" HU proteins on the nucleoid is replaced by structural homologs such as IHF (integration host factor) and Dps (DNA protection during starvation) upon entering early stationary phase (373). As a consequence, these types of labeling strategies have to be used with care in studies on the growth phase dependence of nucleoid organization. Such issues can be at least partially avoided by using exogeneous strategies that are less growth phase dependent, such as fluorescently labeled dNTP derivates (179) and DNA dyes (see the following section).

(ii) Nucleoid morphology, localization, and organization in the two-dimensional cell space. Temporal changes in nucleoid morphology can contain valuable information on the bacterial cell status and ongoing cellular processes and can be easily monitored using wide-field epifluorescence microscopy in combination with "whole nucleoid labeling" approaches (374–382). To attain such a full labeling of the bacterial nucleoid, small DNA-binding molecules (376, 378, 379, 383) or fluorescently labeled DNA-binding proteins (371, 381, 382) can be used (Fig. 4A).

DAPI is the earliest and currently most widespread small DNA-binding molecule used for visualizing the bacterial nucleoid (28, 371, 373, 377, 378, 380, 384, 385). This

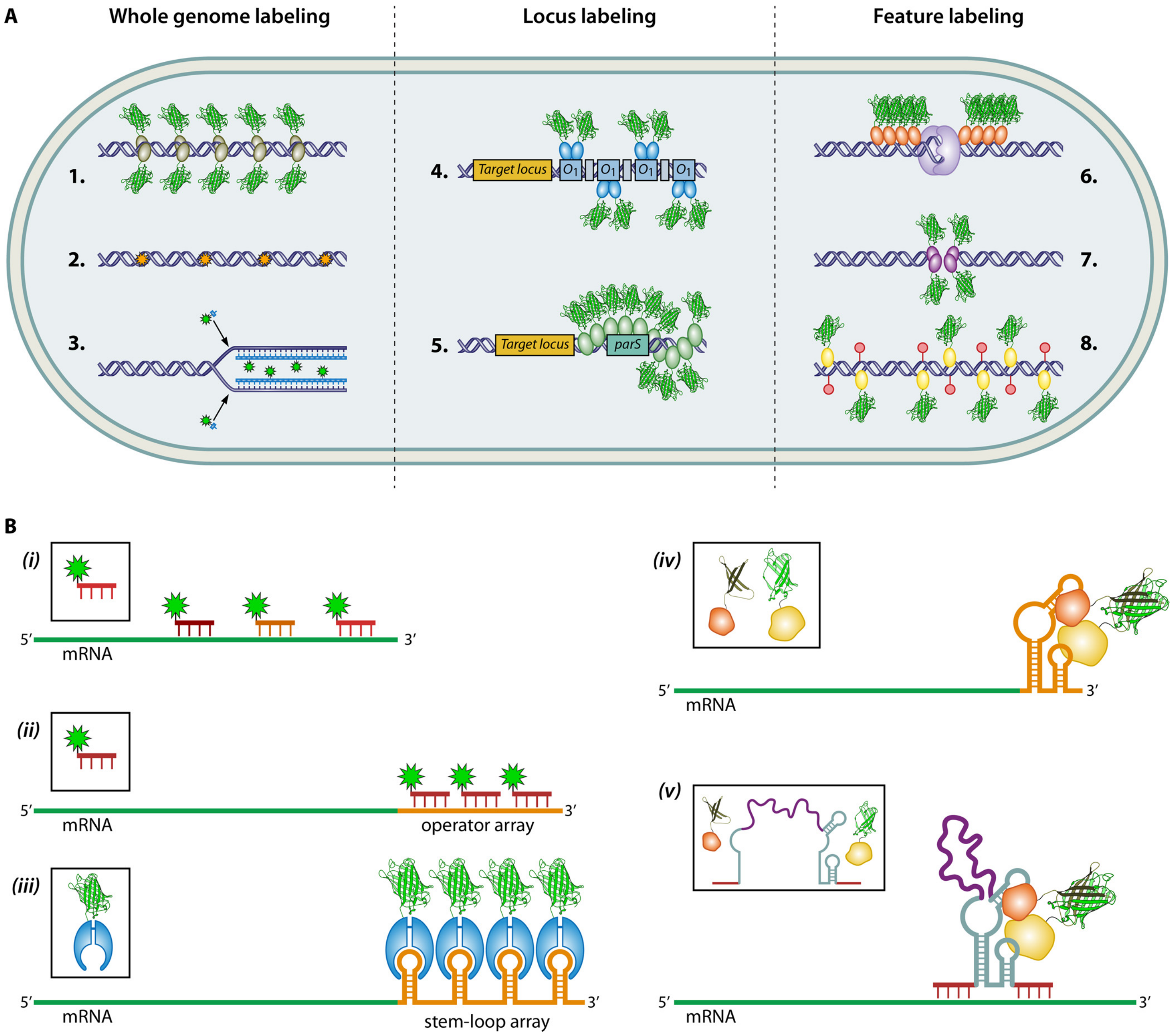

FIG 4 Overview of strategies to fluorescently label nucleic acids in bacteria. (A) Methods to visualize the genetic blueprint of a bacterium can be subdivided into three categories depending on their mode-of-action: whole-genome labeling (diagrams 1 to 3), locus labeling (diagrams 4 and 5), and feature labeling (diagrams 6 to 8). For whole-genome labeling, the strategies support the labeling of the entire nucleoid (and other DNA elements) in the cell and are regarded as nonspecific, referring to the ample presence of labeling sites rather than to the labeling mechanism itself. (Diagram 1) Fluorescently labeled DNA-binding proteins such as nucleoid-associated proteins (NAPs) may be used to decorate the chromosomal DNA. Depending on the intrinsic features of the DNA-binding protein at hand, a different localization motif and coverage density will be attained. (Diagram 2) Likewise, small DNA-binding molecules can be used for whole-genome labeling. Every type of DNA-binding dye targets a specific (recurrent) structural motif in the DNA macromolecule. (Diagram 3) Adding fluorescently labeled dNTP derivates to the growth medium leads to effective incorporation of these fluorescent precursors in the newly synthesized DNA strands. For certain applications, increased resolution into a specific region of the genetic material (i.e., locus labeling) may be desirable. (Diagram 4) A fluorescent repressor-operator system (FROS) incorporates a tandem array of operator DNA into the region of interest which specifically attracts the cognate fluorescently labeled repressor to highlight the targeted DNA. (Diagram 5) Similarly, a single *parS* locus can be inserted into the genome to serve as a binding site for fluorescent ParB protein. These latter proteins form a filament on *parS* that spreads out into neighboring sequences and forms a detectable focus. DNA-specific features such as DNA mismatches and methylation patterns may also serve as probe binding sites to highlight specific events or DNA strands (i.e., feature labeling). (Diagram 6) The small fraction of (spontaneous) mismatches that occur during DNA replication and become fixed into the DNA can be visualized through the exploitation of the methyl-directed mismatch repair system (MMR). Here, fluorescent MutL polymerizes at the mutated site and prevents mismatch-bound (and unlabeled) MutS from sliding away from the targeted region. (Diagram 7) Double-stranded DNA breaks can be fluorescently labeled using the Gam protein from bacteriophage Mu that directly binds to the double-stranded DNA ends. (Diagram 8) SeqA-FP has a high affinity for hemimethylated DNA and solely binds on DNA duplexes in which one of the strands is methylated (red circle). (B) Overview of methods that enable direct RNA visualization in individual bacterial cells, with only (iii to v) supporting real-time, *in vivo* measurements of RNA dynamics in the cytoplasm. (i and ii) In fluorescence *in situ* hybridization (FISH), complementary oligonucleotides labeled with fluorophores are added exogenously to light up the RNA molecules of interest in fixed and permeabilized cells. These probes can either target the native RNA molecule (i) or a genetically fused operator array added to the RNA molecule (ii), with the latter approach increasing sensitivity and signal-to-noise ratio. (iii) A fluorescent derivative of the RNA-binding coat protein of bacteriophage MS2 allows *in vivo*, real-time visualization of RNA molecules by targetting tandem repeats of its cognate stem-loop, transcriptionally linked to one of the UTRs of the target RNA

(Continued on next page)

membrane-permeable dye preferentially binds AT-rich regions (173) and absorbs light in the UV region, making this molecule highly suited for snapshot imaging but less valuable for longer *in vivo* live-cell imaging due to inherent phototoxicity (98). Bakshi et al. (379) compared several commercially available DNA stains while looking for the ideal dye to stain the nucleoid in both Gram-negative and Gram-positive species with minimal physiological perturbations. Surprisingly, they found that so-called "dead-cell stains" (SYTOX orange and SYTOX green) are nearly ideal for imaging living cells, at least for the model organisms *B. subtilis* and *E. coli*. In contrast, "live-cell stains" (such as DRAQ5 and SYTO 61), together with the commonly used DAPI, seem to cause unwanted effects such as nucleoid expansions, cell permeabilization, and growth defects. This classification of "live/dead-cell" stain stems from the ability of these dyes to intercalate the bacterial DNA of uncompromised (living) and compromised (dead) cells, respectively, providing the power to discriminate between both types in flow cytometric measurements. However, modern microscopy equipment can pick up the signals of the small amounts of such "dead-cell" stains that enter uncompromised cells, surprisingly providing less disturbed read-outs. More recent work of Lopez-Garrido et al. (383) confirmed the time-lapse compatibility of SYTOX green, showing that chromosome translocation helps to inflate the *Bacillus* forespore during sporulation. A major disadvantage of this dye-based approach is the need for a constant addition of these potentially toxic reagents that can interfere with DNA stability since they often work via intercalation. Furthermore, the permeability of these molecules can vary between different bacterial species, and even between individual cells in an isogenic population, while also being influenced by the experimental conditions. However, since no genetic alterations are necessary, the use of these dye molecules allows for a broad host spectrum, extending beyond commonly used model organisms (386).

Nevertheless, full labeling of the nucleoid does not provide the necessary resolution to shed light on how internal chromosomal organization and processes such as duplication or segregation are organized in the cellular space. Dissecting those dynamic processes requires labeling specific sections of the nucleoid, creating the ability to track them for longer periods of time in the cytoplasmic volume. The first technique that allowed such specific labeling in real-time was originally developed for the analysis of chromosome behavior in yeast (387, 388) but was soon after modified to monitor the spatial dynamics of the replication origin (*oriC*) and terminus (*ter*) in *Bacillus subtilis* (10, 389). This strategy relies on a Fluorescent Repressor-Operator System (FROS), where arrays of operator DNA containing multiple repressor binding sites are incorporated into the region of interest. This specific region in the chromosome can later be fluorescently highlighted and tracked *in vivo* through the binding of (multiple copies of) the labeled cognate repressor (Fig. 4A, diagram 4). These fluorescent proteins bound on the ROI are then visible as foci that are clearly distinct from the free-floating unbound repressor molecules in the cytoplasm. The first FROS element consisted of tandem *lac* operator sites (ca. 250 repeats) forming an ~10-kb fragment that needed to be genetically inserted into the targeted region of the bacterial chromosome and truncated GFP-labeled LacI molecules as the cognate binding partners. This seminal work of Webb et al. (10) confirmed the earlier genetic prediction of a defined chromosomal orientation during sporulation (390) and further showed that this orientation was also present during vegetative growth where *ter* and *oriC* were reproducibly localized to the new and old pole, respectively. Besides the precise localization of *oriC* and *ter* regions, it was later on shown by extensive work of Viollier et al. (391) that every locus on the *Caulobacter* chromosome has a specific subcellular address relative to both *ori*

FIG 4 Legend (Continued)
(mostly 3′). (iv) Bimolecular Fluorescence Complementation (BiFC) in combination with a spliced eukaryotic initiation factor 4A (eIF4A) can be utilized to attain a very high signal-to-noise ratio. The labeled, dual eIF4 reporter only forms a reconstituted fluorescent complex when it binds to its cognate, 58-nucleotide long binding site attached to the target RNA molecule. The latter system can be modified with an additional split aptamer (v) to minimize the amount of interference in the biological system and alleviate the need for genetic alterations. In this approach, the 58-nucleotide stem-loop is split into two modules interconnected with an internal flexible linker and reforms via an interaction with the specific, native RNA molecule of interest.

and *ter* region, indicating that there is something as a reproducible *ori*-*ter* configuration of the chromosome along the cellular axis. Viollier et al. (391) used an improved strategy devised by Lau et al. (392) that allows multiplexing different loci at the same time by using compatible FROS systems (i.e., *lacO*/LacI and *tetO*/TetR) labeled with spectrally different FPs. Furthermore, this altered system also provided a solution for the inherent genetic instability of the tandem operator repeats by inserting random sequences between every *lacO* (21 bp) or *tetO* (19 bp) site in the arrays. Unlike these earlier fluorescent repressor-operator systems, typically containing tens to hundreds of tandem repeats of the operator site, Wang et al. (309) showed that only six interspersed *tetO* repeats (219 bp) are sufficient to label the precise position of target genes within the cells since strains carrying large numbers of repressor binding sites tend to display growth defects. Via the latter system, Wang et al. (309) obtained indications that the broad spatially distributed H-NS-regulated operons in the *E. coli* genome (366, 393) preferentially sequester into clusters. These clusters are formed by long-distance H-NS oligomerizations driven by the N-terminal domain of the protein, leading to a substantial folding and reorganization of the chromosomal DNA on a global scale.

Recently, the signal-to-noise ratio of this method was further improved by the development of a FROS system consisting of two different repressor-operator modules combined with Bimolecular Fluorescence Complementation (BiFC) (67, 69). This new system uses two different repressor proteins (λCI and Gal4), each fused to one subfragment of a "split" mVenus molecule, and enables the fluorescence signal to be reconstituted on a hybrid array constructed by combining the cognate operator sites of both repressors in an alternating fashion (71).

A second type of locus-specific labeling system is based on modules of the temperate P1 bacteriophage partitioning system and were used in the first studies going into depth on chromosomal segregation in *E. coli* (394, 395). It comprises of a partitioning site, *parS* (286 bp) that in its native system works together with two P1 proteins (ParA and ParB) to allow faithful distribution of P1 plasmid copies to both daughter cells (396). Li and coworkers (394, 397, 398) were able to show that this system can be modified not only to faithfully track the dynamics of the P1 plasmid but also to monitor specific bacterial loci on the chromosome. In this artificial system, a truncated ParB protein devoid of its first 30 amino acids is labeled with GFP at its N terminus and can be used to highlight the *parS* region in the absence of ParA. This fusion forms bright fluorescent foci without the need for tandem repeats of the target sequence (as seen in FROS) since binding of the ParB dimer to the *parS* locus primes the formation of ParB filaments that spread out to neighboring sequences (399–401) (Fig. 4A, diagram 5). This mechanism can, however, lead to unwanted gene silencing in the close vicinity of the *parS* insertion site. Furthermore, the modified ParB molecules can interfere with the partitioning of other plasmids in the target strain and can also aspecifically highlight other closely related plasmid sequences (402). Dual labeling with this *parS*-based system can be achieved by combining the *parS* of P1 with other compatible *par* modules such as that of pMT1 of *Yersinia pestis* (403). This type of multiplex labeling was used in the past to follow nucleoid segregation and phage integration dynamics in *E. coli* (404, 405).

(iii) Bacterial damage and repair systems as tools for DNA lesion detection. Bacterial evolvability is shaped by a balancing act between DNA damage and its concomitant repair mechanisms, safeguarding genome integrity while leaving room for genetic alterations that can provide fitness benefits. To thoroughly understand the dynamics of these processes, new experimental approaches were necessary to replace the traditional population averaged readouts. Indeed, single-cell and single-molecule strategies now allow investigators to monitor how specific subpopulations contribute to the average population mutation rate and to determine which molecular dynamics drive these phenomena.

During DNA replication, a template is copied by the bacterial replisome with high fidelity throughout the process. Sporadically, however, the DNA polymerase incorporates a wrong nucleotide, leading to a mismatch that is typically recognized and repaired by the methyl-directed mismatch repair (MMR) system before it gives rise to permanent genetic change. To visualize the small fraction of mismatches in a bacterial population that are inadvertently fixed into a mutation during a subsequent round of replication, Elez et al. (406) developed a fluorescent probe based on a modified but still functional MMR system in *E. coli* (consisting of the MutS, MutL, and MutH proteins) (Fig. 4A, diagram 6). In the MMR-assisted repair process, MutS detects and binds the nucleotide mismatches, while MutL polymerizes at the mismatch sites to prevent the mismatch-bound MutS from sliding away from the targeted region (407, 408). By fluorescently labeling MutL, foci can be detected on those mismatches that will become fixed in the next round of replication since in these affected region the fluorescent protein accumulations have the time to become bright and persistent enough to be imaged, whereas the repaired mismatches are too short-lived for focus formation (406, 409). Several biological factors impact the number of MutL foci that can be microscopically detected, namely, the error frequency in DNA replication, the error repair rate efficiency and efficacy, and the functionality of both MutL and MutS (406). More recently, Robert et al. (410, 411) combined time-lapse imaging, microfluidics, and this specific fluorescent tag to monitor the dynamics and fitness effects of spontaneous point mutations on the single-cell level in *E. coli*. Going a step further, both Uphoff (412) and Woo et al. (413) combined the MutL-FP reporter with transcriptional readouts to couple gene expression dynamics to mismatch events, showing that DNA replication errors arise with different frequencies in subsets of the population due to cell-to-cell variance in the expression of DNA damage responses and endogenous stress (such as problems with proteostasis, genome maintenance, and reactive oxygen species). An important limitation of this approach is that different types of mismatches are recognized by the MMR system with different efficiencies leading to a possible detection bias, with some lesions not properly showing up in this microscopy-based approach (412, 414). However, the resolving power of this method far more than complements the traditional mutation assays that show only time and population averaged mutation rates, thus deepening the understanding on the underlying molecular processes (412).

Double-strand breaks (DSBs) in the chromosome work as a highly genome-destabilizing type of damage that can contribute to bacterial evolution (415–417). These DNA lesions occur spontaneously in a small percentage of the bacterial population under normal growth conditions but become more prevalent when certain stressors are applied. To calculate precise rates of spontaneous (or induced) DSBs, Shee et al. (418) recently constructed a synthetic system based on a fluorescently labeled Gam protein. This protein originates from bacteriophage Mu and is able to bind double-stranded DNA (dsDNA) ends. The fluorescent Gam probe can therefore be used to visualize the subchromosomal location of DSBs by focus formation and allows for an exact quantification of the number of double-strand ends inside the cell (Fig. 4A, diagram 7). Rather than being a multibreak catastrophe, spontaneous DSBs mostly show up as a single breakpoint in the nucleoid of affected cells. Furthermore, the number of lesions formed in a population within a specific time frame displays a precise correlation with the number of divisions, implying that a replication/generation-dependent (and not time-dependent) mechanism is at the base of spontaneous DNA breakage. These two findings enabled Shee et al. (418) to calculate the first true rates of spontaneous DSB formation ($\sim$0.021 per cell division), putting them 10 to 20 times lower than initially postulated (416). In contrast to the λ phage Gam protein that binds to the *E. coli* RecBCD (DSBs repair) protein complex, the Mu variant directly protects linear DNA without performing any repairs or binding to other known proteins (419–421). However, as Gam-GFP will directly bind to the linear dsDNA pieces in the cytoplasm it will prevent the bacterial RecBCD complex from repairing the damage and will lead to a loss of viability, making visualization of the postbreakage repair dynamics impossible (418, 422).

An important second part of these evolutionary dynamics is governed by bacterial DNA repair mechanisms that protect the genome and its host chassis from the detrimental effects of these mutational mechanisms. How these DNA repair machineries work *in vivo* and how they coordinate their function in single cells can be investigated by different fluorescence imaging techniques gauging different characteristics of the target molecules (423). Many insights into DNA repair dynamics have been attained by looking at the direct action of proteins inside single cells, thereby overcoming the limitations inherent to measuring averages over large populations of molecules and cells (326, 335, 424, 425). Using photoactivation and longtime tracking of single fluorescently labeled DNA polymerase I (Pol) and ligase (Lig) molecules during their *in vivo* working, Uphoff et al. (319) showed that both proteins spent most of their time searching for free damaged DNA substrates and that their numbers rapidly increase within minutes after DNA damage is inflicted, thereby minimizing both the number and the lifetime of toxic intermediates that need repair. Furthermore, they could also show that individual Pol and Lig complexes float around in the cytoplasm with a very low affinity for undamaged DNA, but transiently bind to damaged sites that need repair. This type of approach using single-molecule tracking provides a framework for quantifying reaction rates of any type of enzyme that changes its diffusion characteristics upon target binding and release.

Another key player in DNA repair is RecA, a protein that orchestrates the response to DNA damage through multiple roles in the bacterial SOS response aimed at protecting and repairing the chromosome. Upon infliction of DNA damage, transcription of the *recA* gene is upregulated, giving rise to an ~10-fold increase in protein levels in the cell within minutes (426–429). Over the years, tools have been developed to probe RecA dynamics within single cells and follow its spatiotemporal changes in response to damaged genetic material. However, making a distinction between functionally different representations of intracellular RecA (free-floating, DNA-bound or DNA-free storage structures, . . .) has been very challenging to achieve solely based a fluorescent fusion visualizing the localization patterns (429–433). Furthermore, these fusions have consistently created proteins with reduced functionality (429, 434) and affected localization patterns due to the presence of the tagging moiety (430). To solve this problem, Ghodke et al. (139) created a novel fluorescent probe based on a monomeric and catalytically dead λCI repressor that uniquely interacts with activated RecA in nucleoprotein filaments formed on ssDNA stretches at lesion sites and has lost its intrinsic ability to directly bind DNA by the removal of its N-terminal domain. Using this probe as part of a wider (single-molecule imaging) approach, Ghodke et al. (139) showed that RecA is largely stored in specific DNA-free aggregates residing outside the nucleoid during normal growth but, upon DNA damage, is rapidly extracted from these storage complexes and nucleated to form early SOS-signaling complexes that can later further mature into nucleoprotein filaments.

(iv) Visualization of lateral elements and horizontal gene transfer. Horizontal gene transfer has an enormous impact on bacterial genome plasticity and its evolution. It comprises the lateral transfer of DNA between different genomes via transformation (uptake of free DNA), conjugation (plasmid-mediated transfer) or transduction (phage-mediated transfer). Tracking the movement of transferable genetic material allows for detailed spatiotemporal information on these processes, starting at the point of cellular entry up to the possible insertion in the recipient chromosome.

An interesting technique to monitor horizontal gene transfer processes was initially developed by Babic et al. (435) to quantitatively look at conjugation on the single-cell level and monitor the fate of the newly acquired genetic material throughout several generations. These researchers exploited two biological features to come to a successful strategy: (i) after the formation of the conjugation pilus by the donor cell, a single-stranded nick is created in the mobilized plasmid, leading to the transfer of a single DNA strand to the recipient via rolling circle replication (436), and (ii) the high affinity of SeqA, a repressor of *E. coli* replication initiation, for DNA methylated in only one strand of the duplex (i.e., hemimethylated) (Fig. 4A, diagram 8) (437–439). In the experimental setup, the *dam*-methylated donor DNA is passed on to a *dam*-null recipient strain that has lost the ability to methylate the 5′ GATC binding site of SeqA. After this transfer, the methylated ssDNA is reconverted to a duplex macromolecule through the synthesis of a complementary (nonmethylated) strand. This hemimethylated dsDNA can then be bound by the fluorescently labeled SeqA expressed in the *dam*-deficient receptor strain (440). In subsequent rounds of replication this partially methylated plasmid gives rise to unmethylated DNA duplexes, while itself permanently remaining in a hemimethylated state. The experimental system therefore enables to distinguish the transferred material from the recipient-produced DNA and to follow its segregation at the single-cell level across several generations by means of time-lapse fluorescence microscopy. Later on, Babic et al. (440) also exploited a FROS-based approach to look at integrative and conjugative elements (ICEs) in *B. subtilis*, verifying ICE delivery in the recipient via focus formation. ICEs reside in the bacterial chromosome but can excise to form a conjugative, double-stranded plasmid that can integrate in the recipient genome (441–445). To corroborate their observation that these mobile elements also spread throughout septated cell chains while only a single recipient cell directly mates with the donor, Babic et al. (440) constructed a recipient population that carried a conditional SsrA protein degradation tag (30, 446) linked to GFP. This tag is derived from a natural prokaryotic process called *trans*-translation, whereby stalled ribosomes are rescued by translationally adding the SsrA tag to the truncated polypeptides via tmRNA. The SsrA peptide will target the modified peptide to the protein degradation machinery, thereby ensuring protein quality control and preventing accumulation of aberrant and incomplete proteins in the cell (447). Thus, by adding the gene encoding SspB (a protein that degrades SsrA-tagged proteins) to the ICE module, they were able to see that the diffusive fluorescent signal not only disappeared in the initial transconjugant due to protein degradation but also turned dark in all the other cells of the same chain, confirming the spread of ICEs.

More recently, the SeqA strategy found applications in a variety of other horizontal gene transfer events. For example, Shao et al. (448) adopted this technique to monitor the movement dynamics of phage DNA inside a bacterial host cell and found that λ phage probes the intracellular environment via two distinct modes: (i) a localized motion, keeping the fluorescent SeqA protein/phage DNA complex confined close to the phage injection site, and (ii) an active motion that spans the entire cell. The preference for one mode or the other was not dependent on the eventual fate of the phage DNA but clearly influenced by the location of λ DNA injection. When the entry point of the DNA into the cell is within the quarter-cell to polar region, the phage material prefers to exhibit a localized motion around the injection site. However, when the entry point is located more to the midcell region, particle motion spans the whole cell volume. A possible explanation for this differential locomotion is the preference of λ phage DNA for the quarter-cell to pole region as workspace for phage replication, packaging, or integration into the host chromosome (448). In short, DNA injected into other regions of the cell has to travel longer distances to find this preferred workspace regardless of the infection pathway that is followed. To achieve entry point and motion labeling, Shao et al. (448) labeled the phage particle via a fluorescent fusion to a capsid protein and detected the injected DNA via SeqA labeling as described above. Unlike for bacterial DNA, SeqA is able to bind λ phage DNA in both a fully methylated and hemimethylated state with similar efficiency and affinity (449, 450). When phage progeny that is formed in a *dam*-proficient strain infects a methylation-deficient host strain that constitutively expresses SeqA-ECFP, fluorescent foci will be directly formed upon the injection of the methylated dsDNA phage DNA. Replication of this DNA in the *dam*-deficient strain will produce only two hemimethylated DNA duplexes that can be monitored over time, as further phage replication will lead to unmethylated double-stranded molecules blinded from SeqA recognition. In a follow-up study, the same group used both the SeqA labeling and FROS approaches to deepen the knowledge on the complexities of the lysis-lysogeny decision-making by monitoring the DNA movements of both the phage and the host during this process (451). Furthermore, similar approaches can be used to monitor the DNA degradation of horizontally transferred DNA and real-time CRISPR-Cas phage degradation (435, 452). Besides using the above-described labeling strategies, phage infection and lysogeny dynamics can be visualized by *parS*-ParB (402, 405, 453), FROS (454), transcriptional (455), or dye labeling (456, 457) methods.

Despite the significant role transposable elements (TEs) play on genome plasticity (458), little is known on their single-cell dynamics. Therefore, Kim et al. (459) recently developed an experimental system that uses fluorescent reporters and an interrupted promoter to directly observe and quantify single TE excision events in real-time. Their system consists of an N-terminally Venus-labeled transposase flanked by imperfect palindromic sequences forming the cognate cleavage sites. Conditionally controlling the expression of the transposase enables to simplify TE excision dynamics and look at TE excision probabilities as a function of the intracellular transposase concentration. As the TE is removed upon excision, the previously interrupted promoter will reconstitute its −10 and −35 promoter sequences, leading to constitutive expression of a blue mCerulean3 reporter. By comparing the intensity of the yellow (i.e., number of transposase molecules) and blue fluorescent signal in single cells titrated over a wide range of transposase inducer, it was for the first time possible to determine an *in vivo* excision response function to transposase concentration.

Lighting up the transcriptome. The early view of the bacterial cell as an uncompartmentalized and unstructured environment led to a focus on the temporal dimension of RNA expression, thereby neglecting the possible spatial localization of some of these molecules in the cytoplasm (460). However, recognizing the intricate intracellular organization within bacteria (5) and the importance of RNA localization in eukaryotes (461, 462) gradually increased interest in their spatial patterns. From then on, new strategies and tools have been developed to allow *in vivo* visualization of single RNA molecules within these micrometer-sized organisms, showing the presence of post-transcriptional localization patterns for at least some RNA species (70, 463–467). Much still needs to be uncovered, but it has become apparent that spatial organization of RNA and their dedicated cellular machineries has a profound impact on gene expression and cellular regulation, as is seen in eukaryotes. Although the driving mechanisms still remain elusive, all these recent findings further underscore the functional compartmentalization of the bacterial cell without the need for physical separators (463).

In the following section, techniques will be discussed that allow for direct RNA visualization in single cells with an emphasis on those techniques that support real-time dynamic tracking. The very low copy numbers in which some bacterial mRNAs are present make their visualization extra challenging and impede the use of certain techniques used in eukaryotic model systems (468). Currently, two main methods exist for direct visualization of the short-lived RNA molecules: (i) fixed cell imaging using *in situ* hybridization, and (ii) live-cell microscopy using aptamer- or protein-based RNA binding beacons (Fig. 3B). Only the latter approach supports real-time, *in vivo* measurements of RNA dynamics in the bacterial cytoplasm.

(i) Fluorescence *in situ* hybridization. Fluorescence *in situ* hybridization (FISH) is the most widely used method for RNA visualization in both eukaryotic and prokaryotic research. It uses exogenously added, complementary oligonucleotide probes labeled with fluorophores to light up the RNA molecules of interest in fixed and permeabilized cells (Fig. 4Bi) (469). Over the years, this method has been vastly improved to resolve major concerns regarding the probes such as delivery efficiency, nuclease-sensitivity and nonspecific background of the signal (463, 469–476).

Montero Llopis et al. (463) were among the first to hint toward a clear spatial organization of mature mRNA. With their improved quantitative FISH protocol, these researchers showed that mRNAs in the model organism *Caulobacter crescentus* tend to stay close to their nascent transcription site during their entire lifetime. Instead of targeting the FISH probe directly to a native mRNA molecule, these researchers devised a new method to improve the signal-to-noise ratio as well as the sensitivity, while at the same time enabling quantitative analysis. This was achieved by transcriptionally fusing 120 noncoding tandem LacI operator sequences (*lacO*$_{120}$) to the gene of interest, enabling a better and brighter visualization of the targeted mRNA (Fig. 4Bii) (392, 463). This specific array was added to the 3′ prime of the mRNA target closely after the stop codon where it is expected to have minimal effects on the stability and the translation of the molecule (463, 477). Upon expression of these tagged mRNA molecules from their native locus, a signal amplification is obtained by using a high-affinity single locked nucleic acid (LNA) probe targeting the *lacO* sequence (478).

(ii) RNA dynamics in living cells. Most of the drawbacks associated with these probe hybridization techniques are avoided in live-cell RNA imaging techniques. The majority of these real-time techniques require no addition of exogenous reagents, allowing for native physiological conditions during the experiment.

A widely used strategy for *in vivo*, real-time visualization of RNA molecules uses a fluorescently labeled RNA bacteriophage MS2 coat protein (here referred to as MS2) (Fig. 4Biii) (479) and was adapted for applications in bacteria by Golding and Cox (480). This system is based on the highly specific interaction between a tandem MS2 dimer (MS2d) and its 19-bp operator stem-loop of which palindromic repeats are transcriptionally linked to the 3′ untranslated region (UTR) of the target RNA. To increase the stability of this array, Golding and Cox (480) inserted random sequences between each of the 96 binding sites, thereby shortening the runs of perfect homology and avoiding spontaneous recombination events at the DNA level. The long array of stem-loops improved the signal-to-noise ratio, enabling for single molecule detection and longer time-lapse experiments in their setup. Later on, Nevo-Dinur et al. (464) further refined the system by reducing the stem-loop array to six tandem repeats, which turned out to be sufficient for spatial and temporal tracking of mRNA molecules. With this improved strategy, Nevo-Dinur et al. (464) showed that certain mRNA molecules in *E. coli* are targeted to the location where their protein counterpart has its functionality (464), underscoring an apparent difference in intracellular environment with *C. crescentus* (463) (see "Fluorescence *in situ* hybridization"). Recently, this difference in macromolecule mobility between species as seen in the comparison between mRNA movement in *E. coli* and *C. crescentus* was addressed by Gray et al. (382). These researchers proved that the nucleocytoplasmic (nucleoid area/cell area) ratio impacts the mobility and biophysical properties in the bacterial cytosol. Higher nucleocytoplasmic ratios, like those found in *C. crescentus*, minimize the DNA-free space in the cytoplasm, in turn limiting the movement of larger macromolecules such as polysomes (mRNA combined with ribosomes). Conversely, the lower ratio for *E. coli* supports a higher mobility for ribosome-bound transcripts since it is easier to escape from the DNA meshwork. However, these cognate mRNA localization patterns remain heavily debated and poorly understood (465, 467).

The high level of background fluorescence stemming from free-floating MS2 significantly decreases the sensitivity of this method. A solution to this problem was found in Bimolecular Fluorescence Complementation (BiFC) [see "(Auto)fluorescent proteins" above], wherein two nonfluorescent fragments of a "split" FP are brought into close proximity via the interaction of their fusion partners to reconstitute the autofluorescent protein and enable the complex to regain the ability to fluoresce (67, 69). Using this strategy, Broude and coworkers (70) built an RNA reporter system that exploits a spliced eukaryotic initiation factor 4A (eIF4A; 29 kDa) and links each part to one half of a split EGFP fragment via a flexible linker (Fig. 4Biv). The split eIF4A reporter can only form a reconstituted fluorescent complex when it binds to its cognate stem-loop. This 58-nucleotide binding site is fused to the RNA target and ensures high-affinity binding to the specific RNA molecules of interest (70, 481). Although this need for fluorescence reconstitution on the RNA stem-loop improves the signal-to-noise ratio, it also decreases the response time compared to other methods since chromophore maturation only starts upon reconstitution. Furthermore, a second drawback to the technique is that it cannot be excluded that the GFP-eIF4A complexes formed on the stem-loops persist after the disappearance of the RNA (70).

All of the above *in vivo* techniques require genetic alterations of the target RNA, potentially leading to changes in its normal kinetics and behavior. Although these tags are usually placed in the 3′ UTR of mRNA to minimize potential interference, turnover kinetics of the RNA could still change through a protective effect of the ribonucleoprotein complex that is formed upon binding of the fluorescent reporter (460, 477). To address these problems and downplay the amount of interference in the biological system, the eIF4A method was further modified by combining BiFC with a split aptamer approach (Fig. 4Bv). In this approach, a targeting aptamer (i.e., oligonucleotide that can bind a specific target RNA) is used that consists of two modules connected with an internal flexible linker. The first module of this aptamer is responsible for the RNA targeting, and the second module forms the eIF4A recognition stem-loop. It is this recognition stem-loop in the aptamer that is split through the insertion of the flexible linker and which can only reconstitute when bound to the specific RNA molecule. Only then the stem-loop becomes available and serves as a landing site for the "split eIF4A" to reconstitute its fluorescence (482, 483). This new technique combines the flexibility and sensitivity of hybridization-based oligonucleotide probes with the low background fluorescence of BiFC to allow detection of unmodified RNAs using only endogenously expressed reagents.

Bacterial Cytoplasm

The cytoplasm comprises the building blocks necessary for bacterial life and provides a compartment shielded from the outside environment where vital functions and reactions can be maintained. It is an aqueous but viscous setting, crowded with molecules ranging from subnanometer (ions and metabolites) to micrometer (protein filaments and chromosomes) sizes (484–486). Since bacteria carry no known cytoskeletal motor proteins, molecular transport and cytoplasmic mixing in the micrometer-sized cytoplasmic space is assumed to primarily depend on diffusion. This diffusion sets the rate at which molecular interactions can occur, and it is thus deterministic for the biological reaction speed and cell physiology. Furthermore, homogeneous distribution of cellular components in the cytoplasm is essential for cell proliferation by ensuring that components are evenly distributed to both daughter siblings. As the sole true bacterial compartment, separated from its surroundings by a semipermeable membrane, the bacterial cytoplasm sustains the necessary gradients required for growth (487).

The bacterial cytoplasmic volume: probing its properties and its use as physiological reporter. Since most cellular processes occur in the cytoplasm, it is logical to assume that the specific physical nature of this fluid space has an enormous impact on cell physiology and intracellular dynamics. However, for a long time there was no unifying view on how this compartmentalized liquid functioned, and many conflicting reports on the diffusive motions in the cytoplasm were published (251, 488–491). A better understanding on how diffusion of molecules is influenced by the properties of the cytoplasm came from the group of Jacobs-Wagner (486). To characterize the internal physical properties of bacteria, these researchers used single-particle tracking of intracellular structures to show that the cytoplasmic fluid displays properties distinctive of colloidal glasses (492, 493), thereby fundamentally changing the view on the bacterial cytoplasm (486). Essentially, this means that for small particles, the cytoplasm behaves as a liquid, while at increasing particle sizes, the cytoplasm is perceived as a glass-forming liquid that approaches the glass transition (494). For the latter situation, the internal fluid mirrors a liquid, yet the mobility in this suspension is slow enough that is can be considered essentially frozen. To prove this size-dependent perception of the "cytoplasmic state," Parry et al. (486) developed a novel probe based on a truncated variant of the avian reovirus (nonstructural) μNS protein that is completely devoid of specific interactions with other endogenous cellular components and used it to sample the state of the cytoplasm. This μNS probe functions as a self-assembling protein forming a globular particle in the cytoplasm, even when fused to GFP (486, 495, 496). By varying the inducer concentration and induction times for the expression of this inert GFP-μNS chimera, particles of different fluorescence intensities (and thus sizes) could be formed intracellularly. It became apparent that the fluorescence intensity of this GFP-μNS particle was inversely correlated with its mobility in a manner disproportional compared to "normal diffusion," pointing out the rise of extra constraints with increasing particle size. Remarkably, these glassy dynamics and constraints are partially overcome by changes in the metabolic activity of the bacterial cell. Parry et al. (486) suggest from their experimental data that the bacterial cytoplasm is “fluidized” by an increased cellular metabolism enhancing the motion of cytoplasmic components and that this effect increases with the component size. Later, a similar energy dependence of intracellular movement was probed as a proxy for individual inactivation and resuscitation dynamics by using a synthetic CI-based protein aggregate in stressed populations of *E. coli* (497).

It is hypothesized that this glass-like state is partially caused by the high macromolecular crowding in the bacterial cytoplasm (486), which implies that crowding is an important parameter influencing biochemical reactions and bacterial proliferation. Recently, a novel tool was developed to directly measure macromolecular crowding via a quantitative temporal read-out using a genetically encoded FRET-based sensor (498) (see “Förster resonance energy transfer”). This sensor contains a flexible domain that changes conformation in response to various degrees of crowding, altering the distance between the mCerulean and mCitrine FRET pair, positioned at the N and C termini, respectively. Boersma et al. (498) validated this sensor in a FRET ratio setup using scanning confocal microscopy and could show that macromolecular crowding changes in live *E. coli* cells exposed to osmotic stress (498, 499).

Besides its role as intracellular reaction fluid and keeper of cellular homeostasis, the cytoplasm can also contribute to intercellular communication. By forming a direct channel or nanotube between two cells, a route can be formed for cytoplasmic communication, exchanging protein factors and plasmids from a donor to an acceptor cell (500). Dubey and Ben-Yehuda (500) were able to visualize this phenomenon in two different ways: (i) by using a cytoplasmic fluorescent protein to see the interaction between a GFP$^+$ and a GFP$^-$ population and (ii) by using the cytoplasmic fluorophore calcein. Calcein is a small acetoxymethylester-derivative that in its native state is sufficiently hydrophobic to transverse the cell membrane but is intracellularly transformed into a cytoplasmically locked fluorophore after hydrolysis by an endogenous esterase (501). In both approaches, a transfer of cytoplasmic volume to naive, recipient cells confirmed the exchange of material, even between evolutionary distant bacterial species. More recently, the Ben-Yehuda group further elaborated on this phenomenon, showing that these nanotubes enable nutrient extraction from other bacteria (502), as well as from infected eukaryotic cells (503). By also providing molecular insight into the apparatus that provides a platform for nanotube biogenesis, the same group was recently able to underscore that nanotubes are a ubiquitous organelle across the bacterial kingdom supporting intercellular molecular trade (504).

The cytoplasmic volume can also be exploited as a reporter system to probe individual growth rates over time. One such approach that uses this compartment as a molecular clock bases itself on the spontaneously changing spectral characteristics of DsRed-E5 timer fluorescent proteins [see “(Auto)fluorescent proteins”] to visualize the wide phenotypic variation of *Salmonella* during infection of eukaryotic host cells (505). Capitalizing on the high resilience of DsRed variants to proteolysis (506), the time-dependent shift in the emission spectrum of the fluorescent timer (FT) protein allowed the investigators to discriminate between the slow-proliferating cells emitting signal in the red side of the spectrum and fast-dividing green cells, in which continued production of fresh (green) FT proteins overpowers the diluted-out older (red) DsRed-E5 molecules (505). A similar concept was recently used to enrich a metabolism-wide CRISPRi knockdown *E. coli* library for slow-growing cells via flow cytometry and cell sorting to retain only the red-shifted cells (507). An important consideration that has to be made in timer-based growth rate measurements is that only changes over longer time periods can be detected, whereas short-term fluctuations will remain under the radar. Furthermore, for *in vivo* infection dynamics oxygen can play an important role as it is needed for the maturation of the chromophore. This presents an important downside to the system, especially in inhomogeneous oxygenated body cavities where green timer protein might reflect fast growth, low oxygen tension (508), or a combination of these two parameters. The use of this system *in vivo* is thus still limited to homogeneously oxygenated tissues such as the spleen (505) until FT proteins can be constructed with lower oxygen dependence sensitivity.

A similar method that enables monitoring single-cell proliferation dynamics in host cells is based on the concept of fluorescence dilution (509, 510). Rather than relying on a color change, these systems use the cytoplasmic dilution that occurs during bacterial cell division to create an informative readout. Here, a dual fluorescence reporter plasmid is in place, with one fluorescent protein being constitutively expressed, whereas a second reporter is only expressed upon induction. Bacterial divisions can then be measured as the dilution rate of the pulse-induced fluorescent protein compared to the constant signal of the constitutively reporter. Alternatively, the temporal range of measurement can be extended by using two different inducible promoters and sequentially removing the inducers (510).

Likewise, growth resumption from stationary phase can be visualized with a two-component fluorescent system (511). This system allows for a single-cell level investigation of the correlation between the timing of entry into the stationary phase, as well as growth resumption in the following period of cell proliferation. Cells carrying two plasmids with different fluorescent reporters (e.g., Crimson and GFP) are initially grown to stationary phase, where the induction of Crimson FP expression is halted. Upon the addition of a new carbon source, GFP expression is induced in cells that resume protein synthesis, while at the same time Crimson is diluted out by the following cell division. In a variation on this theme, the timing of the Crimson induction can be changed to the transition period from growth to stationary phase, leading to a bifurcation of the population: one population will express Crimson FP since it was still metabolically active at the time of induction, while a second population will show no Crimson fluorescence since their metabolism was already halted leaving them unable to respond to the inducer. Jõers and Tenson (511) noted a "last in, first out" rule under certain growth conditions: the last ones to shut down their metabolism at the onset of stationary phase are the first to resume proliferation in response to nutrients. More recently, this approach was used in combination with flow cytometry to show that muropeptides stimulate growth resumption in stationary *E. coli* cells (512).

Visually gauging the physiological state of individual cells. Every bacterium is programmed to safeguard its homeostasis by keeping a myriad of different physiologic features such as intracellular pH, ATP level and redox balance, in check. An important shortcoming in current live-cell biology is the lack of insights into the homeostasis of individual cells within a (bacterial) population. While metabolomics technologies are skyrocketing and addressing a decisive layer of complexity in bacterial physiology (513–518), they are typically restricted to ensemble measurements on bulk populations and therefore blind to intercellular differences and heterogeneity. Over the past few years, however, it has become possible to (semi-)quantitatively acquire information on the physiological state of individuals cells, mainly by using ratiometric-based fluorophores (267–269, 519).

An overview of the current state of the art on these biosensors can be found in a recent review by Jin Zhang's group (520). Since the whole field of fluorescent biosensors is mainly focused on eukaryotic applications, most applications require optimization for prokaryotic use. Below, we discuss different examples of these applications and show how they enable physiological and metabolic readouts in bacterial cells. It should be noted that some of these approaches still suffer from limitations and artifacts, especially on the single-cell level. For batch culture use, however, several of these biosensors have already been successfully applied (521–524).

(i) Intracellular pH. How the bacterial pH changes in response to acid stress is a well-debated topic that requires a thorough understanding as pH stress is often encountered throughout bacterial life and has a determining influence on protein stability and intracellular reaction rates.

A widely established method for monitoring pH homeostasis is based on a pH-sensitive variant of GFP named pHluorin (pronounced as "fluorin") (519, 525). This genetically encoded ratiometric probe exploits the bimodal excitation spectrum of wild-type GFP [see "(Auto)fluorescent proteins"] (74–76) to support continuous and noninvasive measurements of the intracellular pH in single bacteria. The original design of pHluorin by Miesenböck et al. (525) incorporated a number of amino-acid substitutions in GFP to obtain a pH-dependent switching between the different protonation states of Tyr^{66} in the chromophore. With an increasing acidity, the ratiometric pHluorin displays a dose-dependent decrease in the excitation at 395 nm (protonated Tyr^{66}) with a concomitant increase in the excitation at 475 nm (deprotonated Tyr^{66}) measured at the emission wavelength of 535 nm (526). This probe was shown to work well in both Gram-negative and Gram-positive bacteria with single-cell resolution (519, 527). However, very recently Chakraborty et al. (270) addressed the limitations of this probe for pH measurements on the single-cell level casting doubt on its validity.

This same research group proposed two other, though non-genetically encoded, methods to measure intracellular pH in real-time with single-cell precision (268, 270). Chakraborty et al. (270) compared the commonly used pHluorin to their proposed I-Switch and BCECF-AM dye approaches that are discussed below. For both of their systems, they obtained results significantly differing from experiments on acid stress carried out with pHluorin. In the I-Switch approach, a DNA-based FRET biosensor (I-Switch) is used to measure the cytoplasmic pH (268). This novel biosensor undergoes non-Watson-Crick base pairing in the presence of an excess of protons, leading to FRET activation (268, 528, 529). The I-Switch nanomachine consists of two DNA duplexes connected to each other by a flexible hinge and bearing cytosine-rich single-stranded overhangs at the duplex termini labeled with Alexa-488 and Alexa-647 dyes. These overhangs will unite to form an I-motive (530) upon protonation, thus adopting a "closed" state at acidic pH leading to an increased FRET signal. At more neutral pHs, this I-motif dissociates and will push the fragment toward an "open" conformation due to entropy and electrostatic repulsion (529), lowering the FRET readout. The downsides of this probe are the need for electroporation to get the FRET sensor inside the cytoplasmic space and the inability to measure basic pH due to its specific response mechanism.

The fluorescent BCECF-AM [2′,7′-*bis*-(2-carboxyethyl)-5-(and-6)-carboxyfluorescein, acetoxymethyl ester] dye (268, 270, 531–533) was originally developed by Roger Tsien and coworkers in 1982 and is a commonly used intracellular pH indicator (534, 535). This specific dye can easily permeate the bacterial membrane and is activated by intracellular esterases once it reaches the cytoplasm leading to a trapped, active fluorescent form (534, 536). Inside the cells, these activated molecules will then change their emission ratio depending on their protonation state, keeping the response to 440-nm light constant, while pH-dependently altering the 525-nm emission signal after excitation at 488 nm (537). The limited pH range of BCECF (pH 6 to 7; compared to pH 5.1 to 7.1 for I-Switch and pH 5.5 to 8.5 for pHluorin) and the need for cellular incubation in dye solution, followed by a mandatory washing step, make this approach less straightforward than the pHluorin method. Another downside is that some of the intracellular BCECF will leak to the outside and can possibly interfere with the measurements. However, this kind of problem can be easily solved upon continuous perfusion in microfluidics setups (535, 538). Other pH dyes are also available, but their ability to support single-cell measurements remains unclear (535, 539, 540).

(ii) Redox balance. Recently, Abraham et al. (267) reported the development of a single-cell sensor for bacteria that is able to read out the intracellular redox (reduction/oxidation) state, something that is considered as an important proxy of the overall metabolic state of the cell (541, 542). This probe carries two fluorescent proteins (i.e., Cerulean and Citrine, linked through a biotinylation domain) that are both modified to have only one reactive cysteine residue on the protein surface, closely located to the FP chromophore. In an oxidized state, the FRET pair will be in closer proximity of each other through the formation of a labile disulfide bond between the donor (Cerulean) and the acceptor (Citrine), resulting in a higher FRET efficiency. In reducing environments, the FRET signal will be diminished as a consequence of the increased distance between the interacting FPs. As such, the buildup of this probe confers a large dynamic measuring range to the sensor (267).

Around the same time, a second system based on a redox-sensitive GFP was also implemented to nondisruptively measure real-time fluctuations in the intrabacterial redox environment and even enabled monitoring these dynamics in bacteria caught inside macrophages (543, 544). In this study, the second generation of reduction-oxidation-sensitive GFP (roGFP2) was adopted to read out the redox balance via a ratiometric output in line with the intracellular concentrations of the two spectrally different isoforms formed (i.e., roGFP2$_{ox}$ and roGFP2$_{red}$) (543, 545, 546).

Other fluorescent tools for redox measurements have been developed, but are not yet all transferred to applications in bacterial model systems or have been tested for single-cell real-time measurements (541, 542, 547–549).

(iii) Single-cell visualization of ATP levels. ATP is the primary energy currency in the cell and fulfills a key role in bacterial physiology and energy management. Conventional methods to measure the ATP levels within bacteria only provide ensemble measurements and often require cell lysis and normalization operations (550–552). This type of approach does not allow differentiating individual cells within a population based on their energy level, nor does it support a detailed, single-cell investigation of energy level fluctuations in different (stressful) conditions.

Some tools are currently available to track ATP levels in bacteria with single-cell resolution for extended time periods, although these approaches still have some drawbacks. The best-described example of real-time *in vivo* ATP measurements was published a few years ago by Maglica et al. (269). These researchers combined microfluidics and time-lapse microscopy to see how exposure to antibiotics changed the mycobacterial energy metabolism and how energy levels during the treatment affected bacterial viability upon removal of the antibacterial component. To retrieve dynamic information on the energy status of single cells, FRET sensors originally developed for real-time ATP measurements in eukaryotic cells were incorporated in the genetic blueprint of *Mycobacterium* (269, 553, 554). In these ATeam biosensors, a donor/acceptor (CFP/YFP) pair flanks a high-affinity and high-specificity ATP-binding domain that is composed of a modified epsilon (ε) subunit of the *Bacillus subtilis* F_0F_1 ATP synthase (554). Recently, Yaginuma et al. (555) presented a new endogenous ratiometric fluorescent ATP indicator called "QUEEN" (quantitative evaluator of cellular energy) as a successor for their ATeam FRET-based ATP biosensor (554). This novel construct is composed of a single circularly permuted enhanced green fluorescent protein inserted between two α-helices of a catalytically inactive bacterial F_0F_1 ATP synthase ε subunit, but it has so far only been used for dynamic measurements in yeast (556).

A third type of ATP sensor actually measures the ATP/ADP ratio and was built by combining a bacterial regulatory protein (Glnk1) from *Methanococcus jannaschii* with a circularly permuted variant of mVenus (557). Under physiological conditions, the sensor is always saturated and changes in the ATP/ADP ratio can be measured from the fluorescent signal as both molecules compete for the same binding site but influence the fluorescent fluctuations in a different manner. Recently, Wilmaerts et al. (524) utilized this sensor to look at the cellular energy ratio in *Escherichia coli* on the population level.

(iv) c-di-GMP, a secondary messenger molecule. Cyclic di-GMP (c-di-GMP) is a bacterial second messenger synthesized from two GTP molecules by diguanylate cyclases and degraded through the work of c-di-GMP specific phosphodiesterases (PDEs). The fine-tuned c-di-GMP balance controls numerous cellular processes such as virulence, motility, surface adherence, and antibiotic resistance via a direct interaction with different transcriptional factors, enzymes, adaptor proteins, and riboswitches (558–561). The tight spatiotemporal and concentration-dependent control of c-di-GMP during cell division and cell differentiation further underscores the critical need for corresponding single-cell biosensors to obtain more insight into the complex physiological responses triggered by these small molecules and their respective effectors (266, 562–564).

In order to monitor this important intracellular molecule, Christen et al. (266) developed a FRET-based sensor that can visualize c-di-GMP concentrations in single cells on a relevant timescale and with a wide dynamic range. These researchers found that a wide dynamic range in the FRET signal could be achieved by using the *Salmonella* Typhimurium YcgR, a PilZ domain protein, as a linker between a CFP and YFP protein pair. Besides direct measurements of individual cellular c-di-GMP dynamics, this sensor also supported a high-throughput, flow cytometry-assisted screening procedure in search of chemical molecules modulating the free concentrations of this signal molecule (266, 565). More recently, the Miller group (564) optimized this biosensor for measurements of c-di-GMP concentrations in single bacteria within host cells by swapping the original CFP-YFP pair with the brighter teal fluorescent protein (mTFP) (566) and kusabira orange variant 2 (mKO2) (567) to overcome the high blue-range background fluorescence of eukaryotic cells (116, 564, 568). Using this approach, Petersen et al. (564) were able to pinpoint three sensor PDEs that are critical for maintaining a low c-di-GMP concentration after phagocytosis, thereby promoting the survival and virulence of the bacterial invaders.

A new type of sensor that is appearing in the field of second messenger molecule measurements utilizes RNA-aptamers as recognition and reporter modules. RNA-based biosensors have long been an underdeveloped tool despite the natural appearance of riboswitches and other similar RNA structures able to selectively recognize small molecules *in vivo* (569). These RNA-based aptamers are engineered in such a way that the structural changes induced by the binding of a specific target molecule enable the activation of an exogenous fluorogen, eventually leading to a visual output signal (570). While the first aptamer setups developed by Roger Tsien and coworkers used the toxic malachite green dye to fluorescently light up the sensor (571), newer aptamer modules such as Spinach, Broccoli, and Mango solve this problem by using nontoxic spectral and diverse fluorophores (572–575). Aptamer biosensors can easily be constructed for all types of intracellular target molecules and have the advantage of being able to work completely anaerobic (576). However, work is still under way to further improve the first generations of this new type of biosensor (576–579).

One of the downsides to the above-described aptamer-based sensors is that they do not allow a ratiometric readout, making the signal prone to concentration variations of the sensor itself. Apta-FRET (RNA aptamer-based FRET) could overcome these limitations and pave the way to new and better applications of these genetically encoded apta-biosensors (580). In fact, Jepsen et al. (580) were able to demonstrate that a Spinach and Mango aptamer module (with modified DFHBI and TO3-biotin as respective FRET pair fluorophores) engineered onto a single-stranded RNA origami scaffold could be used to create a dynamic RNA sensor for ratiometric readouts in living *E. coli* (580). By incorporating molecular recognition modules in these apta-FRET systems, conformational changes of the FRET structure (and the concomitant change in signal) can be used to gauge cellular levels of specific small molecules.

Transcription

Transcription presents the first step in the gene expression cascade and sits at the heart of bacterial success since it determines how swiftly these single-celled organisms respond to environmental perturbations. Even before the conception of the central "DNA over RNA to protein" dogma (581, 582), bacterial transcription and its mechanism were already subject of ongoing research eventually culminating in the Jacob-Monod transcription model (583). This model established a framework in which promoters control gene expression and transcription factors (TFs) fine-tune the accessibility of these sequences by site-specific binding to sequences or structures in the chromosome. Later, it became apparent that this model represented a too straightforward order of transcription leaving out a myriad of other factors that make the process less tidy and ideal (584).

The process of transcription starts with the recognition of the promoter sequence by the DNA-dependent RNA polymerase (RNAP) (584). Unlike the situation in eukaryotes, where transcription is driven by three different RNAPs, bacteria depend on a single type of this multisubunit complex (β-subunit, β'-subunit, two α-subunits, and the small ω-subunit) to produce different types of RNA molecules from sites all over the nucleoid (320, 585). The RNAP core enzyme can autonomously support RNA synthesis but relies on its association with sigma (σ) factors to direct the holoenzyme (i.e., RNAP and σ) to the correct (subset of) promoters and initiate transcription by orchestrating the formation of an “open complex” at the promoter site (586–590).

Probing sigma factor activity. While the majority of bacterial promoters are controlled by the housekeeping factor, most bacteria have one or more alternative sigma factors able to rewire the baseline gene expression program to tailor-fit specific situations (588, 591, 592). Both types of sigma factors compete for the same binding site on the limited amount of RNAP molecules in the cell and significantly differ in their action, with the alternative sigma factors producing a much narrower and more controlled transcriptional profile (591, 593–604).

The activity of sigma factors is determined by a complex interplay of several mechanisms, such as sequestration by anti-σ factors, intersigma competition, σ concentration, and proteolytic turnover. This makes that transcriptional fusions to specific promoters provide more valuable information on σ action than a direct visualization of the factor itself (589, 592, 605–610). In essence, this means that sigma factor activity is best quantified as the rate of fluorescent protein production stemming from a specific σ-controlled promoter, taking into account photobleaching and growth dilution effects (611–615). It is this instantaneous activity that reflects the rate of (i) free sigma factor association with the available core RNAP and (ii) initiation of transcription at the selected promoters (611, 612, 614, 616).

By constructing *B. subtilis* reporter strains carrying fluorescent protein genes under the general stress sigma factor (σ^B), Locke et al. (612) demonstrated that the activation of this response goes via discrete, stochastic σ^B pulses and underscored that this behavior stems from processes such as the interaction of negative (i.e., anti-sigma factor) and positive-feedback loops (i.e., sigma factor expression). More recently, Park et al. (613) found that in certain steady-state stress conditions, up to seven of the 17 alternative sigma factors of *B. subtilis* (592) generate a similar heterogeneous and pulsatile expression pattern, contrasting the homogeneous activity of the housekeeping σ^A factor. This seems to suggest that the complex, stochastic σ-activity dynamics that were first seen by Locke et al. (612) might be a more general mode of alternative sigma factor activation.

Based on these observations, Park et al. (613) further explored whether RNAP sharing by different sigma factors could be more dynamic in time then assumed. Generally, it was thought that regulators competing for a limited amount of core enzymes (as is the case for σ-factors) occupy an approximate constant fraction of that enzyme under steady-state conditions. However, by performing a pairwise analysis of different combinations of σ-factors, Park et al. (613) noticed that sigma factors rarely pulse simultaneously and are often anticorrelated in their activity. According to their mathematical framework, this indicates that the different alternative sigma factors take turns on utilizing the core resource, a concept known as time sharing. In the specific case of imperfect time-sharing dynamics, as is the case for the σ-RNAP interaction, inputs to the systems could effectively regulate the fraction of time that cells spend in various sigma factor activation states. Basically, this means that at any given moment in time only one or a few sigma factors are interacting with the RNAP core.

Single-molecule RNA polymerase localization. With the rise of super-resolution and single-molecule *in vivo* imaging methods over the past decade, the cellular localization and distribution patterns of RNAPs under diverse environmental conditions have received more attention (298, 299). These advanced microscopy techniques enable the gathering of high-resolution, quantitative data on the transcription system, making them well suited to test the extent and the validity of specific mechanistic hypotheses (299, 310, 313, 320, 325, 617–620).

Since bacteria carry only a single type of RNAP essential for cell viability, it is imperative that approaches for direct visualization of this multisubunit complex do not affect its native functionality or localization pattern. For both *B. subtilis* (621) and *E. coli* (622), it was shown early on that a C-terminal GFP fusion to the β'-subunit (*rpoC*) did not disrupt the normal growth pattern of the bacteria and allowed investigators to determine RNAP localization in both fixed (622) and nonfixed cells (621). It was quickly appreciated that the behavior of the RNAP in the cytoplasm was extremely sensitive to changing growth conditions with large rearrangements in RNAP distributions in response to environmental fluctuations. As long as growth conditions remain poor, polymerase molecules distribute fairly homogenously over the nucleoid, whereas under nutrient-rich growth conditions, "RNAP foci" or transcription factories emerge in a typical dual-lobed spatial pattern coarsely mimicking the DNA outlines (Fig. 5A and B) (310, 313, 619, 621–625). Since the majority of cellular RNAP is dedicated to rRNA synthesis in such fast-growing cells (626, 627), it was long assumed that these foci consist of hundreds of RNAP molecules actively performing rRNA transcription in fast growing cells (622, 623, 628, 629).

Despite the efforts of many groups looking into the characteristics and spatial distribution of these RNAP clusters (310, 313, 619, 623, 624), the precise nature of these factories, how they are formed, and their relation to rRNA transcription long remained elusive. To investigate these active transcription centers in more detail, Weng et al. (325) recently combined a photoactivatable *rpoC-PAmCherry* fusion (313, 320, 619) with quantitative super-resolution imaging and perturbation analyses. Since RNAP clusters have been previously linked to sites of rRNA transcription without direct evidence (629), Weng et al. (325) first looked at the degree of colocalization of the transcription factories with nascent or newly synthesized rRNAs in a two-color super-resolution experiment (Fig. 5C). To specifically probe these locations of rRNA transcription activity, Weng et al. (325) targeted the 5′ leader sequence of the 16S precursor rRNA with FISH probes because this region is lost before the incorporation of mature rRNA into the ribosome (630). Since RNAP clusters nearly exclusively colocalize with the rRNA transcriptional activity, it was suggested that the majority of the RNAP foci are indeed active in rRNA synthesis/transcription under rich growth conditions. However, the main drivers for the formation of these transcription factories still remain elusive, but it is believed that still cryptic characteristics of the nucleoid could play a significant role in their organization (325).

Transcription factors. Transcription factors play a pivotal role in redirecting gene expression in response to specific triggers and can either activate or repress transcription, depending on the relative location of their binding site with respect to promoter elements (631). Each TF regulates a set of genes and is evolved to promptly locate its specific binding sites among millions of nonspecific sites on the nucleoid (632, 633). Traditionally, studying these *in vivo* search kinetics was rather difficult since it could only happen indirectly via monitoring of the regulated gene products, either on the population (634) or the single-cell (13, 477, 635–638) level. Again, the rise of nanoscopy imaging enabled direct and quantitative observations of the target search process of DNA-binding factors such as TFs and RNAP (299, 320–322, 324, 330, 618, 639).

The *lac* operon is a well-established and thoroughly understood transcription factor system wherein the LacI repressor binds to different operator sites (O_1, O_2, and O_3) and represses transcription in the absence of its (allo)lactose inducer (640). Over the years, this system has provided the basis for research into TF-mediated dynamics (633, 641–644). As for many DNA-binding proteins, the time needed for LacI to find its cognate binding partners, the *lac* operator sites, turns out to be many times lower than expected if the process was solely driven by three-dimensional diffusion (645). This led to the hypothesis that these observations could be explained by facilitated diffusion, a mechanism where the DNA-binding factor searches for its docking sites through a combination of one-dimensional (1D) sliding along short DNA segments and three-dimensional (3D) diffusion throughout the cytoplasm (632, 646, 647).

The search of LacI for its operator (a 21-bp region) among the millions of base pairs of nonspecific chromosomal DNA in *E. coli* has been extensively studied (633, 642–645,

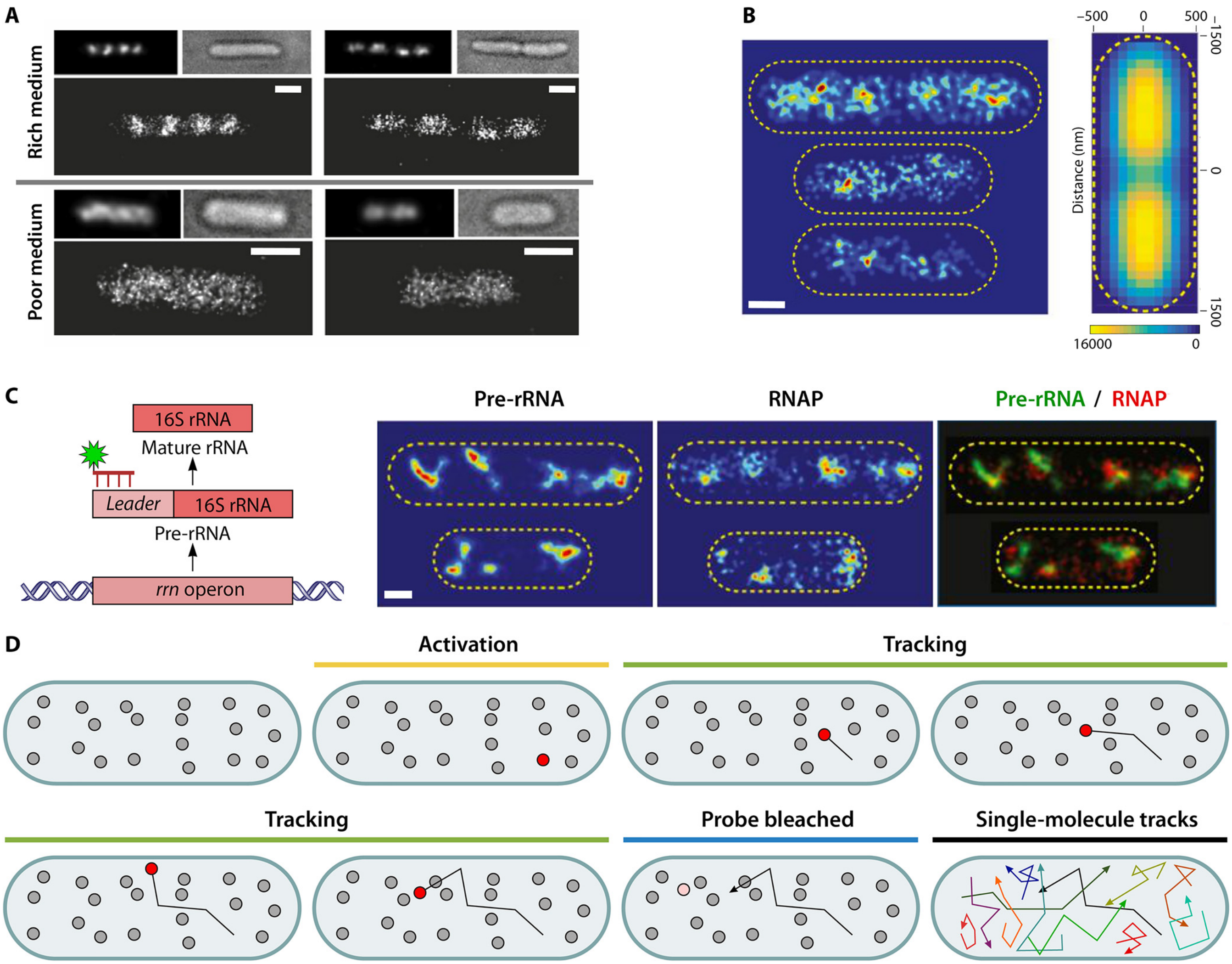

FIG 5 Super-resolution microscopy and single-molecule tracking as tools to unravel the intracellular organization of bacterial transcription. (A) Under nutrient-rich conditions, RNAP is clustered in foci or transcription factories throughout the cell, while under nutrient-poor conditions, the RNAP molecules remain fairly homogenously distributed over the nucleoid (Photos are reproduced from reference 619 with permission of the Biophysical Society.) Scale bar, 0.5 μm. Each image square is built out of a conventional fluorescence (top left image), brightfield image (top right image), and a PALM super-resolution image (large bottom image). (B) In rich medium conditions, these RNAP foci form a typical dual-lobed spatial pattern that coarsely mimics the DNA outlines. The left image shows the localization pattern of all individual RNAP molecules in three representative living *E. coli* cells grown under nutrient-rich medium conditions (blue, low abundance; red, high abundance). The right image shows a two-dimensional, normalized histogram of the RNAP localizations in 664 cells under rich medium growth conditions (Adapted from reference 325 with permission of the National Academy of Sciences, U.S.A.). Scale bar, 0.5 μm. The color bar indicates the number of localization events in each bin; the bin size of the 2D histogram is 100 × 100 nm. (C) RNAP foci almost exclusively colocalize with rRNA transcriptional activity (i.e., with nascent pre-rRNA clusters) in nutrient-rich conditions. (Left) A FISH probe is specifically targeted to the 5′ leader sequence of 16S pre-rRNA, a region that is lost before mature rRNA is incorporated into the ribosomes. (Right) Representative super-resolution images of two cells with, from left to right, the localization pattern of pre-rRNA, the localization pattern for RNAP molecules, and the combined two-color super-resolution image (red, RNAP-PAmCherry; green, pre-rRNA FISH) (Adapted from reference 325 with permission of the National Academy of Sciences, U.S.A.). Scale bar, 0.5 μm. (D) Schematic representation of "tracking PALM" as a method to study intracellular mobility of proteins such as RNAP and transcription factors at native (and higher) copy numbers. The protein factor of interest is labeled with a photoactivatable fluorescent probe to allow activation of single molecules in each activation round. The activated, fluorescently labeled target is subsequently tracked as a single particle until it eventually bleaches. For this cycle of activation, tracking and bleaching can be continued until all photoactivatable probes are bleached, giving rise to a collection of individual tracks. Original figure indexations and scale bars were either removed or masked without altering the content of the images. New indexations and scales were added to provide consistency throughout the figure.

648). However, most of this work has focused on *in vitro* biochemistry and single-molecule studies that tend to ignore much of the *in vivo* context such as salt concentrations and DNA deformations (643–645, 647). Elf et al. (322) were the first to visualize and quantify the kinetics of this target search process in real-time by applying high laser excitation intensities and stroboscopic illuminations to image single LacI-Venus molecules in the *E. coli* cytoplasm. It turned out that in search of the operator, LacI spends the majority of its time (~90%) nonspecifically bound to the DNA and diffuses along the strands with residence times of <5 ms. Later, Hammar et al. (324) suggested that the quick 1D sliding search kinetics on nonspecific sequences might be a tradeoff with a fast binding of the TF at the specific target site.

All of these earlier experiments looked at the behavior of LacI in strains with an artificially low copy number of the protein to ensure clear (single-molecule) visualization (322, 324, 473, 649, 650), thereby possibly influencing the native behavior of this protein (321). Recently, Garza de Leon et al. (321) investigated "tracking PALM" (Fig. 5D) as a method (251, 306, 319, 651, 652) to study the intracellular mobility and spatial distribution of TFs under their native (and higher) copy numbers. In their study, LacI-PAmCherry was stochastically photoactivated *in vivo* in such a way that individual molecules lighted up in each activation round, preparing them to be tracked as single particles until they eventually photobleached. This strategy alleviates copy number limitations and paves the way for high-resolution imaging over a very broad copy number range (10 to 10,000 molecules per cell) (321). Since the majority of the TFs in *E. coli* reside in the low- to medium-copy-number range (1 to 100 monomers per cell) (653), PALM presents itself as one of the best methods to study *in vivo* functionality of these regulators due to its sensitive and quantitative nature (321). More specifically, Garza de Leon et al. (321) focused on the different types of DNA-binding interactions that LacI and other TFs can display: specific, near specific, and nonspecific. In the absence of its inducer, LacI binds to its three operator sites with high specificity. However, it can also interact with multiple other sites on the genome that are closely related to the cognate operator site sequence (i.e., near specific). On the contrary, in the presence of lactose, these two DNA interaction modes are overthrown, leaving only room for nonspecific interaction with the nucleoid. To dissect these three modes and determine their relative abundance, Garza de Leon et al. (321) monitored native and truncated photoactivatable LacI molecules under different inducing conditions and in different genetic backgrounds to create an array of systems in which each mode is easily discernible. For example, by examining a strain devoid of all *lac* operator sites, the near-specific mode can easily be investigated without interference of the two other possible interaction profiles. The specific decrease of bound LacI (ca. 30 to 35%) that is seen in this strain upon induction provides a means to directly probe the near-specific interactions of this TF.

Divisome

Bacterial proliferation is critically dependent on the ability of a mother cell to divide into two (most often identical) daughter cells using a large and dynamic macromolecular cytokinesis machine called the divisome (654). This heavy-duty machinery is essential under almost all conditions and has a complex architecture consisting of more than 30 protein building blocks located in either the cytoplasm or the cytoplasmic membrane (655–660). Although around one-third of this ring-like, cell-centered structure is essential for cell envelope invagination and cytokinesis to proceed, many of the building blocks display some redundancy.

Since the initial finding of cell division genes in thermosensitive mutants (*fts*, filamentous temperature sensitive) of *E. coli*, interest was raised in their structural engineering and three-dimensional architecture (654, 661, 662). Classical approaches did not allow early studies to unravel the workings of this membrane-located complex, since its size and highly dynamic nature made it extremely difficult to purify the structure as a whole (654). The first structural understanding stemmed from immunogold labeling experiments (663), setting the stage for new methods based on fluorescence microscopy to directly visualize the divisome's structural proteins in intact cells (Fig. 6). The current view on the bacterial cytokinesis machinery and its dynamics mainly comes from high-resolution imaging in *E. coli* and *B. subtilis*, fine-tuning earlier "divisome paradigms" partially based on artifact-prone techniques (303, 312, 662, 664–669).

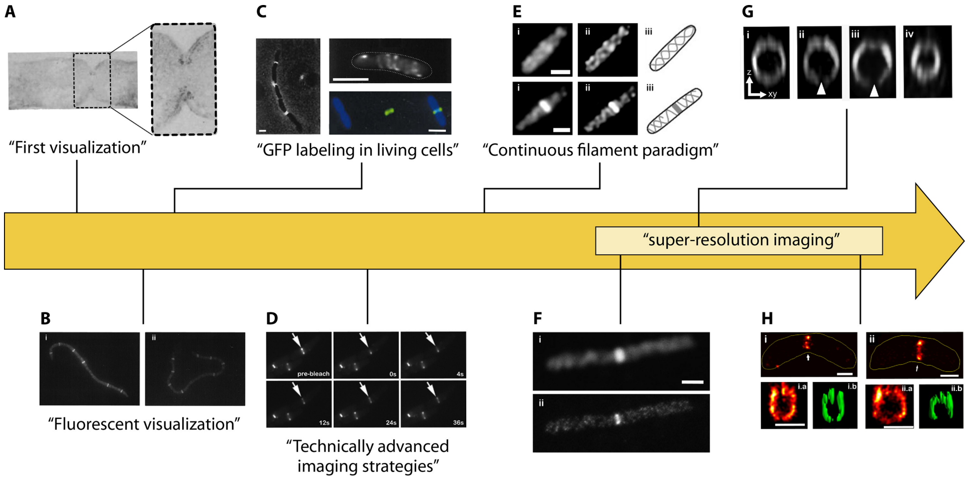

FIG 6 High-resolution imaging drives the untangling of the bacterial divisome architecture: examples of FtsZ visualization through time. Much of the current understanding on the bacterial cytokinesis machinery stems from visual experiments with high-resolution imaging, fine-tuning older "divisome paradigms" that were partially based on artifact-prone techniques. In this figure, we give an overview of how FtsZ visualization improved in the past 3 decades, leading to a better understanding of Z ring formation and localization. (A) Immunogold labeling experiments gave the first structural insight into FtsZ midcell localization during cytokinesis, a structure now known as the Z ring. (Adapted from reference 663 by permission from Springer Nature.) (B) FtsZ localization in fixed cells of different *fts* mutants (i, *ftsA* mutant; ii, *ftsQ* mutant) visualized with immunofluorescence microscopy. (Photos reproduced from reference 671 with permission.) (C) First use of GFP for labeling FtsZ in living cells. The left panel shows the formation of Z rings at septation sites in a filamentous cell. The top right panel shows a wide-field fluorescence image that was processed with a deconvolution algorithm, displaying apparent helical structures in a growing *E. coli* cell. In the bottom right image, the FtsZ ring localizes to the internucleoid space. Left to right in this panel: DAPI (nucleoid), GFP (FtsZ), and combined image. (Photos reproduced from reference 9 with permission of the National Academy of Sciences, U.S.A.). Scale bar, 1 μm. (D) FRAP time series indicating the bleached area (white arrow) and the recovery of FtsZ (time-stamp) after photobleaching. (Adapted from reference 634 with permission.) The rise of more technically advanced studies enabled a better understanding of the assembly dynamics of the FtsZ ring. (E) Conventional fluorescence microscopy supported a model for a smooth-cable like appearance of FtsZ helical filaments in growing cells. In the top row, a cell with a FtsZ helix is shown, while the bottom row displays a cell with a Z ring and FtsZ helix. Both rows are composed of the original image (i), an image processed with a 3D deconvolution algorithm (ii), and a schematic representation of the interpreted FtsZ location in the cell (iii) (Adapted from reference 639 with permission of John Wiley and Sons.) Scale bar, 1 μm. (F) With super-resolution microscopy and its increased resolution, it can be seen that helical Z filaments are in fact highly irregular and discontinuous. Panel i is a confocal image, and panel ii is the concomitant STED super-resolution image (Photos reproduced from reference 665 with permission of Elsevier.) Scale bar, 1 μm. Likewise, the Z structure at the midcell was shown to consist predominantly of patches and incomplete, discontinuous rings, as shown in panel G. (G, i to iv) Distribution of FtsZ molecules in the Z ring, as imaged with 3D-SIM. Arrows point toward small gaps in the fluorescence intensity profile indicative of lower abundance of FtsZ at those locations. (Adapted from reference 303, published under the terms of the Creative Commons Attribution License.) (H) PALM images of FtsZ localization during cell division with images in the *x-y* dimension (i and ii), the corresponding 2D cross-section image of the region indicated with the arrow (i.a and ii.a), and the three-dimensional volume reconstruction (ii.a and ii.b). (Photos reproduced from reference 668 with permission of the National Academy of Sciences, U.S.A.) Scale bar, 0.5 μm. Original figure indexations and scale bars were either removed or masked without altering the content of the images. New indexations and scales were added to provide consistency throughout the figure.

The prokaryotic tubulin homolog FtsZ forms the central component of the bacterial divisome and assembles in a circumferential ring-like structure at the midcell, where it recruits dozens of other proteins, ultimately triggering cytokinesis. This main structural element of the cell division machinery was the first component of the divisome to be visualized (albeit nonfluorescently) and led to a breakthrough by showing a clear division site localization pattern forming what is now known as the Z ring at the septum (663). Soon thereafter, Richard Losick's lab refined immunofluorescence microscopy (IFM) for use in bacteria (4, 8), leading to a series of papers from different research groups using IFM in fixed cells to confirm the localization of FtsZ and for the first time demonstrating that other known products of *fts* genes, provided the presence of FtsZ, also localize to the division site (670–676). These direct visualization experiments uncovered the first glimpse of the recruitment dependency and temporal hierarchy of the divisome that would later be uncovered. Around the same time, the first FtsZ-GFP fusions were engineered and, using advanced image processing, the first *in vivo* three-dimensional view of the Z ring was obtained (9). Other divisome proteins, such as ZapA and ZipA in *E. coli* or EzrA in *B. subtilis*, that directly bind to FtsZ were later on also used to indirectly label the structure with fluorescence and minimize perturbations or artifacts (135, 136, 138). The use of IFM and fluorescent protein tags (and ideally both) thus for the first time allowed obtaining a low-resolution, operational structure of the divisome in several prokaryotic model organisms and enabled the visualization of similar structures in other bacterial species. Furthermore, this benefit of direct fluorescent localization in the cell was crucial in the further search for Z ring binding proteins and the confirmation of binary protein-protein interactions, since many of these proteins have highly dynamic interaction patterns or subtle deletion phenotypes that tend to obscure straightforward detection of their involvement (677–683).

With the advent of more advanced microscopy techniques, a more accurate closeup of the divisome on the spatial and temporal level could be achieved (Fig. 6D to H). One of the first more technically advanced studies focused on the dynamics of the Z ring structure and used Fluorescence Recovery After Photobleaching (FRAP) (see "Fluorescence recovery after photobleaching") to demonstrate a monomer turnover rate in the ring structure of ~9 s (684). These researchers monitored the time it took for a section of the Z ring to regain its fluorescence after being permanently bleached via high-intensity laser light. The high turnover rate seen in these experiments underscored the rapid interchange between FtsZ-GFP proteins bound to the divisome and those observed elsewhere in the cell (684). Although FtsZ forms a clear distinct ring at the midcell, at least half of the cellular FtsZ is located out of the ring structure itself (256), where it oscillates to the Min system metronome together with other divisome components (685–687).

With the advent of new (mostly super-resolution) microscopy methods, it became feasible to uncover some of the nanometer-sized architectural gems of this complex without being hampered by crude and insensitive methods, as in electron microscopy (660, 688). The first super-resolution approach to get more insights in the fine structure of the divisome, relied on IFM in combination with Stimulated Emission Depletion (STED) microscopy (665) (see "Super-resolution microscopy"). In this study, Jennings et al. (665) took advantage of the power of nanoscopy to resolve the structure of the dynamical FtsZ helices that can be seen in *B. subtilis* throughout the cell cycle and that culminate into a ring-like assembly of the protein in the divisome. In contrast to the smooth cable-like appearance that was described earlier for these polymeric FtsZ sinks (689), STED resolved the helices as being highly irregular and discontinuous (665). Furthermore, this study, together with two contemporaneous super-resolution studies using the faster three-dimensional structured illumination microscopy (3D-SIM), underscored that FtsZ does not form a continuous ring at the septum but rather localizes at the midcell as dynamic, discontinuous patches (303, 667).

All of this was further supported by techniques such as PALM and STORM at even higher resolution (664, 668, 690). Taking together the wealth of new super-resolution information on the FtsZ ultrastructure, the current model of the divisome is a patchy ring or toroid structure that contains at least three concentric rings composed of different sets of proteins (654, 691). These observations thus suggest that this complex machinery has spatially separated modules that are clustered in concentric rings, and it is hypothesized that all rings have a different functionality: a peptidoglycan synthesizing-ring (outer layer), a proto-ring providing the force for constriction (middle layer), and a ring taking up a regulatory role (inner layer).

Two other landmark studies recently showed that the ring scaffold serves as a treadmilling platform for the septal peptidoglycan synthesis machinery, in contrast to the popular belief that constriction of the FtsZ septum itself serves as a force-generating mechanism driving cytokinesis (14, 692). These two elegant studies are excellent examples of how the combination of diverse, state-of-the-art experimental setups can help to gain a profound understanding of a fundamental aspect of bacterial cell biology. Even more recently, Söderström et al. (318) used (time-gated) Stimulated

Emission Depletion [(g)STED] nanoscopy to study the behavior of FtsZ-mNeonGreen clusters in geometrically sculpted *E. coli* cells and concluded that membrane geometry is not a decisive factor for FtsZ clustering characteristics.

Outer Shell

The bacterial cell envelope provides the necessary compartmentalization to allow bacterial life, enclosing nucleic acids and other necessities of life to prevent them from leaking away to the external environment. This bacterial cell envelope comprises multiple layers that all serve to protect the bacterium from the hostile environments they live in and form the major targets of antibacterial strategies (693). While many efforts were made over the past decades to reveal the dynamic architecture of structures inside the bacterial cell, less is still understood on the spatiotemporal dynamics of the external layers. In part, this can be explained by the difficulties GFP experiences in these cellular spaces (694, 695) (see "Periplasmic space"), however, several new techniques and strategies have eased the work in the past decade and are fostering enormous progress in understanding the cell envelope.

Inner membrane. The cytoplasmic space of both Gram-negative and -positive bacteria is delimited by a symmetrical phospholipid bilayer filled with various (trans-)membrane and lipid-anchored proteins. Visualizing this inner membrane or its associated features can be achieved via two routes, in which a first one capitalizes on these floating proteins to light up the lipid sea (696–698), while the second route exploits the unique chemical composition of this bilayer to enable specific chemical dye labeling (698–703).

When using (specific parts of) inner membrane proteins to visualize the cytoplasmic membrane, it is important to bear in mind that some fluorescent tags are restricted to the cytoplasm for reliable signal generation. This is especially the case for (auto)fluorescent proteins, as most GFP derivatives (in contrast to proteins from the Anthozoa family) lose their fluorescence when exported to the periplasm (695, 704) (see "Periplasmic space" below). In essence, this implies that for labeling proteins or protein fragments on the cytoplasmic side of the membrane basically all different fluorescent proteins can be translationally fused, whereas protein fusions attached to the inner membrane from the periplasmic side require a more thoughtful labeling strategy (185, 695, 705). An example of such a protein-based inner membrane labeling can be found in the study of Lewenza et al. (696), who exploited a fluorescent chimera build up out of the anthozoan RFP and an *Enterobacteriaceae* membrane targeting signal. To verify the targetting of the FP to the cytoplasmic membrane in *E. coli* by the canonical, inner membrane signal, the authors relied on the formation of so-called plasmolysis bays that are only visible when the fluorescent signal is located in the inner membrane. The formation of these structures can be induced by hyperosmotic shock, leading to the retraction of the membrane from its close interaction with the peptidoglycan outer membrane layer and the formation of bay-like inlets (706).

Cardiolipin is a glycerophospholipid that closely interacts with various important proteins and preferentially localizes in the inner membrane, where it forms microdomains at the septa and poles (699, 707–710). The uniqueness of its composition allows visualization based on specific chemical dye components and thus exemplifies the second route for inner membrane structure labeling. In one method for visually tracking the location and reorganization of these cardiolipin rafts, the bacterial membrane was enriched with Topfluor-cardiolipin (TF-LP), a fluorescent analogue of cardiolipin that needs to be externally added to the cell environment in order to become incorporated in the membrane of the target bacterium (703, 711, 712). A less disturbing way to visualize the same phenomena applies 10-*N*-nonyl acridine orange (NAO) to label native cardiolipin in a variety of species (699, 700, 713, 714). This positively charged NAO dye preferentially binds anionic phospholipids in membranes and shifts its emission to the red side of the spectrum upon interaction with cardiolipin (715–719). Although NAO is based on the DNA-binding dye acridine orange, the replacement of one of the functional groups in the original structure with a *N*-nonyl group increased its hydrophobicity, thereby impairing the nucleic acid preference of the molecule (716). More recently, however, some questions have been raised regarding the cardiolipin specificity of NAO, pointing out that the characteristic red-shifted fluorescence is not specific for cardiolipin interaction but rather promiscuous for interactions with anionic phospholipids in general (720, 721). This possible artifact further underscores the need for different imaging approaches using mechanistically independent routes to visualize the same structure.

Since membrane viscosity is a determining factor for the diffusion of small molecules and proteins in and across the plasma membrane, it also affects the speed of intracellular reactions. Because a direct measurement of this feature in living cells could shed light on the instantaneous membrane responses of bacteria in changing situations, a new technical setup combining Fluorescence Lifetime Imaging Microscopy (FLIM) and molecular rotor probes (e.g., BODIPY C_{10}, BODIPY FL C_{12}) was developed (701, 702, 722, 723). The fluorescence emission of this novel type of small synthetic molecule changes depending on its molecular surroundings and stems from the unique way these molecular rotors can lose the energy of an absorbed excitation photon: (i) either via radiative decay with emission of a fluorescent photon or (ii) via nonradiative decay using intramolecular rotations. Since the latter type of decay is directly affected by the environment in which the molecular rotor resides (and both decay types are in constant competition), the fluorescent properties (quantum yield and fluorescence lifetime) of the molecular rotor change with viscosity (724). Looking at the fluorescence lifetimes of these probes therefore provides a concentration-independent manner to obtain a quantitative measurement of the viscosity with micrometer resolution. With this method, Mika et al. (701) demonstrated that within isogenic *E. coli* populations a large intercellular heterogeneity in viscosity can be seen, possibly reflecting cell-to-cell variation in lipid composition. The same technical setup was already used earlier to study the fluctuations in the inner membrane viscosity of *Bacillus* endospores showing that the high viscosity seen in the spore state decreases throughout the germination process (722) and in response to ethanol treatment (702). Similar and other methods have also been developed to look at membrane and protein mobility in the membrane without the use of molecular rotors (723, 725, 726).

Periplasmic space. In Gram-negative bacteria the cell envelope is equipped with a third, delimited structure that is lined by two lipid bilayer membranes separating it from both the intra- and extracellular environment. This periplasmic space contains a densely packed gel-like matrix and constitutes an oxidizing reaction environment for many important processes involved in cell division, environmental sensing, and cellular transport (704). Following their translation in the reduced inner core of the bacterium, proteins targeted to the periplasmic space first need to cross the inner membrane, a transport that mainly proceeds via the general secretory (Sec) pathway. This translocation machinery catalyzes the transfer of unfolded and loosely folded proteins tagged with a signal sequence to the periplasm, where they will eventually fold into the proper conformation (727). Proteins that do require full cytoplasmic folding are transported by a second translocation apparatus, the twin-arginine (Tat) machinery, that helps folded cytoplasmic proteins to cross the inner membrane dismissing the need for periplasmic protein folding (728).

Early attempts to visualize Sec-translocated proteins via translational GFP fusions were unsuccessful (694) since the folding and formation of active GFP molecules is inhibited under the oxidizing conditions of the periplasm (694, 729–731). Because GFP's native environment is the reducing cytoplasm, its tertiary structure is independent of possible disulfide bonds that can be formed by its two cysteine residues (Cys^{48} and Cys^{70}). However, as unfolded GFP molecules get secreted via Sec to the periplasmic space, promiscuous interchain-disulfide bridges can form with other proteins or GFP folding intermediates, thereby hampering chromophore maturation and trapping the FPs in a nonfluorescent state (61, 704, 732). Using the Tat translocation pathway, these specific problems can be avoided since mature and fully folded GFP molecules transferred into the oxidizing periplasm remain active (733). Nevertheless, this method presents some challenges as well and does not support fluorescent fusion approaches to track the translocation of the majority of periplasmic proteins under native conditions (695, 733–735).

Anthozoa-derived fluorescent proteins (e.g., mRFP1, mCherry, and mScarlet) present a first possible solution to the challenges encountered during *in vivo* studies of periplasmic proteins. Although the tertiary structure of this fluorescent protein family is highly similar to the β-barrel of *Aequorea* FPs, the absence of cysteines in their primary sequence allows for the transportation of unfolded Anthozoa proteins via the Sec pathway without suffering from folding and chromophore maturation errors (695, 704, 705). Furthermore, the green/yellow mNeonGreen derived from the marine invertebrate *Branchiostoma lanceolatum* (109) was also reported to properly fold and mature outside the cytoplasm despite the presence of a single cysteine residue in its amino acid sequence (736). Over the years, different solutions have been developed enabling the use of GFP-derivates for periplasmic tagging via the general secretory pathway. Superfolder *Aequorea* FPs are characterized by high folding kinetics introduced via directed evolution [see "(Auto)fluorescent proteins"]. Two of these specific superfolder mutations (S30R and Y39N) are found ahead of the cysteine residues in the amino acid sequence and consequently are translocated earlier than these reactive residues. These mutations influence the folding of the first three β-strands during the membrane transfer, allowing the autocatalytic formation of an intact chromophore in the bacterial periplasmic space (80, 730, 731, 737). More recently, Meiresonne et al. (705) constructed a novel superfolder GFP-derivative that can be pumped into the periplasm at high concentration without any toxicity. Besides its improved folding capabilities, superfolder Turquoise2ox (sfTq2ox) is characterized by the replacement of the native cysteines that would otherwise possibly form promiscuous disulfide bonds. Similarly, El Khatib et al. (738) developed two reversibly switchable fluorescent proteins that properly fold and photoswitch in the bacterial periplasm, enabling several nanoscopy approaches to be amendable to the bacterial periplasm. The development of these new probes addresses the issue of the limited FP toolbox that is currently available to do multiplex and FRET imaging in this compartment (705, 736, 739).

Alternatively, other visualization strategies can be adopted to circumvent possible problems in the periplasmic space. For example, it was already shown that the self-labeling HaloTag can be a valuable option for the visualization of periplasmic proteins in Gram-negative bacteria (185). The ligands that need to be added exogenously to light up this hybrid probe are sufficiently small to enter the periplasm of living bacterial cells and support fluorescence even under the oxidizing conditions in the periplasm.

Peptidoglycan. The peptidoglycan (PG) macromolecule forms an elastic net-like structure around the bacterial protoplast, shaping the cell and providing mechanic protection against the high internal turgor pressures. This load-bearing element consists of long glycan chains built up out of alternating β-1,4-linked *N*-acetylglucosamine (GlcNAc) and *N*-acetylmuramic acid (MurNAc) monosaccharides, interlinked via short peptide stems (four or five amino acids) on the carboxyl group of the MurNAc subunit (740, 741). These peptide cross bridges that contain both L- and D-amino acids, carry most of the interspecies variation, whereas the rest of the overall composition is fairly similar between different bacteria. Following the production of the GlcNAc-MurNAc-pentapeptide precursors in the cytoplasmic space, these molecules are converted into lipid-linked intermediates at the cytoplasmic membrane and transported into the periplasm, where they are subsequently incorporated into the existing PG framework (740, 741). This precursor incorporation is accompanied by the formation of peptide cross bridges between the different glycan strands taking advantage of the dibasic amino acid (e.g., meso-diaminopimelic acid [meso-DAP] or L-lysine) at the terminus of the pentapeptide side chains.

Early work on peptidoglycan visualization focused on the location of PG synthesis and turnover by combining radioactively labeled PG precursors and electron microscopy with thin sectioning. However, this approach is unable to provide enough spatial

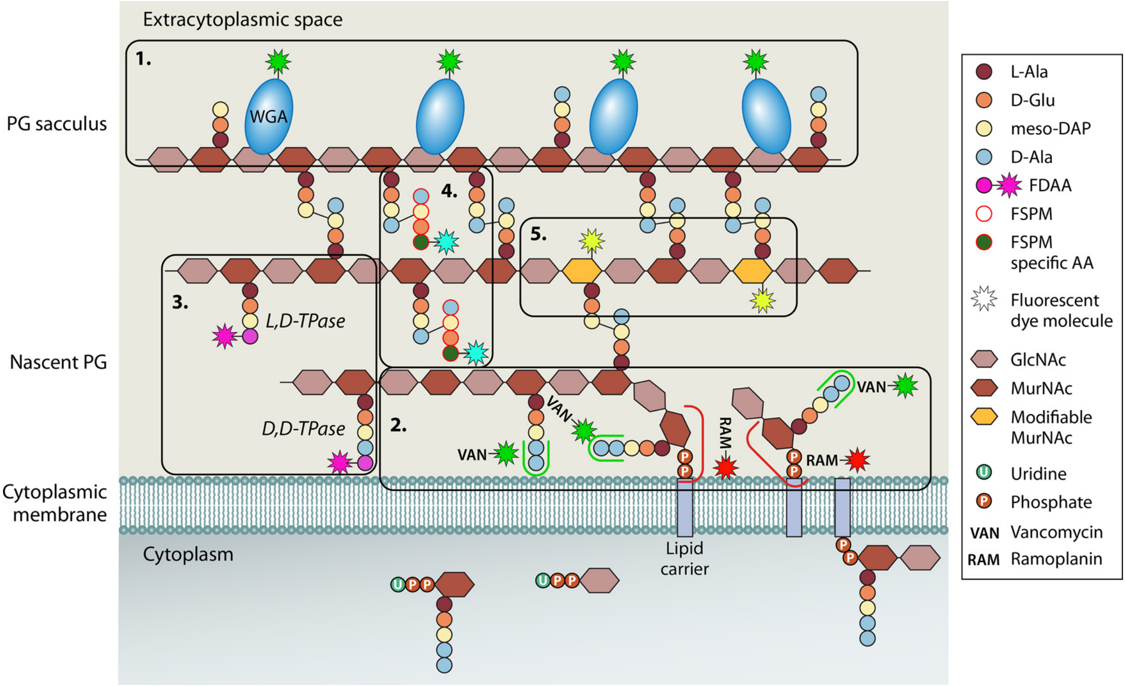

FIG 7 Labeling the peptidoglycan. Schematic representation of the different described approaches for *in vivo* labeling of the peptidoglycan layer based on the *E. coli* PG build-up. The peptidoglycan layer of bacteria consists of alternating *β*-1,4-linked *N*-acetylglucosamine (GlcNAc; light brown hexagon) and *N*-acetylmuramic acid (MurNAc; dark brown hexagon) monosaccharides, interlinked via short peptide stems (four or five amino acids; colored circles) on the carboxyl group of the MurNAc subunit. The precursors of these cross-links are pentapeptide chains containing both L- and D- amino acids accompanied by a single dibasic amino acid, here represented by meso-diaminopimelic acid (meso-DAP; light yellow circle). In the cytoplasm, GlcNAc-MurNAc-pentapeptide precursors are converted into lipid-linked intermediates and transported over the membrane into the extracytoplasmic space, where they are incorporated in the existing meshwork. (Box 1) Wheat germ agglutinin (WGA) binds specifically to all GlcNAc residues in the peptidoglycan framework and enables highlighting the entire PG sacculus. (Box 2) The use of fluorescently labeled antibiotics such as vancomycin or ramoplanin can support visualization of nascent PG in living cells. Vancomycin detects the terminal D-Ala-D-Ala (light blue circles) residues found on lipid-linked PG precursors and recently inserted, uncrosslinked subunits at the growing end of a glycan strand (green line). Ramoplanin, on the other hand, binds to the reducing ends of the growing glycan chains found at the initiation sites of PG synthesis and on lipid II carriers (red line). (Box 3) Fluorescent D-amino acids (FDAA) can be integrated into the bacterial cell wall via a periplasmic remodeling reaction on free pentapeptides in the existing PG promoted by D,D- and L,D-transpeptidases. (Box 4) PG cross-linking event are specifically visualized by using fluorescent stem peptide mimics (FSPM) that imitate the natural substrate in the transpeptidation reaction and install fluorophores instead of cross-links in the PG framework. (Box 5) PG sacculus labeling can also be achieved via the metabolic incorporation of modifiable MurNac carbohydrate subunits into the core structure, followed by fluorescent labeling via click chemistry.

resolution to determine the pattern of incorporation and often requires a significant amount of sample processing (742–746). The arrival of fluorescence microscopy and more advanced fluorescent labeling strategies provided the necessary spatiotemporal resolution to monitor the incorporation of PG building blocks (46, 747–749) and study the spatial dynamics of PG synthesis enzymes in living cells (178, 750, 751).

Fluorescently labeled wheat germ agglutinin (flWGA) was originally developed as an alternative for the Gram-staining procedure (752) but has shown promise as a visualization tool to light up the peptidoglycan sacculus. This lectin protein takes advantage of its ability to specifically bind all the *N*-acetylglucosamine (GlcNAc) subunits in the entire peptidoglycan meshwork (Fig. 7, box 1). Misra et al. (753) were the first to utilize such a probe (labeled with Alexa Fluor 488) in a live-cell setup with the Gram-positive *B. subtilis* bacterium to measure the global strain on the cell wall during the exposure to an osmotic shock. Unexpectedly, the same strategy can be implemented to label the peptidoglycan in living Gram-negative bacteria even though the layer is shielded by an intact outer membrane (176).

More often, researchers are interested in visualizing the sites of nascent PG synthesis rather than lining the entire peptidoglycan meshwork. This can be achieved by using a variety of probes that directly bind to the newly incorporated structures (754, 755) or get incorporated themselves (46, 747, 748). The Errington group introduced the use of fluorescently labeled antibiotics to highlight the sites of PG growth in living cells and applied fluorescent vancomycin to detect terminal D-Ala-D-Ala residues found on lipid-linked PG precursors and recently inserted subunits at the growing end of a glycan strand before cross-link (Fig. 7, box 2) (754). Since this terminal dipeptide is no longer present in the older PG structures of most species (756), this fluorescent antibiotic only labels nascent PG synthesis sites. Tiyanont et al. (755) developed a second fluorescently labeled antibiotic, ramoplanin, that in contrast to vancomycin does not label the incorporating intermediates but rather binds to the reducing ends of the growing glycan chains found at the initiation sites of PG synthesis and on lipid II carriers (757, 758). Both of the above antibiotics can be used in Gram-positive bacteria without fixation and permeabilization but tend to interfere with the continuation of PG synthesis making them unsuitable for live follow-up.

In 2012, Brun and coworkers (46) revolutionized the field of PG labeling by introducing a novel group of fluorescent D-amino acids conjugates that can be integrated into the peptidoglycan and supports the real-time tracking of PG synthesis and modification in different bacteria (14, 692, 754, 755, 759–771). This fluorescent D-amino acid (FDAA) strategy offers significant advantages in terms of speed and sensitivity over other approaches and is not limited by toxic effects or poor membrane permeability of the probes. The rationale behind this technique is based on the premise that most bacteria by nature are able to incorporate noncanonical D-amino acids (NCDAAs) into their cell walls. This incorporation proceeds via periplasmic remodeling of the existing PG by the activity of D,D-transpeptidases (and L,D-transpeptidases if present) and not via the incorporation of FDAAs into PG precursors in the cytoplasm (46, 772–776). Exploiting the ability of bacteria to use these FDAAs, Kuru et al. (46) showed that these fluorescent molecules can be stably incorporated into the peptide stem during PG synthesis because of their D-amino acid (DAA) backbone (Fig. 7, box 3). Since these FDAAs will only be incorporated into a small fraction of the PG (ca. 0.2 to 2.8%) and are unable to become integrated into any protein structure, possible toxicity, high background signals, and aspecific labeling are avoided (46). The addition of FDAAs to growing cultures of different species allows for rapid PG labeling in the entire population without affecting the growth rate and easily enables pulse-chase setups (46, 766). Whereas the first studies on peptidoglycan biosynthesis suggested a helical incorporation pattern for the new building blocks (754, 755), newer reports with FDAAs find incorporation activity to be highly punctuated along the cell (14, 46, 176, 692). Very recently, Hsu et al. (749) have expanded this technique with new probes, so-called rotor-fluogenic D-amino acids (RfDAAs). The emission intensity of these probes is influenced by the molecular environment (777), enabling to follow transpeptidation activity and glycan cross-linking in real-time. Moreover, these RfDAAs provide a higher temporal resolution than FDAAs without the need for sequential labeling steps and remove the need for vigorous washing steps between labeling and imaging (749, 766, 778).

Despite the numerous advantages inherently linked to the FDAA method, it is not always best practice. In their study to map the relation between MreB and cell wall growth, Ursell et al. (176) compared FDAA and WGA labeling in the same experimental setup. The low labeling density and the short fluorescent lifetimes of the FDAA probes make the system poorly suitable for tracking PG growth at short length scales and across generational time scales. Instead, they used fluorescently labeled WGA (bound to, for example, Alexa Fluor 488) to cover the entire cell surface homogeneously with high affinity, keeping the long-living probes locally stationed. Here, the fluorescent markers attach to the cell's peptidoglycan during the initial incubation step, followed by subsequent insertion of new dark (unlabeled) material at nascent PG synthesis sites, showing the true punctuated incorporation pattern of the process (176, 779). Since the chemical reaction that incorporates FDAAs in the pentapeptide stem is a D-amino acid exchange reaction mediated by transpeptidases (775, 776), the approach is nearly ideal for examining the sites of nascent PG synthesis but might fail in visualizing and quantifying true cross-linking events *in vivo*. Therefore, Gautam et al. (747) developed a set of fluorescent probes that mimic the natural substrate of transpeptidases (i.e., the pentapeptide stem) and install fluorophores instead of cross-links in the PG, making the transpeptidation process truly quantifiable (Fig. 7, box 4).

Labeling the murein sacculus can also be achieved via the glycan carbohydrate core of the PG polymer (Fig. 7, box 5). Liang et al. (748) developed modifiable MurNAc derivatives that can be incorporated in the cell wall of bacteria by exploiting the metabolic cell wall recycling and biosynthetic machineries. These modifiable residues can be fluorescently visualized via click chemistry and support super-resolution approaches since the labeling of the MurNac residues rather than the pentapeptide cross-links increases the lifetime of the probe and allows for long-term monitoring.

A different way to identify the places where PG is synthesized is to look at the localization of the main PG-synthesizing enzymes (i.e., the penicillin-binding proteins [PBPs]), a suite of proteins that often display extensive redundancy. This can be done via immunofluorescence labeling of fixed cells (674, 675, 780–782) or translational FP fusions to specific protein targets (750, 751, 783–785). However, small selective chemical compounds can also be used, sometimes providing the necessary specificity to highlight different subsets of PG-synthesizing enzymes (178, 786).

Outer membrane. In Gram-negative bacteria, the peptidoglycan is covered by an additional outer membrane (OM) layer that functions as a molecular sieve keeping out noxious environmental compounds (787, 788). The interior side of this asymmetric lipid bilayer is lined with phospholipids, while glycosylated lipids (mainly lipopolysaccharide) constitute the outer leaflet (693, 789). This unusual membrane environment is home to lipoproteins that are embedded in the lipid layer via a lipid side group and to integral membrane proteins (named outer membrane proteins [OMPs]) that span the entire OM (790). The complex nature of the OM paves the way for a myriad of specific labeling strategies but also presents some obstacles. Below, we will discuss a variety of approaches that target different components of this membrane compartment and support its single-cell imaging, in turn fostering deeper insight into this Gram-negative barrier.

The application of fluorescently labeled lipophilic dyes provides a low-disruptive strategy to visualize the outer membrane cell lining. Originally, the use of these membrane dyes in prokaryotic cell biology was rather limited (791), but now these dyes are commercially available and widely used. Nonetheless, for many of these dyes, conflicting reports exist on the specific lipid target that is labeled upon application. For example, the commonly used fluorescent lipophilic dye FM 4-64 was first reported as an inner membrane dye using plasmolyzed, filament-forming *E. coli pbpB* mutants (792). Later on, however, it was clearly shown by Lewenza et al. (696) that both FM 4-64 and FM 1-63 specifically stain the outer membrane of Gram-negative bacteria since no plasmolysis bays were formed in response to a hyperosmotic shock. These selective styryl dyes are expected to be unable to cross membranes due to their amphiphilic nature and therefore get trapped in the outermost bilayer. The main application of membrane dyes, such as FM4-64, lies in highlighting the outer edge of bacterial cells to improve the tracking of this structure visually or in cell tracker programs (696, 698, 793–795). However, these fluorescent, membrane-intercalating dyes can also be used as a tool in more elaborate strategies. For example, Kotte et al. (796) were able to show that the characteristic population growth lag time seen in clonal *E. coli* populations after a carbon source shift is caused by the phenotypic diversification into growers and nongrowers rather than a temporary population-wide growth stop. These researchers designed a flow cytometry-based experimental method to uncover these different growth phenotypes based on the use of membrane dyes to follow the cells' fluorescence intensity distribution over time. By pulse-labeling just before the nutrient shift, a population homogeneously labeled with the specific fluorescent dye was obtained. As these cells grow and divide, the concentration of the dye molecules attached to the cell membrane will decrease depending on the amount of binary fissions the cell has undergone. As the fluorescence of each cell halves per generation, the dye loss (after subtraction of the unspecific dye loss) can serve as a useful proxy for an individual cell's growth history in the new environment. In another more mechanistic study, lipid dyes were used to visualize lipid transfer dynamics between spatially adjacent *Myxococcus* cells. Here, Ducret et al. (698) mixed a population of cells labeled with DiO, a small C_{18} backbone dye that intercalates into the lipid layer, with unlabeled cells. Since the DiO^+ cells only carry a finite amount of dye molecules in their membranes, the transfer of membrane material can be noticed by an increase of fluorescence in the receiving cells, while the signal of the donor decreases as in a system of communicating vessels.

The need for exogenous addition of lipophilic reagents can be inconvenient and labeling the outer membrane by tagging fluorescent proteins with endogenous localization signals can be a valuable alternative (696, 698). Because all OM proteins have to cross the periplasmic space to reach their destination, only specific fluorescent probes can be used (see "Periplasmic space"). Ducret et al. (698) applied this strategy to investigate the exchange of OM proteins in the lipid transfer dynamics between *Myxococcus* cells by equipping sfGFP with an OM signal sequence, and demonstrated that physical contact between a labeled donor and an unlabeled recipient resulted in fluorescent OM labeling of the latter cell, indicative of protein transfer between both.

For a long time, the behavioral and organizational features of OMPs have remained unclear. However, direct fluorescent tracking of their movement has provided new means to investigate their spatiotemporal dynamics. Translational FP fusions are commonly used as the method-of-choice for investigating the localization of cytoplasmic, inner membrane, and periplasmic proteins (797) but have been known to inhibit OMP maturation. Another downside of such an approach is that the generated fluorescent signal does not exclusively stem from incorporated proteins in the OM but can also carry contributions from unincorporated OMPs still residing in the cytoplasmic and periplasmic space. Therefore, other strategies that focus solely on proteins that are exposed at the cell surface are more common in OMP research. Taking advantage of the high affinity of λ phage tails for the *E. coli* LamB maltoporin, Gibbs et al. (137) came up with a tagging strategy that exploits purified λ tails labeled with Texas Red for time-lapse microscopy of its localization pattern on the outer membrane. Later, Ursell et al. (779) thought of a new method to increase resolution during the visualization of the OMP incorporation pattern by using an epitope tag that only turns fluorescent after reacting with an exogenously added transferase enzyme at the extracellular surface. This method thus utilizes a sequence-specific labeling system, based on the Sfp phosphopantetheinyl transferase, that can covalently link single fluorophores to a genetically encoded 20-residue peptide tag inserted into a native surface-exposed external loop of LamB (798, 799). Ursell et al. (779) reported that the protein appears at discrete punctae before getting further dispersed over the cell surface during cell elongation, making room for new patches of OM material added in discrete bursts over time. In contrast, during the absence of cellular growth, these punctae remain virtually immobile. This probe has the additional advantage that the peptide tag and covalently attached fluorophore are physically small compared to FPs and other probes previously used to study OMP surface motion (137, 800); this therefore minimally perturbs the protein dynamics while offering higher spatial resolution.

More recently, Rassam et al. (801) visualized the OMP turnover dynamics in *E. coli*. This process is tightly controlled to ensure the right array of OMPs are present to comply with the requirements set by the ecological niche the bacterium resides in (790). Long-time tracking of OMPs, such as the vitamin B_{12} transporter BtuB and the iron siderophore transporter Cir, can be achieved with fluorescently labeled colicin molecules (ColE9 and ColIa, respectively) (802). These colicins were modified with disulfide bonds to block their import into (and toxicity to) bacterial cells (803) and are covalently bound to organic fluorophores (Alexa Fluor 488 [AF488] or tetra-methyl rhodamine [TMR]) to enable fluorescent visualization.

The most important building blocks of the bacterial outer membrane are lipopolysaccharides (LPS) since they add an additional layer of protection and stabilization to the outer leaflet of this Gram-negative structure (804). LPS molecules consist of three core regions: (i) the hydrophobic lipid A, which is embedded in the outer membrane; (ii) a core oligosaccharide built up from nonrepeating saccharide units such as heptose and 3-deoxy-D-manno-oct-2-ulosonic acid (KDO); and (iii) an O-antigen made up of small, repeating oligosaccharides (804). Visualizing LPS on the outer cell leaflet can be accomplished by either metabolically incorporating residues into the structure that later can be covalently linked with fluorescent dyes (181, 805, 806) or by using conjugated dye molecules specifically targeting native LPS on the cell surface (807–811). The first strategy relies on the endogenous cellular machinery to assimilate modified monosaccharides containing bio-orthogonal chemical tags into the LPS molecules (181, 812) and is further followed by chemical ligation with a fluorescent label once the LPS is externalized. Since KDO is a specific component of the core oligosaccharide and forms the linkage to lipid A in many Gram-negative species, this molecule presents an attractive candidate for labeling (181, 813, 814). Dumont et al. (181) were the first to test the LPS-specific KDO pathway for its tolerance toward the incorporation of azide-modified KDO molecules (8-azido-3,8-dideoxy-D-manno-octo-2-ulosonic acid [KDO-N3]) in the inner core of Gram-negative lipopolysaccharides. These researchers assumed that if cell penetration for this analogue was sufficient, activation and incorporation would follow, thereby replacing a part of the endogenous KDO in the LPS molecules. Combining these bio-orthogonal analogues with click chemistry, Dumont et al. (181) were indeed able to label this most outer layer in different, metabolically active bacteria. More recently, this technique also proved useful for selective imaging of Gram-negative bacteria in the mouse gut (806). Alternatively, conjugated fluorophores containing an LPS-specific binding moiety can assist in highlighting the external lipopolysaccharides. For example, concanavalin A can label the glucose and mannose residues of the O antigen (807–809) when added externally to the growth medium. Furthermore, also fluorescently labeled polymyxin B nonapeptide (PMBN) enables the detection of fluctuations in the LPS level on the cell surface via the interactions of its positively charged diaminobutyric acid (Dab) residues with negative charges on lipid A (810, 811).

Extracellular macromolecular complexes. The cell bodies of both Gram-negative and Gram-positive bacteria are lined with surface-exposed macromolecular complexes and structures that span the entire cell envelope reaching from the outside world down to the cytoplasm. These nanomachines (encompassing *inter alia* flagella, pili, and secretion systems) play a pivotal role in many essential processes such as cell-cell communication, pathogenesis, motility and biofilm formation (500, 503, 504, 815–820). Early experiments focusing on their visualization mainly relied on electron microscopy techniques to provide nanoscale resolution, requiring harsh conditions while only providing a very limited view on the time dynamics (821). Dark-field light microscopy, on the other hand, was able to improve this temporal information, but the large amount of light scattered by the cell bodies in this technique brings about a flare effect, obscuring detailed observations of molecular complexes close to the cell surface. Visualization of nanomachines with fluorescence microscopy eliminates most of the problems associated with the aforementioned techniques, albeit not without posing its own limitations. Since the assembly scheme and extracellular localization of these anchored appendages can cause difficulties in tolerating bulky probes such as FPs or fluorescence-conjugated antibodies (821–825), small synthetic fluorophores are generally used to label nanomachines, enabling their dynamics in the extracellular space to be recorded and quantified (821, 822, 826–833). Because flagella are seen as a paradigm for how molecular complexes can be built outside of living cells (834), we will focus on these particular nanomachines in the following section to showcase different labeling approaches that allow for spatial and/or temporal monitoring (Fig. 8).

Bacterial flagella are whip-like protein organelles that protrude from the cell body and are assembled from thousands of flagellin subunits exported to the extracellular space through a flagellar type III secretion system. These bacterial propellers get their energy from ion gradient-driven rotary motors anchored in the cell envelope and play an important role in cellular locomotion (835–841). Generally, bacterial propulsion

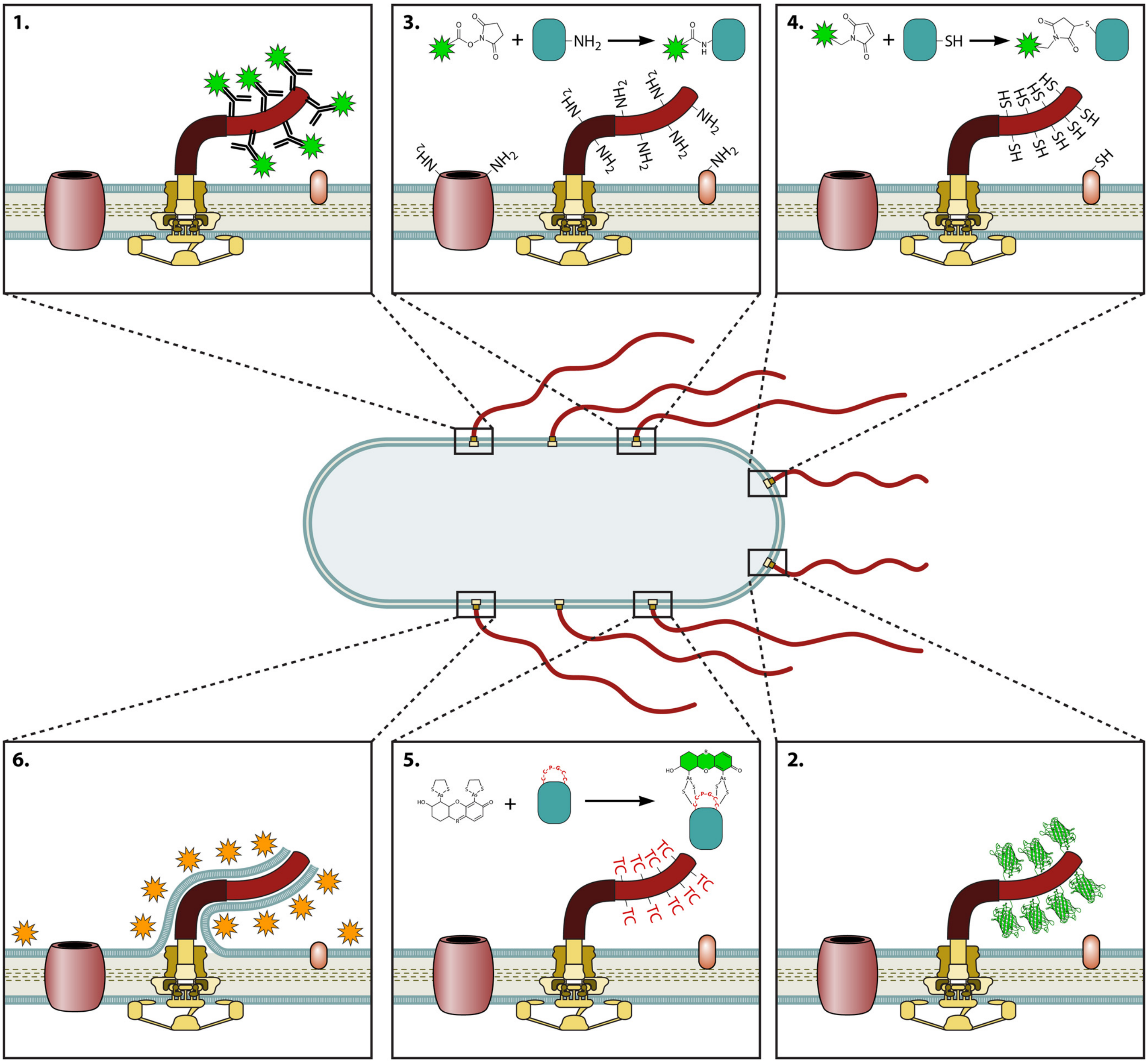

FIG 8 Labeling extracellular molecular complexes with fluorescence. Schematic overview of commonly used strategies to label extracellular structures in bacteria, exemplified by a flagellum case study. Bulky probes such as fluorescence conjugated antibodies and (auto)fluorescent proteins (boxes 1 and 2, respectively) targeted to specific subunits of the nanomachine may lead to visualization artifacts. Therefore, smaller labeling probes are often used to minimize the influence of the label on the extracellular complex. Fluorophore-linked succinimydyl (NHS) esters (box 3) can react with the primary amine (R-NH$_2$) group on the N-terminal and lysine residues found in proteins on both the cell body and the proteinaceous flagellum, fluorescently labeling mostly the latter because of its higher primary amine-to-surface ratio. Thiol-reactive maleimide dyes (box 4) can increase the signal-to-noise ratio as they form covalent bonds with free sulhydryl (-SH) groups, naturally occurring in relatively small numbers on the cell surface. Through minor genetic modifications (i.e., insertion or removal of cysteines), the desired extracellular structure can be highlighted with this type of dye. Both of these strategies (boxes 3 and 4) enable the imaging of living cells but do not support real-time staining as specific chemical conditions and long staining periods are required. Small hybrid probes, such as tetracysteine tags (TC; here exemplified by -C-C-P-G-C-C-) (box 5), do allow live staining of complexes on the outer shell of the bacterial cell since unbound labels are low fluorescent and reaction conditions are mild. (Box 6) Dyes such as NanoOrange that specifically interact with the hydrophobic membrane may also be used for real-time imaging in strains where membrane sheaths cover the molecular nanomachine.

follows a characteristic scheme of linear runs discontinued by random tumbling events, the length and frequency of both depending on the chemical gradients in the environment. Over the decades, it has become apparent that depending on the number of flagellar filaments and their location on the cell body, the detailed swimming behavior can vary immensely between species. The Howard Berg group at Harvard University were the first to develop a method that supported fluorescent visualization of single flagella in a way that did not affect bacterial motility and allowed for real-time spatiotemporal tracking of the filament movement in Gram-negative bacteria (822). Using succinimidyl (NHS) esters conjugated to specific Alexa Fluor dyes, these researchers were able to light up all the flagella across the cell envelope (i.e., peritrichous flagellation) of the *E. coli* bacterium and succeeded in obtaining a detailed picture of their individual behavior throughout propulsion, even when filaments crossed over the cell surface. These amino-specific dyes covalently react with primary amine (R-NH_2) groups found on the N terminus and lysine residue side chains of proteins on both the cell body surface and the proteinaceous flagellum, where they more densely label the latter because of the higher primary amine-to-surface ratio (Fig. 8, box 3). Following a dye incubation period and subsequent washing steps, Turner et al. (822) could prove that counterclockwise rotation of all flagellar motors makes the filaments form a coherent bundle that pushes the cell forward into a linear run. This trajectory ends when the rotation of one or more motors reverses into clockwise orientation, leading to bundle disassembly and random tumbling of the cell body until the start of a next run. More recently, Kinosita et al. (842) used a similar approach based on Cy3-NHS esters to stain flagella in *Burkholderia* and decipher the swimming motility of this symbiotic bacterium. To further limit background fluorescence from deeper in the sample ($<$200 nm), these researchers exploited a state-of-the-art TIRF microscopy setup and found a peculiar locomotion strategy in which the flagella wrap around the cell body in a screw-like pattern propelling the bacterium forward. Since the same type of flagellar behavior was seen in other symbiotic bacteria, it was hypothesized that this type of motility might support movement through mucus-filled narrow passages in the symbiotic host.

Succinimidyl (NHS) esters support the labeling of the flagellum structure without the need for any genetic modifications, but this aspecific primary amine tagging inevitably produces large amounts of background fluorescence. Over the years, other methods have been developed relying on minor genetic modifications to more specifically highlight the desired extracellular structure, thereby increasing the signal-to-noise ratio (827, 830, 833, 843–845). Thiol-reactive maleimide dyes depend on a combination of genetics and click chemistry to allow covalent bonds to be formed between the organic compound and free sulfhydryl (-SH) groups on proteins covering the cell surface (Fig. 8, box 4) (821). This milder reaction is more specific and selective than NHS ester tagging since sulfhydryl groups are not that numerous compared to primary amines, and their amount can be easily adjusted via incorporation and removal of (nonperturbing) cysteine residues. The specific location of these cysteine residues in the target protein is rather critical as resolution and signal strength are highly affected by their intramolecular position (821). Furthermore, serine and threonine are the preferred cysteine substitution partners because those exchanges are less likely to disrupt protein folding and maintain similar nucleophilic properties after the replacement (821, 843, 844, 846–848). Since thiol groups are sparsely scattered over the cell body and the extracellular appendages, performing the same staining procedure with a noncysteine knock-in control strain to detect technical artifacts is pivotal (821). In the past, maleimide dyes have been used to label flagella, not only providing insight into how bacteria regulate motility (843) and flagellar assembly (849) but also unveiling the dynamics of flagellar growth (846, 847). Both Turner et al. (846) and Paradis et al. (847) addressed the longstanding question of what happens to the growth dynamics of flagella when they are damaged by shear force experienced in the environment. By consecutively labeling flagella to saturation with two (846) or three (847) colors, respectively, both groups showed that flagella can resume growth after encountering mechanical shearing forces. It is worth mentioning that neither amino- nor sulfhydryl-specific dyes support real-time staining since specific chemical conditions and long staining periods are required. However, a temporal dimension can be obtained in these experiments by either following the dynamics of a previously stained surface structure (e.g., flagellar movement) (822) or using a consecutive staining protocol (e.g., flagellar regrowth)

(846). A second important remark is that maleimide dyes can be used in Gram-positive strains (843, 850) as well, in contrast to NHS ester dyes that were found to produce toxic side effects in these species (822). Reviews and protocols on amino- or sulfhydryl-specific staining can be found in studies by Ellison et al. (821) and Turner and Berg (845).

Real-time visualization of flagellar assembly dynamics is, however, supported by several other techniques that do facilitate "under the microscope" staining (828, 833). Zhao et al. (833), for example, developed a method using an optimized tetracysteine tag (TC tag; see "Hybrid tags") introduced into the flagellin protein to enable dynamic labeling and tracking of single-flagellar growth (Fig. 8, box 5) (40, 827). This improved TC tag (FMNCCPGCCMEP) (851) increases the binding affinity of the tetracysteine motif to the biarsenical dyes FlAsH and ReAsH, making it possible to perform high-resolution fluorescence imaging of extracellular nanomachines without the need for washing away the low-fluorescence, unbound labeling reagents (833). Consequently, these studies were able to shed some new light on flagellar assembly dynamics, a process that is still poorly understood and well-debated (828, 829, 846, 852–855). Early work on this topic exploited electron microscopy (856) and dark-field light microscopy (857) to suggest that the flagellar growth rate decreases exponentially with increased length of the filament. However, this was contradicted by later work (846, 855) proposing flagellar growth to be independent of filament length and maintaining a constant growth pace throughout the process. In contrast to these earlier studies, Zhao et al. (833) were able to track flagellar assembly in real-time on a single cell for extended time periods, rather than observing different cells at specific time points followed by a population-based analysis (846, 856–858). This new level of resolution showed that the flagellar growth speed in *E. coli* displays large intercellular fluctuations but remains rather constant on the single-cell level, being paced by the intracellular flagellin concentration (833). Furthermore, these real-time measurements also indicated an overall decreased assembly speed with increasing filament length, albeit large variations in growth rates could be seen among flagella of similar length. Around the same time, Chen et al. (828) made similar observations using a different real-time labeling approach and model system. They exploited the bacterium *Vibrio alginolyticus* that provides the benefit of carrying a single polar flagellum (i.e., monotrichous) (859, 860) covered by a membrane-like sheath (861) synchronously following the growth pattern of the flagellar filament (828). This unique feature allows the use of fluorescent dyes such as NanoOrange (862), targeting the hydrophobic membrane and enabling high-resolution fluorescence imaging of newly growing filaments without any intermittent washing steps (Fig. 8, box 6). Since NanoOrange does not engage in the formation of covalent bounds, the labeling speed of this dye is very fast ($<$1 min), ensuring direct visualization of the growing filament.

CONCLUSIONS AND FUTURE PERSPECTIVES

The use of fluorescence microscopy in bacteriology has clearly deepened our understanding on the inner workings of these organisms, turning long-standing theories into visual observations and even paving the way for completely new paradigms on their intracellular architecture. Starting a little over 2 decades ago, the quest for new and improved (auto)fluorescent proteins instigated a broader movement searching for more advanced fluorescent probes, eventually culminating in a novel hybrid probe type that combines the genetic specificity of (auto)fluorescent protein fusions on the one hand and the exquisite spectral properties of chemical dyes on the other. As this greenhorn is gradually maturing into a versatile and practical tool, the two more traditional probe types [see "(Auto)fluorescent proteins" and "Chemical dyes"] are still being used routinely in cell biology.

Especially during the last decade, these great strides in fluorescent probe development have been accompanied by advancements in fluorescence imaging modalities, thereby increasingly defying the diffraction limit and the traditional trade-off between spatial and temporal resolution. Foremost, the increasing dissemination of super-resolution and single-molecule microscopy is bringing researchers closer to further unraveling the internal, bacterial architecture by enabling vivisection at the nanometer level.

In addition to the clever use and combination of (emerging) fluorophores and imaging modalities, additional drivers toward unrivaled vivisection of microorganisms will stem from the further development of microfluidics and image analysis approaches. These will support an increase in the spatial and conditional accommodation and command of cells, as well as the throughput and quantification of monitored features. In fact, full maturation and integration of these approaches will in turn also enable genetic and chemical phenomics screens with an unprecedented throughput and intra- and intercellular resolution, which are poised to fuel future discoveries.

It can be concluded that the maturation of fluorescence microscopy in all of its aspects has revolutionized cell biology and will keep on doing for the period to come. Much of the future ground-breaking work can be expected at the intersection of fluorescence microscopy and other disciplines, drawing upon their particular strengths to create new perspectives.

ACKNOWLEDGMENTS

This study was supported by a PhD fellowship (project 1135116N) from the Research Foundation—Flanders (FWO-Vlaanderen to A.C.). The content of the work has not been influenced by any funding agency or company, and we confirm that there is no conflict of interest to disclose.

REFERENCES

1. Lane N. 2015. The unseen world: reflections on Leeuwenhoek (1677) “Concerning little animals.” Philos Trans R Soc Lond B Biol Sci 370: 20140344. https://doi.org/10.1098/rstb.2014.0344.
2. Maddock JR, Shapiro L. 1993. Polar location of the chemoreceptor complex in the *Escherichia coli* cell. Science 259:1717–1723. https://doi.org/10.1126/science.8456299.
3. Chalfie M, Tu Y, Euskirchen G, Ward WW, Prasher DC. 1994. Green fluorescent protein as a marker for gene expression. Science 263: 802–805. https://doi.org/10.1126/science.8303295.
4. Arigoni F, Pogliano K, Webb CD, Stragier P, Losick R. 1995. Localization of protein implicated in establishment of cell type to sites of asymmetric division. Science 270:637–640. https://doi.org/10.1126/science.270.5236.637.
5. Thanbichler M, Shapiro L. 2008. Getting organized: how bacterial cells move proteins and DNA. Nat Rev Microbiol 6:28–40. https://doi.org/10.1038/nrmicro1795.
6. Schneider JP, Basler M. 2016. Shedding light on biology of bacterial cells. Philos Trans R Soc Lond B Biol Sci 371:20150499. https://doi.org/10.1098/rstb.2015.0499.
7. Bayas CA, Wang J, Lee MK, Schrader JM, Shapiro L, Moerner WE. 2018. Spatial organization and dynamics of RNase E and ribosomes in *Caulobacter crescentus*. Proc Natl Acad Sci U S A 115:E3712–E3721. https://doi.org/10.1073/pnas.1721648115.
8. Harry EJ, Pogliano K, Losick R. 1995. Use of immunofluorescence to visualize cell-specific gene expression during sporulation in *Bacillus subtilis*. J Bacteriol 177:3386–3393. https://doi.org/10.1128/JB.177.12.3386-3393.1995.
9. Ma X, Ehrhardt DW, Margolin W. 1996. Colocalization of cell division proteins FtsZ and FtsA to cytoskeletal structures in living *Escherichia coli* cells by using green fluorescent protein. Proc Natl Acad Sci U S A 93:12998–13003. https://doi.org/10.1073/pnas.93.23.12998.
10. Webb CD, Teleman A, Gordon S, Straight A, Belmont A, Lin DC, Grossman AD, Wright A, Losick R. 1997. Bipolar localization of the replication origin regions of chromosomes in vegetative and sporulating cells of *Bacillus subtilis*. Cell 88:667–674. https://doi.org/10.1016/S0092-8674(00)81909-1.
11. Valdivia RH, Falkow S. 1997. Fluorescence-based isolation of bacterial genes expressed within host cells. Science 277:2007–2011. https://doi.org/10.1126/science.277.5334.2007.
12. Marston AL, Thomaides HB, Edwards DH, Sharpe ME, Errington J. 1998. Polar localization of the MinD protein of *Bacillus subtilis* and its role in selection of the mid-cell division site. Genes Dev 12:3419–3430. https://doi.org/10.1101/gad.12.21.3419.
13. Elowitz MB, Levine AJ, Siggia ED, Swain PS. 2002. Stochastic gene expression in a single cell. Science 297:1183–1186. https://doi.org/10.1126/science.1070919.
14. Bisson-Filho AW, Hsu YP, Squyres GR, Kuru E, Wu F, Jukes C, Sun Y, Dekker C, Holden S, VanNieuwenhze MS, Brun YV, Garner EC. 2017. Treadmilling by FtsZ filaments drives peptidoglycan synthesis and bacterial cell division. Science 355:739–743. https://doi.org/10.1126/science.aak9973.
15. van Vliet S, Dal Co A, Winkler AR, Spriewald S, Stecher B, Ackermann M. 2018. Spatially correlated gene expression in bacterial groups: the role of lineage history, spatial gradients, and cell-cell interactions. Cell Syst 6:496–507.e6. https://doi.org/10.1016/j.cels.2018.03.009.
16. Campos M, Govers SK, Irnov I, Dobihal GS, Cornet F, Jacobs-Wagner C. 2018. Genomewide phenotypic analysis of growth, cell morphogenesis, and cell cycle events in *Escherichia coli*. Mol Syst Biol 14:e7573. https://doi.org/10.15252/msb.20177573.
17. Avery SV. 2006. Microbial cell individuality and the underlying sources of heterogeneity. Nat Rev Microbiol 4:577–587. https://doi.org/10.1038/nrmicro1460.
18. Davidson CJ, Surette MG. 2008. Individuality in bacteria. Annu Rev Genet 42:253–268. https://doi.org/10.1146/annurev.genet.42.110807.091601.
19. Raj A, van Oudenaarden A. 2008. Nature, nurture, or chance: stochastic gene expression and its consequences. Cell 135:216–226. https://doi.org/10.1016/j.cell.2008.09.050.
20. Herschel JFW. 1845. On a case of superficial colour presented by a homogeneous liquid internally colourless. Philos Trans R Soc London 1845:143–145.
21. Baeyer A. 1871. Ueber eine neue Klasse von Farbstoffen. Ber Dtsch Chem Ges 4:555–558. https://doi.org/10.1002/cber.18710040209.
22. Heimstiidt O. 1911. Das fluoreszenzmikroskop. Zeitschr Wissenschaft Mikroskopie Mikroskopische Technik 28:330.
23. Lehmann H. 1913. Das lumineszenz-mikroskop seine grundlagen und seine anwendungen. Z Wiss Mikr 417.
24. Ellinger P, Hirt A. 1929. Mikroskopische Untersuchungen an lebenden Organen. Arch Exp Pathol Pharmakol 145:193–210. https://doi.org/10.1007/BF01862317.
25. Coons AH, Creech HJ, Jones RN, Berliner E. 1942. The demonstration of pneumococcal antigen in tissues by the use of fluorescent antibody. J Immunol 45:159–170.

26. Darken MA. 1961. Microbiological process report: natural and induced fluorescence in microscopic organisms. Appl Microbiol 9:354–360. https://doi.org/10.1128/AEM.9.4.354-360.1961.
27. Kasten FH. 1993. Introduction to fluorescent probes: properties, history, and applications, p 12–33. *In* Mason WT (ed), Fluorescent and luminescent probes for biological activity. Academic Press, Cambridge, UK.
28. Hiraga S, Niki H, Ogura T, Ichinose C, Mori H, Ezaki B, Jaffé A. 1989. Chromosome partitioning in *Escherichia coli*: novel mutants producing anucleate cells. J Bacteriol 171:1496–1505. https://doi.org/10.1128/JB.171.3.1496-1505.1989.
29. Cubitt AB, Heim R, Adams SR, Boyd AE, Gross LA, Tsien RY. 1995. Understanding, improving and using green fluorescent proteins. Trends Biochem Sci 20:448–455. https://doi.org/10.1016/S0968-0004(00)89099-4.
30. Andersen JB, Sternberg C, Poulsen LK, Bjorn SP, Givskov M, Molin S. 1998. New unstable variants of green fluorescent protein for studies of transient gene expression in bacteria. Appl Environ Microbiol 64:2240–2246. https://doi.org/10.1128/AEM.64.6.2240-2246.1998.
31. Urano Y, Kamiya M, Kanda K, Ueno T, Hirose K, Nagano T. 2005. Evolution of fluorescein as a platform for finely tunable fluorescence probes. J Am Chem Soc 127:4888–4894. https://doi.org/10.1021/ja043919h.
32. Zacharias DA, Tsien RY. 2006. Molecular biology and mutation of green fluorescent protein. Methods Biochem Anal 47:83–120.
33. Kim YK, Ha HH, Lee JS, Bi X, Ahn YH, Hajar S, Lee JJ, Chang YT. 2010. Control of muscle differentiation by a mitochondria-targeted fluorophore. J Am Chem Soc 132:576–579. https://doi.org/10.1021/ja906862g.
34. Im CN, Kang NY, Ha HH, Bi X, Lee JJ, Park SJ, Lee SY, Vendrell M, Kim YK, Lee JS, Li J, Ahn YH, Feng B, Ng HH, Yun SW, Chang YT. 2010. A fluorescent rosamine compound selectively stains pluripotent stem cells. Angew Chem Int Ed Engl 49:7497–7500. https://doi.org/10.1002/anie.201002463.
35. Koide Y, Urano Y, Hanaoka K, Piao W, Kusakabe M, Saito N, Terai T, Okabe T, Nagano T. 2012. Development of NIR fluorescent dyes based on Si-rhodamine for *in vivo* imaging. J Am Chem Soc 134:5029–5031. https://doi.org/10.1021/ja210375e.
36. Grimm JB, Muthusamy AK, Liang Y, Brown TA, Lemon WC, Patel R, Lu R, Macklin JJ, Keller PJ, Ji N, Lavis LD. 2017. A general method to fine-tune fluorophores for live-cell and *in vivo* imaging. Nat Methods 14:987–994. https://doi.org/10.1038/nmeth.4403.
37. Heim R, Prasher DC, Tsien RY. 1994. Wavelength mutations and posttranslational autoxidation of green fluorescent protein. Proc Natl Acad Sci U S A 91:12501–12504. https://doi.org/10.1073/pnas.91.26.12501.
38. Orm M, Cubitt AB, Kallio K, Gross LA, Tsien RY, Remington SJ. 1996. Crystal structure of the *Aequorea victoria* green fluorescent protein. Science 273:1392–1395. https://doi.org/10.1126/science.273.5280.1392.
39. Heim R, Tsien RY. 1996. Engineering green fluorescent protein for improved brightness, longer wavelengths, and fluorescence resonance energy transfer. Curr Biol 6:178–182. https://doi.org/10.1016/S0960-9822(02)00450-5.
40. Griffin BA, Adams SR, Tsien RY. 1998. Specific covalent labeling of recombinant protein molecules inside live cells. Science 281:269–272. https://doi.org/10.1126/science.281.5374.269.
41. Matz MV, Fradkov AF, Labas YA, Savitsky AP, Zaraisky AG, Markelov ML, Lukyanov SA. 1999. Fluorescent proteins from nonbioluminescent *Anthozoa* species. Nat Biotechnol 17:969–973. https://doi.org/10.1038/13657.
42. Keppler A, Gendreizig S, Gronemeyer T, Pick H, Vogel H, Johnsson K. 2003. A general method for the covalent labeling of fusion proteins with small molecules *in vivo*. Nat Biotechnol 21:86–89. https://doi.org/10.1038/nbt765.
43. Shaner NC, Campbell RE, Steinbach PA, Giepmans BN, Palmer AE, Tsien RY. 2004. Improved monomeric red, orange and yellow fluorescent proteins derived from *Discosoma* sp. red fluorescent protein. Nat Biotechnol 22:1567–1572. https://doi.org/10.1038/nbt1037.
44. Los GV, Darzins A, Zimprich C, Karassina N, Learish R, McDougall MG, Encell LP, Friedman-Ohana R, Wood M, Vidugiris G, Zimmerman K, Otto P, Klaubert DH, Wood K. 2005. HaloTag™ interchangeable labeling technology for cell imaging protein capture and immobilization. Promega Cell Notes 11:2–6.
45. Chapman S, Faulkner C, Kaiserli E, Garcia-Mata C, Savenkov EI, Roberts AG, Oparka KJ, Christie JM. 2008. The photoreversible fluorescent protein iLOV outperforms GFP as a reporter of plant virus infection. Proc Natl Acad Sci U S A 105:20038–20043. https://doi.org/10.1073/pnas.0807551105.
46. Kuru E, Hughes HV, Brown PJ, Hall E, Tekkam S, Cava F, de Pedro MA, Brun YV, VanNieuwenhze MS. 2012. *In situ* probing of newly synthesized peptidoglycan in live bacteria with fluorescent D-amino acids. Angew Chem Int Ed Engl 51:12519–12523. https://doi.org/10.1002/anie.201206749.
47. Kumagai A, Ando R, Miyatake H, Greimel P, Kobayashi T, Hirabayashi Y, Shimogori T, Miyawaki A. 2013. A bilirubin-inducible fluorescent protein from eel muscle. Cell 153:1602–1611. https://doi.org/10.1016/j.cell.2013.05.038.
48. Plamont MA, Billon-Denis E, Maurin S, Gauron C, Pimenta FM, Specht CG, Shi J, Quérard J, Pan B, Rossignol J, Moncoq K, Morellet N, Volovitch M, Lescop E, Chen Y, Triller A, Vriz S, Le Saux T, Jullien L, Gautier A. 2016. Small fluorescence-activating and absorption-shifting tag for tunable protein imaging *in vivo*. Proc Natl Acad Sci U S A 113:497–502. https://doi.org/10.1073/pnas.1513094113.
49. Bindels DS, Haarbosch L, van Weeren L, Postma M, Wiese KE, Mastop M, Aumonier S, Gotthard G, Royant A, Hink MA, Gadella TW. 2017. mScarlet: a bright monomeric red fluorescent protein for cellular imaging. Nat Methods 14:53–56. https://doi.org/10.1038/nmeth.4074.
50. Day RN, Davidson MW. 2009. The fluorescent protein palette: tools for cellular imaging. Chem Soc Rev 38:2887–2921. https://doi.org/10.1039/b901966a.
51. Reid BG, Flynn GC. 1997. Chromophore formation in green fluorescent protein. Biochemistry 36:6786–6791. https://doi.org/10.1021/bi970281w.
52. Cranfill PJ, Sell BR, Baird MA, Allen JR, Lavagnino Z, de Gruiter HM, Kremers GJ, Davidson MW, Ustione A, Piston DW. 2016. Quantitative assessment of fluorescent proteins. Nat Methods 13:557–562. https://doi.org/10.1038/nmeth.3891.
53. Rodriguez EA, Campbell RE, Lin JY, Lin MZ, Miyawaki A, Palmer AE, Shu X, Zhang J, Tsien RY. 2017. The growing and glowing toolbox of fluorescent and photoactive proteins. Trends Biochem Sci 42:111–129. https://doi.org/10.1016/j.tibs.2016.09.010.
54. Balleza E, Kim JM, Cluzel P. 2018. Systematic characterization of maturation time of fluorescent proteins in living cells. Nat Methods 15:47–51. https://doi.org/10.1038/nmeth.4509.
55. Lambert TJ. 2019. FPbase: a community-editable fluorescent protein database. Nat Methods 16:277–278. https://doi.org/10.1038/s41592-019-0352-8.
56. Shimomura O, Johnson FH, Saiga Y. 1962. Extraction, purification, and properties of aequorin, a bioluminescent protein from the luminous hydromedusan. J Cell Comp Physiol 59:223–239. https://doi.org/10.1002/jcp.1030590302.
57. Morise H, Shimomura O, Johnson FH, Winant J. 1974. Intermolecular energy transfer in the bioluminescent system of *Aequorea*. Biochemistry 13:2656–2662. https://doi.org/10.1021/bi00709a028.
58. Campbell RE, Tour O, Palmer AE, Steinbach PA, Baird GS, Zacharias DA, Tsien RY. 2002. A monomeric red fluorescent protein. Proc Natl Acad Sci U S A 99:7877–7882. https://doi.org/10.1073/pnas.082243699.
59. Yarbrough D, Wachter RM, Kallio K, Matz MV, Remington SJ. 2001. Refined crystal structure of DsRed, a red fluorescent protein from coral, at 2.0-Å resolution. Proc Natl Acad Sci U S A 98:462–467. https://doi.org/10.1073/pnas.98.2.462.
60. Thorn K. 2017. Genetically encoded fluorescent tags. Mol Biol Cell 28:848–857. https://doi.org/10.1091/mbc.e16-07-0504.
61. Craggs TD. 2009. Green fluorescent protein: structure, folding, and chromophore maturation. Chem Soc Rev 38:2865–2875. https://doi.org/10.1039/b903641p.
62. Baird GS, Zacharias DA, Tsien RY. 1999. Circular permutation and receptor insertion within green fluorescent proteins. Proc Natl Acad Sci U S A 96:11241–11246. https://doi.org/10.1073/pnas.96.20.11241.
63. Topell S, Glockshuber R. 2002. Circular permutation of the green fluorescent protein. Methods Mol Biol 183:31–48. https://doi.org/10.1385/1-59259-280-5:031.
64. Shui B, Wang Q, Lee F, Byrnes LJ, Chudakov DM, Lukyanov SA, Sondermann H, Kotlikoff MI. 2011. Circular permutation of red fluorescent proteins. PLoS One 6:e20505. https://doi.org/10.1371/journal.pone.0020505.
65. Carlson HJ, Cotton DW, Campbell RE. 2010. Circularly permuted monomeric red fluorescent proteins with new termini in the beta-sheet. Protein Sci 19:1490–1499. https://doi.org/10.1002/pro.428.
66. Ghosh I, Hamilton AD, Regan L. 2000. Antiparallel leucine zipper-directed protein reassembly: application to the green fluorescent protein. J Am Chem Soc 122:5658–5659. https://doi.org/10.1021/ja994421w.
67. Michnick SW. 2003. Protein fragment complementation strategies for

biochemical network mapping. Curr Opin Biotechnol 14:610–617. https://doi.org/10.1016/j.copbio.2003.10.014.

68. Magliery TJ, Wilson CG, Pan W, Mishler D, Ghosh I, Hamilton AD, Regan L. 2005. Detecting protein-protein interactions with a green fluorescent protein fragment reassembly trap: scope and mechanism. J Am Chem Soc 127:146–157. https://doi.org/10.1021/ja046699g.
69. Kerppola TK. 2006. Design and implementation of bimolecular fluorescence complementation (BiFC) assays for the visualization of protein interactions in living cells. Nat Protoc 1:1278–1286. https://doi.org/10.1038/nprot.2006.201.
70. Valencia-Burton M, McCullough RM, Cantor CR, Broude NE. 2007. RNA visualization in live bacterial cells using fluorescent protein complementation. Nat Methods 4:421–427. https://doi.org/10.1038/nmeth1023.
71. Milbredt S, Waldminghaus T. 2017. BiFCROS: a low-background fluorescence repressor operator system for labeling of genomic loci. G3 (Bethesda) 7:1969–1977. https://doi.org/10.1534/g3.117.040782.
72. Romei MG, Boxer SG. 2019. Split green fluorescent proteins: scope, limitations, and outlook. Annu Rev Biophys 48:19–44. https://doi.org/10.1146/annurev-biophys-051013-022846.
73. Kerppola TK. 2008. Bimolecular fluorescence complementation (BiFC) analysis as a probe of protein interactions in living cells. Annu Rev Biophys 37:465–487. https://doi.org/10.1146/annurev.biophys.37.032807.125842.
74. Ward WW, Bokman SH. 1982. Reversible denaturation of *Aequorea* green-fluorescent protein: physical separation and characterization of the renatured protein. Biochemistry 21:4535–4540. https://doi.org/10.1021/bi00262a003.
75. Ward WW, Prentice HJ, Roth AF, Cody CW, Reeves SC. 1982. Spectral perturbations of the *Aequorea* green fluorescent protein. Photochem Photobiol 35:803–808. https://doi.org/10.1111/j.1751-1097.1982.tb02651.x.
76. Brejc K, Sixma TK, Kitts PA, Kain SR, Tsien RY, Ormö M, Remington SJ. 1997. Structural basis for dual excitation and photoisomerization of the *Aequorea victoria* green fluorescent protein. Proc Natl Acad Sci U S A 94:2306–2311. https://doi.org/10.1073/pnas.94.6.2306.
77. Heim R, Cubitt AB, Tsien RY. 1995. Improved green fluorescence. Nature 373:663–664. https://doi.org/10.1038/373663b0.
78. Chattoraj M, King BA, Bublitz GU, Boxer SG. 1996. Ultra-fast excited state dynamics in green fluorescent protein: multiple states and proton transfer. Proc Natl Acad Sci U S A 93:8362–8367. https://doi.org/10.1073/pnas.93.16.8362.
79. Cormack BP, Valdivia RH, Falkow S. 1996. FACS-optimized mutants of the green fluorescent protein (GFP). Gene 173:33–38. https://doi.org/10.1016/0378-1119(95)00685-0.
80. Pédelacq JD, Cabantous S, Tran T, Terwilliger TC, Waldo GS. 2006. Engineering and characterization of a superfolder green fluorescent protein. Nat Biotechnol 24:79–88. https://doi.org/10.1038/nbt1172.
81. Shaner NC, Steinbach PA, Tsien RY. 2005. A guide to choosing fluorescent proteins. Nat Methods 2:905–909. https://doi.org/10.1038/nmeth819.
82. Lichtman JW, Conchello JA. 2005. Fluorescence microscopy. Nat Methods 2:910–919. https://doi.org/10.1038/nmeth817.
83. Grecco HE, Imtiaz S, Zamir E. 2016. Multiplexed imaging of intracellular protein networks. Cytometry A 89:761–775. https://doi.org/10.1002/cyto.a.22876.
84. Zimmermann T, Marrison J, Hogg K, O'Toole P. 2014. Clearing up the signal: spectral imaging and linear unmixing in fluorescence microscopy. Methods Mol Biol 1075:129–148. https://doi.org/10.1007/978-1-60761-847-8_5.
85. Cubitt AB, Woollenweber LA, Heim R. 1999. Understanding structure-function relationships in the *Aequorea victoria* green fluorescent protein. Methods Cell Biol 58:19–30.
86. Rizzo MA, Springer GH, Granada B, Piston DW. 2004. An improved cyan fluorescent protein variant useful for FRET. Nat Biotechnol 22:445–449. https://doi.org/10.1038/nbt945.
87. Goedhart J, van Weeren L, Hink MA, Vischer NO, Jalink K, Gadella TW. 2010. Bright cyan fluorescent protein variants identified by fluorescence lifetime screening. Nat Methods 7:137–139. https://doi.org/10.1038/nmeth.1415.
88. Goedhart J, von Stetten D, Noirclerc-Savoye M, Lelimousin M, Joosen L, Hink MA, van Weeren L, Gadella TW, Royant A. 2012. Structure-guided evolution of cyan fluorescent proteins towards a quantum yield of 93%. Nat Commun 3:751. https://doi.org/10.1038/ncomms1738.
89. Nguyen AW, Daugherty PS. 2005. Evolutionary optimization of fluorescent proteins for intracellular FRET. Nat Biotechnol 23:355–360. https://doi.org/10.1038/nbt1066.
90. Tsien RY. 1998. The green fluorescent protein. Annu Rev Biochem 67:509–544. https://doi.org/10.1146/annurev.biochem.67.1.509.
91. Wachter RM, Elsliger MA, Kallio K, Hanson GT, Remington SJ. 1998. Structural basis of spectral shifts in the yellow-emission variants of green fluorescent protein. Structure 6:1267–1277. https://doi.org/10.1016/S0969-2126(98)00127-0.
92. Miyawaki A, Nagai T, Mizuno H. 2005. Engineering fluorescent proteins. Adv Biochem Eng Biotechnol 95:1–15. https://doi.org/10.1007/b102208.
93. Griesbeck O, Baird GS, Campbell RE, Zacharias DA, Tsien RY. 2001. Reducing the environmental sensitivity of yellow fluorescent protein: mechanism and applications. J Biol Chem 276:29188–29194. https://doi.org/10.1074/jbc.M102815200.
94. Nagai T, Ibata K, Park ES, Kubota M, Mikoshiba K, Miyawaki A. 2002. A variant of yellow fluorescent protein with fast and efficient maturation for cell-biological applications. Nat Biotechnol 20:87–90. https://doi.org/10.1038/nbt0102-87.
95. Shaner NC, Patterson GH, Davidson MW. 2007. Advances in fluorescent protein technology. J Cell Sci 120:4247–4260. https://doi.org/10.1242/jcs.005801.
96. Andersson H, Baechi T, Hoechl M, Richter C. 1998. Autofluorescence of living cells. J Microsc 191:1–7. https://doi.org/10.1046/j.1365-2818.1998.00347.x.
97. Shcherbakova DM, Subach OM, Verkhusha VV. 2012. Red fluorescent proteins: advanced imaging applications and future design. Angew Chem Int Ed Engl 51:10724–10738. https://doi.org/10.1002/anie.201200408.
98. El Najjar N, van Teeseling MCF, Mayer B, Hermann S, Thanbichler M, Graumann PL. 2020. Bacterial cell growth is arrested by violet and blue, but not yellow light excitation during fluorescence microscopy. BMC Mol Cell Biol 21:35. https://doi.org/10.1186/s12860-020-00277-y.
99. Matz MV, Lukyanov KA, Lukyanov SA. 2002. Family of the green fluorescent protein: journey to the end of the rainbow. Bioessays 24:953–959. https://doi.org/10.1002/bies.10154.
100. Shagin DA, Barsova EV, Yanushevich YG, Fradkov AF, Lukyanov KA, Labas YA, Semenova TN, Ugalde JA, Meyers A, Nunez JM, Widder EA, Lukyanov SA, Matz MV. 2004. GFP-like proteins as ubiquitous metazoan superfamily: evolution of functional features and structural complexity. Mol Biol Evol 21:841–850. https://doi.org/10.1093/molbev/msh079.
101. Baird GS, Zacharias DA, Tsien RY. 2000. Biochemistry, mutagenesis, and oligomerization of DsRed, a red fluorescent protein from coral. Proc Natl Acad Sci U S A 97:11984–11989. https://doi.org/10.1073/pnas.97.22.11984.
102. Verkhusha VV, Lukyanov KA. 2004. The molecular properties and applications of *Anthozoa* fluorescent proteins and chromoproteins. Nat Biotechnol 22:289–296. https://doi.org/10.1038/nbt943.
103. Gross LA, Baird GS, Hoffman RC, Baldridge KK, Tsien RY. 2000. The structure of the chromophore within DsRed, a red fluorescent protein from coral. Proc Natl Acad Sci U S A 97:11990–11995. https://doi.org/10.1073/pnas.97.22.11990.
104. Merzlyak EM, Goedhart J, Shcherbo D, Bulina ME, Shcheglov AS, Fradkov AF, Gaintzeva A, Lukyanov KA, Lukyanov S, Gadella TW, Chudakov DM. 2007. Bright monomeric red fluorescent protein with an extended fluorescence lifetime. Nat Methods 4:555–557. https://doi.org/10.1038/nmeth1062.
105. Kredel S, Oswald F, Nienhaus K, Deuschle K, Röcker C, Wolff M, Heilker R, Nienhaus GU, Wiedenmann J. 2009. mRuby, a bright monomeric red fluorescent protein for labeling of subcellular structures. PLoS One 4:e4391. https://doi.org/10.1371/journal.pone.0004391.
106. Shcherbo D, Murphy CS, Ermakova GV, Solovieva EA, Chepurnykh TV, Shcheglov AS, Verkhusha VV, Pletnev VZ, Hazelwood KL, Roche PM, Lukyanov S, Zaraisky AG, Davidson MW, Chudakov DM. 2009. Far-red fluorescent tags for protein imaging in living tissues. Biochem J 418:567–574. https://doi.org/10.1042/BJ20081949.
107. Karasawa S, Araki T, Nagai T, Mizuno H, Miyawaki A. 2004. Cyan-emitting and orange-emitting fluorescent proteins as a donor/acceptor pair for fluorescence resonance energy transfer. Biochem J 381:307–312. https://doi.org/10.1042/BJ20040321.
108. Shcherbo D, Merzlyak EM, Chepurnykh TV, Fradkov AF, Ermakova GV, Solovieva EA, Lukyanov KA, Bogdanova EA, Zaraisky AG, Lukyanov S, Chudakov DM. 2007. Bright far-red fluorescent protein for whole-body imaging. Nat Methods 4:741–746. https://doi.org/10.1038/nmeth1083.
109. Shaner NC, Lambert GG, Chammas A, Ni Y, Cranfill PJ, Baird MA, Sell BR, Allen JR, Day RN, Israelsson M, Davidson MW, Wang J. 2013. A bright monomeric green fluorescent protein derived from *Branchiostoma*

lanceolatum. Nat Methods 10:407–409. https://doi.org/10.1038/nmeth.2413.
110. Landgraf D, Okumus B, Chien P, Baker TA, Paulsson J. 2012. Segregation of molecules at cell division reveals native protein localization. Nat Methods 9:480–482. https://doi.org/10.1038/nmeth.1955.
111. Margolin W. 2012. The price of tags in protein localization studies. J Bacteriol 194:6369–6371. https://doi.org/10.1128/JB.01640-12.
112. Zacharias DA, Violin JD, Newton AC, Tsien RY. 2002. Partitioning of lipid-modified monomeric GFPs into membrane microdomains of live cells. Science 296:913–916. https://doi.org/10.1126/science.1068539.
113. Zhang J, Campbell RE, Ting AY, Tsien RY. 2002. Creating new fluorescent probes for cell biology. Nat Rev Mol Cell Biol 3:906–918. https://doi.org/10.1038/nrm976.
114. Wannier TM, Gillespie SK, Hutchins N, McIsaac RS, Wu SY, Shen Y, Campbell RE, Brown KS, Mayo SL. 2018. Monomerization of far-red fluorescent proteins. Proc Natl Acad Sci U S A 115:E11294–E11301. https://doi.org/10.1073/pnas.1807449115.
115. Costantini LM, Fossati M, Francolini M, Snapp EL. 2012. Assessing the tendency of fluorescent proteins to oligomerize under physiologic conditions. Traffic 13:643–649. https://doi.org/10.1111/j.1600-0854.2012.01336.x.
116. Chudakov DM, Matz MV, Lukyanov S, Lukyanov KA. 2010. Fluorescent proteins and their applications in imaging living cells and tissues. Physiol Rev 90:1103–1163. https://doi.org/10.1152/physrev.00038.2009.
117. Wang S, Moffitt JR, Dempsey GT, Xie XS, Zhuang X. 2014. Characterization and development of photoactivatable fluorescent proteins for single-molecule-based superresolution imaging. Proc Natl Acad Sci U S A 111:8452–8457. https://doi.org/10.1073/pnas.1406593111.
118. Botman D, de Groot DH, Schmidt P, Goedhart J, Teusink B. 2019. *In vivo* characterization of fluorescent proteins in budding yeast. Sci Rep 9:2234. https://doi.org/10.1038/s41598-019-38913-z.
119. Kitagawa M, Ara T, Arifuzzaman M, Ioka-Nakamichi T, Inamoto E, Toyonaga H, Mori H. 2005. Complete set of ORF clones of *Escherichia coli* ASKA library (a complete set of *E. coli* K-12 ORF archive): unique resources for biological research. DNA Res 12:291–299. https://doi.org/10.1093/dnares/dsi012.
120. McGrath PT, Iniesta AA, Ryan KR, Shapiro L, McAdams HH. 2006. A dynamically localized protease complex and a polar specificity factor control a cell cycle master regulator. Cell 124:535–547. https://doi.org/10.1016/j.cell.2005.12.033.
121. Kirstein J, Strahl H, Molière N, Hamoen LW, Turgay K. 2008. Localization of general and regulatory proteolysis in *Bacillus subtilis* cells. Mol Microbiol 70:682–694. https://doi.org/10.1111/j.1365-2958.2008.06438.x.
122. Simmons LA, Grossman AD, Walker GC. 2008. Clp and Lon proteases occupy distinct subcellular positions in *Bacillus subtilis*. J Bacteriol 190:6758–6768. https://doi.org/10.1128/JB.00590-08.
123. Kirstein J, Hoffmann A, Lilie H, Schmidt R, Rübsamen-Waigmann H, Brötz-Oesterhelt H, Mogk A, Turgay K. 2009. The antibiotic ADEP reprogrammes ClpP, switching it from a regulated to an uncontrolled protease. EMBO Mol Med 1:37–49. https://doi.org/10.1002/emmm.200900002.
124. Werner JN, Chen EY, Guberman JM, Zippilli AR, Irgon JJ, Gitai Z. 2009. Quantitative genome-scale analysis of protein localization in an asymmetric bacterium. Proc Natl Acad Sci U S A 106:7858–7863. https://doi.org/10.1073/pnas.0901781106.
125. Jones LJ, Carballido-López R, Errington J. 2001. Control of cell shape in bacteria: helical, actin-like filaments in *Bacillus subtilis*. Cell 104:913–922. https://doi.org/10.1016/S0092-8674(01)00287-2.
126. Defeu Soufo HJ, Graumann PL. 2004. Dynamic movement of actin-like proteins within bacterial cells. EMBO Rep 5:789–794. https://doi.org/10.1038/sj.embor.7400209.
127. Defeu Soufo HJ, Graumann PL. 2006. Dynamic localization and interaction with other *Bacillus subtilis* actin-like proteins are important for the function of MreB. Mol Microbiol 62:1340–1356. https://doi.org/10.1111/j.1365-2958.2006.05457.x.
128. Shih YL, Kawagishi I, Rothfield L. 2005. The MreB and Min cytoskeletal-like systems play independent roles in prokaryotic polar differentiation. Mol Microbiol 58:917–928. https://doi.org/10.1111/j.1365-2958.2005.04841.x.
129. Vats P, Rothfield L. 2007. Duplication and segregation of the actin (MreB) cytoskeleton during the prokaryotic cell cycle. Proc Natl Acad Sci U S A 104:17795–17800. https://doi.org/10.1073/pnas.0708739104.
130. Vats P, Shih YL, Rothfield L. 2009. Assembly of the MreB-associated cytoskeletal ring of *Escherichia coli*. Mol Microbiol 72:170–182. https://doi.org/10.1111/j.1365-2958.2009.06632.x.
131. Wang S, Furchtgott L, Huang KC, Shaevitz JW. 2012. Helical insertion of peptidoglycan produces chiral ordering of the bacterial cell wall. Proc Natl Acad Sci U S A 109:E595–604. https://doi.org/10.1073/pnas.1117132109.
132. Swulius MT, Jensen GJ. 2012. The helical MreB cytoskeleton in *Escherichia coli* MC1000/pLE7 is an artifact of the N-terminal yellow fluorescent protein tag. J Bacteriol 194:6382–6386. https://doi.org/10.1128/JB.00505-12.
133. Ghodke H, Caldas VE, Punter CM, van Oijen AM, Robinson A. 2016. Single-molecule specific mislocalization of red fluorescent proteins in live *Escherichia coli*. Biophys J 111:25–27. https://doi.org/10.1016/j.bpj.2016.05.047.
134. Govers SK, Mortier J, Adam A, Aertsen A. 2018. Protein aggregates encode epigenetic memory of stressful encounters in individual *Escherichia coli* cells. PLoS Biol 16:e2003853. https://doi.org/10.1371/journal.pbio.2003853.
135. Hale CA, de Boer PA. 1997. Direct binding of FtsZ to ZipA, an essential component of the septal ring structure that mediates cell division in *Escherichia coli*. Cell 88:175–185. https://doi.org/10.1016/S0092-8674(00)81838-3.
136. Gueiros-Filho FJ, Losick R. 2002. A widely conserved bacterial cell division protein that promotes assembly of the tubulin-like protein FtsZ. Genes Dev 16:2544–2556. https://doi.org/10.1101/gad.1014102.
137. Gibbs KA, Isaac DD, Xu J, Hendrix RW, Silhavy TJ, Theriot JA. 2004. Complex spatial distribution and dynamics of an abundant *Escherichia coli* outer membrane protein, LamB. Mol Microbiol 53:1771–1783. https://doi.org/10.1111/j.1365-2958.2004.04242.x.
138. Haeusser DP, Schwartz RL, Smith AM, Oates ME, Levin PA. 2004. EzrA prevents aberrant cell division by modulating assembly of the cytoskeletal protein FtsZ. Mol Microbiol 52:801–814. https://doi.org/10.1111/j.1365-2958.2004.04016.x.
139. Ghodke H, Paudel BP, Lewis JS, Jergic S, Gopal K, Romero ZJ, Wood EA, Woodgate R, Cox MM, van Oijen AM. 2019. Spatial and temporal organization of RecA in the *Escherichia coli* DNA-damage response. Elife 8:e42761. https://doi.org/10.7554/eLife.42761.
140. Dedecker P, De Schryver FC, Hofkens J. 2013. Fluorescent proteins: shine on, you crazy diamond. J Am Chem Soc 135:2387–2402. https://doi.org/10.1021/ja309768d.
141. Tiwari DK, Nagai T. 2013. Smart fluorescent proteins: innovation for barrier-free superresolution imaging in living cells. Dev Growth Differ 55:491–507. https://doi.org/10.1111/dgd.12064.
142. Lukyanov KA, Chudakov DM, Lukyanov S, Verkhusha VV. 2005. Innovation: photoactivatable fluorescent proteins. Nat Rev Mol Cell Biol 6:885–891. https://doi.org/10.1038/nrm1741.
143. Terskikh A, Fradkov A, Ermakova G, Zaraisky A, Tan P, Kajava AV, Zhao X, Lukyanov S, Matz M, Kim S, Weissman I, Siebert P. 2000. "Fluorescent timer": protein that changes color with time. Science 290:1585–1588. https://doi.org/10.1126/science.290.5496.1585.
144. Patterson GH, Lippincott-Schwartz J. 2002. A photoactivatable GFP for selective photolabeling of proteins and cells. Science 297:1873–1877. https://doi.org/10.1126/science.1074952.
145. Verkhusha VV, Sorkin A. 2005. Conversion of the monomeric red fluorescent protein into a photoactivatable probe. Chem Biol 12:279–285. https://doi.org/10.1016/j.chembiol.2005.01.005.
146. Subach FV, Patterson GH, Manley S, Gillette JM, Lippincott-Schwartz J, Verkhusha VV. 2009. Photoactivatable mCherry for high-resolution two-color fluorescence microscopy. Nat Methods 6:153–159. https://doi.org/10.1038/nmeth.1298.
147. Subach FV, Patterson GH, Renz M, Lippincott-Schwartz J, Verkhusha VV. 2010. Bright monomeric photoactivatable red fluorescent protein for two-color super-resolution sptPALM of live cells. J Am Chem Soc 132:6481–6491. https://doi.org/10.1021/ja100906g.
148. Gunewardene MS, Subach FV, Gould TJ, Penoncello GP, Gudheti MV, Verkhusha VV, Hess ST. 2011. Superresolution imaging of multiple fluorescent proteins with highly overlapping emission spectra in living cells. Biophys J 101:1522–1528. https://doi.org/10.1016/j.bpj.2011.07.049.
149. Wachter RM, Watkins JL, Kim H. 2010. Mechanistic diversity of red fluorescence acquisition by GFP-like proteins. Biochemistry 49:7417–7427. https://doi.org/10.1021/bi100901h.
150. Wachter RM. 2017. Photoconvertible fluorescent proteins and the role

of dynamics in protein evolution. Int J Mol Sci 18:1792. https://doi.org/10.3390/ijms18081792.
151. Ando R, Hama H, Yamamoto-Hino M, Mizuno H, Miyawaki A. 2002. An optical marker based on the UV-induced green-to-red photoconversion of a fluorescent protein. Proc Natl Acad Sci U S A 99:12651–12656. https://doi.org/10.1073/pnas.202320599.
152. Gurskaya NG, Verkhusha VV, Shcheglov AS, Staroverov DB, Chepurnykh TV, Fradkov AF, Lukyanov S, Lukyanov KA. 2006. Engineering of a monomeric green-to-red photoactivatable fluorescent protein induced by blue light. Nat Biotechnol 24:461–465. https://doi.org/10.1038/nbt1191.
153. Habuchi S, Tsutsui H, Kochaniak AB, Miyawaki A, van Oijen AM. 2008. mKikGR, a monomeric photoswitchable fluorescent protein. PLoS One 3:e3944. https://doi.org/10.1371/journal.pone.0003944.
154. McKinney SA, Murphy CS, Hazelwood KL, Davidson MW, Looger LL. 2009. A bright and photostable photoconvertible fluorescent protein. Nat Methods 6:131–133. https://doi.org/10.1038/nmeth.1296.
155. McEvoy AL, Hoi H, Bates M, Platonova E, Cranfill PJ, Baird MA, Davidson MW, Ewers H, Liphardt J, Campbell RE. 2012. mMaple: a photoconvertible fluorescent protein for use in multiple imaging modalities. PLoS One 7:e51314. https://doi.org/10.1371/journal.pone.0051314.
156. Zhang M, Chang H, Zhang Y, Yu J, Wu L, Ji W, Chen J, Liu B, Lu J, Liu Y, Zhang J, Xu P, Xu T. 2012. Rational design of true monomeric and bright photoactivatable fluorescent proteins. Nat Methods 9:727–729. https://doi.org/10.1038/nmeth.2021.
157. Ando R, Mizuno H, Miyawaki A. 2004. Regulated fast nucleocytoplasmic shuttling observed by reversible protein highlighting. Science 306:1370–1373. https://doi.org/10.1126/science.1102506.
158. Habuchi S, Ando R, Dedecker P, Verheijen W, Mizuno H, Miyawaki A, Hofkens J. 2005. Reversible single-molecule photoswitching in the GFP-like fluorescent protein Dronpa. Proc Natl Acad Sci U S A 102:9511–9516. https://doi.org/10.1073/pnas.0500489102.
159. Dedecker P, Hotta J, Ando R, Miyawaki A, Engelborghs Y, Hofkens J. 2006. Fast and reversible photoswitching of the fluorescent protein Dronpa as evidenced by fluorescence correlation spectroscopy. Biophys J 91:L45–L47. https://doi.org/10.1529/biophysj.106.089789.
160. Adam V, Lelimousin M, Boehme S, Desfonds G, Nienhaus K, Field MJ, Wiedenmann J, McSweeney S, Nienhaus GU, Bourgeois D. 2008. Structural characterization of IrisFP, an optical highlighter undergoing multiple photo-induced transformations. Proc Natl Acad Sci U S A 105:18343–18348. https://doi.org/10.1073/pnas.0805949105.
161. Adam V, Moeyaert B, David CC, Mizuno H, Lelimousin M, Dedecker P, Ando R, Miyawaki A, Michiels J, Engelborghs Y, Hofkens J. 2011. Rational design of photoconvertible and biphotochromic fluorescent proteins for advanced microscopy applications. Chem Biol 18:1241–1251. https://doi.org/10.1016/j.chembiol.2011.08.007.
162. Brakemann T, Stiel AC, Weber G, Andresen M, Testa I, Grotjohann T, Leutenegger M, Plessmann U, Urlaub H, Eggeling C, Wahl MC, Hell SW, Jakobs S. 2011. A reversibly photoswitchable GFP-like protein with fluorescence excitation decoupled from switching. Nat Biotechnol 29:942–947. https://doi.org/10.1038/nbt.1952.
163. Duncan RR, Greaves J, Wiegand UK, Matskevich I, Bodammer G, Apps DK, Shipston MJ, Chow RH. 2003. Functional and spatial segregation of secretory vesicle pools according to vesicle age. Nature 422:176–180. https://doi.org/10.1038/nature01389.
164. Mirabella R, Franken C, van der Krogt GN, Bisseling T, Geurts R. 2004. Use of the fluorescent timer DsRED-E5 as reporter to monitor dynamics of gene activity in plants. Plant Physiol 135:1879–1887. https://doi.org/10.1104/pp.103.038539.
165. Subach FV, Subach OM, Gundorov IS, Morozova KS, Piatkevich KD, Cuervo AM, Verkhusha VV. 2009. Monomeric fluorescent timers that change color from blue to red report on cellular trafficking. Nat Chem Biol 5:118–126. https://doi.org/10.1038/nchembio.138.
166. Lavis LD. 2017. Teaching old dyes new tricks: biological probes built from fluoresceins and rhodamines. Annu Rev Biochem 86:825–843. https://doi.org/10.1146/annurev-biochem-061516-044839.
167. Kocaoglu O, Carlson EE. 2016. Progress and prospects for small-molecule probes of bacterial imaging. Nat Chem Biol 12:472–478. https://doi.org/10.1038/nchembio.2109.
168. Lavis LD, Raines RT. 2008. Bright ideas for chemical biology. ACS Chem Biol 3:142–155. https://doi.org/10.1021/cb700248m.
169. Lavis LD, Raines RT. 2014. Bright building blocks for chemical biology. ACS Chem Biol 9:855–866. https://doi.org/10.1021/cb500078u.
170. Fu Y, Finney NS. 2018. Small-molecule fluorescent probes and their design. RSC Adv 8:29051–29061. https://doi.org/10.1039/C8RA02297F.
171. Sun Q, Margolin W. 1998. FtsZ dynamics during the division cycle of live *Escherichia coli* cells. J Bacteriol 180:2050–2056. https://doi.org/10.1128/JB.180.8.2050-2056.1998.
172. Pogliano J, Osborne N, Sharp MD, Abanes-De Mello A, Perez A, Sun YL, Pogliano K. 1999. A vital stain for studying membrane dynamics in bacteria: a novel mechanism controlling septation during *Bacillus subtilis* sporulation. Mol Microbiol 31:1149–1159. https://doi.org/10.1046/j.1365-2958.1999.01255.x.
173. Kubista M, Akerman B, Nordén B. 1987. Characterization of interaction between DNA and 4′,6-diamidino-2-phenylindole by optical spectroscopy. Biochemistry 26:4545–4553. https://doi.org/10.1021/bi00388a057.
174. Eriksson S, Kim SK, Kubista M, Nordén B. 1993. Binding of 4′,6-diamidino-2-phenylindole (DAPI) to AT regions of DNA: evidence for an allosteric conformational change. Biochemistry 32:2987–2998. https://doi.org/10.1021/bi00063a009.
175. Wery M, Woldringh CL, Rouviere-Yaniv J. 2001. HU-GFP and DAPI colocalize on the *Escherichia coli* nucleoid. Biochimie 83:193–200. https://doi.org/10.1016/S0300-9084(01)01254-8.
176. Ursell TS, Nguyen J, Monds RD, Colavin A, Billings G, Ouzounov N, Gitai Z, Shaevitz JW, Huang KC. 2014. Rod-like bacterial shape is maintained by feedback between cell curvature and cytoskeletal localization. Proc Natl Acad Sci U S A 111:E1025–E1034. https://doi.org/10.1073/pnas.1317174111.
177. Jensen RB, Shapiro L. 1999. The *Caulobacter crescentus smc* gene is required for cell cycle progression and chromosome segregation. Proc Natl Acad Sci U S A 96:10661–10666. https://doi.org/10.1073/pnas.96.19.10661.
178. Kocaoglu O, Calvo RA, Sham LT, Cozy LM, Lanning BR, Francis S, Winkler ME, Kearns DB, Carlson EE. 2012. Selective penicillin-binding protein imaging probes reveal substructure in bacterial cell division. ACS Chem Biol 7:1746–1753. https://doi.org/10.1021/cb300329r.
179. Berlatzky IA, Rouvinski A, Ben-Yehuda S. 2008. Spatial organization of a replicating bacterial chromosome. Proc Natl Acad Sci U S A 105:14136–14140. https://doi.org/10.1073/pnas.0804982105.
180. Den Blaauwen T, Buddelmeijer N, Aarsman ME, Hameete CM, Nanninga N. 1999. Timing of FtsZ assembly in *Escherichia coli*. J Bacteriol 181:5167–5175. https://doi.org/10.1128/JB.181.17.5167-5175.1999.
181. Dumont A, Malleron A, Awwad M, Dukan S, Vauzeilles B. 2012. Click-mediated labeling of bacterial membranes through metabolic modification of the lipopolysaccharide inner core. Angew Chem Int Ed Engl 51:3143–3146. https://doi.org/10.1002/anie.201108127.
182. Diaper JP, Tither K, Edwards C. 1992. Rapid assessment of bacterial viability by flow cytometry. Appl Microbiol Biotechnol 38:268–272. https://doi.org/10.1007/BF00174481.
183. Thanbichler M, Shapiro L. 2006. MipZ, a spatial regulator coordinating chromosome segregation with cell division in *Caulobacter*. Cell 126:147–162. https://doi.org/10.1016/j.cell.2006.05.038.
184. Barlag B, Beutel O, Janning D, Czarniak F, Richter CP, Kommnick C, Göser V, Kurre R, Fabiani F, Erhardt M, Piehler J, Hensel M. 2016. Single molecule super-resolution imaging of proteins in living *Salmonella enterica* using self-labelling enzymes. Sci Rep 6:31601. https://doi.org/10.1038/srep31601.
185. Ke N, Landgraf D, Paulsson J, Berkmen M. 2016. Visualization of periplasmic and cytoplasmic proteins with a self-labeling protein tag. J Bacteriol 198:1035–1043. https://doi.org/10.1128/JB.00864-15.
186. Yang Z, Weisshaar JC. 2018. HaloTag assay suggests common mechanism of *E. coli* membrane permeabilization induced by cationic peptides. ACS Chem Biol 13:2161–2169. https://doi.org/10.1021/acschembio.8b00336.
187. Monmeyran A, Thomen P, Jonquière H, Sureau F, Li C, Plamont MA, Douarche C, Casella JF, Gautier A, Henry N. 2018. The inducible chemical-genetic fluorescent marker FAST outperforms classical fluorescent proteins in the quantitative reporting of bacterial biofilm dynamics. Sci Rep 8:10336. https://doi.org/10.1038/s41598-018-28643-z.
188. Bruchez MP. 2015. Dark dyes-bright complexes: fluorogenic protein labeling. Curr Opin Chem Biol 27:18–23. https://doi.org/10.1016/j.cbpa.2015.05.014.
189. Jullien L, Gautier A. 2015. Fluorogen-based reporters for fluorescence imaging: a review. Methods Appl Fluoresc 3:042007. https://doi.org/10.1088/2050-6120/3/4/042007.
190. Li C, Tebo AG, Gautier A. 2017. Fluorogenic labeling strategies for biological imaging. Int J Mol Sci 18.
191. Adams SR, Campbell RE, Gross LA, Martin BR, Walkup GK, Yao Y, Llopis J,

Tsien RY. 2002. New biarsenical ligands and tetracysteine motifs for protein labeling *in vitro* and *in vivo*: synthesis and biological applications. J Am Chem Soc 124:6063–6076. https://doi.org/10.1021/ja017687n.

192. Adams SR, Tsien RY. 2008. Preparation of the membrane-permeant biarsenicals FlAsH-EDT2 and ReAsH-EDT2 for fluorescent labeling of tetracysteine-tagged proteins. Nat Protoc 3:1527–1534. https://doi.org/10.1038/nprot.2008.144.
193. Hoffmann C, Gaietta G, Zürn A, Adams SR, Terrillon S, Ellisman MH, Tsien RY, Lohse MJ. 2010. Fluorescent labeling of tetracysteine-tagged proteins in intact cells. Nat Protoc 5:1666–1677. https://doi.org/10.1038/nprot.2010.129.
194. Cabeen MT, Charbon G, Vollmer W, Born P, Ausmees N, Weibel DB, Jacobs-Wagner C. 2009. Bacterial cell curvature through mechanical control of cell growth. EMBO J 28:1208–1219. https://doi.org/10.1038/emboj.2009.61.
195. Charbon G, Cabeen MT, Jacobs-Wagner C. 2009. Bacterial intermediate filaments: *in vivo* assembly, organization, and dynamics of crescentin. Genes Dev 23:1131–1144. https://doi.org/10.1101/gad.1795509.
196. Laloux G, Jacobs-Wagner C. 2013. Spatiotemporal control of PopZ localization through cell cycle-coupled multimerization. J Cell Biol 201:827–841. https://doi.org/10.1083/jcb.201303036.
197. Los GV, Encell LP, McDougall MG, Hartzell DD, Karassina N, Zimprich C, Wood MG, Learish R, Ohana RF, Urh M, Simpson D, Mendez J, Zimmerman K, Otto P, Vidugiris G, Zhu J, Darzins A, Klaubert DH, Bulleit RF, Wood KV. 2008. HaloTag: a novel protein labeling technology for cell imaging and protein analysis. ACS Chem Biol 3:373–382. https://doi.org/10.1021/cb800025k.
198. Encell LP, Friedman Ohana R, Zimmerman K, Otto P, Vidugiris G, Wood MG, Los GV, McDougall MG, Zimprich C, Karassina N, Learish RD, Hurst R, Hartnett J, Wheeler S, Stecha P, English J, Zhao K, Mendez J, Benink HA, Murphy N, Daniels DL, Slater MR, Urh M, Darzins A, Klaubert DH, Bulleit RF, Wood KV. 2012. Development of a dehalogenase-based protein fusion tag capable of rapid, selective and covalent attachment to customizable ligands. Curr Chem Genomics 6:55–71. https://doi.org/10.2174/1875397301206010055.
199. Peterson SN, Kwon K. 2012. The HaloTag: improving soluble expression and applications in protein functional analysis. Curr Chem Genomics 6:8–17. https://doi.org/10.2174/1875397301206010008.
200. Silpe JE, Bassler BL. 2019. A host-produced quorum-sensing autoinducer controls a phage lysis-lysogeny decision. Cell 176:268–280.e13. https://doi.org/10.1016/j.cell.2018.10.059.
201. Peluso EA, Updegrove TB, Chen J, Shroff H, Ramamurthi KS. 2019. A 2-dimensional ratchet model describes assembly initiation of a specialized bacterial cell surface. Proc Natl Acad Sci U S A 116:21789–21799. https://doi.org/10.1073/pnas.1907397116.
202. Gautier A, Juillerat A, Heinis C, Corrêa IR, Kindermann M, Beaufils F, Johnsson K. 2008. An engineered protein tag for multiprotein labeling in living cells. Chem Biol 15:128–136. https://doi.org/10.1016/j.chembiol.2008.01.007.
203. Pereira FC, Saujet L, Tomé AR, Serrano M, Monot M, Couture-Tosi E, Martin-Verstraete I, Dupuy B, Henriques AO. 2013. The spore differentiation pathway in the enteric pathogen *Clostridium difficile*. PLoS Genet 9:e1003782. https://doi.org/10.1371/journal.pgen.1003782.
204. Saujet L, Pereira FC, Serrano M, Soutourina O, Monot M, Shelyakin PV, Gelfand MS, Dupuy B, Henriques AO, Martin-Verstraete I. 2013. Genome-wide analysis of cell type-specific gene transcription during spore formation in *Clostridium difficile*. PLoS Genet 9:e1003756. https://doi.org/10.1371/journal.pgen.1003756.
205. Sun X, Zhang A, Baker B, Sun L, Howard A, Buswell J, Maurel D, Masharina A, Johnsson K, Noren CJ, Xu MQ, Corrêa IR. 2011. Development of SNAP-tag fluorogenic probes for wash-free fluorescence imaging. Chembiochem 12:2217–2226. https://doi.org/10.1002/cbic.201100173.
206. Yapici I, Lee KS, Berbasova T, Nosrati M, Jia X, Vasileiou C, Wang W, Santos EM, Geiger JH, Borhan B. 2015. Turn-on" protein fluorescence: *in situ* formation of cyanine dyes. J Am Chem Soc 137:1073–1080. https://doi.org/10.1021/ja506376j.
207. Herwig L, Rice AJ, Bedbrook CN, Zhang RK, Lignell A, Cahn JKB, Renata H, Dodani SC, Cho I, Cai L, Gradinaru V, Arnold FH. 2017. Directed evolution of a bright near-infrared fluorescent rhodopsin using a synthetic chromophore. Cell Chem Biol 24:415–425. https://doi.org/10.1016/j.chembiol.2017.02.008.
208. McRee DE, Tainer JA, Meyer TE, Van Beeumen J, Cusanovich MA, Getzoff ED. 1989. Crystallographic structure of a photoreceptor protein at 2.4 A resolution. Proc Natl Acad Sci U S A 86:6533–6537. https://doi.org/10.1073/pnas.86.17.6533.
209. Baca M, Borgstahl GE, Boissinot M, Burke PM, Williams DR, Slater KA, Getzoff ED. 1994. Complete chemical structure of photoactive yellow protein: novel thioester-linked 4-hydroxycinnamyl chromophore and photocycle chemistry. Biochemistry 33:14369–14377. https://doi.org/10.1021/bi00252a001.
210. Borgstahl GE, Williams DR, Getzoff ED. 1995. 1.4 Å structure of photoactive yellow protein, a cytosolic photoreceptor: unusual fold, active site, and chromophore. Biochemistry 34:6278–6287. https://doi.org/10.1021/bi00019a004.
211. Murphy JT, Lagarias JC. 1997. The phytofluors: a new class of fluorescent protein probes. Curr Biol 7:870–876. https://doi.org/10.1016/S0960-9822(06)00375-7.
212. Fischer AJ, Lagarias JC. 2004. Harnessing phytochrome's glowing potential. Proc Natl Acad Sci U S A 101:17334–17339. https://doi.org/10.1073/pnas.0407645101.
213. Filonov GS, Piatkevich KD, Ting LM, Zhang J, Kim K, Verkhusha VV. 2011. Bright and stable near-infrared fluorescent protein for *in vivo* imaging. Nat Biotechnol 29:757–761. https://doi.org/10.1038/nbt.1918.
214. Auldridge ME, Satyshur KA, Anstrom DM, Forest KT. 2012. Structure-guided engineering enhances a phytochrome-based infrared fluorescent protein. J Biol Chem 287:7000–7009. https://doi.org/10.1074/jbc.M111.295121.
215. Bhattacharya S, Auldridge ME, Lehtivuori H, Ihalainen JA, Forest KT. 2014. Origins of fluorescence in evolved bacteriophytochromes. J Biol Chem 289:32144–32152. https://doi.org/10.1074/jbc.M114.589739.
216. Mukherjee A, Schroeder CM. 2015. Flavin-based fluorescent proteins: emerging paradigms in biological imaging. Curr Opin Biotechnol 31:16–23. https://doi.org/10.1016/j.copbio.2014.07.010.
217. Shcherbakova DM, Baloban M, Verkhusha VV. 2015. Near-infrared fluorescent proteins engineered from bacterial phytochromes. Curr Opin Chem Biol 27:52–63. https://doi.org/10.1016/j.cbpa.2015.06.005.
218. Chernov KG, Redchuk TA, Omelina ES, Verkhusha VV. 2017. Near-infrared fluorescent proteins, biosensors, and optogenetic tools engineered from phytochromes. Chem Rev 117:6423–6446. https://doi.org/10.1021/acs.chemrev.6b00700.
219. Simon J, Losi A, Zhao KH, Gärtner W. 2017. FRET in a synthetic flavin- and bilin-binding protein. Photochem Photobiol 93:1057–1062. https://doi.org/10.1111/php.12707.
220. Oliinyk OS, Shemetov AA, Pletnev S, Shcherbakova DM, Verkhusha VV. 2019. Smallest near-infrared fluorescent protein evolved from cyanobacteriochrome as versatile tag for spectral multiplexing. Nat Commun 10:279. https://doi.org/10.1038/s41467-018-08050-8.
221. Buckley AM, Petersen J, Roe AJ, Douce GR, Christie JM. 2015. LOV-based reporters for fluorescence imaging. Curr Opin Chem Biol 27:39–45. https://doi.org/10.1016/j.cbpa.2015.05.011.
222. Salomon M, Christie JM, Knieb E, Lempert U, Briggs WR. 2000. Photochemical and mutational analysis of the FMN-binding domains of the plant blue light receptor, phototropin. Biochemistry 39:9401–9410. https://doi.org/10.1021/bi000585+.
223. Swartz TE, Corchnoy SB, Christie JM, Lewis JW, Szundi I, Briggs WR, Bogomolni RA. 2001. The photocycle of a flavin-binding domain of the blue light photoreceptor phototropin. J Biol Chem 276:36493–36500. https://doi.org/10.1074/jbc.M103114200.
224. Kasahara M, Swartz TE, Olney MA, Onodera A, Mochizuki N, Fukuzawa H, Asamizu E, Tabata S, Kanegae H, Takano M, Christie JM, Nagatani A, Briggs WR. 2002. Photochemical properties of the flavin mononucleotide-binding domains of the phototropins from *Arabidopsis*, rice, and *Chlamydomonas reinhardtii*. Plant Physiol 129:762–773. https://doi.org/10.1104/pp.002410.
225. Christie JM, Corchnoy SB, Swartz TE, Hokenson M, Han IS, Briggs WR, Bogomolni RA. 2007. Steric interactions stabilize the signaling state of the LOV2 domain of phototropin 1. Biochemistry 46:9310–9319. https://doi.org/10.1021/bi700852w.
226. Bonazzi D, Lo Schiavo V, Machata S, Djafer-Cherif I, Nivoit P, Manriquez V, Tanimoto H, Husson J, Henry N, Chaté H, Voituriez R, Duménil G. 2018. Intermittent pili-mediated forces fluidize *Neisseria meningitidis* aggregates promoting vascular colonization. Cell 174:143–155.e16. https://doi.org/10.1016/j.cell.2018.04.010.
227. Zhang LC, Risoul V, Latifi A, Christie JM, Zhang CC. 2013. Exploring the size limit of protein diffusion through the periplasm in cyanobacterium *Anabaena* sp. PCC 7120 using the 13-kDa iLOV fluorescent protein. Res Microbiol 164:710–717. https://doi.org/10.1016/j.resmic.2013.05.004.

228. Drepper T, Eggert T, Circolone F, Heck A, Krauss U, Guterl J-K, Wendorff M, Losi A, Gärtner W, Jaeger K-E. 2007. Reporter proteins for *in vivo* fluorescence without oxygen. Nat Biotechnol 25:443–445. https://doi.org/10.1038/nbt1293.
229. Drepper T, Huber R, Heck A, Circolone F, Hillmer AK, Büchs J, Jaeger KE. 2010. Flavin mononucleotide-based fluorescent reporter proteins outperform green fluorescent protein-like proteins as quantitative *in vivo* real-time reporters. Appl Environ Microbiol 76:5990–5994. https://doi.org/10.1128/AEM.00701-10.
230. Takacs CN, Kloos ZA, Scott M, Rosa PA, Jacobs-Wagner C. 2018. Fluorescent proteins, promoters, and selectable markers for applications in the Lyme disease spirochete *Borrelia burgdorferi*. Appl Environ Microbiol 84:e01824-18. https://doi.org/10.1128/AEM.01824-18.
231. Webb DJ, Brown CM. 2013. Epi-fluorescence microscopy. Methods Mol Biol 931:29–59. https://doi.org/10.1007/978-1-62703-056-4_2.
232. Fisher JK, Bourniquel A, Witz G, Weiner B, Prentiss M, Kleckner N. 2013. Four-dimensional imaging of *Escherichia coli* nucleoid organization and dynamics in living cells. Cell 153:882–895. https://doi.org/10.1016/j.cell.2013.04.006.
233. Combs CA, Shroff H. 2017. Fluorescence microscopy: a concise guide to current imaging methods. Curr Protoc Neurosci 79:2.1.1–2.1.25.
234. Yao Z, Carballido-López R. 2014. Fluorescence imaging for bacterial cell biology: from localization to dynamics, from ensembles to single molecules. Annu Rev Microbiol 68:459–476. https://doi.org/10.1146/annurev-micro-091213-113034.
235. Hardham AR. 2012. Confocal microscopy in plant-pathogen interactions. Methods Mol Biol 835:295–309. https://doi.org/10.1007/978-1-61779-501-5_18.
236. Lepanto P, Lecumberry F, Rossello J, Kierbel A. 2014. A confocal microscopy image analysis method to measure adhesion and internalization of *Pseudomonas aeruginosa* multicellular structures into epithelial cells. Mol Cell Probes 28:1–5. https://doi.org/10.1016/j.mcp.2013.10.001.
237. Sommerfeld Ross S, Tu MH, Falsetta ML, Ketterer MR, Kiedrowski MR, Horswill AR, Apicella MA, Reinhardt JM, Fiegel J. 2014. Quantification of confocal images of biofilms grown on irregular surfaces. J Microbiol Methods 100:111–120. https://doi.org/10.1016/j.mimet.2014.02.020.
238. Makovcova J, Babak V, Kulich P, Masek J, Slany M, Cincarova L. 2017. Dynamics of mono- and dual-species biofilm formation and interactions between *Staphylococcus aureus* and Gram-negative bacteria. Microb Biotechnol 10:819–832. https://doi.org/10.1111/1751-7915.12705.
239. Cornilleau C, Chastanet A, Billaudeau C, Carballido-López R. 2020. Methods for studying membrane-associated bacterial cytoskeleton proteins *in vivo* by TIRF microscopy. Methods Mol Biol 2101:123–133. https://doi.org/10.1007/978-1-0716-0219-5_8.
240. Domínguez-Escobar J, Chastanet A, Crevenna AH, Fromion V, Wedlich-Söldner R, Carballido-López R. 2011. Processive movement of MreB-associated cell wall biosynthetic complexes in bacteria. Science 333:225–228. https://doi.org/10.1126/science.1203466.
241. Garner EC, Bernard R, Wang W, Zhuang X, Rudner DZ, Mitchison T. 2011. Coupled, circumferential motions of the cell wall synthesis machinery and MreB filaments in *B. subtilis*. Science 333:222–225. https://doi.org/10.1126/science.1203285.
242. Dempwolff F, Wischhusen HM, Specht M, Graumann PL. 2012. The deletion of bacterial dynamin and flotillin genes results in pleiotrophic effects on cell division, cell growth, and in cell shape maintenance. BMC Microbiol 12:298. https://doi.org/10.1186/1471-2180-12-298.
243. Perez AJ, Cesbron Y, Shaw SL, Bazan Villicana J, Tsui HT, Boersma MJ, Ye ZA, Tovpeko Y, Dekker C, Holden S, Winkler ME. 2019. Movement dynamics of divisome proteins and PBP2x:FtsW in cells of *Streptococcus pneumonia*. Proc Natl Acad Sci U S A 116:3211–3220. https://doi.org/10.1073/pnas.1816018116.
244. Sako Y. 2006. Imaging single molecules in living cells for systems biology. Mol Syst Biol 2:56. https://doi.org/10.1038/msb4100100.
245. Tokunaga M, Imamoto N, Sakata-Sogawa K. 2008. Highly inclined thin illumination enables clear single-molecule imaging in cells. Nat Methods 5:159–161. https://doi.org/10.1038/nmeth1171.
246. Fleming TC, Shin JY, Lee SH, Becker E, Huang KC, Bustamante C, Pogliano K. 2010. Dynamic SpoIIIE assembly mediates septal membrane fission during *Bacillus subtilis* sporulation. Genes Dev 24:1160–1172. https://doi.org/10.1101/gad.1925210.
247. Sharp MD, Pogliano K. 2002. Role of cell-specific SpoIIIE assembly in polarity of DNA transfer. Science 295:137–139. https://doi.org/10.1126/science.1066274.
248. Rueff AS, Chastanet A, Domínguez-Escobar J, Yao Z, Yates J, Prejean MV, Delumeau O, Noirot P, Wedlich-Söldner R, Filipe SR, Carballido-López R. 2014. An early cytoplasmic step of peptidoglycan synthesis is associated with MreB in *Bacillus subtilis*. Mol Microbiol 91:348–362. https://doi.org/10.1111/mmi.12467.
249. Raskin DM, de Boer PA. 1999. Rapid pole-to-pole oscillation of a protein required for directing division to the middle of *Escherichia coli*. Proc Natl Acad Sci U S A 96:4971–4976. https://doi.org/10.1073/pnas.96.9.4971.
250. Elowitz MB, Surette MG, Wolf PE, Stock JB, Leibler S. 1999. Protein mobility in the cytoplasm of *Escherichia coli*. J Bacteriol 181:197–203. https://doi.org/10.1128/JB.181.1.197-203.1999.
251. English BP, Hauryliuk V, Sanamrad A, Tankov S, Dekker NH, Elf J. 2011. Single-molecule investigations of the stringent response machinery in living bacterial cells. Proc Natl Acad Sci U S A 108:E365–E373. https://doi.org/10.1073/pnas.1102255108.
252. Mullineaux CW, Nenninger A, Ray N, Robinson C. 2006. Diffusion of green fluorescent protein in three cell environments in *Escherichia coli*. J Bacteriol 188:3442–3448. https://doi.org/10.1128/JB.188.10.3442-3448.2006.
253. Axelrod D, Koppel DE, Schlessinger J, Elson E, Webb WW. 1976. Mobility measurement by analysis of fluorescence photobleaching recovery kinetics. Biophys J 16:1055–1069. https://doi.org/10.1016/S0006-3495(76)85755-4.
254. Koppel DE, Axelrod D, Schlessinger J, Elson EL, Webb WW. 1976. Dynamics of fluorescence marker concentration as a probe of mobility. Biophys J 16:1315–1329. https://doi.org/10.1016/S0006-3495(76)85776-1.
255. Cowan AE, Koppel DE, Setlow B, Setlow P. 2003. A soluble protein is immobile in dormant spores of *Bacillus subtilis* but is mobile in germinated spores: implications for spore dormancy. Proc Natl Acad Sci U S A 100:4209–4214. https://doi.org/10.1073/pnas.0636762100.
256. Stricker J, Maddox P, Salmon ED, Erickson HP. 2002. Rapid assembly dynamics of the *Escherichia coli* FtsZ-ring demonstrated by fluorescence recovery after photobleaching. Proc Natl Acad Sci U S A 99:3171–3175. https://doi.org/10.1073/pnas.052595099.
257. Carballido-López R, Errington J. 2003. The bacterial cytoskeleton: *in vivo* dynamics of the actin-like protein Mbl of *Bacillus subtilis*. Dev Cell 4:19–28. https://doi.org/10.1016/S1534-5807(02)00403-3.
258. Matroule JY, Lam H, Burnette DT, Jacobs-Wagner C. 2004. Cytokinesis monitoring during development; rapid pole-to-pole shuttling of a signaling protein by localized kinase and phosphatase in *Caulobacter*. Cell 118:579–590. https://doi.org/10.1016/j.cell.2004.08.019.
259. Mignot T, Merlie JP, Zusman DR. 2005. Regulated pole-to-pole oscillations of a bacterial gliding motility protein. Science 310:855–857. https://doi.org/10.1126/science.1119052.
260. Liu NJ, Dutton RJ, Pogliano K. 2006. Evidence that the SpoIIIE DNA translocase participates in membrane fusion during cytokinesis and engulfment. Mol Microbiol 59:1097–1113. https://doi.org/10.1111/j.1365-2958.2005.05004.x.
261. Phair RD, Misteli T. 2001. Kinetic modelling approaches to *in vivo* imaging. Nat Rev Mol Cell Biol 2:898–907. https://doi.org/10.1038/35103000.
262. Kentner D, Sourjik V. 2010. Use of fluorescence microscopy to study intracellular signaling in bacteria. Annu Rev Microbiol 64:373–390. https://doi.org/10.1146/annurev.micro.112408.134205.
263. Clegg RM. 1995. Fluorescence resonance energy transfer. Curr Opin Biotechnol 6:103–110. https://doi.org/10.1016/0958-1669(95)80016-6.
264. Sourjik V, Berg HC. 2002. Receptor sensitivity in bacterial chemotaxis. Proc Natl Acad Sci U S A 99:123–127. https://doi.org/10.1073/pnas.011589998.
265. Truong K, Ikura M. 2001. The use of FRET imaging microscopy to detect protein-protein interactions and protein conformational changes *in vivo*. Curr Opin Struct Biol 11:573–578. https://doi.org/10.1016/S0959-440X(00)00249-9.
266. Christen M, Kulasekara HD, Christen B, Kulasekara BR, Hoffman LR, Miller SI. 2010. Asymmetrical distribution of the second messenger c-di-GMP upon bacterial cell division. Science 328:1295–1297. https://doi.org/10.1126/science.1188658.
267. Abraham BG, Santala V, Tkachenko NV, Karp M. 2014. Fluorescent protein-based FRET sensor for intracellular monitoring of redox status in bacteria at single cell level. Anal Bioanal Chem 406:7195–7204. https://doi.org/10.1007/s00216-014-8165-1.
268. Chakraborty S, Mizusaki H, Kenney LJ. 2015. A FRET-based DNA biosensor tracks OmpR-dependent acidification of *Salmonella* during mac-

rophage infection. PLoS Biol 13:e1002116. https://doi.org/10.1371/journal.pbio.1002116.

269. Maglica Ž, Özdemir E, McKinney JD. 2015. Single-cell tracking reveals antibiotic-induced changes in mycobacterial energy metabolism. mBio 6:e02236-14 – e02214. https://doi.org/10.1128/mBio.02236-14.
270. Chakraborty S, Winardhi RS, Morgan LK, Yan J, Kenney LJ. 2017. Non-canonical activation of OmpR drives acid and osmotic stress responses in single bacterial cells. Nat Commun 8:1587. https://doi.org/10.1038/s41467-017-02030-0.
271. Piston DW, Kremers GJ. 2007. Fluorescent protein FRET: the good, the bad and the ugly. Trends Biochem Sci 32:407–414. https://doi.org/10.1016/j.tibs.2007.08.003.
272. Wouters FS, Bastiaens PI. 2001. Imaging protein-protein interactions by fluorescence resonance energy transfer (FRET) microscopy. Curr Protoc Cell Biol Chapter 17:Unit 17.1.
273. Zeug A, Woehler A, Neher E, Ponimaskin EG. 2012. Quantitative intensity-based FRET approaches–a comparative snapshot. Biophys J 103:1821–1827. https://doi.org/10.1016/j.bpj.2012.09.031.
274. Ma L, Yang F, Zheng J. 2014. Application of fluorescence resonance energy transfer in protein studies. J Mol Struct 1077:87–100. https://doi.org/10.1016/j.molstruc.2013.12.071.
275. Bajar BT, Wang ES, Zhang S, Lin MZ, Chu J. 2016. A guide to fluorescent protein FRET pairs. Sensors (Basel) 16:1488. https://doi.org/10.3390/s16091488.
276. Cui B, Wang Y, Song Y, Wang T, Li C, Wei Y, Luo ZQ, Shen X. 2014. Bioluminescence resonance energy transfer system for measuring dynamic protein-protein interactions in bacteria. mBio 5:e01050-14. https://doi.org/10.1128/mBio.01050-14.
277. Cluzel P, Surette M, Leibler S. 2000. An ultrasensitive bacterial motor revealed by monitoring signaling proteins in single cells. Science 287:1652–1655. https://doi.org/10.1126/science.287.5458.1652.
278. Le TT, Harlepp S, Guet CC, Dittmar K, Emonet T, Pan T, Cluzel P. 2005. Real-time RNA profiling within a single bacterium. Proc Natl Acad Sci U S A 102:9160–9164. https://doi.org/10.1073/pnas.0503311102.
279. Meacci G, Ries J, Fischer-Friedrich E, Kahya N, Schwille P, Kruse K. 2006. Mobility of Min-proteins in *Escherichia coli* measured by fluorescence correlation spectroscopy. Phys Biol 3:255–263. https://doi.org/10.1088/1478-3975/3/4/003.
280. Ferguson ML, Le Coq D, Jules M, Aymerich S, Declerck N, Royer CA. 2011. Absolute quantification of gene expression in individual bacterial cells using two-photon fluctuation microscopy. Anal Biochem 419:250–259. https://doi.org/10.1016/j.ab.2011.08.017.
281. Chow D, Guo L, Gai F, Goulian M. 2012. Fluorescence correlation spectroscopy measurements of the membrane protein TetA in *Escherichia coli* suggest rapid diffusion at short length scales. PLoS One 7:e48600. https://doi.org/10.1371/journal.pone.0048600.
282. Fiche JB, Cattoni DI, Diekmann N, Langerak JM, Clerte C, Royer CA, Margeat E, Doan T, Nöllmann M. 2013. Recruitment, assembly, and molecular architecture of the SpoIIIE DNA pump revealed by super-resolution microscopy. PLoS Biol 11:e1001557. https://doi.org/10.1371/journal.pbio.1001557.
283. Foo YH, Spahn C, Zhang H, Heilemann M, Kenney LJ. 2015. Single cell super-resolution imaging of *E. coli* OmpR during environmental stress. Integr Biol (Camb) 7:1297–1308. https://doi.org/10.1039/c5ib00077g.
284. Diepold A, Sezgin E, Huseyin M, Mortimer T, Eggeling C, Armitage JP. 2017. A dynamic and adaptive network of cytosolic interactions governs protein export by the T3SS injectisome. Nat Commun 8:15940. https://doi.org/10.1038/ncomms15940.
285. Bourges AC, Torres Montaguth OE, Ghosh A, Tadesse WM, Declerck N, Aertsen A, Royer CA. 2017. High pressure activation of the Mrr restriction endonuclease in *Escherichia coli* involves tetramer dissociation. Nucleic Acids Res 45:5323–5332. https://doi.org/10.1093/nar/gkx192.
286. Elson EL. 2011. Fluorescence correlation spectroscopy: past, present, future. Biophys J 101:2855–2870. https://doi.org/10.1016/j.bpj.2011.11.012.
287. Haustein E, Schwille P. 2007. Fluorescence correlation spectroscopy: novel variations of an established technique. Annu Rev Biophys Biomol Struct 36:151–169. https://doi.org/10.1146/annurev.biophys.36.040306.132612.
288. Jameson DM, Ross JA, Albanesi JP. 2009. Fluorescence fluctuation spectroscopy: ushering in a new age of enlightenment for cellular dynamics. Biophys Rev 1:105–118. https://doi.org/10.1007/s12551-009-0013-8.
289. Tian Y, Martinez MM, Pappas D. 2011. Fluorescence correlation spectroscopy: a review of biochemical and microfluidic applications. Appl Spectrosc 65:115A–124A. https://doi.org/10.1366/10-06224.
290. Digman MA, Gratton E. 2011. Lessons in fluctuation correlation spectroscopy. Annu Rev Phys Chem 62:645–668. https://doi.org/10.1146/annurev-physchem-032210-103424.
291. Bag N, Wohland T. 2014. Imaging fluorescence fluctuation spectroscopy: new tools for quantitative bioimaging. Annu Rev Phys Chem 65:225–248. https://doi.org/10.1146/annurev-physchem-040513-103641.
292. Bacia K, Kim SA, Schwille P. 2006. Fluorescence cross-correlation spectroscopy in living cells. Nat Methods 3:83–89. https://doi.org/10.1038/nmeth822.
293. Ferguson ML, Le Coq D, Jules M, Aymerich S, Radulescu O, Declerck N, Royer CA. 2012. Reconciling molecular regulatory mechanisms with noise patterns of bacterial metabolic promoters in induced and repressed states. Proc Natl Acad Sci U S A 109:155–160. https://doi.org/10.1073/pnas.1110541108.
294. Qian H, Elson EL. 1990. On the analysis of high order moments of fluorescence fluctuations. Biophys J 57:375–380. https://doi.org/10.1016/S0006-3495(90)82539-X.
295. Digman MA, Dalal R, Horwitz AF, Gratton E. 2008. Mapping the number of molecules and brightness in the laser scanning microscope. Biophys J 94:2320–2332. https://doi.org/10.1529/biophysj.107.114645.
296. Huang B, Babcock H, Zhuang X. 2010. Breaking the diffraction barrier: super-resolution imaging of cells. Cell 143:1047–1058. https://doi.org/10.1016/j.cell.2010.12.002.
297. Cox S. 2015. Super-resolution imaging in live cells. Dev Biol 401:175–181. https://doi.org/10.1016/j.ydbio.2014.11.025.
298. Coltharp C, Xiao J. 2012. Superresolution microscopy for microbiology. Cell Microbiol 14:1808–1818. https://doi.org/10.1111/cmi.12024.
299. Gahlmann A, Moerner WE. 2014. Exploring bacterial cell biology with single-molecule tracking and super-resolution imaging. Nat Rev Microbiol 12:9–22. https://doi.org/10.1038/nrmicro3154.
300. Tuson HH, Biteen JS. 2015. Unveiling the inner workings of live bacteria using super-resolution microscopy. Anal Chem 87:42–63. https://doi.org/10.1021/ac5041346.
301. Gustafsson MG. 2000. Surpassing the lateral resolution limit by a factor of two using structured illumination microscopy. J Microsc 198:82–87. https://doi.org/10.1046/j.1365-2818.2000.00710.x.
302. Kner P, Chhun BB, Griffis ER, Winoto L, Gustafsson MG. 2009. Super-resolution video microscopy of live cells by structured illumination. Nat Methods 6:339–342. https://doi.org/10.1038/nmeth.1324.
303. Strauss MP, Liew AT, Turnbull L, Whitchurch CB, Monahan LG, Harry EJ. 2012. 3D-SIM super resolution microscopy reveals a bead-like arrangement for FtsZ and the division machinery: implications for triggering cytokinesis. PLoS Biol 10:e1001389. https://doi.org/10.1371/journal.pbio.1001389.
304. Reimold C, Defeu Soufo HJ, Dempwolff F, Graumann PL. 2013. Motion of variable-length MreB filaments at the bacterial cell membrane influences cell morphology. Mol Biol Cell 24:2340–2349. https://doi.org/10.1091/mbc.e12-10-0728.
305. Rust MJ, Bates M, Zhuang X. 2006. Sub-diffraction-limit imaging by stochastic optical reconstruction microscopy (STORM). Nat Methods 3:793–795. https://doi.org/10.1038/nmeth929.
306. Betzig E, Patterson GH, Sougrat R, Lindwasser OW, Olenych S, Bonifacino JS, Davidson MW, Lippincott-Schwartz J, Hess HF. 2006. Imaging intracellular fluorescent proteins at nanometer resolution. Science 313:1642–1645. https://doi.org/10.1126/science.1127344.
307. Ha T, Tinnefeld P. 2012. Photophysics of fluorescent probes for single-molecule biophysics and super-resolution imaging. Annu Rev Phys Chem 63:595–617. https://doi.org/10.1146/annurev-physchem-032210-103340.
308. Greenfield D, McEvoy AL, Shroff H, Crooks GE, Wingreen NS, Betzig E, Liphardt J. 2009. Self-organization of the *Escherichia coli* chemotaxis network imaged with super-resolution light microscopy. PLoS Biol 7:e1000137. https://doi.org/10.1371/journal.pbio.1000137.
309. Wang W, Li GW, Chen C, Xie XS, Zhuang X. 2011. Chromosome organization by a nucleoid-associated protein in live bacteria. Science 333:1445–1449. https://doi.org/10.1126/science.1204697.
310. Bakshi S, Siryaporn A, Goulian M, Weisshaar JC. 2012. Superresolution imaging of ribosomes and RNA polymerase in live *Escherichia coli* cells. Mol Microbiol 85:21–38. https://doi.org/10.1111/j.1365-2958.2012.08081.x.
311. Turner RD, Hurd AF, Cadby A, Hobbs JK, Foster SJ. 2013. Cell wall

elongation mode in Gram-negative bacteria is determined by peptidoglycan architecture. Nat Commun 4:1496. https://doi.org/10.1038/ncomms2503.

312. Jacq M, Adam V, Bourgeois D, Moriscot C, Di Guilmi AM, Vernet T, Morlot C. 2015. Remodeling of the Z-ring nanostructure during the *Streptococcus pneumoniae* cell cycle revealed by photoactivated localization microscopy. mBio 6:e01108-15. https://doi.org/10.1128/mBio.01108-15.
313. Stracy M, Lesterlin C, Garza de Leon F, Uphoff S, Zawadzki P, Kapanidis AN. 2015. Live-cell superresolution microscopy reveals the organization of RNA polymerase in the bacterial nucleoid. Proc Natl Acad Sci U S A 112:E4390–E4399. https://doi.org/10.1073/pnas.1507592112.
314. Liu R, Liu Y, Liu S, Wang Y, Li K, Li N, Xu D, Zeng Q. 2017. Three-dimensional superresolution imaging of the FtsZ ring during cell division of the *Cyanobacterium prochlorococcus*. mBio 8:e00657-17. https://doi.org/10.1128/mBio.00657-17.
315. Grotjohann T, Testa I, Leutenegger M, Bock H, Urban NT, Lavoie-Cardinal F, Willig KI, Eggeling C, Jakobs S, Hell SW. 2011. Diffraction-unlimited all-optical imaging and writing with a photochromic GFP. Nature 478:204–208. https://doi.org/10.1038/nature10497.
316. Lukinavičius G, Reymond L, D'Este E, Masharina A, Göttfert F, Ta H, Güther A, Fournier M, Rizzo S, Waldmann H, Blaukopf C, Sommer C, Gerlich DW, Arndt HD, Hell SW, Johnsson K. 2014. Fluorogenic probes for live-cell imaging of the cytoskeleton. Nat Methods 11:731–733. https://doi.org/10.1038/nmeth.2972.
317. Mishina NM, Mishin AS, Belyaev Y, Bogdanova EA, Lukyanov S, Schultz C, Belousov VV. 2015. Live-cell STED microscopy with genetically encoded biosensor. Nano Lett 15:2928–2932. https://doi.org/10.1021/nl504710z.
318. Söderström B, Badrutdinov A, Chan H, Skoglund U. 2018. Cell shape-independent FtsZ dynamics in synthetically remodeled bacterial cells. Nat Commun 9:4323. https://doi.org/10.1038/s41467-018-06887-7.
319. Uphoff S, Reyes-Lamothe R, Garza de Leon F, Sherratt DJ, Kapanidis AN. 2013. Single-molecule DNA repair in live bacteria. Proc Natl Acad Sci U S A 110:8063–8068. https://doi.org/10.1073/pnas.1301804110.
320. Stracy M, Kapanidis AN. 2017. Single-molecule and super-resolution imaging of transcription in living bacteria. Methods 120:103–114. https://doi.org/10.1016/j.ymeth.2017.04.001.
321. Garza de Leon F, Sellars L, Stracy M, Busby SJW, Kapanidis AN. 2017. Tracking low-copy transcription factors in living bacteria: the case of the *lac* repressor. Biophys J 112:1316–1327. https://doi.org/10.1016/j.bpj.2017.02.028.
322. Elf J, Li GW, Xie XS. 2007. Probing transcription factor dynamics at the single-molecule level in a living cell. Science 316:1191–1194. https://doi.org/10.1126/science.1141967.
323. Reyes-Lamothe R, Sherratt DJ, Leake MC. 2010. Stoichiometry and architecture of active DNA replication machinery in *Escherichia coli*. Science 328:498–501. https://doi.org/10.1126/science.1185757.
324. Hammar P, Leroy P, Mahmutovic A, Marklund EG, Berg OG, Elf J. 2012. The *lac* repressor displays facilitated diffusion in living cells. Science 336:1595–1598. https://doi.org/10.1126/science.1221648.
325. Weng X, Bohrer CH, Bettridge K, Lagda AC, Cagliero C, Jin DJ, Xiao J. 2019. Spatial organization of RNA polymerase and its relationship with transcription in *Escherichia coli*. Proc Natl Acad Sci U S A 116:20115–20123. https://doi.org/10.1073/pnas.1903968116.
326. Rösch TC, Oviedo-Bocanegra LM, Fritz G, Graumann PL. 2018. SMTracker: a tool for quantitative analysis, exploration and visualization of single-molecule tracking data reveals highly dynamic binding of *Bacillus subtilis* global repressor AbrB throughout the genome. Sci Rep 8:15747. https://doi.org/10.1038/s41598-018-33842-9.
327. Kapanidis AN, Lepore A, El Karoui M. 2018. Rediscovering bacteria through single-molecule imaging in living cells. Biophys J 115:190–202. https://doi.org/10.1016/j.bpj.2018.03.028.
328. Xie XS, Choi PJ, Li GW, Lee NK, Lia G. 2008. Single-molecule approach to molecular biology in living bacterial cells. Annu Rev Biophys 37:417–444. https://doi.org/10.1146/annurev.biophys.37.092607.174640.
329. Ritchie K, Lill Y, Sood C, Lee H, Zhang S. 2013. Single-molecule imaging in live bacteria cells. Philos Trans R Soc Lond B Biol Sci 368:20120355. https://doi.org/10.1098/rstb.2012.0355.
330. Stracy M, Uphoff S, Garza de Leon F, Kapanidis AN. 2014. *In vivo* single-molecule imaging of bacterial DNA replication, transcription, and repair. FEBS Lett 588:3585–3594. https://doi.org/10.1016/j.febslet.2014.05.026.
331. Shashkova S, Leake MC. 2017. Single-molecule fluorescence microscopy review: shedding new light on old problems. Biosci Rep 37:BSR20170031. https://doi.org/10.1042/BSR20170031.
332. Kleine Borgmann LA, Ries J, Ewers H, Ulbrich MH, Graumann PL. 2013. The bacterial SMC complex displays two distinct modes of interaction with the chromosome. Cell Rep 3:1483–1492. https://doi.org/10.1016/j.celrep.2013.04.005.
333. Liao Y, Schroeder JW, Gao B, Simmons LA, Biteen JS. 2015. Single-molecule motions and interactions in live cells reveal target search dynamics in mismatch repair. Proc Natl Acad Sci U S A 112:E6898–E6906. https://doi.org/10.1073/pnas.1507386112.
334. Zawadzki P, Stracy M, Ginda K, Zawadzka K, Lesterlin C, Kapanidis AN, Sherratt DJ. 2015. The localization and action of topoisomerase IV in *Escherichia coli* chromosome segregation is coordinated by the SMC complex, MukBEF. Cell Rep 13:2587–2596. https://doi.org/10.1016/j.celrep.2015.11.034.
335. Stracy M, Jaciuk M, Uphoff S, Kapanidis AN, Nowotny M, Sherratt DJ, Zawadzki P. 2016. Single-molecule imaging of UvrA and UvrB recruitment to DNA lesions in living *Escherichia coli*. Nat Commun 7:12568. https://doi.org/10.1038/ncomms12568.
336. Li W, Bouveret E, Zhang Y, Liu K, Wang JD, Weisshaar JC. 2016. Effects of amino acid starvation on RelA diffusive behavior in live *Escherichia coli*. Mol Microbiol 99:571–585. https://doi.org/10.1111/mmi.13252.
337. Schenk K, Hervás AB, Rösch TC, Eisemann M, Schmitt BA, Dahlke S, Kleine-Borgmann L, Murray SM, Graumann PL. 2017. Rapid turnover of DnaA at replication origin regions contributes to initiation control of DNA replication. PLoS Genet 13:e1006561. https://doi.org/10.1371/journal.pgen.1006561.
338. Schibany S, Kleine Borgmann LAK, Rösch TC, Knust T, Ulbrich MH, Graumann PL. 2018. Single molecule tracking reveals that the bacterial SMC complex moves slowly relative to the diffusion of the chromosome. Nucleic Acids Res 46:7805–7819. https://doi.org/10.1093/nar/gky581.
339. Romero H, Rösch TC, Hernández-Tamayo R, Lucena D, Ayora S, Alonso JC, Graumann PL. 2019. Single molecule tracking reveals functions for RarA at replication forks but also independently from replication during DNA repair in *Bacillus subtilis*. Sci Rep 9:1997. https://doi.org/10.1038/s41598-018-38289-6.
340. Ducret A, Maisonneuve E, Notareschi P, Grossi A, Mignot T, Dukan S. 2009. A microscope automated fluidic system to study bacterial processes in real time. PLoS One 4:e7282. https://doi.org/10.1371/journal.pone.0007282.
341. Fero M, Pogliano K. 2010. Automated quantitative live cell fluorescence microscopy. Cold Spring Harb Perspect Biol 2:a000455. https://doi.org/10.1101/cshperspect.a000455.
342. van Teeffelen S, Shaevitz JW, Gitai Z. 2012. Image analysis in fluorescence microscopy: bacterial dynamics as a case study. Bioessays 34:427–436. https://doi.org/10.1002/bies.201100148.
343. Sliusarenko O, Heinritz J, Emonet T, Jacobs-Wagner C. 2011. High-throughput, subpixel precision analysis of bacterial morphogenesis and intracellular spatio-temporal dynamics. Mol Microbiol 80:612–627. https://doi.org/10.1111/j.1365-2958.2011.07579.x.
344. Ducret A, Quardokus EM, Brun YV. 2016. MicrobeJ, a tool for high throughput bacterial cell detection and quantitative analysis. Nat Microbiol 1:16077. https://doi.org/10.1038/nmicrobiol.2016.77.
345. Paintdakhi A, Parry B, Campos M, Irnov I, Elf J, Surovtsev I, Jacobs-Wagner C. 2016. Oufti: an integrated software package for high-accuracy, high-throughput quantitative microscopy analysis. Mol Microbiol 99:767–777. https://doi.org/10.1111/mmi.13264.
346. Danielsen J, Nordenfelt P. 2017. Computer vision-based image analysis of bacteria. Methods Mol Biol 1535:161–172. https://doi.org/10.1007/978-1-4939-6673-8_10.
347. Ursell T, Lee TK, Shiomi D, Shi H, Tropini C, Monds RD, Colavin A, Billings G, Bhaya-Grossman I, Broxton M, Huang BE, Niki H, Huang KC. 2017. Rapid, precise quantification of bacterial cellular dimensions across a genomic-scale knockout library. BMC Biol 15:17. https://doi.org/10.1186/s12915-017-0348-8.
348. Shi H, Colavin A, Lee TK, Huang KC. 2017. Strain library imaging protocol for high-throughput, automated single-cell microscopy of large bacterial collections arrayed on multiwell plates. Nat Protoc 12:429–438. https://doi.org/10.1038/nprot.2016.181.
349. Potvin-Trottier L, Luro S, Paulsson J. 2018. Microfluidics and single-cell microscopy to study stochastic processes in bacteria. Curr Opin Microbiol 43:186–192. https://doi.org/10.1016/j.mib.2017.12.004.
350. Okumus B, Baker CJ, Arias-Castro JC, Lai GC, Leoncini E, Bakshi S, Luro

S, Landgraf D, Paulsson J. 2018. Single-cell microscopy of suspension cultures using a microfluidics-assisted cell screening platform. Nat Protoc 13:170–194. https://doi.org/10.1038/nprot.2017.127.

351. Reyer MA, McLean EL, Chennakesavalu S, Fei J. 2018. An automated image analysis method for segmenting fluorescent bacteria in three dimensions. Biochemistry 57:209–215. https://doi.org/10.1021/acs.biochem.7b00839.
352. Camsund D, Lawson MJ, Larsson J, Jones D, Zikrin S, Fange D, Elf J. 2020. Time-resolved imaging-based CRISPRi screening. Nat Methods 17:86–92. https://doi.org/10.1038/s41592-019-0629-y.
353. Nebe-von-Caron G. 2009. Standardization in microbial cytometry. Cytometry A 75:86–89. https://doi.org/10.1002/cyto.a.20696.
354. Müller S, Davey H. 2009. Recent advances in the analysis of individual microbial cells. Cytometry A 75:83–85. https://doi.org/10.1002/cyto.a.20702.
355. Quixabeira VB, Nabout JC, Rodrigues FM. 2010. Trends in genetic literature with the use of flow cytometry. Cytometry A 77:207–210. https://doi.org/10.1002/cyto.a.20837.
356. Czechowska K, Johnson DR, van der Meer JR. 2008. Use of flow cytometric methods for single-cell analysis in environmental microbiology. Curr Opin Microbiol 11:205–212. https://doi.org/10.1016/j.mib.2008.04.006.
357. Müller S, Nebe-von-Caron G. 2010. Functional single-cell analyses: flow cytometry and cell sorting of microbial populations and communities. FEMS Microbiol Rev 34:554–587. https://doi.org/10.1111/j.1574-6976.2010.00214.x.
358. Rego EH, Audette RE, Rubin EJ. 2017. Deletion of a mycobacterial divisome factor collapses single-cell phenotypic heterogeneity. Nature 546:153–157. https://doi.org/10.1038/nature22361.
359. Robinow C, Kellenberger E. 1994. The bacterial nucleoid revisited. Microbiol Rev 58:211–232. https://doi.org/10.1128/MMBR.58.2.211-232.1994.
360. Dame RT. 2005. The role of nucleoid-associated proteins in the organization and compaction of bacterial chromatin. Mol Microbiol 56:858–870. https://doi.org/10.1111/j.1365-2958.2005.04598.x.
361. Dillon SC, Dorman CJ. 2010. Bacterial nucleoid-associated proteins, nucleoid structure, and gene expression. Nat Rev Microbiol 8:185–195. https://doi.org/10.1038/nrmicro2261.
362. Wang X, Rudner DZ. 2014. Spatial organization of bacterial chromosomes. Curr Opin Microbiol 22:66–72. https://doi.org/10.1016/j.mib.2014.09.016.
363. Ptacin JL, Shapiro L. 2013. Chromosome architecture is a key element of bacterial cellular organization. Cell Microbiol 15:45–52. https://doi.org/10.1111/cmi.12049.
364. Wang X, Montero Llopis P, Rudner DZ. 2013. Organization and segregation of bacterial chromosomes. Nat Rev Genet 14:191–203. https://doi.org/10.1038/nrg3375.
365. Li G-W, Berg OG, Elf J. 2009. Effects of macromolecular crowding and DNA looping on gene regulation kinetics. Nature Phys 5:294–297. https://doi.org/10.1038/nphys1222.
366. Grainger DC, Hurd D, Goldberg MD, Busby SJ. 2006. Association of nucleoid proteins with coding and noncoding segments of the *Escherichia coli* genome. Nucleic Acids Res 34:4642–4652. https://doi.org/10.1093/nar/gkl542.
367. Smits WK, Grossman AD. 2010. The transcriptional regulator Rok binds A+T-rich DNA and is involved in repression of a mobile genetic element in *Bacillus subtilis*. PLoS Genet 6:e1001207. https://doi.org/10.1371/journal.pgen.1001207.
368. Lee SF, Thompson MA, Schwartz MA, Shapiro L, Moerner WE. 2011. Super-resolution imaging of the nucleoid-associated protein HU in *Caulobacter crescentus*. Biophys J 100:L31–L33. https://doi.org/10.1016/j.bpj.2011.02.022.
369. Hołówka J, Trojanowski D, Ginda K, Wojtaś B, Gielniewski B, Jakimowicz D, Zakrzewska-Czerwińska J. 2017. HupB is a bacterial nucleoid-associated protein with an indispensable eukaryotic-like tail. mBio 8:e01272-17. https://doi.org/10.1128/mBio.01272-17.
370. Hadizadeh Yazdi N, Guet CC, Johnson RC, Marko JF. 2012. Variation of the folding and dynamics of the *Escherichia coli* chromosome with growth conditions. Mol Microbiol 86:1318–1333. https://doi.org/10.1111/mmi.12071.
371. Passaris I, Ghosh A, Cenens W, Michiels CW, Lammertyn J, Aertsen A. 2014. Isolation and validation of an endogenous fluorescent nucleoid reporter in *Salmonella* Typhimurium. PLoS One 9:e93785. https://doi.org/10.1371/journal.pone.0093785.
372. Wang X, Montero Llopis P, Rudner DZ. 2014. *Bacillus subtilis* chromosome organization oscillates between two distinct patterns. Proc Natl Acad Sci U S A 111:12877–12882. https://doi.org/10.1073/pnas.1407461111.
373. Ali Azam T, Iwata A, Nishimura A, Ueda S, Ishihama A. 1999. Growth phase-dependent variation in protein composition of the *Escherichia coli* nucleoid. J Bacteriol 181:6361–6370. https://doi.org/10.1128/JB.181.20.6361-6370.1999.
374. Morikawa K, Ohniwa RL, Kim J, Maruyama A, Ohta T, Takeyasu K. 2006. Bacterial nucleoid dynamics: oxidative stress response in *Staphylococcus aureus*. Genes Cells 11:409–423. https://doi.org/10.1111/j.1365-2443.2006.00949.x.
375. Ko KC, Tai PC, Derby CD. 2012. Mechanisms of action of escapin, a bactericidal agent in the ink secretion of the sea hare *Aplysia californica*: rapid and long-lasting DNA condensation and involvement of the OxyR-regulated oxidative stress pathway. Antimicrob Agents Chemother 56:1725–1734. https://doi.org/10.1128/AAC.05874-11.
376. Dwyer DJ, Camacho DM, Kohanski MA, Callura JM, Collins JJ. 2012. Antibiotic-induced bacterial cell death exhibits physiological and biochemical hallmarks of apoptosis. Mol Cell 46:561–572. https://doi.org/10.1016/j.molcel.2012.04.027.
377. Shechter N, Zaltzman L, Weiner A, Brumfeld V, Shimoni E, Fridmann-Sirkis Y, Minsky A. 2013. Stress-induced condensation of bacterial genomes results in re-pairing of sister chromosomes: implications for double strand DNA break repair. J Biol Chem 288:25659–25667. https://doi.org/10.1074/jbc.M113.473025.
378. Ghosh A, Passaris I, Tesfazgi Mebrhatu M, Rocha S, Vanoirbeek K, Hofkens J, Aertsen A. 2014. Cellular localization and dynamics of the Mrr type IV restriction endonuclease of *Escherichia coli*. Nucleic Acids Res 42:3908–3918. https://doi.org/10.1093/nar/gkt1370.
379. Bakshi S, Choi H, Rangarajan N, Barns KJ, Bratton BP, Weisshaar JC. 2014. Nonperturbative imaging of nucleoid morphology in live bacterial cells during an antimicrobial peptide attack. Appl Environ Microbiol 80:4977–4986. https://doi.org/10.1128/AEM.00989-14.
380. Dewachter L, Verstraeten N, Monteyne D, Kint CI, Versées W, Pérez-Morga D, Michiels J, Fauvart M. 2015. A single-amino-acid substitution in Obg activates a new programmed cell death pathway in *Escherichia coli*. mBio 6:e01935-15–e01915. https://doi.org/10.1128/mBio.01935-15.
381. Govers SK, Adam A, Blockeel H, Aertsen A. 2017. Rapid phenotypic individualization of bacterial sister cells. Sci Rep 7:8473. https://doi.org/10.1038/s41598-017-08660-0.
382. Gray WT, Govers SK, Xiang Y, Parry BR, Campos M, Kim S, Jacobs-Wagner C. 2019. Nucleoid size scaling and intracellular organization of translation across bacteria. Cell 177:1632–1648.e20. https://doi.org/10.1016/j.cell.2019.05.017.
383. Lopez-Garrido J, Ojkic N, Khanna K, Wagner FR, Villa E, Endres RG, Pogliano K. 2018. Chromosome translocation inflates *Bacillus* forespores and impacts cellular morphology. Cell 172:758–770.e14. https://doi.org/10.1016/j.cell.2018.01.027.
384. Russell WC, Newman C, Williamson DH. 1975. A simple cytochemical technique for demonstration of DNA in cells infected with mycoplasmas and viruses. Nature 253:461–462. https://doi.org/10.1038/253461a0.
385. Bos J, Zhang Q, Vyawahare S, Rogers E, Rosenberg SM, Austin RH. 2015. Emergence of antibiotic resistance from multinucleated bacterial filaments. Proc Natl Acad Sci U S A 112:178–183. https://doi.org/10.1073/pnas.1420702111.
386. Atwal S, Giengkam S, VanNieuwenhze M, Salje J. 2016. Live imaging of the genetically intractable obligate intracellular bacteria *Orientia tsutsugamushi* using a panel of fluorescent dyes. J Microbiol Methods 130:169–176. https://doi.org/10.1016/j.mimet.2016.08.022.
387. Robinett CC, Straight A, Li G, Willhelm C, Sudlow G, Murray A, Belmont AS. 1996. *In vivo* localization of DNA sequences and visualization of large-scale chromatin organization using *lac* operator/repressor recognition. J Cell Biol 135:1685–1700. https://doi.org/10.1083/jcb.135.6.1685.
388. Straight AF, Belmont AS, Robinett CC, Murray AW. 1996. GFP tagging of budding yeast chromosomes reveals that protein-protein interactions can mediate sister chromatid cohesion. Curr Biol 6:1599–1608. https://doi.org/10.1016/S0960-9822(02)70783-5.
389. Webb CD, Graumann PL, Kahana JA, Teleman AA, Silver PA, Losick R. 1998. Use of time-lapse microscopy to visualize rapid movement of the replication origin region of the chromosome during the cell cycle in *Bacillus subtilis*. Mol Microbiol 28:883–892. https://doi.org/10.1046/j.1365-2958.1998.00808.x.
390. Wu LJ, Errington J. 1994. *Bacillus subtilis* SpoIIIE protein required for

DNA segregation during asymmetric cell division. Science 264:572–575. https://doi.org/10.1126/science.8160014.

391. Viollier PH, Thanbichler M, McGrath PT, West L, Meewan M, McAdams HH, Shapiro L. 2004. Rapid and sequential movement of individual chromosomal loci to specific subcellular locations during bacterial DNA replication. Proc Natl Acad Sci U S A 101:9257–9262. https://doi.org/10.1073/pnas.0402606101.
392. Lau IF, Filipe SR, Søballe B, Økstad OA, Barre FX, Sherratt DJ. 2003. Spatial and temporal organization of replicating *Escherichia coli* chromosomes. Mol Microbiol 49:731–743. https://doi.org/10.1046/j.1365-2958.2003.03640.x.
393. Oshima T, Ishikawa S, Kurokawa K, Aiba H, Ogasawara N. 2006. *Escherichia coli* histone-like protein H-NS preferentially binds to horizontally acquired DNA in association with RNA polymerase. DNA Res 13:141–153. https://doi.org/10.1093/dnares/dsl009.
394. Li Y, Sergueev K, Austin S. 2002. The segregation of the *Escherichia coli* origin and terminus of replication. Mol Microbiol 46:985–996. https://doi.org/10.1046/j.1365-2958.2002.03234.x.
395. Nielsen HJ, Youngren B, Hansen FG, Austin S. 2007. Dynamics of *Escherichia coli* chromosome segregation during multifork replication. J Bacteriol 189:8660–8666. https://doi.org/10.1128/JB.01212-07.
396. Nordström K, Austin SJ. 1989. Mechanisms that contribute to the stable segregation of plasmids. Annu Rev Genet 23:37–69. https://doi.org/10.1146/annurev.ge.23.120189.000345.
397. Li Y, Austin S. 2002. The P1 plasmid in action: time-lapse photomicroscopy reveals some unexpected aspects of plasmid partition. Plasmid 48:174–178. https://doi.org/10.1016/S0147-619X(02)00104-X.
398. Li Y, Austin S. 2002. The P1 plasmid is segregated to daughter cells by a 'capture and ejection' mechanism coordinated with *Escherichia coli* cell division. Mol Microbiol 46:63–74. https://doi.org/10.1046/j.1365-2958.2002.03156.x.
399. Rodionov O, Lobocka M, Yarmolinsky M. 1999. Silencing of genes flanking the P1 plasmid centromere. Science 283:546–549. https://doi.org/10.1126/science.283.5401.546.
400. Bouet JY, Surtees JA, Funnell BE. 2000. Stoichiometry of P1 plasmid partition complexes. J Biol Chem 275:8213–8219. https://doi.org/10.1074/jbc.275.11.8213.
401. Rodionov O, Yarmolinsky M. 2004. Plasmid partitioning and the spreading of P1 partition protein ParB. Mol Microbiol 52:1215–1223. https://doi.org/10.1111/j.1365-2958.2004.04055.x.
402. Cenens W, Makumi A, Govers SK, Lavigne R, Aertsen A. 2015. Viral transmission dynamics at single-cell resolution reveal transiently immune subpopulations caused by a carrier state association. PLoS Genet 11:e1005770. https://doi.org/10.1371/journal.pgen.1005770.
403. Youngren B, Radnedge L, Hu P, Garcia E, Austin S. 2000. A plasmid partition system of the P1-P7*par* family from the pMT1 virulence plasmid of *Yersinia pestis*. J Bacteriol 182:3924–3928. https://doi.org/10.1128/JB.182.14.3924-3928.2000.
404. Youngren B, Nielsen HJ, Jun S, Austin S. 2014. The multifork *Escherichia coli* chromosome is a self-duplicating and self-segregating thermodynamic ring polymer. Genes Dev 28:71–84. https://doi.org/10.1101/gad.231050.113.
405. Tal A, Arbel-Goren R, Costantino N, Court DL, Stavans J. 2014. Location of the unique integration site on an *Escherichia coli* chromosome by bacteriophage lambda DNA *in vivo*. Proc Natl Acad Sci U S A 111:7308–7312. https://doi.org/10.1073/pnas.1324066111.
406. Elez M, Murray AW, Bi LJ, Zhang XE, Matic I, Radman M. 2010. Seeing mutations in living cells. Curr Biol 20:1432–1437. https://doi.org/10.1016/j.cub.2010.06.071.
407. Marinus MG. 2012. DNA mismatch repair. EcoSal Plus 5:ecosalplus7.2.5. https://doi.org/10.1128/ecosalplus.7.2.5.
408. Qiu R, Sakato M, Sacho EJ, Wilkins H, Zhang X, Modrich P, Hingorani MM, Erie DA, Weninger KR. 2015. MutL traps MutS at a DNA mismatch. Proc Natl Acad Sci U S A 112:10914–10919. https://doi.org/10.1073/pnas.1505655112.
409. Elez M, Radman M, Matic I. 2012. Stoichiometry of MutS and MutL at unrepaired mismatches *in vivo* suggests a mechanism of repair. Nucleic Acids Res 40:3929–3938. https://doi.org/10.1093/nar/gkr1298.
410. Robert L, Ollion J, Robert J, Song X, Matic I, Elez M. 2018. Mutation dynamics and fitness effects followed in single cells. Science 359:1283–1286. https://doi.org/10.1126/science.aan0797.
411. Robert L, Ollion J, Elez M. 2019. Real-time visualization of mutations and their fitness effects in single bacteria. Nat Protoc 14:3126–3143. https://doi.org/10.1038/s41596-019-0215-x.
412. Uphoff S. 2018. Real-time dynamics of mutagenesis reveal the chronology of DNA repair and damage tolerance responses in single cells. Proc Natl Acad Sci U S A 115:E6516–E6525. https://doi.org/10.1073/pnas.1801101115.
413. Woo AC, Faure L, Dapa T, Matic I. 2018. Heterogeneity of spontaneous DNA replication errors in single isogenic. Sci Adv 4:eaat1608. https://doi.org/10.1126/sciadv.aat1608.
414. Brown J, Brown T, Fox KR. 2001. Affinity of mismatch-binding protein MutS for heteroduplexes containing different mismatches. Biochem J 354:627–633. https://doi.org/10.1042/0264-6021:3540627.
415. Kuzminov A. 1999. Recombinational repair of DNA damage in *Escherichia coli* and bacteriophage lambda. Microbiol Mol Biol Rev 63:751–813. https://doi.org/10.1128/MMBR.63.4.751-813.1999.
416. Cox MM, Goodman MF, Kreuzer KN, Sherratt DJ, Sandler SJ, Marians KJ. 2000. The importance of repairing stalled replication forks. Nature 404:37–41. https://doi.org/10.1038/35003501.
417. Pennington JM, Rosenberg SM. 2007. Spontaneous DNA breakage in single living *Escherichia coli* cells. Nat Genet 39:797–802. https://doi.org/10.1038/ng2051.
418. Shee C, Cox BD, Gu F, Luengas EM, Joshi MC, Chiu LY, Magnan D, Halliday JA, Frisch RL, Gibson JL, Nehring RB, Do HG, Hernandez M, Li L, Herman C, Hastings PJ, Bates D, Harris RS, Miller KM, Rosenberg SM. 2013. Engineered proteins detect spontaneous DNA breakage in human and bacterial cells. Elife 2:e01222. https://doi.org/10.7554/eLife.01222.
419. Abraham ZH, Symonds N. 1990. Purification of overexpressed gam gene protein from bacteriophage Mu by denaturation-renaturation techniques and a study of its DNA-binding properties. Biochem J 269:679–684. https://doi.org/10.1042/bj2690679.
420. Akroyd J, Symonds N. 1986. Localization of the *gam* gene of bacteriophage Mu and characterization of the gene product. Gene 49:273–282. https://doi.org/10.1016/0378-1119(86)90288-X.
421. d'Adda di Fagagna F, Weller GR, Doherty AJ, Jackson SP. 2003. The Gam protein of bacteriophage Mu is an orthologue of eukaryotic Ku. EMBO Rep 4:47–52. https://doi.org/10.1038/sj.embor.embor709.
422. Kotlajich MV, Xia J, Zhai Y, Lin HY, Bradley CC, Shen X, Mei Q, Wang AZ, Lynn EJ, Shee C, Chen LT, Li L, Miller KM, Herman C, Hastings PJ, Rosenberg SM. 2018. Fluorescent fusions of the N protein of phage Mu label DNA damage in living cells. DNA Repair (Amst) 72:86–92. https://doi.org/10.1016/j.dnarep.2018.09.005.
423. Uphoff S, Kapanidis AN. 2014. Studying the organization of DNA repair by single-cell and single-molecule imaging. DNA Repair (Amst) 20:32–40. https://doi.org/10.1016/j.dnarep.2014.02.015.
424. Yokota H, Chujo YA, Harada Y. 2013. Single-molecule imaging of the oligomer formation of the nonhexameric *Escherichia coli* UvrD helicase. Biophys J 104:924–933. https://doi.org/10.1016/j.bpj.2013.01.014.
425. Uphoff S, Lord ND, Okumus B, Potvin-Trottier L, Sherratt DJ, Paulsson J. 2016. Stochastic activation of a DNA damage response causes cell-to-cell mutation rate variation. Science 351:1094–1097. https://doi.org/10.1126/science.aac9786.
426. Boudsocq F, Campbell M, Devoret R, Bailone A. 1997. Quantitation of the inhibition of Hfr × F- recombination by the mutagenesis complex UmuD′C. J Mol Biol 270:201–211. https://doi.org/10.1006/jmbi.1997.1098.
427. Courcelle J, Khodursky A, Peter B, Brown PO, Hanawalt PC. 2001. Comparative gene expression profiles following UV exposure in wild-type and SOS-deficient *Escherichia coli*. Genetics 158:41–64.
428. Stohl EA, Brockman JP, Burkle KL, Morimatsu K, Kowalczykowski SC, Seifert HS. 2003. *Escherichia coli* RecX inhibits RecA recombinase and coprotease activities *in vitro* and *in vivo*. J Biol Chem 278:2278–2285. https://doi.org/10.1074/jbc.M210496200.
429. Renzette N, Gumlaw N, Nordman JT, Krieger M, Yeh SP, Long E, Centore R, Boonsombat R, Sandler SJ. 2005. Localization of RecA in *Escherichia coli* K-12 using RecA-GFP. Mol Microbiol 57:1074–1085. https://doi.org/10.1111/j.1365-2958.2005.04755.x.
430. Kidane D, Graumann PL. 2005. Dynamic formation of RecA filaments at DNA double strand break repair centers in live cells. J Cell Biol 170:357–366. https://doi.org/10.1083/jcb.200412090.
431. Renzette N, Gumlaw N, Sandler SJ. 2007. DinI and RecX modulate RecA-DNA structures in *Escherichia coli* K-12. Mol Microbiol 63:103–115. https://doi.org/10.1111/j.1365-2958.2006.05496.x.
432. Lesterlin C, Ball G, Schermelleh L, Sherratt DJ. 2014. RecA bundles mediate homology pairing between distant sisters during DNA break repair. Nature 506:249–253. https://doi.org/10.1038/nature12868.

433. Rajendram M, Zhang L, Reynolds BJ, Auer GK, Tuson HH, Ngo KV, Cox MM, Yethiraj A, Cui Q, Weibel DB. 2015. Anionic phospholipids stabilize RecA filament bundles in *Escherichia coli*. Mol Cell 60:374–384. https://doi.org/10.1016/j.molcel.2015.09.009.
434. Handa N, Amitani I, Gumlaw N, Sandler SJ, Kowalczykowski SC. 2009. Single molecule analysis of a red fluorescent RecA protein reveals a defect in nucleoprotein filament nucleation that relates to its reduced biological functions. J Biol Chem 284:18664–18673. https://doi.org/10.1074/jbc.M109.004895.
435. Babic A, Lindner AB, Vulic M, Stewart EJ, Radman M. 2008. Direct visualization of horizontal gene transfer. Science 319:1533–1536. https://doi.org/10.1126/science.1153498.
436. Llosa M, Gomis-Rüth FX, Coll M, de la Cruz Fd F. 2002. Bacterial conjugation: a two-step mechanism for DNA transport. Mol Microbiol 45:1–8. https://doi.org/10.1046/j.1365-2958.2002.03014.x.
437. Lu M, Campbell JL, Boye E, Kleckner N. 1994. SeqA: a negative modulator of replication initiation in *E. coli*. Cell 77:413–426. https://doi.org/10.1016/0092-8674(94)90156-2.
438. Brendler T, Abeles A, Austin S. 1995. A protein that binds to the P1 origin core and the *oriC* 13mer region in a methylation-specific fashion is the product of the host *seqA* gene. EMBO J 14:4083–4089. https://doi.org/10.1002/j.1460-2075.1995.tb00080.x.
439. Slater S, Wold S, Lu M, Boye E, Skarstad K, Kleckner N. 1995. *Escherichia coli* SeqA protein binds *oriC* in two different methyl-modulated reactions appropriate to its roles in DNA replication initiation and origin sequestration. Cell 82:927–936. https://doi.org/10.1016/0092-8674(95)90272-4.
440. Babic A, Berkmen MB, Lee CA, Grossman AD. 2011. Efficient gene transfer in bacterial cell chains. mBio 2:e00027-11. https://doi.org/10.1128/mBio.00027-11.
441. Burrus V, Pavlovic G, Decaris B, Guédon G. 2002. Conjugative transposons: the tip of the iceberg. Mol Microbiol 46:601–610. https://doi.org/10.1046/j.1365-2958.2002.03191.x.
442. Burrus V, Waldor MK. 2004. Shaping bacterial genomes with integrative and conjugative elements. Res Microbiol 155:376–386. https://doi.org/10.1016/j.resmic.2004.01.012.
443. Roberts AP, Mullany P. 2009. A modular master on the move: the Tn*916* family of mobile genetic elements. Trends Microbiol 17:251–258. https://doi.org/10.1016/j.tim.2009.03.002.
444. Lee CA, Babic A, Grossman AD. 2010. Autonomous plasmid-like replication of a conjugative transposon. Mol Microbiol 75:268–279. https://doi.org/10.1111/j.1365-2958.2009.06985.x.
445. Wozniak RA, Waldor MK. 2010. Integrative and conjugative elements: mosaic mobile genetic elements enabling dynamic lateral gene flow. Nat Rev Microbiol 8:552–563. https://doi.org/10.1038/nrmicro2382.
446. Farrell CM, Grossman AD, Sauer RT. 2005. Cytoplasmic degradation of ssrA-tagged proteins. Mol Microbiol 57:1750–1761. https://doi.org/10.1111/j.1365-2958.2005.04798.x.
447. Keiler KC, Waller PR, Sauer RT. 1996. Role of a peptide tagging system in degradation of proteins synthesized from damaged messenger RNA. Science 271:990–993. https://doi.org/10.1126/science.271.5251.990.
448. Shao Q, Hawkins A, Zeng L. 2015. Phage DNA dynamics in cells with different fates. Biophys J 108:2048–2060. https://doi.org/10.1016/j.bpj.2015.03.027.
449. Slomińska M, Wegrzyn A, Konopa G, Skarstad K, Wegrzyn G. 2001. SeqA, the *Escherichia coli* origin sequestration protein, is also a specific transcription factor. Mol Microbiol 40:1371–1379. https://doi.org/10.1046/j.1365-2958.2001.02480.x.
450. Słomińska M, Konopa G, Barańska S, Wegrzyn G, Wegrzyn A. 2003. Interplay between DnaA and SeqA proteins during regulation of bacteriophage lambda pR promoter activity. J Mol Biol 329:59–68. https://doi.org/10.1016/S0022-2836(03)00378-4.
451. Shao Q, Trinh JT, McIntosh CS, Christenson B, Balázsi G, Zeng L. 2017. Lysis-lysogeny coexistence: prophage integration during lytic development. Microbiologyopen 6:e00395. https://doi.org/10.1002/mbo3.395.
452. Guan J, Shi X, Burgos R, Zeng L. 2017. Visualization of phage DNA degradation by a type I CRISPR-Cas system at the single-cell level. Quant Biol 5:67–75. https://doi.org/10.1007/s40484-017-0099-0.
453. Cenens W, Mebrhatu MT, Makumi A, Ceyssens PJ, Lavigne R, Van Houdt R, Taddei F, Aertsen A. 2013. Expression of a novel P22 ORFan gene reveals the phage carrier state in *Salmonella* Typhimurium. PLoS Genet 9:e1003269. https://doi.org/10.1371/journal.pgen.1003269.
454. Fekete RA, Chattoraj DK. 2005. A cis-acting sequence involved in chromosome segregation in *Escherichia coli*. Mol Microbiol 55:175–183. https://doi.org/10.1111/j.1365-2958.2004.04392.x.
455. St-Pierre F, Endy D. 2008. Determination of cell fate selection during phage lambda infection. Proc Natl Acad Sci U S A 105:20705–20710. https://doi.org/10.1073/pnas.0808831105.
456. Zeng L, Skinner SO, Zong C, Sippy J, Feiss M, Golding I. 2010. Decision making at a subcellular level determines the outcome of bacteriophage infection. Cell 141:682–691. https://doi.org/10.1016/j.cell.2010.03.034.
457. Van Valen D, Wu D, Chen YJ, Tuson H, Wiggins P, Phillips R. 2012. A single-molecule Hershey-Chase experiment. Curr Biol 22:1339–1343. https://doi.org/10.1016/j.cub.2012.05.023.
458. Vandecraen J, Chandler M, Aertsen A, Van Houdt R. 2017. The impact of insertion sequences on bacterial genome plasticity and adaptability. Crit Rev Microbiol 43:709–730. https://doi.org/10.1080/1040841X.2017.1303661.
459. Kim NH, Lee G, Sherer NA, Martini KM, Goldenfeld N, Kuhlman TE. 2016. Real-time transposable element activity in individual live cells. Proc Natl Acad Sci U S A 113:7278–7283. https://doi.org/10.1073/pnas.1601833113.
460. Broude NE. 2011. Analysis of RNA localization and metabolism in single live bacterial cells: achievements and challenges. Mol Microbiol 80:1137–1147. https://doi.org/10.1111/j.1365-2958.2011.07652.x.
461. Bashirullah A, Cooperstock RL, Lipshitz HD. 1998. RNA localization in development. Annu Rev Biochem 67:335–394. https://doi.org/10.1146/annurev.biochem.67.1.335.
462. Kloc M, Zearfoss NR, Etkin LD. 2002. Mechanisms of subcellular mRNA localization. Cell 108:533–544. https://doi.org/10.1016/S0092-8674(02)00651-7.
463. Montero Llopis P, Jackson AF, Sliusarenko O, Surovtsev I, Heinritz J, Emonet T, Jacobs-Wagner C. 2010. Spatial organization of the flow of genetic information in bacteria. Nature 466:77–81. https://doi.org/10.1038/nature09152.
464. Nevo-Dinur K, Nussbaum-Shochat A, Ben-Yehuda S, Amster-Choder O. 2011. Translation-independent localization of mRNA in *Escherichia coli*. Science 331:1081–1084. https://doi.org/10.1126/science.1195691.
465. Moffitt JR, Pandey S, Boettiger AN, Wang S, Zhuang X. 2016. Spatial organization shapes the turnover of a bacterial transcriptome. Elife 5:eLife.13065. https://doi.org/10.7554/eLife.13065.
466. Fei J, Sharma CM. 2018. RNA localization in bacteria. Microbiol Spectr 6. https://doi.org/10.1128/microbiolspec.RWR-0024-2018.
467. Kannaiah S, Livny J, Amster-Choder O. 2019. Spatiotemporal organization of the *Escherichia coli* transcriptome: translation independence and engagement in regulation. Mol Cell 76:574–5897. https://doi.org/10.1016/j.molcel.2019.08.013.
468. Passalacqua KD, Varadarajan A, Ondov BD, Okou DT, Zwick ME, Bergman NH. 2009. Structure and complexity of a bacterial transcriptome. J Bacteriol 191:3203–3211. https://doi.org/10.1128/JB.00122-09.
469. Raj A, van den Bogaard P, Rifkin SA, van Oudenaarden A, Tyagi S. 2008. Imaging individual mRNA molecules using multiple singly labeled probes. Nat Methods 5:877–879. https://doi.org/10.1038/nmeth.1253.
470. Femino AM, Fay FS, Fogarty K, Singer RH. 1998. Visualization of single RNA transcripts *in situ*. Science 280:585–590. https://doi.org/10.1126/science.280.5363.585.
471. Sando S, Kool ET. 2002. Imaging of RNA in bacteria with self-ligating quenched probes. J Am Chem Soc 124:9686–9687. https://doi.org/10.1021/ja026649g.
472. Russell JH, Keiler KC. 2009. Subcellular localization of a bacterial regulatory RNA. Proc Natl Acad Sci U S A 106:16405–16409. https://doi.org/10.1073/pnas.0904904106.
473. Kuhlman TE, Cox EC. 2012. Gene location and DNA density determine transcription factor distributions in *Escherichia coli*. Mol Syst Biol 8:610. https://doi.org/10.1038/msb.2012.42.
474. Shepherd DP, Li N, Micheva-Viteva SN, Munsky B, Hong-Geller E, Werner JH. 2013. Counting small RNA in pathogenic bacteria. Anal Chem 85:4938–4943. https://doi.org/10.1021/ac303792p.
475. Skinner SO, Sepúlveda LA, Xu H, Golding I. 2013. Measuring mRNA copy number in individual *Escherichia coli* cells using single-molecule fluorescent *in situ* hybridization. Nat Protoc 8:1100–1113. https://doi.org/10.1038/nprot.2013.066.
476. Kannaiah S, Amster-Choder O. 2016. Methods for studying RNA localization in bacteria. Methods 98:99–103. https://doi.org/10.1016/j.ymeth.2015.12.010.
477. Golding I, Paulsson J, Zawilski SM, Cox EC. 2005. Real-time kinetics of

gene activity in individual bacteria. Cell 123:1025–1036. https://doi.org/10.1016/j.cell.2005.09.031.

478. Silahtaroglu A, Pfundheller H, Koshkin A, Tommerup N, Kauppinen S. 2004. LNA-modified oligonucleotides are highly efficient as FISH probes. Cytogenet Genome Res 107:32–37. https://doi.org/10.1159/000079569.
479. Bertrand E, Chartrand P, Schaefer M, Shenoy SM, Singer RH, Long RM. 1998. Localization of ASH1 mRNA particles in living yeast. Mol Cell 2:437–445. https://doi.org/10.1016/S1097-2765(00)80143-4.
480. Golding I, Cox EC. 2004. RNA dynamics in live *Escherichia coli* cells. Proc Natl Acad Sci U S A 101:11310–11315. https://doi.org/10.1073/pnas.0404443101.
481. Oguro A, Ohtsu T, Svitkin YV, Sonenberg N, Nakamura Y. 2003. RNA aptamers to initiation factor 4A helicase hinder cap-dependent translation by blocking ATP hydrolysis. RNA 9:394–407. https://doi.org/10.1261/rna.2161303.
482. Toran P, Smolina I, Driscoll H, Ding F, Sun Y, Cantor CR, Broude NE. 2014. Labeling native bacterial RNA in live cells. Cell Res 24:894–897. https://doi.org/10.1038/cr.2014.47.
483. Smolina I, Broude N. 2015. A universal method for labeling native RNA in live bacterial cells. Methods Mol Biol 1316:75–85. https://doi.org/10.1007/978-1-4939-2730-2_7.
484. Cayley S, Lewis BA, Guttman HJ, Record MT. 1991. Characterization of the cytoplasm of *Escherichia coli* K-12 as a function of external osmolarity: implications for protein-DNA interactions *in vivo*. J Mol Biol 222:281–300. https://doi.org/10.1016/0022-2836(91)90212-O.
485. Zimmerman SB, Trach SO. 1991. Estimation of macromolecule concentrations and excluded volume effects for the cytoplasm of *Escherichia coli*. J Mol Biol 222:599–620. https://doi.org/10.1016/0022-2836(91)90499-V.
486. Parry BR, Surovtsev IV, Cabeen MT, O'Hern CS, Dufresne ER, Jacobs-Wagner C. 2014. The bacterial cytoplasm has glass-like properties and is fluidized by metabolic activity. Cell 156:183–194. https://doi.org/10.1016/j.cell.2013.11.028.
487. Konings WN, Albers SV, Koning S, Driessen AJ. 2002. The cell membrane plays a crucial role in survival of bacteria and archaea in extreme environments. Antonie Van Leeuwenhoek 81:61–72. https://doi.org/10.1023/A:1020573408652.
488. Golding I, Cox EC. 2006. Physical nature of bacterial cytoplasm. Phys Rev Lett 96:098102. https://doi.org/10.1103/PhysRevLett.96.098102.
489. Niu L, Yu J. 2008. Investigating intracellular dynamics of FtsZ cytoskeleton with photoactivation single-molecule tracking. Biophys J 95:2009–2016. https://doi.org/10.1529/biophysj.108.128751.
490. Weber SC, Spakowitz AJ, Theriot JA. 2010. Bacterial chromosomal loci move subdiffusively through a viscoelastic cytoplasm. Phys Rev Lett 104:238102. https://doi.org/10.1103/PhysRevLett.104.238102.
491. Bakshi S, Bratton BP, Weisshaar JC. 2011. Subdiffraction-limit study of Kaede diffusion and spatial distribution in live *Escherichia coli*. Biophys J 101:2535–2544. https://doi.org/10.1016/j.bpj.2011.10.013.
492. Cipelletti L, Ramos L. 2005. Slow dynamics in glassy soft matter. J Phys Condens Matter 17:R253–R285. https://doi.org/10.1088/0953-8984/17/6/R01.
493. Hunter GL, Weeks ER. 2012. The physics of the colloidal glass transition. Rep Prog Phys 75:066501. https://doi.org/10.1088/0034-4885/75/6/066501.
494. Zaccarelli E, Mayer C, Asteriadi A, Likos CN, Sciortino F, Roovers J, Iatrou H, Hadjichristidis N, Tartaglia P, Löwen H, Vlassopoulos D. 2005. Tailoring the flow of soft glasses by soft additives. Phys Rev Lett 95:268301. https://doi.org/10.1103/PhysRevLett.95.268301.
495. Broering TJ, Arnold MM, Miller CL, Hurt JA, Joyce PL, Nibert ML. 2005. Carboxyl-proximal regions of reovirus nonstructural protein muNS necessary and sufficient for forming factory-like inclusions. J Virol 79:6194–6206. https://doi.org/10.1128/JVI.79.10.6194-6206.2005.
496. Broering TJ, Parker JS, Joyce PL, Kim J, Nibert ML. 2002. Mammalian reovirus nonstructural protein microNS forms large inclusions and colocalizes with reovirus microtubule-associated protein micro2 in transfected cells. J Virol 76:8285–8297. https://doi.org/10.1128/JVI.76.16.8285-8297.2002.
497. Govers SK, Gayan E, Aertsen A. 2017. Intracellular movement of protein aggregates reveals heterogeneous inactivation and resuscitation dynamics in stressed populations of *Escherichia coli*. Environ Microbiol 19:511–523. https://doi.org/10.1111/1462-2920.13460.
498. Boersma AJ, Zuhorn IS, Poolman B. 2015. A sensor for quantification of macromolecular crowding in living cells. Nat Methods 12:227–229. https://doi.org/10.1038/nmeth.3257.
499. Liu B, Åberg C, van Eerden FJ, Marrink SJ, Poolman B, Boersma AJ. 2017. Design and properties of genetically encoded probes for sensing macromolecular crowding. Biophys J 112:1929–1939. https://doi.org/10.1016/j.bpj.2017.04.004.
500. Dubey GP, Ben-Yehuda S. 2011. Intercellular nanotubes mediate bacterial communication. Cell 144:590–600. https://doi.org/10.1016/j.cell.2011.01.015.
501. Haugland R. 2005. The handbook: a guidebook to fluorescent probes and labelling technologies, p 520–566. Invitrogen Corp., Carlsbad, CA.
502. Stempler O, Baidya AK, Bhattacharya S, Malli Mohan GB, Tzipilevich E, Sinai L, Mamou G, Ben-Yehuda S. 2017. Interspecies nutrient extraction and toxin delivery between bacteria. Nat Commun 8:315. https://doi.org/10.1038/s41467-017-00344-7.
503. Pal RR, Baidya AK, Mamou G, Bhattacharya S, Socol Y, Kobi S, Katsowich N, Ben-Yehuda S, Rosenshine I. 2019. Pathogenic *Escherichia coli* extracts nutrients from infected host cells utilizing injectisome components. Cell 177:683–696.e18. https://doi.org/10.1016/j.cell.2019.02.022.
504. Bhattacharya S, Baidya AK, Pal RR, Mamou G, Gatt YE, Margalit H, Rosenshine I, Ben-Yehuda S. 2019. A ubiquitous platform for bacterial nanotube biogenesis. Cell Rep 27:334–342.e10. https://doi.org/10.1016/j.celrep.2019.02.055.
505. Claudi B, Spröte P, Chirkova A, Personnic N, Zankl J, Schürmann N, Schmidt A, Bumann D. 2014. Phenotypic variation of *Salmonella* in host tissues delays eradication by antimicrobial chemotherapy. Cell 158:722–733. https://doi.org/10.1016/j.cell.2014.06.045.
506. Verkhusha VV, Kuznetsova IM, Stepanenko OV, Zaraisky AG, Shavlovsky MM, Turoverov KK, Uversky VN. 2003. High stability of *Discosoma* DsRed as compared to *Aequorea* EGFP. Biochemistry 42:7879–7884. https://doi.org/10.1021/bi034555t.
507. Beuter D, Gomes-Filho JV, Randau L, Díaz-Pascual F, Drescher K, Link H. 2018. Selective enrichment of slow-growing bacteria in a metabolism-wide CRISPRi library with a TIMER protein. ACS Synth Biol.
508. Lidsky PV, Lukyanov KA, Misra T, Handke B, Mishin AS, Lehner CF. 2018. A genetically encoded fluorescent probe for imaging of oxygenation gradients in living *Drosophila*. Development 145:dev156257. https://doi.org/10.1242/dev.156257.
509. Roostalu J, Jõers A, Luidalepp H, Kaldalu N, Tenson T. 2008. Cell division in *Escherichia coli* cultures monitored at single cell resolution. BMC Microbiol 8:68. https://doi.org/10.1186/1471-2180-8-68.
510. Helaine S, Thompson JA, Watson KG, Liu M, Boyle C, Holden DW. 2010. Dynamics of intracellular bacterial replication at the single cell level. Proc Natl Acad Sci U S A 107:3746–3751. https://doi.org/10.1073/pnas.1000041107.
511. Jõers A, Tenson T. 2016. Growth resumption from stationary phase reveals memory in *Escherichia coli* cultures. Sci Rep 6:24055. https://doi.org/10.1038/srep24055.
512. Jõers A, Vind K, Hernández SB, Maruste R, Pereira M, Brauer A, Remm M, Cava F, Tenson T. 2019. Muropeptides stimulate growth resumption from stationary phase in *Escherichia coli*. Sci Rep 9:18043. https://doi.org/10.1038/s41598-019-54646-5.
513. Cambré A, Zimmermann M, Sauer U, Vivijs B, Cenens W, Michiels CW, Aertsen A, Loessner MJ, Noben JP, Ayala JA, Lavigne R, Briers Y. 2015. Metabolite profiling and peptidoglycan analysis of transient cell wall-deficient bacteria in a new *Escherichia coli* model system. Environ Microbiol 17:1586–1599. https://doi.org/10.1111/1462-2920.12594.
514. De Smet J, Zimmermann M, Kogadeeva M, Ceyssens PJ, Vermaelen W, Blasdel B, Bin Jang H, Sauer U, Lavigne R. 2016. High coverage metabolomics analysis reveals phage-specific alterations to *Pseudomonas aeruginosa* physiology during infection. ISME J 10:1823–1835. https://doi.org/10.1038/ismej.2016.3.
515. Chevallereau A, Blasdel BG, De Smet J, Monot M, Zimmermann M, Kogadeeva M, Sauer U, Jorth P, Whiteley M, Debarbieux L, Lavigne R. 2016. Next-generation "-omics" approaches reveal a massive alteration of host RNA metabolism during bacteriophage infection of *Pseudomonas aeruginosa*. PLoS Genet 12:e1006134. https://doi.org/10.1371/journal.pgen.1006134.
516. Campos AI, Zampieri M. 2019. Metabolomics-driven exploration of the chemical drug space to predict combination antimicrobial therapies. Mol Cell 74:1291–1303.e6. https://doi.org/10.1016/j.molcel.2019.04.001.
517. Zampieri M, Zimmermann M, Claassen M, Sauer U. 2017. Nontargeted metabolomics reveals the multilevel response to antibiotic perturbations. Cell Rep 19:1214–1228. https://doi.org/10.1016/j.celrep.2017.04.002.
518. Joshua CJ. 2019. Metabolomics: a microbial physiology and metabo-

lism perspective. Methods Mol Biol 1859:71–94. https://doi.org/10.1007/978-1-4939-8757-3_3.

519. Martinez KA, Kitko RD, Mershon JP, Adcox HE, Malek KA, Berkmen MB, Slonczewski JL. 2012. Cytoplasmic pH response to acid stress in individual cells of *Escherichia coli* and *Bacillus subtilis* observed by fluorescence ratio imaging microscopy. Appl Environ Microbiol 78:3706–3714. https://doi.org/10.1128/AEM.00354-12.
520. Greenwald EC, Mehta S, Zhang J. 2018. Genetically encoded fluorescent biosensors illuminate the spatiotemporal regulation of signaling networks. Chem Rev 118:11707–11794. https://doi.org/10.1021/acs.chemrev.8b00333.
521. Kaper T, Lager I, Looger LL, Chermak D, Frommer WB. 2008. Fluorescence resonance energy transfer sensors for quantitative monitoring of pentose and disaccharide accumulation in bacteria. Biotechnol Biofuels 1:11. https://doi.org/10.1186/1754-6834-1-11.
522. Ewald JC, Reich S, Baumann S, Frommer WB, Zamboni N. 2011. Engineering genetically encoded nanosensors for real-time *in vivo* measurements of citrate concentrations. PLoS One 6:e28245. https://doi.org/10.1371/journal.pone.0028245.
523. Potzkei J, Kunze M, Drepper T, Gensch T, Jaeger KE, Büchs J. 2012. Real-time determination of intracellular oxygen in bacteria using a genetically encoded FRET-based biosensor. BMC Biol 10:28. https://doi.org/10.1186/1741-7007-10-28.
524. Wilmaerts D, Bayoumi M, Dewachter L, Knapen W, Mika JT, Hofkens J, Dedecker P, Maglia G, Verstraeten N, Michiels J. 2018. The persistence-inducing toxin HokB forms dynamic pores that cause ATP leakage. mBio 9:e00744-18. https://doi.org/10.1128/mBio.00744-18.
525. Miesenböck G, De Angelis DA, Rothman JE. 1998. Visualizing secretion and synaptic transmission with pH-sensitive green fluorescent proteins. Nature 394:192–195. https://doi.org/10.1038/28190.
526. Mahon MJ. 2011. pHluorin2: an enhanced, ratiometric, pH-sensitive green florescent protein. Adv Biosci Biotechnol 2:132–137. https://doi.org/10.4236/abb.2011.23021.
527. Pandey R, Vischer NO, Smelt JP, van Beilen JW, Ter Beek A, De Vos WH, Brul S, Manders EM. 2016. Intracellular pH response to weak acid stress in individual vegetative *Bacillus subtilis* cells. Appl Environ Microbiol 82:6463–6471. https://doi.org/10.1128/AEM.02063-16.
528. Modi S, M G S, Goswami D, Gupta GD, Mayor S, Krishnan Y. 2009. A DNA nanomachine that maps spatial and temporal pH changes inside living cells. Nat Nanotechnol 4:325–330. https://doi.org/10.1038/nnano.2009.83.
529. Surana S, Bhat JM, Koushika SP, Krishnan Y. 2011. An autonomous DNA nanomachine maps spatiotemporal pH changes in a multicellular living organism. Nat Commun 2:340. https://doi.org/10.1038/ncomms1340.
530. Guéron M, Leroy JL. 2000. The i-motif in nucleic acids. Curr Opin Struct Biol 10:326–331. https://doi.org/10.1016/S0959-440X(00)00091-9.
531. Molenaar D, Abee T, Konings WN. 1991. Continuous measurement of the cytoplasmic pH in *Lactococcus lactis* with a fluorescent pH indicator. Biochim Biophys Acta 1115:75–83. https://doi.org/10.1016/0304-4165(91)90014-8.
532. van Veen HW, Abee T, Kortstee GJ, Pereira H, Konings WN, Zehnder AJ. 1994. Generation of a proton motive force by the excretion of metal-phosphate in the polyphosphate-accumulating *Acinetobacter johnsonii* strain 210A. J Biol Chem 269:29509–29514.
533. Magill NG, Cowan AE, Koppel DE, Setlow P. 1994. The internal pH of the forespore compartment of *Bacillus megaterium* decreases by about 1 pH unit during sporulation. J Bacteriol 176:2252–2258. https://doi.org/10.1128/JB.176.8.2252-2258.1994.
534. Rink TJ, Tsien RY, Pozzan T. 1982. Cytoplasmic pH and free Mg^{2+} in lymphocytes. J Cell Biol 95:189–196. https://doi.org/10.1083/jcb.95.1.189.
535. Han J, Burgess K. 2010. Fluorescent indicators for intracellular pH. Chem Rev 110:2709–2728. https://doi.org/10.1021/cr900249z.
536. Rotman B, Papermaster BW. 1966. Membrane properties of living mammalian cells as studied by enzymatic hydrolysis of fluorogenic esters. Proc Natl Acad Sci U S A 55:134–141. https://doi.org/10.1073/pnas.55.1.134.
537. Boens N, Qin W, Basarić N, Orte A, Talavera EM, Alvarez-Pez JM. 2006. Photophysics of the fluorescent pH indicator BCECF. J Phys Chem A 110:9334–9343. https://doi.org/10.1021/jp0615712.
538. Ozkan P, Mutharasan R. 2002. A rapid method for measuring intracellular pH using BCECF-AM. Biochim Biophys Acta 1572:143–148. https://doi.org/10.1016/S0304-4165(02)00303-3.
539. Riondet C, Cachon R, Waché Y, Alcaraz G, Diviès C. 1997. Measurement of the intracellular pH in *Escherichia coli* with the internally conjugated fluorescent probe 5- (and 6-)carboxyfluorescein succinimidyl ester. Biotechnol Tech 11:735–738. https://doi.org/10.1023/A:1018492217623.
540. Chitarra LG, Breeuwer P, Van Den Bulk RW, Abee T. 2000. Rapid fluorescence assessment of intracellular pH as a viability indicator of *Clavibacter michiganensis* subsp. *michiganensis*. J Appl Microbiol 88: 809–816. https://doi.org/10.1046/j.1365-2672.2000.01014.x.
541. Yano T, Oku M, Akeyama N, Itoyama A, Yurimoto H, Kuge S, Fujiki Y, Sakai Y. 2010. A novel fluorescent sensor protein for visualization of redox states in the cytoplasm and in peroxisomes. Mol Cell Biol 30: 3758–3766. https://doi.org/10.1128/MCB.00121-10.
542. Sugiura K, Nagai T, Nakano M, Ichinose H, Nakabayashi T, Ohta N, Hisabori T. 2015. Redox sensor proteins for highly sensitive direct imaging of intracellular redox state. Biochem Biophys Res Commun 457:242–248. https://doi.org/10.1016/j.bbrc.2014.12.095.
543. van der Heijden J, Bosman ES, Reynolds LA, Finlay BB. 2015. Direct measurement of oxidative and nitrosative stress dynamics in *Salmonella* inside macrophages. Proc Natl Acad Sci U S A 112:560–565. https://doi.org/10.1073/pnas.1414569112.
544. van der Heijden J, Finlay BB. 2015. *In vitro* real-time measurement of the intra-bacterial redox potential. Bio Protoc 5:1–9. https://doi.org/10.21769/bioprotoc.1579.
545. Hanson GT, Aggeler R, Oglesbee D, Cannon M, Capaldi RA, Tsien RY, Remington SJ. 2004. Investigating mitochondrial redox potential with redox-sensitive green fluorescent protein indicators. J Biol Chem 279: 13044–13053. https://doi.org/10.1074/jbc.M312846200.
546. Morgan B, Sobotta MC, Dick TP. 2011. Measuring E(GSH) and H_2O_2 with roGFP2-based redox probes. Free Radic Biol Med 51:1943–1951. https://doi.org/10.1016/j.freeradbiomed.2011.08.035.
547. Dwyer DJ, Belenky PA, Yang JH, MacDonald IC, Martell JD, Takahashi N, Chan CT, Lobritz MA, Braff D, Schwarz EG, Ye JD, Pati M, Vercruysse M, Ralifo PS, Allison KR, Khalil AS, Ting AY, Walker GC, Collins JJ. 2014. Antibiotics induce redox-related physiological alterations as part of their lethality. Proc Natl Acad Sci U S A 111:E2100–E2109. https://doi.org/10.1073/pnas.1401876111.
548. Choi H, Yang Z, Weisshaar JC. 2015. Single-cell, real-time detection of oxidative stress induced in *Escherichia coli* by the antimicrobial peptide CM15. Proc Natl Acad Sci U S A 112:E303–E310. https://doi.org/10.1073/pnas.1417703112.
549. McBee ME, Chionh YH, Sharaf ML, Ho P, Cai MW, Dedon PC. 2017. Production of superoxide in bacteria is stress- and cell state-dependent: a gating-optimized flow cytometry method that minimizes ROS measurement artifacts with fluorescent dyes. Front Microbiol 8:459. https://doi.org/10.3389/fmicb.2017.00459.
550. Parrish NM, Ko CG, Hughes MA, Townsend CA, Dick JD. 2004. Effect of n-octanesulphonylacetamide (OSA) on ATP and protein expression in *Mycobacterium bovis* BCG. J Antimicrob Chemother 54:722–729. https://doi.org/10.1093/jac/dkh408.
551. Rao SP, Alonso S, Rand L, Dick T, Pethe K. 2008. The protonmotive force is required for maintaining ATP homeostasis and viability of hypoxic, nonreplicating *Mycobacterium tuberculosis*. Proc Natl Acad Sci U S A 105:11945–11950. https://doi.org/10.1073/pnas.0711697105.
552. Koul A, Vranckx L, Dendouga N, Balemans W, Van den Wyngaert I, Vergauwen K, Göhlmann HW, Willebrords R, Poncelet A, Guillemont J, Bald D, Andries K. 2008. Diarylquinolines are bactericidal for dormant mycobacteria as a result of disturbed ATP homeostasis. J Biol Chem 283:25273–25280. https://doi.org/10.1074/jbc.M803899200.
553. Ando T, Imamura H, Suzuki R, Aizaki H, Watanabe T, Wakita T, Suzuki T. 2012. Visualization and measurement of ATP levels in living cells replicating hepatitis C virus genome RNA. PLoS Pathog 8:e1002561. https://doi.org/10.1371/journal.ppat.1002561.
554. Imamura H, Nhat KP, Togawa H, Saito K, Iino R, Kato-Yamada Y, Nagai T, Noji H. 2009. Visualization of ATP levels inside single living cells with fluorescence resonance energy transfer-based genetically encoded indicators. Proc Natl Acad Sci U S A 106:15651–15656. https://doi.org/10.1073/pnas.0904764106.
555. Yaginuma H, Kawai S, Tabata KV, Tomiyama K, Kakizuka A, Komatsuzaki T, Noji H, Imamura H. 2015. Diversity in ATP concentrations in a single bacterial cell population revealed by quantitative single-cell imaging. Sci Rep 4:6522. https://doi.org/10.1038/srep06522.
556. Takaine M, Ueno M, Kitamura K, Imamura H, Yoshida S. 2019. Reliable imaging of ATP in living budding and fission yeast. J Cell Sci 132: jcs230649. https://doi.org/10.1242/jcs.230649.
557. Berg J, Hung YP, Yellen G. 2009. A genetically encoded fluorescent

reporter of ATP:ADP ratio. Nat Methods 6:161–166. https://doi.org/10.1038/nmeth.1288.

558. Hengge R. 2009. Principles of c-di-GMP signalling in bacteria. Nat Rev Microbiol 7:263–273. https://doi.org/10.1038/nrmicro2109.
559. Ryan RP, Tolker-Nielsen T, Dow JM. 2012. When the PilZ don't work: effectors for cyclic di-GMP action in bacteria. Trends Microbiol 20:235–242. https://doi.org/10.1016/j.tim.2012.02.008.
560. Valentini M, Filloux A. 2016. Biofilms and cyclic di-GMP (c-di-GMP) signaling: lessons from *Pseudomonas aeruginosa* and other bacteria. J Biol Chem 291:12547–12555. https://doi.org/10.1074/jbc.R115.711507.
561. Jenal U, Reinders A, Lori C. 2017. Cyclic di-GMP: second messenger extraordinaire. Nat Rev Microbiol 15:271–284. https://doi.org/10.1038/nrmicro.2016.190.
562. Kulasekara BR, Kamischke C, Kulasekara HD, Christen M, Wiggins PA, Miller SI. 2013. c-di-GMP heterogeneity is generated by the chemotaxis machinery to regulate flagellar motility. Elife 2:e01402. https://doi.org/10.7554/eLife.01402.
563. Weiss CA, Hoberg JA, Liu K, Tu BP, Winkler WC. 2019. Single-cell microscopy reveals that levels of cyclic di-GMP vary among *Bacillus subtilis* subpopulations. J Bacteriol 201:e00247-19. https://doi.org/10.1128/JB.00247-19.
564. Petersen E, Mills E, Miller SI. 2019. Cyclic-di-GMP regulation promotes survival of a slow-replicating subpopulation of intracellular *Salmonella* Typhimurium. Proc Natl Acad Sci U S A 116:6335–6340. https://doi.org/10.1073/pnas.1901051116.
565. Mills E, Petersen E, Kulasekara BR, Miller SI. 2015. A direct screen for c-di-GMP modulators reveals a *Salmonella* Typhimurium periplasmic L-arginine-sensing pathway. Sci Signal 8:ra57. https://doi.org/10.1126/scisignal.aaa1796.
566. Ai HW, Henderson JN, Remington SJ, Campbell RE. 2006. Directed evolution of a monomeric, bright and photostable version of *Clavularia* cyan fluorescent protein: structural characterization and applications in fluorescence imaging. Biochem J 400:531–540. https://doi.org/10.1042/BJ20060874.
567. Sakaue-Sawano A, Kurokawa H, Morimura T, Hanyu A, Hama H, Osawa H, Kashiwagi S, Fukami K, Miyata T, Miyoshi H, Imamura T, Ogawa M, Masai H, Miyawaki A. 2008. Visualizing spatiotemporal dynamics of multicellular cell cycle progression. Cell 132:487–498. https://doi.org/10.1016/j.cell.2007.12.033.
568. Croce AC, Bottiroli G. 2014. Autofluorescence spectroscopy and imaging: a tool for biomedical research and diagnosis. Eur J Histochem 58:2461. https://doi.org/10.4081/ejh.2014.2461.
569. Kellenberger CA, Wilson SC, Sales-Lee J, Hammond MC. 2013. RNA-based fluorescent biosensors for live cell imaging of second messengers cyclic di-GMP and cyclic AMP-GMP. J Am Chem Soc 135:4906–4909. https://doi.org/10.1021/ja311960g.
570. Ouellet J, Schorr S, Iqbal A, Wilson TJ, Lilley DM. 2011. Orientation of cyanine fluorophores terminally attached to DNA via long, flexible tethers. Biophys J 101:1148–1154. https://doi.org/10.1016/j.bpj.2011.07.007.
571. Babendure JR, Adams SR, Tsien RY. 2003. Aptamers switch on fluorescence of triphenylmethane dyes. J Am Chem Soc 125:14716–14717. https://doi.org/10.1021/ja037994o.
572. Paige JS, Wu KY, Jaffrey SR. 2011. RNA mimics of green fluorescent protein. Science 333:642–646. https://doi.org/10.1126/science.1207339.
573. Filonov GS, Moon JD, Svensen N, Jaffrey SR. 2014. Broccoli: rapid selection of an RNA mimic of green fluorescent protein by fluorescence-based selection and directed evolution. J Am Chem Soc 136:16299–16308. https://doi.org/10.1021/ja508478x.
574. Dolgosheina EV, Jeng SC, Panchapakesan SS, Cojocaru R, Chen PS, Wilson PD, Hawkins N, Wiggins PA, Unrau PJ. 2014. RNA mango aptamer-fluorophore: a bright, high-affinity complex for RNA labeling and tracking. ACS Chem Biol 9:2412–2420. https://doi.org/10.1021/cb500499x.
575. Song W, Strack RL, Svensen N, Jaffrey SR. 2014. Plug-and-play fluorophores extend the spectral properties of Spinach. J Am Chem Soc 136:1198–1201. https://doi.org/10.1021/ja410819x.
576. Wang XC, Wilson SC, Hammond MC. 2016. Next-generation RNA-based fluorescent biosensors enable anaerobic detection of cyclic di-GMP. Nucleic Acids Res 44:e139. https://doi.org/10.1093/nar/gkw580.
577. Paige JS, Nguyen-Duc T, Song W, Jaffrey SR. 2012. Fluorescence imaging of cellular metabolites with RNA. Science 335:1194. https://doi.org/10.1126/science.1218298.
578. Strack RL, Disney MD, Jaffrey SR. 2013. A superfolding Spinach2 reveals the dynamic nature of trinucleotide repeat-containing RNA. Nat Methods 10:1219–1224. https://doi.org/10.1038/nmeth.2701.
579. You M, Litke JL, Jaffrey SR. 2015. Imaging metabolite dynamics in living cells using a Spinach-based riboswitch. Proc Natl Acad Sci U S A 112:E2756–E2765. https://doi.org/10.1073/pnas.1504354112.
580. Jepsen MDE, Sparvath SM, Nielsen TB, Langvad AH, Grossi G, Gothelf KV, Andersen ES. 2018. Development of a genetically encodable FRET system using fluorescent RNA aptamers. Nat Commun 9:18. https://doi.org/10.1038/s41467-018-03075-5.
581. Crick FH. 1958. On protein synthesis. Symp Soc Exp Biol 12:138–163.
582. Crick F. 1970. Central dogma of molecular biology. Nature 227:561–563. https://doi.org/10.1038/227561a0.
583. Jacob F, Monod J. 1961. Genetic regulatory mechanisms in the synthesis of proteins. J Mol Biol 3:318–356. https://doi.org/10.1016/S0022-2836(61)80072-7.
584. Browning DF, Busby SJ. 2016. Local and global regulation of transcription initiation in bacteria. Nat Rev Microbiol 14:638–650. https://doi.org/10.1038/nrmicro.2016.103.
585. Cramer P, Armache KJ, Baumli S, Benkert S, Brueckner F, Buchen C, Damsma GE, Dengl S, Geiger SR, Jasiak AJ, Jawhari A, Jennebach S, Kamenski T, Kettenberger H, Kuhn CD, Lehmann E, Leike K, Sydow JF, Vannini A. 2008. Structure of eukaryotic RNA polymerases. Annu Rev Biophys 37:337–352. https://doi.org/10.1146/annurev.biophys.37.032807.130008.
586. Boylan SA, Redfield AR, Brody MS, Price CW. 1993. Stress-induced activation of the sigma B transcription factor of *Bacillus subtilis*. J Bacteriol 175:7931–7937. https://doi.org/10.1128/JB.175.24.7931-7937.1993.
587. Price CW, Fawcett P, Cérémonie H, Su N, Murphy CK, Youngman P. 2001. Genome-wide analysis of the general stress response in *Bacillus subtilis*. Mol Microbiol 41:757–774. https://doi.org/10.1046/j.1365-2958.2001.02534.x.
588. Feklístov A, Sharon BD, Darst SA, Gross CA. 2014. Bacterial sigma factors: a historical, structural, and genomic perspective. Annu Rev Microbiol 68:357–376. https://doi.org/10.1146/annurev-micro-092412-155737.
589. Paget MS. 2015. Bacterial sigma factors and anti-sigma factors: structure, function and distribution. Biomolecules 5:1245–1265. https://doi.org/10.3390/biom5031245.
590. Helmann JD. 2016. *Bacillus subtilis* extracytoplasmic function (ECF) sigma factors and defense of the cell envelope. Curr Opin Microbiol 30:122–132. https://doi.org/10.1016/j.mib.2016.02.002.
591. Maeda H, Fujita N, Ishihama A. 2000. Competition among seven *Escherichia coli* sigma subunits: relative binding affinities to the core RNA polymerase. Nucleic Acids Res 28:3497–3503. https://doi.org/10.1093/nar/28.18.3497.
592. Gruber TM, Gross CA. 2003. Multiple sigma subunits and the partitioning of bacterial transcription space. Annu Rev Microbiol 57:441–466. https://doi.org/10.1146/annurev.micro.57.030502.090913.
593. Jishage M, Iwata A, Ueda S, Ishihama A. 1996. Regulation of RNA polymerase sigma subunit synthesis in *Escherichia coli*: intracellular levels of four species of sigma subunit under various growth conditions. J Bacteriol 178:5447–5451. https://doi.org/10.1128/JB.178.18.5447-5451.1996.
594. Hicks KA, Grossman AD. 1996. Altering the level and regulation of the major sigma subunit of RNA polymerase affects gene expression and development in *Bacillus subtilis*. Mol Microbiol 20:201–212. https://doi.org/10.1111/j.1365-2958.1996.tb02501.x.
595. Murakami KS, Masuda S, Campbell EA, Muzzin O, Darst SA. 2002. Structural basis of transcription initiation: an RNA polymerase holoenzyme-DNA complex. Science 296:1285–1290. https://doi.org/10.1126/science.1069595.
596. Vassylyev DG, Sekine S, Laptenko O, Lee J, Vassylyeva MN, Borukhov S, Yokoyama S. 2002. Crystal structure of a bacterial RNA polymerase holoenzyme at 2.6 Å resolution. Nature 417:712–719. https://doi.org/10.1038/nature752.
597. Murakami KS, Darst SA. 2003. Bacterial RNA polymerases: the wholo story. Curr Opin Struct Biol 13:31–39. https://doi.org/10.1016/S0959-440X(02)00005-2.
598. Grigorova IL, Phleger NJ, Mutalik VK, Gross CA. 2006. Insights into transcriptional regulation and sigma competition from an equilibrium model of RNA polymerase binding to DNA. Proc Natl Acad Sci U S A 103:5332–5337. https://doi.org/10.1073/pnas.0600828103.
599. Koo BM, Rhodius VA, Nonaka G, deHaseth PL, Gross CA. 2009. Reduced capacity of alternative sigmas to melt promoters ensures stringent

promoter recognition. Genes Dev 23:2426–2436. https://doi.org/10.1101/gad.1843709.

600. Ganguly A, Chatterji D. 2012. A comparative kinetic and thermodynamic perspective of the σ-competition model in *Escherichia coli*. Biophys J 103:1325–1333. https://doi.org/10.1016/j.bpj.2012.08.013.
601. Murakami KS. 2013. X-ray crystal structure of *Escherichia coli* RNA polymerase σ70 holoenzyme. J Biol Chem 288:9126–9134. https://doi.org/10.1074/jbc.M112.430900.
602. Rhodius VA, Segall-Shapiro TH, Sharon BD, Ghodasara A, Orlova E, Tabakh H, Burkhardt DH, Clancy K, Peterson TC, Gross CA, Voigt CA. 2013. Design of orthogonal genetic switches based on a crosstalk map of σs, anti-σs, and promoters. Mol Syst Biol 9:702. https://doi.org/10.1038/msb.2013.58.
603. Campagne S, Marsh ME, Capitani G, Vorholt JA, Allain FH. 2014. Structural basis for -10 promoter element melting by environmentally induced sigma factors. Nat Struct Mol Biol 21:269–276. https://doi.org/10.1038/nsmb.2777.
604. Yang Y, Darbari VC, Zhang N, Lu D, Glyde R, Wang YP, Winkelman JT, Gourse RL, Murakami KS, Buck M, Zhang X. 2015. Transcription: structures of the RNA polymerase-σ54 reveal new and conserved regulatory strategies. Science 349:882–885. https://doi.org/10.1126/science.aab1478.
605. Cao M, Wang T, Ye R, Helmann JD. 2002. Antibiotics that inhibit cell wall biosynthesis induce expression of the *Bacillus subtilis* sigma(W) and sigma(M) regulons. Mol Microbiol 45:1267–1276. https://doi.org/10.1046/j.1365-2958.2002.03050.x.
606. Cao M, Helmann JD. 2002. Regulation of the *Bacillus subtilis bcrC* bacitracin resistance gene by two extracytoplasmic function sigma factors. J Bacteriol 184:6123–6129. https://doi.org/10.1128/JB.184.22.6123-6129.2002.
607. Cao M, Salzberg L, Tsai CS, Mascher T, Bonilla C, Wang T, Ye RW, Márquez-Magaña L, Helmann JD. 2003. Regulation of the *Bacillus subtilis* extracytoplasmic function protein sigma(Y) and its target promoters. J Bacteriol 185:4883–4890. https://doi.org/10.1128/JB.185.16.4883-4890.2003.
608. Estacio W, Anna-Arriola SS, Adedipe M, Márquez-Magaña LM. 1998. Dual promoters are responsible for transcription initiation of the *fla/che* operon in *Bacillus subtilis*. J Bacteriol 180:3548–3555. https://doi.org/10.1128/JB.180.14.3548-3555.1998.
609. Huang X, Gaballa A, Cao M, Helmann JD. 1999. Identification of target promoters for the *Bacillus subtilis* extracytoplasmic function sigma factor, sigma W. Mol Microbiol 31:361–371. https://doi.org/10.1046/j.1365-2958.1999.01180.x.
610. Yoshimura M, Asai K, Sadaie Y, Yoshikawa H. 2004. Interaction of *Bacillus subtilis* extracytoplasmic function (ECF) sigma factors with the N-terminal regions of their potential anti-sigma factors. Microbiology (Reading) 150:591–599. https://doi.org/10.1099/mic.0.26712-0.
611. Locke JC, Elowitz MB. 2009. Using movies to analyse gene circuit dynamics in single cells. Nat Rev Microbiol 7:383–392. https://doi.org/10.1038/nrmicro2056.
612. Locke JC, Young JW, Fontes M, Hernández Jiménez MJ, Elowitz MB. 2011. Stochastic pulse regulation in bacterial stress response. Science 334:366–369. https://doi.org/10.1126/science.1208144.
613. Park J, Dies M, Lin Y, Hormoz S, Smith-Unna SE, Quinodoz S, Hernández-Jiménez MJ, Garcia-Ojalvo J, Locke JCW, Elowitz MB. 2018. Molecular time sharing through dynamic pulsing in single cells. Cell Syst 6:216–229. https://doi.org/10.1016/j.cels.2018.01.011.
614. Young JW, Locke JC, Altinok A, Rosenfeld N, Bacarian T, Swain PS, Mjolsness E, Elowitz MB. 2011. Measuring single-cell gene expression dynamics in bacteria using fluorescence time-lapse microscopy. Nat Protoc 7:80–88. https://doi.org/10.1038/nprot.2011.432.
615. Dunlop MJ. 2014. Quantitative single-cell gene expression measurements in bacteria using time-lapse microscopy. Microsc Microanal 20:1174–1175. https://doi.org/10.1017/S1431927614007600.
616. Young JW, Locke JC, Elowitz MB. 2013. Rate of environmental change determines stress response specificity. Proc Natl Acad Sci U S A 110:4140–4145. https://doi.org/10.1073/pnas.1213060110.
617. Bratton BP, Mooney RA, Weisshaar JC. 2011. Spatial distribution and diffusive motion of RNA polymerase in live *Escherichia coli*. J Bacteriol 193:5138–5146. https://doi.org/10.1128/JB.00198-11.
618. Bakshi S, Dalrymple RM, Li W, Choi H, Weisshaar JC. 2013. Partitioning of RNA polymerase activity in live *Escherichia coli* from analysis of single-molecule diffusive trajectories. Biophys J 105:2676–2686. https://doi.org/10.1016/j.bpj.2013.10.024.
619. Endesfelder U, Finan K, Holden SJ, Cook PR, Kapanidis AN, Heilemann M. 2013. Multiscale spatial organization of RNA polymerase in *Escherichia coli*. Biophys J 105:172–181. https://doi.org/10.1016/j.bpj.2013.05.048.
620. Bakshi S, Choi H, Weisshaar JC. 2015. The spatial biology of transcription and translation in rapidly growing *Escherichia coli*. Front Microbiol 6:636. https://doi.org/10.3389/fmicb.2015.00636.
621. Lewis PJ, Thaker SD, Errington J. 2000. Compartmentalization of transcription and translation in *Bacillus subtilis*. EMBO J 19:710–718. https://doi.org/10.1093/emboj/19.4.710.
622. Cabrera JE, Jin DJ. 2003. The distribution of RNA polymerase in *Escherichia coli* is dynamic and sensitive to environmental cues. Mol Microbiol 50:1493–1505. https://doi.org/10.1046/j.1365-2958.2003.03805.x.
623. Cabrera JE, Jin DJ. 2006. Active transcription of rRNA operons is a driving force for the distribution of RNA polymerase in bacteria: effect of extrachromosomal copies of *rrnB* on the *in vivo* localization of RNA polymerase. J Bacteriol 188:4007–4014. https://doi.org/10.1128/JB.01893-05.
624. Cabrera JE, Cagliero C, Quan S, Squires CL, Jin DJ. 2009. Active transcription of rRNA operons condenses the nucleoid in *Escherichia coli*: examining the effect of transcription on nucleoid structure in the absence of transertion. J Bacteriol 191:4180–4185. https://doi.org/10.1128/JB.01707-08.
625. Martin CM, Cagliero C, Sun Z, Chen D, Jin DJ. 2018. Imaging of transcription and replication in the bacterial chromosome with multicolor three-dimensional superresolution structured illumination microscopy. Methods Mol Biol 1837:117–129. https://doi.org/10.1007/978-1-4939-8675-0_7.
626. Jensen KF, Pedersen S. 1990. Metabolic growth rate control in *Escherichia coli* may be a consequence of subsaturation of the macromolecular biosynthetic apparatus with substrates and catalytic components. Microbiol Rev 54:89–100. https://doi.org/10.1128/MMBR.54.2.89-100.1990.
627. Bremer H, Dennis P, Ehrenberg M. 2003. Free RNA polymerase and modeling global transcription in *Escherichia coli*. Biochimie 85:597–609. https://doi.org/10.1016/S0300-9084(03)00105-6.
628. Jin DJ, Cabrera JE. 2006. Coupling the distribution of RNA polymerase to global gene regulation and the dynamic structure of the bacterial nucleoid in *Escherichia coli*. J Struct Biol 156:284–291. https://doi.org/10.1016/j.jsb.2006.07.005.
629. Jin DJ, Mata Martin C, Sun Z, Cagliero C, Zhou YN. 2017. Nucleolus-like compartmentalization of the transcription machinery in fast-growing bacterial cells. Crit Rev Biochem Mol Biol 52:96–106. https://doi.org/10.1080/10409238.2016.1269717.
630. Malagon F. 2013. RNase III is required for localization to the nucleoid of the 5′ pre-rRNA leader and for optimal induction of rRNA synthesis in *Escherichia coli*. RNA 19:1200–1207. https://doi.org/10.1261/rna.038588.113.
631. Browning DF, Busby SJ. 2004. The regulation of bacterial transcription initiation. Nat Rev Microbiol 2:57–65. https://doi.org/10.1038/nrmicro787.
632. von Hippel PH, Berg OG. 1989. Facilitated target location in biological systems. J Biol Chem 264:675–678.
633. Redding S, Greene EC. 2013. How do proteins locate specific targets in DNA? Chem Phys Lett 570:1–11. https://doi.org/10.1016/j.cplett.2013.03.035.
634. Kepes A. 1969. Transcription and translation in the lactose operon of *Escherichia coli* studied by *in vivo* kinetics. Prog Biophys Mol Biol 19:199–236. https://doi.org/10.1016/0079-6107(69)90006-6.
635. Ozbudak EM, Thattai M, Kurtser I, Grossman AD, van Oudenaarden A. 2002. Regulation of noise in the expression of a single gene. Nat Genet 31:69–73. https://doi.org/10.1038/ng869.
636. Ozbudak EM, Thattai M, Lim HN, Shraiman BI, Van Oudenaarden A. 2004. Multistability in the lactose utilization network of *Escherichia coli*. Nature 427:737–740. https://doi.org/10.1038/nature02298.
637. Rosenfeld N, Young JW, Alon U, Swain PS, Elowitz MB. 2005. Gene regulation at the single-cell level. Science 307:1962–1965. https://doi.org/10.1126/science.1106914.
638. Yu J, Xiao J, Ren X, Lao K, Xie XS. 2006. Probing gene expression in live cells, one protein molecule at a time. Science 311:1600–1603. https://doi.org/10.1126/science.1119623.
639. Li GW, Elf J. 2009. Single molecule approaches to transcription factor kinetics in living cells. FEBS Lett 583:3979–3983. https://doi.org/10.1016/j.febslet.2009.11.035.
640. Oehler S, Eismann ER, Krämer H, Müller-Hill B. 1990. The three operators of the *lac* operon cooperate in repression. EMBO J 9:973–979. https://doi.org/10.1002/j.1460-2075.1990.tb08199.x.

641. Riggs AD, Suzuki H, Bourgeois S. 1970. Lac repressor-operator interaction. I. Equilibrium studies. J Mol Biol 48:67–83. https://doi.org/10.1016/0022-2836(70)90219-6.
642. Wang AC, Revzin A, Butler AP, von Hippel PH. 1977. Binding of *E. coli lac* repressor to non-operator DNA. Nucleic Acids Res 4:1579–1593. https://doi.org/10.1093/nar/4.5.1579.
643. Wang YM, Tegenfeldt JO, Reisner W, Riehn R, Guan XJ, Guo L, Golding I, Cox EC, Sturm J, Austin RH. 2005. Single-molecule studies of repressor-DNA interactions show long-range interactions. Proc Natl Acad Sci U S A 102:9796–9801. https://doi.org/10.1073/pnas.0502917102.
644. Wang YM, Austin RH, Cox EC. 2006. Single molecule measurements of repressor protein 1D diffusion on DNA. Phys Rev Lett 97:048302. https://doi.org/10.1103/PhysRevLett.97.048302.
645. Riggs AD, Bourgeois S, Cohn M. 1970. The *lac* repressor-operator interaction. 3. Kinetic studies. J Mol Biol 53:401–417. https://doi.org/10.1016/0022-2836(70)90074-4.
646. Richter PH, Eigen M. 1974. Diffusion controlled reaction rates in spheroidal geometry. Application to repressor–operator association and membrane bound enzymes. Biophys Chem 2:255–263. https://doi.org/10.1016/0301-4622(74)80050-5.
647. Berg OG, Winter RB, von Hippel PH. 1981. Diffusion-driven mechanisms of protein translocation on nucleic acids. 1. Models and theory. Biochemistry 20:6929–6948. https://doi.org/10.1021/bi00527a028.
648. Bajar BT, Wang ES, Lam AJ, Kim BB, Jacobs CL, Howe ES, Davidson MW, Lin MZ, Chu J. 2016. Improving brightness and photostability of green and red fluorescent proteins for live cell imaging and FRET reporting. Sci Rep 6:20889. https://doi.org/10.1038/srep20889.
649. Hammar P, Walldén M, Fange D, Persson F, Baltekin O, Ullman G, Leroy P, Elf J. 2014. Direct measurement of transcription factor dissociation excludes a simple operator occupancy model for gene regulation. Nat Genet 46:405–408. https://doi.org/10.1038/ng.2905.
650. Kuhlman TE, Cox EC. 2013. DNA-binding-protein inhomogeneity in *E. coli* modeled as biphasic facilitated diffusion. Phys Rev E Stat Nonlin Soft Matter Phys 88:022701. https://doi.org/10.1103/PhysRevE.88.022701.
651. Manley S, Gillette JM, Patterson GH, Shroff H, Hess HF, Betzig E, Lippincott-Schwartz J. 2008. High-density mapping of single-molecule trajectories with photoactivated localization microscopy. Nat Methods 5:155–157. https://doi.org/10.1038/nmeth.1176.
652. Liu Z, Xing D, Su QP, Zhu Y, Zhang J, Kong X, Xue B, Wang S, Sun H, Tao Y, Sun Y. 2014. Super-resolution imaging and tracking of protein-protein interactions in sub-diffraction cellular space. Nat Commun 5:4443. https://doi.org/10.1038/ncomms5443.
653. Li GW, Burkhardt D, Gross C, Weissman JS. 2014. Quantifying absolute protein synthesis rates reveals principles underlying allocation of cellular resources. Cell 157:624–635. https://doi.org/10.1016/j.cell.2014.02.033.
654. Söderström B, Daley DO. 2017. The bacterial divisome: more than a ring? Curr Genet 63:161–164. https://doi.org/10.1007/s00294-016-0630-2.
655. Adams DW, Errington J. 2009. Bacterial cell division: assembly, maintenance and disassembly of the Z ring. Nat Rev Microbiol 7:642–653. https://doi.org/10.1038/nrmicro2198.
656. Lutkenhaus J, Pichoff S, Du S. 2012. Bacterial cytokinesis: from Z ring to divisome. Cytoskeleton (Hoboken) 69:778–790. https://doi.org/10.1002/cm.21054.
657. Egan AJ, Vollmer W. 2013. The physiology of bacterial cell division. Ann N Y Acad Sci 1277:8–28. https://doi.org/10.1111/j.1749-6632.2012.06818.x.
658. Meier EL, Goley ED. 2014. Form and function of the bacterial cytokinetic ring. Curr Opin Cell Biol 26:19–27. https://doi.org/10.1016/j.ceb.2013.08.006.
659. Haeusser DP, Margolin W. 2016. Splitsville: structural and functional insights into the dynamic bacterial Z ring. Nat Rev Microbiol 14:305–319. https://doi.org/10.1038/nrmicro.2016.26.
660. den Blaauwen T, Hamoen LW, Levin PA. 2017. The divisome at 25: the road ahead. Curr Opin Microbiol 36:85–94. https://doi.org/10.1016/j.mib.2017.01.007.
661. Allen RG, Smith JA, Knudsen RC, Walker JR. 1972. Initial characterization of temperature-sensitive cell division mutants of *Escherichia coli*. Biochem Biophys Res Commun 47:1074–1079. https://doi.org/10.1016/0006-291X(72)90943-6.
662. Rowlett VW, Margolin W. 2015. The bacterial divisome: ready for its close-up. Philos Trans R Soc Lond B Biol Sci 370:20150028. https://doi.org/10.1098/rstb.2015.0028.
663. Bi EF, Lutkenhaus J. 1991. FtsZ ring structure associated with division in *Escherichia coli*. Nature 354:161–164. https://doi.org/10.1038/354161a0.
664. Fu G, Huang T, Buss J, Coltharp C, Hensel Z, Xiao J. 2010. *In vivo* structure of the *E. coli* FtsZ-ring revealed by photoactivated localization microscopy (PALM). PLoS One 5:e12682. https://doi.org/10.1371/journal.pone.0012680.
665. Jennings PC, Cox GC, Monahan LG, Harry EJ. 2011. Super-resolution imaging of the bacterial cytokinetic protein FtsZ. Micron 42:336–341. https://doi.org/10.1016/j.micron.2010.09.003.
666. Turnbull L, Strauss MP, Liew AT, Monahan LG, Whitchurch CB, Harry EJ. 2014. Super-resolution imaging of the cytokinetic Z ring in live bacteria using fast 3D-structured illumination microscopy (f3D-SIM). J Vis Exp :51469.
667. Rowlett VW, Margolin W. 2014. 3D-SIM super-resolution of FtsZ and its membrane tethers in *Escherichia coli* cells. Biophys J 107:L17–L20. https://doi.org/10.1016/j.bpj.2014.08.024.
668. Holden SJ, Pengo T, Meibom KL, Fernandez Fernandez C, Collier J, Manley S. 2014. High throughput 3D super-resolution microscopy reveals *Caulobacter crescentus in vivo* Z-ring organization. Proc Natl Acad Sci U S A 111:4566–4571. https://doi.org/10.1073/pnas.1313368111.
669. Coltharp C, Buss J, Plumer TM, Xiao J. 2016. Defining the rate-limiting processes of bacterial cytokinesis. Proc Natl Acad Sci U S A 113:E1044–E1053. https://doi.org/10.1073/pnas.1514296113.
670. Addinall SG, Lutkenhaus J. 1996. FtsA is localized to the septum in an FtsZ-dependent manner. J Bacteriol 178:7167–7172. https://doi.org/10.1128/JB.178.24.7167-7172.1996.
671. Addinall SG, Bi E, Lutkenhaus J. 1996. FtsZ ring formation in *fts* mutants. J Bacteriol 178:3877–3884. https://doi.org/10.1128/JB.178.13.3877-3884.1996.
672. Levin PA, Losick R. 1996. Transcription factor Spo0A switches the localization of the cell division protein FtsZ from a medial to a bipolar pattern in *Bacillus subtilis*. Genes Dev 10:478–488. https://doi.org/10.1101/gad.10.4.478.
673. Addinall SG, Cao C, Lutkenhaus J. 1997. FtsN, a late recruit to the septum in *Escherichia coli*. Mol Microbiol 25:303–309. https://doi.org/10.1046/j.1365-2958.1997.4641833.x.
674. Weiss DS, Pogliano K, Carson M, Guzman LM, Fraipont C, Nguyen-Distèche M, Losick R, Beckwith J. 1997. Localization of the *Escherichia coli* cell division protein FtsI (PBP3) to the division site and cell pole. Mol Microbiol 25:671–681. https://doi.org/10.1046/j.1365-2958.1997.5041869.x.
675. Wang L, Khattar MK, Donachie WD, Lutkenhaus J. 1998. FtsI and FtsW are localized to the septum in *Escherichia coli*. J Bacteriol 180:2810–2816. https://doi.org/10.1128/JB.180.11.2810-2816.1998.
676. Buddelmeijer N, Aarsman ME, Kolk AH, Vicente M, Nanninga N. 1998. Localization of cell division protein FtsQ by immunofluorescence microscopy in dividing and nondividing cells of *Escherichia coli*. J Bacteriol 180:6107–6116. https://doi.org/10.1128/.180.23.6107-6116.1998.
677. Alexeeva S, Gadella TW, Verheul J, Verhoeven GS, den Blaauwen T. 2010. Direct interactions of early and late assembling division proteins in *Escherichia coli* cells resolved by FRET. Mol Microbiol 77:384–398. https://doi.org/10.1111/j.1365-2958.2010.07211.x.
678. Goley ED, Dye NA, Werner JN, Gitai Z, Shapiro L. 2010. Imaging-based identification of a critical regulator of FtsZ protofilament curvature in *Caulobacter*. Mol Cell 39:975–987. https://doi.org/10.1016/j.molcel.2010.08.027.
679. Hale CA, Shiomi D, Liu B, Bernhardt TG, Margolin W, Niki H, de Boer PA. 2011. Identification of *Escherichia coli* ZapC (YcbW) as a component of the division apparatus that binds and bundles FtsZ polymers. J Bacteriol 193:1393–1404. https://doi.org/10.1128/JB.01245-10.
680. Willemse J, Borst JW, de Waal E, Bisseling T, van Wezel GP. 2011. Positive control of cell division: FtsZ is recruited by SsgB during sporulation of *Streptomyces*. Genes Dev 25:89–99. https://doi.org/10.1101/gad.600211.
681. Durand-Heredia JM, Yu HH, De Carlo S, Lesser CF, Janakiraman A. 2011. Identification and characterization of ZapC, a stabilizer of the FtsZ ring in *Escherichia coli*. J Bacteriol 193:1405–1413. https://doi.org/10.1128/JB.01258-10.
682. Durand-Heredia J, Rivkin E, Fan G, Morales J, Janakiraman A. 2012. Identification of ZapD as a cell division factor that promotes the assembly of FtsZ in *Escherichia coli*. J Bacteriol 194:3189–3198. https://doi.org/10.1128/JB.00176-12.
683. Pazos M, Natale P, Margolin W, Vicente M. 2013. Interactions among the early *Escherichia coli* divisome proteins revealed by bimolecular fluo-

rescence complementation. Environ Microbiol 15:3282–3291. https://doi.org/10.1111/1462-2920.12225.

684. Anderson DE, Gueiros-Filho FJ, Erickson HP. 2004. Assembly dynamics of FtsZ rings in *Bacillus subtilis* and *Escherichia coli* and effects of FtsZ-regulating proteins. J Bacteriol 186:5775–5781. https://doi.org/10.1128/JB.186.17.5775-5781.2004.
685. Thanedar S, Margolin W. 2004. FtsZ exhibits rapid movement and oscillation waves in helix-like patterns in *Escherichia coli*. Curr Biol 14:1167–1173. https://doi.org/10.1016/j.cub.2004.06.048.
686. Bisicchia P, Arumugam S, Schwille P, Sherratt D. 2013. MinC, MinD, and MinE drive counter-oscillation of early-cell-division proteins prior to *Escherichia coli* septum formation. mBio 4:e00856-13. https://doi.org/10.1128/mBio.00856-13.
687. Tonthat NK, Milam SL, Chinnam N, Whitfill T, Margolin W, Schumacher MA. 2013. SlmA forms a higher-order structure on DNA that inhibits cytokinetic Z-ring formation over the nucleoid. Proc Natl Acad Sci U S A 110:10586–10591. https://doi.org/10.1073/pnas.1221036110.
688. Holden S. 2018. Probing the mechanistic principles of bacterial cell division with super-resolution microscopy. Curr Opin Microbiol 43:84–91. https://doi.org/10.1016/j.mib.2017.12.005.
689. Peters PC, Migocki MD, Thoni C, Harry EJ. 2007. A new assembly pathway for the cytokinetic Z ring from a dynamic helical structure in vegetatively growing cells of *Bacillus subtilis*. Mol Microbiol 64:487–499. https://doi.org/10.1111/j.1365-2958.2007.05673.x.
690. Buss J, Coltharp C, Huang T, Pohlmeyer C, Wang SC, Hatem C, Xiao J. 2013. *In vivo* organization of the FtsZ-ring by ZapA and ZapB revealed by quantitative super-resolution microscopy. Mol Microbiol 89:1099–1120. https://doi.org/10.1111/mmi.12331.
691. Söderström B, Chan H, Daley DO. 2019. Super-resolution images of peptidoglycan remodelling enzymes at the division site of *Escherichia coli*. Curr Genet 65:99–101. https://doi.org/10.1007/s00294-018-0869-x.
692. Yang X, Lyu Z, Miguel A, McQuillen R, Huang KC, Xiao J. 2017. GTPase activity-coupled treadmilling of the bacterial tubulin FtsZ organizes septal cell wall synthesis. Science 355:744–747. https://doi.org/10.1126/science.aak9995.
693. Silhavy TJ, Kahne D, Walker S. 2010. The bacterial cell envelope. Cold Spring Harb Perspect Biol 2:a000414. https://doi.org/10.1101/cshperspect.a000414.
694. Feilmeier BJ, Iseminger G, Schroeder D, Webber H, Phillips GJ. 2000. Green fluorescent protein functions as a reporter for protein localization in *Escherichia coli*. J Bacteriol 182:4068–4076. https://doi.org/10.1128/JB.182.14.4068-4076.2000.
695. Chen JC, Viollier PH, Shapiro L. 2005. A membrane metalloprotease participates in the sequential degradation of a *Caulobacter* polarity determinant. Mol Microbiol 55:1085–1103. https://doi.org/10.1111/j.1365-2958.2004.04443.x.
696. Lewenza S, Vidal-Ingigliardi D, Pugsley AP. 2006. Direct visualization of red fluorescent lipoproteins indicates conservation of the membrane sorting rules in the family *Enterobacteriaceae*. J Bacteriol 188:3516–3524. https://doi.org/10.1128/JB.188.10.3516-3524.2006.
697. Wei X, Pathak DT, Wall D. 2011. Heterologous protein transfer within structured myxobacteria biofilms. Mol Microbiol 81:315–326. https://doi.org/10.1111/j.1365-2958.2011.07710.x.
698. Ducret A, Fleuchot B, Bergam P, Mignot T. 2013. Direct live imaging of cell-cell protein transfer by transient outer membrane fusion in *Myxococcus xanthus*. Elife 2:e00868. https://doi.org/10.7554/eLife.00868.
699. Mileykovskaya E, Dowhan W. 2000. Visualization of phospholipid domains in *Escherichia coli* by using the cardiolipin-specific fluorescent dye 10-*N*-nonyl acridine orange. J Bacteriol 182:1172–1175. https://doi.org/10.1128/JB.182.4.1172-1175.2000.
700. Renner LD, Weibel DB. 2011. Cardiolipin microdomains localize to negatively curved regions of *Escherichia coli* membranes. Proc Natl Acad Sci U S A 108:6264–6269. https://doi.org/10.1073/pnas.1015757108.
701. Mika JT, Thompson AJ, Dent MR, Brooks NJ, Michiels J, Hofkens J, Kuimova MK. 2016. Measuring the viscosity of the *Escherichia coli* plasma membrane using molecular rotors. Biophys J 111:1528–1540. https://doi.org/10.1016/j.bpj.2016.08.020.
702. Loison P, Gervais P, Perrier-Cornet JM, Kuimova MK. 2016. Effect of ethanol perturbation on viscosity and permeability of an inner membrane in *Bacillus subtilis* spores. Biochim Biophys Acta 1858:2060–2069. https://doi.org/10.1016/j.bbamem.2016.06.003.
703. El Khoury M, Swain J, Sautrey G, Zimmermann L, Van Der Smissen P, Décout JL, Mingeot-Leclercq MP. 2017. Targeting bacterial cardiolipin enriched microdomains: an antimicrobial strategy used by amphiphilic aminoglycoside antibiotics. Sci Rep 7:10697. https://doi.org/10.1038/s41598-017-10543-3.
704. Dammeyer T, Tinnefeld P. 2012. Engineered fluorescent proteins illuminate the bacterial periplasm. Comput Struct Biotechnol J 3:e201210013. https://doi.org/10.5936/csbj.201210013.
705. Meiresonne NY, Consoli E, Mertens LMY, Chertkova AO, Goedhart J, den Blaauwen T. 2019. Superfolder mTurquoise2^{ox} optimized for the bacterial periplasm allows high efficiency *in vivo* FRET of cell division antibiotic targets. Mol Microbiol 111:1025–1038. https://doi.org/10.1111/mmi.14206.
706. Cook WR, MacAlister TJ, Rothfield LI. 1986. Compartmentalization of the periplasmic space at division sites in gram-negative bacteria. J Bacteriol 168:1430–1438. https://doi.org/10.1128/JB.168.3.1430-1438.1986.
707. Mileykovskaya E, Dowhan W. 2009. Cardiolipin membrane domains in prokaryotes and eukaryotes. Biochim Biophys Acta 1788:2084–2091. https://doi.org/10.1016/j.bbamem.2009.04.003.
708. Arnarez C, Marrink SJ, Periole X. 2013. Identification of cardiolipin binding sites on cytochrome c oxidase at the entrance of proton channels. Sci Rep 3:1263. https://doi.org/10.1038/srep01263.
709. Sohlenkamp C, Geiger O. 2016. Bacterial membrane lipids: diversity in structures and pathways. FEMS Microbiol Rev 40:133–159. https://doi.org/10.1093/femsre/fuv008.
710. Lin TY, Weibel DB. 2016. Organization and function of anionic phospholipids in bacteria. Appl Microbiol Biotechnol 100:4255–4267. https://doi.org/10.1007/s00253-016-7468-x.
711. Kawai C, Ferreira JC, Baptista MS, Nantes IL. 2014. Not only oxidation of cardiolipin affects the affinity of cytochrome C for lipid bilayers. J Phys Chem B 118:11863–11872. https://doi.org/10.1021/jp504518g.
712. Sautrey G, El Khoury M, Dos Santos AG, Zimmermann L, Deleu M, Lins L, Décout JL, Mingeot-Leclercq MP. 2016. Negatively charged lipids as a potential target for new amphiphilic aminoglycoside antibiotics: a biophysical study. J Biol Chem 291:13864–13874. https://doi.org/10.1074/jbc.M115.665364.
713. Matsumoto K, Kusaka J, Nishibori A, Hara H. 2006. Lipid domains in bacterial membranes. Mol Microbiol 61:1110–1117. https://doi.org/10.1111/j.1365-2958.2006.05317.x.
714. Bernal P, Muñoz-Rojas J, Hurtado A, Ramos JL, Segura A. 2007. A *Pseudomonas putida* cardiolipin synthesis mutant exhibits increased sensitivity to drugs related to transport functionality. Environ Microbiol 9:1135–1145. https://doi.org/10.1111/j.1462-2920.2006.01236.x.
715. Gallet PF, Maftah A, Petit JM, Denis-Gay M, Julien R. 1995. Direct cardiolipin assay in yeast using the red fluorescence emission of 10-*N*-nonyl acridine orange. Eur J Biochem 228:113–119. https://doi.org/10.1111/j.1432-1033.1995.tb20238.x.
716. Petit JM, Maftah A, Ratinaud MH, Julien R. 1992. 10-*N*-nonyl acridine orange interacts with cardiolipin and allows the quantification of this phospholipid in isolated mitochondria. Eur J Biochem 209:267–273. https://doi.org/10.1111/j.1432-1033.1992.tb17285.x.
717. Petit JM, Huet O, Gallet PF, Maftah A, Ratinaud MH, Julien R. 1994. Direct analysis and significance of cardiolipin transverse distribution in mitochondrial inner membranes. Eur J Biochem 220:871–879. https://doi.org/10.1111/j.1432-1033.1994.tb18690.x.
718. Chang SC, Heacock PN, Mileykovskaya E, Voelker DR, Dowhan W. 1998. Isolation and characterization of the gene (CLS1) encoding cardiolipin synthase in *Saccharomyces cerevisiae*. J Biol Chem 273:14933–14941. https://doi.org/10.1074/jbc.273.24.14933.
719. Mileykovskaya E, Dowhan W, Birke RL, Zheng D, Lutterodt L, Haines TH. 2001. Cardiolipin binds nonyl acridine orange by aggregating the dye at exposed hydrophobic domains on bilayer surfaces. FEBS Lett 507:187–190. https://doi.org/10.1016/S0014-5793(01)02948-9.
720. Oliver PM, Crooks JA, Leidl M, Yoon EJ, Saghatelian A, Weibel DB. 2014. Localization of anionic phospholipids in *Escherichia coli* cells. J Bacteriol 196:3386–3398. https://doi.org/10.1128/JB.01877-14.
721. Pogmore AR, Seistrup KH, Strahl H. 2018. The Gram-positive model organism *Bacillus subtilis* does not form microscopically detectable cardiolipin-specific lipid domains. Microbiology 164:475–482. https://doi.org/10.1099/mic.0.000639.
722. Loison P, Hosny NA, Gervais P, Champion D, Kuimova MK, Perrier-Cornet JM. 2013. Direct investigation of viscosity of an atypical inner membrane of *Bacillus* spores: a molecular rotor/FLIM study. Biochim Biophys Acta 1828:2436–2443. https://doi.org/10.1016/j.bbamem.2013.06.028.
723. Nenninger A, Mastroianni G, Robson A, Lenn T, Xue Q, Leake MC, Mullineaux CW. 2014. Independent mobility of proteins and lipids in

the plasma membrane of *Escherichia coli*. Mol Microbiol 92:1142–1153. https://doi.org/10.1111/mmi.12619.

724. Kuimova MK. 2012. Mapping viscosity in cells using molecular rotors. Phys Chem Chem Phys 14:12671–12686. https://doi.org/10.1039/c2cp41674c.
725. Scheinpflug K, Krylova O, Strahl H. 2017. Measurement of cell membrane fluidity by Laurdan GP: fluorescence spectroscopy and microscopy. Methods Mol Biol 1520:159–174. https://doi.org/10.1007/978-1-4939-6634-9_10.
726. Wenzel M, Rautenbach M, Vosloo JA, Siersma T, Aisenbrey CHM, Zaitseva E, Laubscher WE, van Rensburg W, Behrends JC, Bechinger B, Hamoen LW. 2018. The multifaceted antibacterial mechanisms of the pioneering peptide antibiotics tyrocidine and gramicidin S. mBio 9:e00802-18. https://doi.org/10.1128/mBio.00802-18.
727. Miot M, Betton JM. 2004. Protein quality control in the bacterial periplasm. Microb Cell Fact 3:4. https://doi.org/10.1186/1475-2859-3-4.
728. Palmer T, Berks BC. 2012. The twin-arginine translocation (Tat) protein export pathway. Nat Rev Microbiol 10:483–496. https://doi.org/10.1038/nrmicro2814.
729. Fisher AC, DeLisa MP. 2008. Laboratory evolution of fast-folding green fluorescent protein using secretory pathway quality control. PLoS One 3:e2351. https://doi.org/10.1371/journal.pone.0002351.
730. Aronson DE, Costantini LM, Snapp EL. 2011. Superfolder GFP is fluorescent in oxidizing environments when targeted via the Sec translocon. Traffic 12:543–548. https://doi.org/10.1111/j.1600-0854.2011.01168.x.
731. Dinh T, Bernhardt TG. 2011. Using superfolder green fluorescent protein for periplasmic protein localization studies. J Bacteriol 193:4984–4987. https://doi.org/10.1128/JB.00315-11.
732. Costantini LM, Baloban M, Markwardt ML, Rizzo M, Guo F, Verkhusha VV, Snapp EL. 2015. A palette of fluorescent proteins optimized for diverse cellular environments. Nat Commun 6:7670. https://doi.org/10.1038/ncomms8670.
733. Thomas JD, Daniel RA, Errington J, Robinson C. 2001. Export of active green fluorescent protein to the periplasm by the twin-arginine translocase (Tat) pathway in *Escherichia coli*. Mol Microbiol 39:47–53. https://doi.org/10.1046/j.1365-2958.2001.02253.x.
734. Santini CL, Bernadac A, Zhang M, Chanal A, Ize B, Blanco C, Wu LF. 2001. Translocation of jellyfish green fluorescent protein via the Tat system of *Escherichia coli* and change of its periplasmic localization in response to osmotic up-shock. J Biol Chem 276:8159–8164. https://doi.org/10.1074/jbc.C000833200.
735. DeLisa MP, Samuelson P, Palmer T, Georgiou G. 2002. Genetic analysis of the twin arginine translocator secretion pathway in bacteria. J Biol Chem 277:29825–29831. https://doi.org/10.1074/jbc.M201956200.
736. Meiresonne NY, van der Ploeg R, Hink MA, den Blaauwen T. 2017. Activity-related conformational changes in D,D-carboxypeptidases revealed by *in vivo* periplasmic Förster resonance energy transfer assay in *Escherichia coli*. mBio 8:e01089-17. https://doi.org/10.1128/mBio.01089-17.
737. Dammeyer T, Timmis KN, Tinnefeld P. 2013. Broad host range vectors for expression of proteins with (Twin-) Strep-tag, His-tag and engineered, export optimized yellow fluorescent protein. Microb Cell Fact 12:49. https://doi.org/10.1186/1475-2859-12-49.
738. El Khatib M, Martins A, Bourgeois D, Colletier JP, Adam V. 2016. Rational design of ultrastable and reversibly photoswitchable fluorescent proteins for super-resolution imaging of the bacterial periplasm. Sci Rep 6:18459. https://doi.org/10.1038/srep18459.
739. Peters NT, Dinh T, Bernhardt TG. 2011. A fail-safe mechanism in the septal ring assembly pathway generated by the sequential recruitment of cell separation amidases and their activators. J Bacteriol 193:4973–4983. https://doi.org/10.1128/JB.00316-11.
740. Typas A, Banzhaf M, Gross CA, Vollmer W. 2011. From the regulation of peptidoglycan synthesis to bacterial growth and morphology. Nat Rev Microbiol 10:123–136. https://doi.org/10.1038/nrmicro2677.
741. Vollmer W, Blanot D, de Pedro MA. 2008. Peptidoglycan structure and architecture. FEMS Microbiol Rev 32:149–167. https://doi.org/10.1111/j.1574-6976.2007.00094.x.
742. Burman LG, Raichler J, Park JT. 1983. Evidence for diffuse growth of the cylindrical portion of the *Escherichia coli* murein sacculus. J Bacteriol 155:983–988. https://doi.org/10.1128/JB.155.3.983-988.1983.
743. Cooper S, Hsieh ML. 1988. The rate and topography of cell wall synthesis during the division cycle of *Escherichia coli* using *N*-acetylglucosamine as a peptidoglycan label. J Gen Microbiol 134:1717–1721. https://doi.org/10.1099/00221287-134-6-1717.
744. Wientjes FB, Nanninga N. 1989. Rate and topography of peptidoglycan synthesis during cell division in *Escherichia coli*: concept of a leading edge. J Bacteriol 171:3412–3419. https://doi.org/10.1128/JB.171.6.3412-3419.1989.
745. Scheffers DJ, Pinho MG. 2005. Bacterial cell wall synthesis: new insights from localization studies. Microbiol Mol Biol Rev 69:585–607. https://doi.org/10.1128/MMBR.69.4.585-607.2005.
746. Cabeen MT, Jacobs-Wagner C. 2005. Bacterial cell shape. Nat Rev Microbiol 3:601–610. https://doi.org/10.1038/nrmicro1205.
747. Gautam S, Kim T, Shoda T, Sen S, Deep D, Luthra R, Ferreira MT, Pinho MG, Spiegel DA. 2015. An activity-based probe for studying crosslinking in live bacteria. Angew Chem Int Ed Engl 54:10492–10496. https://doi.org/10.1002/anie.201503869.
748. Liang H, DeMeester KE, Hou CW, Parent MA, Caplan JL, Grimes CL. 2017. Metabolic labelling of the carbohydrate core in bacterial peptidoglycan and its applications. Nat Commun 8:15015. https://doi.org/10.1038/ncomms15015.
749. Hsu YP, Hall E, Booher G, Murphy B, Radkov AD, Yablonowski J, Mulcahey C, Alvarez L, Cava F, Brun YV, Kuru E, VanNieuwenhze MS. 2019. Fluorogenic D-amino acids enable real-time monitoring of peptidoglycan biosynthesis and high-throughput transpeptidation assays. Nat Chem 11:335–341. https://doi.org/10.1038/s41557-019-0217-x.
750. Den Blaauwen T, Aarsman ME, Vischer NO, Nanninga N. 2003. Penicillin-binding protein PBP2 of *Escherichia coli* localizes preferentially in the lateral wall and at mid-cell in comparison with the old cell pole. Mol Microbiol 47:539–547. https://doi.org/10.1046/j.1365-2958.2003.03316.x.
751. Scheffers DJ. 2005. Dynamic localization of penicillin-binding proteins during spore development in *Bacillus subtilis*. Microbiology (Reading) 151:999–1012. https://doi.org/10.1099/mic.0.27692-0.
752. Sizemore RK, Caldwell JJ, Kendrick AS. 1990. Alternate Gram staining technique using a fluorescent lectin. Appl Environ Microbiol 56:2245–2247. https://doi.org/10.1128/AEM.56.7.2245-2247.1990.
753. Misra G, Rojas ER, Gopinathan A, Huang KC. 2013. Mechanical consequences of cell-wall turnover in the elongation of a Gram-positive bacterium. Biophys J 104:2342–2352. https://doi.org/10.1016/j.bpj.2013.04.047.
754. Daniel RA, Errington J. 2003. Control of cell morphogenesis in bacteria: two distinct ways to make a rod-shaped cell. Cell 113:767–776. https://doi.org/10.1016/S0092-8674(03)00421-5.
755. Tiyanont K, Doan T, Lazarus MB, Fang X, Rudner DZ, Walker S. 2006. Imaging peptidoglycan biosynthesis in *Bacillus subtilis* with fluorescent antibiotics. Proc Natl Acad Sci U S A 103:11033–11038. https://doi.org/10.1073/pnas.0600829103.
756. Pinho MG, Errington J. 2003. Dispersed mode of *Staphylococcus aureus* cell wall synthesis in the absence of the division machinery. Mol Microbiol 50:871–881. https://doi.org/10.1046/j.1365-2958.2003.03719.x.
757. Fang X, Tiyanont K, Zhang Y, Wanner J, Boger D, Walker S. 2006. The mechanism of action of ramoplanin and enduracidin. Mol Biosyst 2:69–76. https://doi.org/10.1039/B515328J.
758. Walker S, Chen L, Hu Y, Rew Y, Shin D, Boger DL. 2005. Chemistry and biology of ramoplanin: a lipoglycodepsipeptide with potent antibiotic activity. Chem Rev 105:449–476. https://doi.org/10.1021/cr030106n.
759. Pilhofer M, Aistleitner K, Biboy J, Gray J, Kuru E, Hall E, Brun YV, VanNieuwenhze MS, Vollmer W, Horn M, Jensen GJ. 2013. Discovery of chlamydial peptidoglycan reveals bacteria with murein sacculi but without FtsZ. Nat Commun 4:2856. https://doi.org/10.1038/ncomms3856.
760. Fleurie A, Lesterlin C, Manuse S, Zhao C, Cluzel C, Lavergne JP, Franz-Wachtel M, Macek B, Combet C, Kuru E, VanNieuwenhze MS, Brun YV, Sherratt D, Grangeasse C. 2014. MapZ marks the division sites and positions FtsZ rings in *Streptococcus pneumoniae*. Nature 516:259–262. https://doi.org/10.1038/nature13966.
761. Lebar MD, May JM, Meeske AJ, Leiman SA, Lupoli TJ, Tsukamoto H, Losick R, Rudner DZ, Walker S, Kahne D. 2014. Reconstitution of peptidoglycan cross-linking leads to improved fluorescent probes of cell wall synthesis. J Am Chem Soc 136:10874–10877. https://doi.org/10.1021/ja505668f.
762. Monteiro JM, Fernandes PB, Vaz F, Pereira AR, Tavares AC, Ferreira MT, Pereira PM, Veiga H, Kuru E, VanNieuwenhze MS, Brun YV, Filipe SR, Pinho MG. 2015. Cell shape dynamics during the staphylococcal cell cycle. Nat Commun 6:8055. https://doi.org/10.1038/ncomms9055.
763. Boersma MJ, Kuru E, Rittichier JT, VanNieuwenhze MS, Brun YV, Winkler ME. 2015. Minimal peptidoglycan (PG) turnover in wild-type and PG hydrolase and cell division mutants of *Streptococcus pneumoniae* D39

growing planktonically and in host-relevant biofilms. J Bacteriol 197: 3472–3485. https://doi.org/10.1128/JB.00541-15.

764. Fenton AK, Mortaji LE, Lau DT, Rudner DZ, Bernhardt TG. 2016. CozE is a member of the MreCD complex that directs cell elongation in *Streptococcus pneumoniae*. Nat Microbiol 2:16237. https://doi.org/10.1038/nmicrobiol.2016.237.
765. Liechti G, Kuru E, Packiam M, Hsu YP, Tekkam S, Hall E, Rittichier JT, VanNieuwenhze M, Brun YV, Maurelli AT. 2016. Pathogenic *Chlamydia* lack a classical sacculus but synthesize a narrow, mid-cell peptidoglycan ring, regulated by MreB, for cell division. PLoS Pathog 12:e1005590. https://doi.org/10.1371/journal.ppat.1005590.
766. Hsu YP, Rittichier J, Kuru E, Yablonowski J, Pasciak E, Tekkam S, Hall E, Murphy B, Lee TK, Garner EC, Huang KC, Brun YV, VanNieuwenhze MS. 2017. Full color palette of fluorescent d-amino acids for *in situ* labeling of bacterial cell walls. Chem Sci 8:6313–6321. https://doi.org/10.1039/C7SC01800B.
767. Bartlett TM, Bratton BP, Duvshani A, Miguel A, Sheng Y, Martin NR, Nguyen JP, Persat A, Desmarais SM, VanNieuwenhze MS, Huang KC, Zhu J, Shaevitz JW, Gitai Z. 2017. A periplasmic polymer curves *Vibrio cholerae* and promotes pathogenesis. Cell 168:172–185.e15. https://doi.org/10.1016/j.cell.2016.12.019.
768. Cserti E, Rosskopf S, Chang YW, Eisheuer S, Selter L, Shi J, Regh C, Koert U, Jensen GJ, Thanbichler M. 2017. Dynamics of the peptidoglycan biosynthetic machinery in the stalked budding bacterium *Hyphomonas neptunium*. Mol Microbiol 103:875–895. https://doi.org/10.1111/mmi.13593.
769. Morales Angeles D, Liu Y, Hartman AM, Borisova M, de Sousa Borges A, de Kok N, Beilharz K, Veening JW, Mayer C, Hirsch AK, Scheffers DJ. 2017. Pentapeptide-rich peptidoglycan at the *Bacillus subtilis* cell-division site. Mol Microbiol 104:319–333. https://doi.org/10.1111/mmi.13629.
770. Radkov AD, Hsu YP, Booher G, VanNieuwenhze MS. 2018. Imaging bacterial cell wall biosynthesis. Annu Rev Biochem 87:991–1014. https://doi.org/10.1146/annurev-biochem-062917-012921.
771. de Pedro MA, Quintela JC, Höltje JV, Schwarz H. 1997. Murein segregation in *Escherichia coli*. J Bacteriol 179:2823–2834. https://doi.org/10.1128/JB.179.9.2823-2834.1997.
772. Cava F, de Pedro MA, Lam H, Davis BM, Waldor MK. 2011. Distinct pathways for modification of the bacterial cell wall by non-canonical D-amino acids. EMBO J 30:3442–3453. https://doi.org/10.1038/emboj.2011.246.
773. Lam H, Oh DC, Cava F, Takacs CN, Clardy J, de Pedro MA, Waldor MK. 2009. D-amino acids govern stationary phase cell wall remodeling in bacteria. Science 325:1552–1555. https://doi.org/10.1126/science.1178123.
774. Lupoli TJ, Tsukamoto H, Doud EH, Wang TS, Walker S, Kahne D. 2011. Transpeptidase-mediated incorporation of D-amino acids into bacterial peptidoglycan. J Am Chem Soc 133:10748–10751. https://doi.org/10.1021/ja2040656.
775. Kuru E, Radkov A, Meng X, Egan A, Alvarez L, Dowson A, Booher G, Breukink E, Roper DI, Cava F, Vollmer W, Brun Y, VanNieuwenhze MS. 2019. Mechanisms of incorporation for D-amino acid probes that target peptidoglycan biosynthesis. ACS Chem Biol 14:2745–2756. https://doi.org/10.1021/acschembio.9b00664.
776. Hsu YP, Booher G, Egan A, Vollmer W, VanNieuwenhze MS. 2019. D-Amino acid derivatives as *in situ* probes for visualizing bacterial peptidoglycan biosynthesis. Acc Chem Res 52:2713–2722. https://doi.org/10.1021/acs.accounts.9b00311.
777. Haidekker MA, Theodorakis EA. 2010. Environment-sensitive behavior of fluorescent molecular rotors. J Biol Eng 4:11. https://doi.org/10.1186/1754-1611-4-11.
778. Kuru E, Tekkam S, Hall E, Brun YV, Van Nieuwenhze MS. 2015. Synthesis of fluorescent D-amino acids and their use for probing peptidoglycan synthesis and bacterial growth *in situ*. Nat Protoc 10:33–52. https://doi.org/10.1038/nprot.2014.197.
779. Ursell TS, Trepagnier EH, Huang KC, Theriot JA. 2012. Analysis of surface protein expression reveals the growth pattern of the gram-negative outer membrane. PLoS Comput Biol 8:e1002680. https://doi.org/10.1371/journal.pcbi.1002680.
780. Pedersen LB, Angert ER, Setlow P. 1999. Septal localization of penicillin-binding protein 1 in *Bacillus subtilis*. J Bacteriol 181:3201–3211. https://doi.org/10.1128/JB.181.10.3201-3211.1999.
781. Daniel RA, Harry EJ, Errington J. 2000. Role of penicillin-binding protein PBP 2B in assembly and functioning of the division machinery of *Bacillus subtilis*. Mol Microbiol 35:299–311. https://doi.org/10.1046/j.1365-2958.2000.01724.x.
782. Morlot C, Zapun A, Dideberg O, Vernet T. 2003. Growth and division of *Streptococcus pneumoniae*: localization of the high molecular weight penicillin-binding proteins during the cell cycle. Mol Microbiol 50: 845–855. https://doi.org/10.1046/j.1365-2958.2003.03767.x.
783. Scheffers DJ, Jones LJ, Errington J. 2004. Several distinct localization patterns for penicillin-binding proteins in *Bacillus subtilis*. Mol Microbiol 51:749–764. https://doi.org/10.1046/j.1365-2958.2003.03854.x.
784. Piette A, Fraipont C, Den Blaauwen T, Aarsman ME, Pastoret S, Nguyen-Distèche M. 2004. Structural determinants required to target penicillin-binding protein 3 to the septum of *Escherichia coli*. J Bacteriol 186: 6110–6117. https://doi.org/10.1128/JB.186.18.6110-6117.2004.
785. Wissel MC, Wendt JL, Mitchell CJ, Weiss DS. 2005. The transmembrane helix of the *Escherichia coli* division protein FtsI localizes to the septal ring. J Bacteriol 187:320–328. https://doi.org/10.1128/JB.187.1.320-328.2005.
786. Hao J, Kendrick KE. 1998. Visualization of penicillin-binding proteins during sporulation of *Streptomyces griseus*. J Bacteriol 180:2125–2132. https://doi.org/10.1128/JB.180.8.2125-2132.1998.
787. Delcour AH. 2009. Outer membrane permeability and antibiotic resistance. Biochim Biophys Acta 1794:808–816. https://doi.org/10.1016/j.bbapap.2008.11.005.
788. Henderson JC, Zimmerman SM, Crofts AA, Boll JM, Kuhns LG, Herrera CM, Trent MS. 2016. The power of asymmetry: architecture and assembly of the Gram-negative outer membrane lipid bilayer. Annu Rev Microbiol 70:255–278. https://doi.org/10.1146/annurev-micro-102215-095308.
789. Kamio Y, Nikaido H. 1976. Outer membrane of *Salmonella* Typhimurium: accessibility of phospholipid head groups to phospholipase C and cyanogen bromide activated dextran in the external medium. Biochemistry 15:2561–2570. https://doi.org/10.1021/bi00657a012.
790. Rollauer SE, Sooreshjani MA, Noinaj N, Buchanan SK. 2015. Outer membrane protein biogenesis in Gram-negative bacteria. Philos Trans R Soc Lond B Biol Sci 370:20170023.
791. Christensen H, Garton NJ, Horobin RW, Minnikin DE, Barer MR. 1999. Lipid domains of mycobacteria studied with fluorescent molecular probes. Mol Microbiol 31:1561–1572. https://doi.org/10.1046/j.1365-2958.1999.01304.x.
792. Fishov I, Woldringh CL. 1999. Visualization of membrane domains in *Escherichia coli*. Mol Microbiol 32:1166–1172. https://doi.org/10.1046/j.1365-2958.1999.01425.x.
793. Cowan AE, Olivastro EM, Koppel DE, Loshon CA, Setlow B, Setlow P. 2004. Lipids in the inner membrane of dormant spores of *Bacillus* species are largely immobile. Proc Natl Acad Sci U S A 101:7733–7738. https://doi.org/10.1073/pnas.0306859101.
794. Zupan JR, Cameron TA, Anderson-Furgeson J, Zambryski PC. 2013. Dynamic FtsA and FtsZ localization and outer membrane alterations during polar growth and cell division in *Agrobacterium tumefaciens*. Proc Natl Acad Sci U S A 110:9060–9065. https://doi.org/10.1073/pnas.1307241110.
795. Rojas ER, Billings G, Odermatt PD, Auer GK, Zhu L, Miguel A, Chang F, Weibel DB, Theriot JA, Huang KC. 2018. The outer membrane is an essential load-bearing element in Gram-negative bacteria. Nature 559: 617–621. https://doi.org/10.1038/s41586-018-0344-3.
796. Kotte O, Volkmer B, Radzikowski JL, Heinemann M. 2014. Phenotypic bistability in *Escherichia coli*'s central carbon metabolism. Mol Syst Biol 10:736. https://doi.org/10.15252/msb.20135022.
797. Shapiro L, McAdams HH, Losick R. 2009. Why and how bacteria localize proteins. Science 326:1225–1228. https://doi.org/10.1126/science.1175685.
798. Yin J, Liu F, Li X, Walsh CT. 2004. Labeling proteins with small molecules by site-specific posttranslational modification. J Am Chem Soc 126: 7754–7755. https://doi.org/10.1021/ja047749k.
799. Yin J, Straight PD, McLoughlin SM, Zhou Z, Lin AJ, Golan DE, Kelleher NL, Kolter R, Walsh CT. 2005. Genetically encoded short peptide tag for versatile protein labeling by Sfp phosphopantetheinyl transferase. Proc Natl Acad Sci U S A 102:15815–15820. https://doi.org/10.1073/pnas.0507705102.
800. Winther T, Xu L, Berg-Sørensen K, Brown S, Oddershede LB. 2009. Effect of energy metabolism on protein motility in the bacterial outer membrane. Biophys J 97:1305–1312. https://doi.org/10.1016/j.bpj.2009.06.027.
801. Rassam P, Copeland NA, Birkholz O, Tóth C, Chavent M, Duncan AL,

Cross SJ, Housden NG, Kaminska R, Seger U, Quinn DM, Garrod TJ, Sansom MS, Piehler J, Baumann CG, Kleanthous C. 2015. Supramolecular assemblies underpin turnover of outer membrane proteins in bacteria. Nature 523:333–336. https://doi.org/10.1038/nature14461.

802. Kleanthous C. 2010. Swimming against the tide: progress and challenges in our understanding of colicin translocation. Nat Rev Microbiol 8:843–848. https://doi.org/10.1038/nrmicro2454.
803. Housden NG, Loftus SR, Moore GR, James R, Kleanthous C. 2005. Cell entry mechanism of enzymatic bacterial colicins: porin recruitment and the thermodynamics of receptor binding. Proc Natl Acad Sci U S A 102:13849–13854. https://doi.org/10.1073/pnas.0503567102.
804. Bertani B, Ruiz N. 2018. Function and biogenesis of lipopolysaccharides. EcoSal Plus 8:ecosalplus.ESP-0001-2018. https://doi.org/10.1128/ecosalplus.ESP-0001-2018.
805. Nilsson I, Grove K, Dovala D, Uehara T, Lapointe G, Six DA. 2017. Molecular characterization and verification of azido-3,8-dideoxy-D-*manno*-oct-2-ulosonic acid incorporation into bacterial lipopolysaccharide. J Biol Chem 292:19840–19848. https://doi.org/10.1074/jbc.M117.814962.
806. Wang W, Zhu Y, Chen X. 2017. Selective imaging of Gram-negative and gram-positive microbiotas in the mouse gut. Biochemistry 56:3889–3893. https://doi.org/10.1021/acs.biochem.7b00539.
807. Debenham SD, Snyder PW, Toone EJ. 2003. Solid-phase synthesis for the identification of high-affinity bivalent lectin ligands. J Org Chem 68:5805–5811. https://doi.org/10.1021/jo0207271.
808. Clarke BR, Cuthbertson L, Whitfield C. 2004. Nonreducing terminal modifications determine the chain length of polymannose O antigens of *Escherichia coli* and couple chain termination to polymer export via an ATP-binding cassette transporter. J Biol Chem 279:35709–35718. https://doi.org/10.1074/jbc.M404738200.
809. Ghosh AS, Young KD. 2005. Helical disposition of proteins and lipopolysaccharide in the outer membrane of *Escherichia coli*. J Bacteriol 187:1913–1922. https://doi.org/10.1128/JB.187.6.1913-1922.2005.
810. Moison E, Xie R, Zhang G, Lebar MD, Meredith TC, Kahne D. 2017. A fluorescent probe distinguishes between inhibition of early and late steps of lipopolysaccharide biogenesis in whole cells. ACS Chem Biol 12:928–932. https://doi.org/10.1021/acschembio.7b00159.
811. Zhang G, Baidin V, Pahil KS, Moison E, Tomasek D, Ramadoss NS, Chatterjee AK, McNamara CW, Young TS, Schultz PG, Meredith TC, Kahne D. 2018. Cell-based screen for discovering lipopolysaccharide biogenesis inhibitors. Proc Natl Acad Sci U S A 115:6834–6839. https://doi.org/10.1073/pnas.1804670115.
812. KenryLiu B. 2019. Bio-orthogonal click chemistry for *in vivo* bioimaging. Trends Chem 1:763–778. https://doi.org/10.1016/j.trechm.2019.08.003.
813. Holst O. 2007. The structures of core regions from enterobacterial lipopolysaccharides: an update. FEMS Microbiol Lett 271:3–11. https://doi.org/10.1111/j.1574-6968.2007.00708.x.
814. Cipolla L, Gabrielli L, Bini D, Russo L, Shaikh N. 2010. Kdo: a critical monosaccharide for bacteria viability. Nat Prod Rep 27:1618–1629. https://doi.org/10.1039/c004750n.
815. Proft T, Baker EN. 2009. Pili in Gram-negative and Gram-positive bacteria: structure, assembly, and their role in disease. Cell Mol Life Sci 66:613–635. https://doi.org/10.1007/s00018-008-8477-4.
816. Haiko J, Westerlund-Wikström B. 2013. The role of the bacterial flagellum in adhesion and virulence. Biology (Basel) 2:1242–1267. https://doi.org/10.3390/biology2041242.
817. Belas R. 2014. Biofilms, flagella, and mechanosensing of surfaces by bacteria. Trends Microbiol 22:517–527. https://doi.org/10.1016/j.tim.2014.05.002.
818. Costa TR, Felisberto-Rodrigues C, Meir A, Prevost MS, Redzej A, Trokter M, Waksman G. 2015. Secretion systems in Gram-negative bacteria: structural and mechanistic insights. Nat Rev Microbiol 13:343–359. https://doi.org/10.1038/nrmicro3456.
819. Chaban B, Hughes HV, Beeby M. 2015. The flagellum in bacterial pathogens: for motility and a whole lot more. Semin Cell Dev Biol 46:91–103. https://doi.org/10.1016/j.semcdb.2015.10.032.
820. Laventie BJ, Sangermani M, Estermann F, Manfredi P, Planes R, Hug I, Jaeger T, Meunier E, Broz P, Jenal U. 2019. A surface-induced asymmetric program promotes tissue colonization by *Pseudomonas aeruginosa*. Cell Host Microbe 25:140–152. https://doi.org/10.1016/j.chom.2018.11.008.
821. Ellison CK, Dalia TN, Dalia AB, Brun YV. 2019. Real-time microscopy and physical perturbation of bacterial pili using maleimide-conjugated molecules. Nat Protoc 14:1803–1819. https://doi.org/10.1038/s41596-019-0162-6.
822. Turner L, Ryu WS, Berg HC. 2000. Real-time imaging of fluorescent flagellar filaments. J Bacteriol 182:2793–2801. https://doi.org/10.1128/JB.182.10.2793-2801.2000.
823. Mahmoud KK, Koval SF. 2010. Characterization of type IV pili in the life cycle of the predator bacterium *Bdellovibrio*. Microbiology (Reading) 156:1040–1051. https://doi.org/10.1099/mic.0.036137-0.
824. Seitz P, Blokesch M. 2013. DNA-uptake machinery of naturally competent *Vibrio cholerae*. Proc Natl Acad Sci U S A 110:17987–17992. https://doi.org/10.1073/pnas.1315647110.
825. Imhaus AF, Duménil G. 2014. The number of *Neisseria meningitidis* type IV pili determines host cell interaction. EMBO J 33:1767–1783. https://doi.org/10.15252/embj.201488031.
826. Skerker JM, Berg HC. 2001. Direct observation of extension and retraction of type IV pili. Proc Natl Acad Sci U S A 98:6901–6904. https://doi.org/10.1073/pnas.121171698.
827. Copeland MF, Flickinger ST, Tuson HH, Weibel DB. 2010. Studying the dynamics of flagella in multicellular communities of *Escherichia coli* by using biarsenical dyes. Appl Environ Microbiol 76:1241–1250. https://doi.org/10.1128/AEM.02153-09.
828. Chen M, Zhao Z, Yang J, Peng K, Baker MA, Bai F, Lo CJ. 2017. Length-dependent flagellar growth of V*ibrio alginolyticus* revealed by real time fluorescent imaging. Elife 6:eLife22140. https://doi.org/10.7554/eLife.22140.
829. Renault TT, Abraham AO, Bergmiller T, Paradis G, Rainville S, Charpentier E, Guet CC, Tu Y, Namba K, Keener JP, Minamino T, Erhardt M. 2017. Bacterial flagella grow through an injection-diffusion mechanism. Elife 6:eLife23136. https://doi.org/10.7554/eLife.23136.
830. Kühn MJ, Schmidt FK, Eckhardt B, Thormann KM. 2017. Bacteria exploit a polymorphic instability of the flagellar filament to escape from traps. Proc Natl Acad Sci U S A 114:6340–6345. https://doi.org/10.1073/pnas.1701644114.
831. Lagage V, Uphoff S. 2018. Filming flagella and pili in action. Nat Rev Microbiol 16:584. https://doi.org/10.1038/s41579-018-0077-1.
832. Ellison CK, Dalia TN, Vidal Ceballos A, Wang JC, Biais N, Brun YV, Dalia AB. 2018. Retraction of DNA-bound type IV competence pili initiates DNA uptake during natural transformation in *Vibrio cholerae*. Nat Microbiol 3:773–780. https://doi.org/10.1038/s41564-018-0174-y.
833. Zhao Z, Zhao Y, Zhuang XY, Lo WC, Baker MAB, Lo CJ, Bai F. 2018. Frequent pauses in *Escherichia coli* flagella elongation revealed by single cell real-time fluorescence imaging. Nat Commun 9:1885. https://doi.org/10.1038/s41467-018-04288-4.
834. Evans LD, Hughes C, Fraser GM. 2014. Building a flagellum outside the bacterial cell. Trends Microbiol 22:566–572. https://doi.org/10.1016/j.tim.2014.05.009.
835. Manson MD, Tedesco P, Berg HC, Harold FM, Van der Drift C. 1977. A protonmotive force drives bacterial flagella. Proc Natl Acad Sci U S A 74:3060–3064. https://doi.org/10.1073/pnas.74.7.3060.
836. Moens S, Vanderleyden J. 1996. Functions of bacterial flagella. Crit Rev Microbiol 22:67–100. https://doi.org/10.3109/10408419609106456.
837. Gabel CV, Berg HC. 2003. The speed of the flagellar rotary motor of *Escherichia coli* varies linearly with protonmotive force. Proc Natl Acad Sci U S A 100:8748–8751. https://doi.org/10.1073/pnas.1533395100.
838. Minamino T, Namba K. 2008. Distinct roles of the FliI ATPase and proton motive force in bacterial flagellar protein export. Nature 451:485–488. https://doi.org/10.1038/nature06449.
839. Bai F, Lo CJ, Berry RM, Xing J. 2009. Model studies of the dynamics of bacterial flagellar motors. Biophys J 96:3154–3167. https://doi.org/10.1016/j.bpj.2009.01.023.
840. Bai F, Minamino T, Wu Z, Namba K, Xing J. 2012. Coupling between switching regulation and torque generation in bacterial flagellar motor. Phys Rev Lett 108:178105. https://doi.org/10.1103/PhysRevLett.108.178105.
841. Lee PC, Rietsch A. 2015. Fueling type III secretion. Trends Microbiol 23:296–300. https://doi.org/10.1016/j.tim.2015.01.012.
842. Kinosita Y, Kikuchi Y, Mikami N, Nakane D, Nishizaka T. 2018. Unforeseen swimming and gliding mode of an insect gut symbiont, *Burkholderia* sp. RPE64, with wrapping of the flagella around its cell body. ISME J 12:838–848. https://doi.org/10.1038/s41396-017-0010-z.
843. Blair KM, Turner L, Winkelman JT, Berg HC, Kearns DB. 2008. A molecular clutch disables flagella in the *Bacillus subtilis* biofilm. Science 320:1636–1638. https://doi.org/10.1126/science.1157877.
844. Turner L, Zhang R, Darnton NC, Berg HC. 2010. Visualization of flagella

during bacterial swarming. J Bacteriol 192:3259–3267. https://doi.org/10.1128/JB.00083-10.

845. Turner L, Berg HC. 2018. Labeling bacterial flagella with fluorescent dyes. Methods Mol Biol 1729:71–76. https://doi.org/10.1007/978-1-4939-7577-8_7.
846. Turner L, Stern AS, Berg HC. 2012. Growth of flagellar filaments of *Escherichia coli* is independent of filament length. J Bacteriol 194:2437–2442. https://doi.org/10.1128/JB.06735-11.
847. Paradis G, Chevance FFV, Liou W, Renault TT, Hughes KT, Rainville S, Erhardt M. 2017. Variability in bacterial flagella re-growth patterns after breakage. Sci Rep 7:1282. https://doi.org/10.1038/s41598-017-01302-5.
848. Berne C, Ellison CK, Agarwal R, Severin GB, Fiebig A, Morton RI, Waters CM, Brun YV. 2018. Feedback regulation of *Caulobacter crescentus* holdfast synthesis by flagellum assembly via the holdfast inhibitor HfiA. Mol Microbiol 110:219–238. https://doi.org/10.1111/mmi.14099.
849. Cairns LS, Marlow VL, Kiley TB, Birchall C, Ostrowski A, Aldridge PD, Stanley-Wall NR. 2014. FlgN is required for flagellum-based motility by *Bacillus subtilis*. J Bacteriol 196:2216–2226. https://doi.org/10.1128/JB.01599-14.
850. Turner L, Ping L, Neubauer M, Berg HC. 2016. Visualizing flagella while tracking bacteria. Biophys J 111:630–639. https://doi.org/10.1016/j.bpj.2016.05.053.
851. Martin BR, Giepmans BN, Adams SR, Tsien RY. 2005. Mammalian cell-based optimization of the biarsenical-binding tetracysteine motif for improved fluorescence and affinity. Nat Biotechnol 23:1308–1314. https://doi.org/10.1038/nbt1136.
852. Keener JP. 2006. How *Salmonella* Typhimurium measures the length of flagellar filaments. Bull Math Biol 68:1761–1778. https://doi.org/10.1007/s11538-005-9033-0.
853. Tanner DE, Ma W, Chen Z, Schulten K. 2011. Theoretical and computational investigation of flagellin translocation and bacterial flagellum growth. Biophys J 100:2548–2556. https://doi.org/10.1016/j.bpj.2011.04.036.
854. Stern AS, Berg HC. 2013. Single-file diffusion of flagellin in flagellar filaments. Biophys J 105:182–184. https://doi.org/10.1016/j.bpj.2013.05.030.
855. Evans LD, Poulter S, Terentjev EM, Hughes C, Fraser GM. 2013. A chain mechanism for flagellum growth. Nature 504:287–290. https://doi.org/10.1038/nature12682.
856. Iino T. 1974. Assembly of *Salmonella* flagellin *in vitro* and *in vivo*. J Supramol Struct 2:372–384. https://doi.org/10.1002/jss.400020226.
857. Aizawa SI, Kubori T. 1998. Bacterial flagellation and cell division. Genes Cells 3:625–634. https://doi.org/10.1046/j.1365-2443.1998.00219.x.
858. Hughes KT. 2017. Flagellum length control: how long is long enough? Curr Biol 27:R413–R415. https://doi.org/10.1016/j.cub.2017.04.008.
859. Furuno M, Atsumi T, Yamada T, Kojima S, Nishioka N, Kawagishi I, Homma M. 1997. Characterization of polar-flagellar-length mutants in *Vibrio alginolyticus*. Microbiology 143:1615–1621. https://doi.org/10.1099/00221287-143-5-1615.
860. Zhu S, Kojima S, Homma M. 2013. Structure, gene regulation, and environmental response of flagella in *Vibrio*. Front Microbiol 4:410. https://doi.org/10.3389/fmicb.2013.00410.
861. McCarter LL. 2001. Polar flagellar motility of the *Vibrionaceae*. Microbiol Mol Biol Rev 65:445–462. https://doi.org/10.1128/MMBR.65.3.445-462.2001.
862. Grossart HP, Steward GF, Martinez J, Azam F. 2000. A simple, rapid method for demonstrating bacterial flagella. Appl Environ Microbiol 66:3632–3636. https://doi.org/10.1128/AEM.66.8.3632-3636.2000.
863. Hazes B, Sastry PA, Hayakawa K, Read RJ, Irvin RT. 2000. Crystal structure of *Pseudomonas aeruginosa* PAK pilin suggests a main-chain-dominated mode of receptor binding. J Mol Biol 299:1005–1017. https://doi.org/10.1006/jmbi.2000.3801.
864. Turkowyd B, Virant D, Endesfelder U. 2016. From single molecules to life: microscopy at the nanoscale. Anal Bioanal Chem 408:6885–6911. https://doi.org/10.1007/s00216-016-9781-8.